

# Surface Modification of Cellulose Nanocrystal for Advanced Applications

by

Zhen Zhang

A thesis  
presented to the University of Waterloo  
in fulfillment of the  
thesis requirement for the degree of  
Doctor of Philosophy  
in  
Chemistry

Waterloo, Ontario, Canada, 2017

©Zhen Zhang 2017

## Examining Committee Membership

The following served on the Examining Committee for this thesis. The decision of the Examining Committee is by majority vote.

External Examiner	Elizabeth Gillies Professor Patrick Navard Directeur de Recherche CNRS
Supervisor(s)	Gilles Sèche Maître de Conférences Xiaosong Wang Associate Professor
Internal Member	Jean Duhamel Professor
Internal-external Member	Michael Tam Professor
Other Member(s)	Alex Adronov Professor Henri Cramail Professor Frédéric Léonardi Maître de Conférences

## **AUTHOR'S DECLARATION**

I hereby declare that I am the sole author of this thesis. This is a true copy of the thesis, including any required final revisions, as accepted by my examiners.

I understand that my thesis may be made electronically available to the public.

## Abstract

Cellulose nanocrystals (CNC) are bio-based nanoparticles, which display an array of interesting properties related to their renewability, biocompatibility, high tensile strength and elastic modulus, high aspect ratio, low density, low coefficient of thermal expansion, and liquid crystal behavior. As a result, CNC can be exploited in a wide variety of applications, which include the fields of composites, catalysts, emulsions or colloidosomes. However, the engineering of innovative nanomaterials from CNC generally requires a fine control of their surface properties by chemical modification, to tailor their dispersive, interfacial and self-assembling properties, or to introduce novel functionalities. In this context, the surface functionalization of cellulose nanocrystals by esterification and Surface-Initiated Atom Transfer Radical Polymerization (SI-ATRP) reactions was envisaged, with the objective to develop novel advanced materials.

The first chapter describes the state-of-the-art of the field in which the cellulose nanocrystals are presented, with their properties, methods of functionalization and potential applications. A brief overview of the SI-ATRP reaction is also given.

In the second chapter, a convenient method is proposed to directly characterize the polymer grafted by SI-ATRP on the CNC surface, without cleaving the polymer from the nanoparticle. The SI-ATRP grafting of polystyrene (PS) at the CNC surface was performed from brominated CNC initiators, in the presence of a sacrificial initiator. With this work, we show that Dynamic light scattering (DLS) is a convenient tool to monitor the polymerization process, while differential scanning calorimetry (DSC) can be used to verify if the polymerization rates of the grafted and free polymers coincide. Finally, we demonstrate that thermogravimetric analysis (TGA) can be used to directly estimate the molecular weight of the PS grafted at the surface of the CNC without cleaving the polymer from the nanoparticle.

In the third chapter, both SI-ATRP and Surface-Initiated Activator Re-Generated by Electron Transfer ATRP (SI-ARGET ATRP) were conducted to graft PS and P4VP on the surface of CNC. The SI-ATRP and SI-ARGET ATRP approaches were systematically compared to evaluate the potential benefit of each method. The surface initiating efficiencies (SIE) of the CNC-Br macroinitiators with regards to styrene or P4VP were evaluated by TGA and EA, respectively. The combination of analytical methods

such as FT-IR, DLS, DSC, TGA, and EA demonstrated that the SI-ARGET ATRP reaction favored the grafting of longer polymer chains with lower grafting densities compared with the classical SI-ATRP method. The impact of catalyst concentration and propagation rate on the differences noted was particularly discussed.

In the fourth chapter, pH-responsive P4VP-*g*-CNC nanohybrids were prepared by SI-ATRP and subsequently used to stabilize gold nanoparticles (Au NPs) and produce recyclable catalysts. The presence of P4VP brushes at the CNC surface led to the growing of Au NPs of lower averaged diameter compared with the diameter of the Au NPs deposited on pristine CNC. The catalytic performance of pristine Au NPs, Au NPs stabilized by CNC (Au@CNC) and Au NPs stabilized by P4VP-*g*-CNC (Au@P4VP-*g*-CNC) were then compared, through the measurement of the turnover frequency (TOF) obtained after catalytic reduction of 4-nitrophenol (4NP), used as a model reaction. Compared with pristine Au NPs, the catalytic activity of Au@CNC and Au@P4VP-*g*-CNC were about 10 and 24 times better, respectively. Moreover, the Au@P4VP-*g*-CNC material could be conveniently recovered by flocculation at basic pH, and the recycled catalyst remained highly active.

In the fifth chapter, Ultraviolet (UV)-responsive poly(cinnamoyloxy ethyl methacrylate) (PCEM) was grafted on CNC using SI-ATRP. The resultant PCEM-grafted CNC (PCEM-*g*-CNC) exhibits high UV absorption properties and undergoes crosslinking under UV irradiation. When the PCEM-*g*-CNC nanohybrids were incorporated in poly(vinyl chloride), transparent composite films with UV-blocking properties were obtained. The comparison of the optical and mechanical properties of the films before and after UV-irradiation allowed it to be demonstrated that the PCEM-*g*-CNC nanoparticles also acted as thermal and UV-stabilizers for PVC. Meanwhile, the tensile mechanical properties of the PVC film were significantly improved, and further increased after UV-irradiation.

In the sixth chapter, a facile method to prepare colloidosomes at room temperature is proposed from w/o inverse Pickering emulsions containing silica precursors and stabilized by cinnamate modified CNC (Cin-CNC). Cin-CNC Pickering surfactants were prepared by acylation with an excess of cinnamoyl chloride. The Cin-CNC surface displayed partial wettability with both toluene and water, which allowed stabilization w/o inverse Pickering emulsions. The Cin-CNC particles around the droplets were subsequently locked by cross-linking TEOS or TBOS silica precursors at the

water/toluene interface, leading to an intricate network of polysiloxane within the Cin-CNC shell. In optimized conditions, the Cin-CNC/silica colloidosomes obtained displayed a robust shell and slow releasing capacity with regards to encapsulated molecules such as rhodamine B or fluorescent deoxyribonucleic acid (DNA).

In the last chapter, we summarized the general conclusions of the thesis and proposed some recommendations for the future work. The cellulose nanocrystals were modified by esterification and surface initiated Atom Transfer Radical Polymerization. The characterization, mechanism and advanced applications of the functionalized CNC were envisaged. Based on the research and results in this project, we also proposed some recommendations for the future work on the modification of CNC and the other advanced applications.

## Acknowledgements

I would like to thank my supervisors, Dr. Gilles Sève and Dr. Xiaosong Wang, for the Ph.D. opportunity and guidance in the past several years. I completed the initial one and half years at Bordeaux, France. Dr. Sève introduced me to the amazing world of CNC. I am impressed by Dr. Sève's interests about scientific research and his prudent scientific attitude. Dr. Sève always tells me "play with your CNC materials." The interests in the CNC keep me full of energy in the process of exploring. Dr. Sève reviewed the slides for the first presentation of the group meeting from word to word. From that moment on, I knew every word on the slides matters. I completed the second part of my Ph.D. program at Waterloo, Canada. The most important thing I learned from Dr. Wang is how to write and revise a draft. I learned a lot from every revision. Moreover, Dr. Wang always tells me the importance of communication and presentation. The presentation is worth revising several times to be better and better as an audience will spend 20 min or longer listening to your presentation.

I am very thankful to all the committee members of Ph.D. defense: Dr. Elizabeth Gillies, Dr. Patrick Navard, Dr. Michael Tam, Dr. Henri Cramail, Dr. Frédéric Léonardi, Dr. Jean Duhamel and Dr. Alex Adronov. Thanks for your help and inspiring discussion. I also would like to thank my Ph.D. committee members: Dr. Michael Tam, Dr. Eric Prouzet, and Dr. John Honek. They gave me many suggestions during the comprehensive exam and the committee meeting. Some ideas of this thesis are inspired by their helpful suggestions. Thanks a lot for the suggestions and help. I also learned a lot from Dr. Tam's attitude to life and his leadership, from which I will benefit through my whole life.

I would like to express my gratitude to University of Waterloo, Bordeaux University, and International Doctoral School in Functional Materials (IDS-FunMat) for all kinds of support.

I am very thankful for my talented labmates, J'é énie Brand, Benjamin Dhuiege, Shaowei Shi, Kai Cao, Dapeng Liu, Nimer Murshid, Nicholas Lanigan, Heyan Jiang, Na Zhou, Diya Geng, Liao Peng, Maria Cheng, Mia San Gabriel, Zengqian Shi, Zhaolin Yao, Juntao Tang, Jianxiang Chen, Nathan Grishkewich, Nishil Mohammed, Li Chen, Xinyao Zhou, Debbie Wu, Fatima Awan, Jiyoo, Parinaz, Maria, Zhenle Cao, Stephen Wei, Yibo Liu, Takayuki Sakajiri, Haoquan Liu, Marjan Ashrafi, Salha Alharthi, and so on. These amazing lab mates always motivated and encouraged.

I also would like to thank all the technician and administrative staff at Bordeaux and Waterloo, such as Cathy, Caroline, Paul, Mishi, Christopher, Audrey, Marianne, Catherine, etc.

I would like to express my gratitude to my friends at Bordeaux and Waterloo, Xuan Wang, Xiaobo Hu, Yan Cai, Haohao Duan, Shusheng Zhang, Kai Huang, Ruie Liu, Jie Yao, Yijun Yuan, Bosi Mao, Yana Zhou, Yingying Yang, Xuesong Li, Wei Chen, Qin Liang, Jinhong Zhang, Qiaodan Fang, Xiang Wang, Hao Pan, Weisheng Liu, Monoj, Tianjiao Cai, Jingwen Diao, Yunjie Xia, Jinkai Yuan, Jian Zhi, Yinghui He, Danny Wang, Luzhu Xu, Zhuo Chen, Yu Pei, Dorothy, Sandeep, Prakash, Sasha, Jinhua Wang, Xin Ma, Hairui Liu, Xin Cong, Jiang Xu, Bin Yang, Rui He, Wei Chen, Xue Cao, Baoshi Sun, Liu Wang, Qiang Zhang, Mi, Dongzhi Zhang, Zijie, Ziming Zhu, Junshan Li, Eids, Sergey, Edgar, Peng Chen, Yuki, . All of you make my life different. I would also like to thank my friends in China, Yuping Qiao, Chengtao Wang, Shiyun Sun, Xu Zhang, Linfei Dong, Yuting Yang, and Antonio. Without their help and support, I would not have finished my Ph.D. I would also like to thank my mentors, Yihua Zhu, Xiaoling Yang, Dong Zheng and Chenan Dai.

I also would like to thank all the people who helped me and all the people who said hi to me in the last four years. At the beginning, I replied “good” when the cleaner of the QNC said “how are you doing today?” He told me “why not great, wonderful? Every day is a special day. You should live in the present.” Thanks for the inspiring and encouraging hi.

When I resigned my career as a supply chain manager from P&G in August of 2013, I was 26 years old. I started the PhD program in May of 2014, which is almost 9 months later after my resignation. It is totally 4 years for me to pursue the Doctor degree from August of 2013 to September of 2017. I am 30 years old now. That was the best ages of my life. I am not sure how many 4-years do I still have. In the last 4 years, I have been happy, hopeful, confused, frustrated and lost. In the last 4 years, I experienced some of my happiest time of my life, and also experienced the worst time of my life. It is a little naïve to say “I never regret”. Sometimes I may regret what I have said and done. But if I had a chance to live my life again, I would make the exactly same choice. In the last 4 years, I have met some wonderful person and also some other people. Some are real friends and worthy treasuring for a lifetime. Everything happens for some reason and purpose. I am grateful for what I have experienced

before and what I possess now. From now on, I am not young anymore, but I will never be old. Therefore, I will try my best to cherish and enjoy every single day of my life.

Last but not the least, I would like to thank my family, Ruiguang Zhang, Shiyang Bin, Yan Zhang, Niu Zhang, Jinshu Lu, Yinuo Li, Jianuo Li and the unborn baby. Your unconditional love and support keep me going. You are the reason and the purpose. I love you!

## Dedication

I would like to dedicate this thesis to my lovely family...

## Table of Contents

Examining Committee Membership.....	ii
AUTHOR'S DECLARATION .....	iii
Abstract .....	iv
Acknowledgements .....	vii
Dedication .....	x
Table of Contents .....	xi
List of Figures .....	xvii
List of Tables.....	xxvi
Chapter 1 State-of-the-art.....	1
1.1 Cellulose nanocrystals (CNC).....	1
1.1.1 Introduction to CNC.....	1
1.1.2 The chemical modification of CNC.....	7
1.1.3 The application of CNC.....	17
1.2 Atom transfer radical polymerization (ATRP).....	26
1.2.1 Living free radical polymerization .....	26
1.2.2 The mechanism of ATRP .....	30
1.2.3 Development of ATRP .....	31

1.3 Conclusions.....	36
Chapter 2 Convenient Method for the Characterization of Polymers Grafted by SI-ATRP on Cellulose Nanocrystals, Using DLS, DSC and TGA.....	38
2.1 Introduction.....	39
2.2 Experimental.....	40
2.2.1 Materials .....	40
2.2.2 Preparation of the brominated CNC nano-initiator: CNC-Br .....	41
2.2.3 Grafting PS from CNC-Br by SI-ATRP: PS-g-CNC.....	41
2.2.4 Characterization .....	42
2.3 Results and discussion .....	43
2.3.1 Preparation and characterization of the CNC-Br initiator.....	43
2.3.2 SI-ATRP grafting of PS from CNC-Br.....	47
2.4 Conclusions.....	55
Chapter 3 A comparative study on the Surface grafting of Polystyrene and Poly(4-vinylpyridine) on Cellulose Nanocrystals by SI-ATRP and SI-ARGET ATRP .....	56
3.1 Introduction.....	57
3.2 Experimental.....	59
3.2.1 Materials .....	59

3.2.2 Preparation of the brominated CNC nano-initiator: CNC-Br.....	59
3.2.3 Grafting PS from CNC-Br using SI-ATRP: PS1- <i>g</i> -CNC.....	59
3.2.4 Grafting PS from CNC-Br using SI-ARGET ATRP: PS2- <i>g</i> -CNC .....	60
3.2.5 Grafting P4VP from CNC-Br using SI-ATRP: P4VP1- <i>g</i> -CNC.....	61
3.2.6 Grafting P4VP from CNC-Br using SI-ARGET ATRP: P4VP2- <i>g</i> -CNC.....	61
3.2.7 Characterization.....	61
3.3 Results and discussion.....	62
3.3.1 Preparation of the CNC-Br initiator .....	62
3.3.2 SI-ATRP and SI-ARGET ATRP grafting of PS on CNC .....	63
3.3.3 SI-ATRP and SI-ARGET ATRP grafting of P4VP on CNC .....	68
3.3.4 Proposed mechanism to account for the different SIE found with SI-ATRP and SI-ARGET ATRP.....	71
3.4 Conclusions .....	72
Chapter 4 Recyclable Gold Nanoparticles Stabilized by Poly(4-vinylpyridine) Grafted Cellulose Nanocrystals for the Efficient Catalysis of 4-Nitrophenol Reduction.....	74
4.1 Introduction .....	75
4.2 Experimental .....	76
4.2.1 Material and instrumentation.....	76

4.2.2 Preparation of the brominated CNC nano-initiator: CNC-Br .....	77
4.2.3 Preparation of P4VP- <i>g</i> -CNC by SI-ATRP.....	77
4.2.4 Preparation of the catalysts dispersions: pristine Au NPs, Au@CNC, and Au@P4VP- <i>g</i> -CNC .....	78
4.2.5 Evaluation of the catalytic performance of pristine Au NPs, Au@CNC, and Au@P4VP- <i>g</i> -CNC .....	78
4.3 Results and discussion .....	79
4.3.1 Preparation and characterization of P4VP- <i>g</i> -CNC.....	79
4.3.2 The preparation and characterization of the Au@ P4VP- <i>g</i> -CNC catalyst.....	82
4.3.3 Catalytic performance and recyclability of Au@ P4VP- <i>g</i> -CNC .....	85
4.4 Conclusions.....	89
Chapter 5 Enhanced Thermal Stability and UV Resistance of Poly(vinyl chloride) Reinforced by UV-absorbing Poly(Cinnamoyloxy Ethyl Methacrylate) Grafted Cellulose Nanocrystals .....	91
5.1 Introduction.....	92
5.2 Experimental.....	94
5.2.1 Materials .....	94
5.2.2 Synthesis of monomer: cinnamoyloxy ethyl methacrylate (CEM).....	94
5.2.3 Preparation of the brominated CNC nano-initiator: CNC-Br .....	95

5.2.4 Preparation of PCEM-g-CNC and PCEM .....	95
5.2.5 Preparation of the PVC films .....	95
5.2.6 UV irradiation experiments .....	96
5.2.7 Characterization.....	96
5.3 Results and discussion.....	97
5.3.1 Preparation and characterizations of the PCEM-g-CNC nanohybrids .....	97
5.3.2 Impact of UV irradiation on PCEM-g-CNC.....	101
5.3.3 Preparation and properties of composite PVC films filled with PCEM-g-CNC nanohybrids .....	105
5.4 Conclusion.....	111
Chapter 6 Inverse Pickering Emulsions Stabilized by Cinnamate Modified Cellulose Nanocrystals (Cin-CNC) as Templates to Prepare Cin-CNC/Silica Colloidosomes .....	
6.1 Introduction .....	113
6.2 Experimental .....	115
6.2.1 Materials .....	115
6.2.2 Preparation of the Cin-CNC Pickering emulsifiers .....	115
6.2.3 Preparation of the inverse Pickering emulsions stabilized by Cin-CNC .....	115
6.2.4 Preparation of the Cin-CNC/silica colloidosomes.....	115

6.2.5 Characterization .....	116
6.3 Results and discussions.....	117
6.3.1 Preparation and characterization of the Cin-CNC Pickering emulsifier .....	117
6.3.2 Preparation and properties of the inverse Pickering emulsions stabilized by Cin-CNC...	122
6.3.3 Preparation and characterization of Cin-CNC/Silica colloidosomes .....	125
6.4 Conclusions.....	131
Chapter 7 General Conclusions.....	132
Bibliography .....	136

## List of Figures

Figure 1.1. The structure of wood: from tree to cellulose <sup>8</sup> .....	2
Figure 1.2. The intramolecular (A) and intermolecular (B) hydrogen bonding in the structure of cellulose <sup>9</sup> .....	2
Figure 1.3. Crystal and amorphous regions in the cellulose found in plant and isolation of CNC by sulfuric acid hydrolysis of the amorphous regions. ....	3
Figure 1.4. (A) Optical image of CNC aqueous dispersion (10 mg/ml); (B) the fingerprint patterns of CNC film when observed by polarized optical microscopy; (C) optical image of flow-induced birefringence for 1.5 mg/mL CNC aqueous suspension observed between cross-polarizers; <sup>20</sup> (D) schematic representation of the chiral nematic self-assembly of CNC, along with an illustration of the half-helical pitch $P/2$ ( $\sim 150\text{-}650$ nm). <sup>21</sup> .....	6
Figure 1.5. Surface chemistry of the CNC extracted by different methods <sup>6</sup> .....	8
Figure 1.6. The surface modification of CNC by adsorption. <sup>7</sup> .....	8
Figure 1.7. Common modification methods used for the surface modification of CNC by small molecules. <sup>6</sup> .....	9
Figure 1.8. The Surface functionalization of CNC by transesterification of vinyl esters. <sup>20,28</sup> .....	10
Figure 1.9. Grafting of polymers on nanoparticles .....	11

Figure 1.10. Main strategies used to graft polymers on nanoparticles: “grafting to” or “grafting from” approaches.....	12
Figure 1.11. Common modification methods used for the surface modification of CNC by polymer grafting (blue arrows = “grafting to”; yellow arrows = “grafting from”). <sup>47</sup> .....	13
Figure 1.12. The preparation of PS- <i>g</i> -CNC by SI-ATRP <sup>57</sup> .....	14
Figure 1.13. The preparation of CNC-Br with high Br content by the two steps method. <sup>55</sup> .....	15
Figure 1.14. The preparation of PtBA- <i>g</i> -CNC and PAA- <i>g</i> -CNC by SI-ATRP. <sup>55</sup> .....	16
Figure 1.15. The preparation of PDMAEMA- <i>g</i> -CNC by SI-ATRP. <sup>58</sup> .....	16
Figure 1.16. The tensile strength (a) and modulus (b) of the PVA film reinforced with increasing amounts of PABA; and schematic representation of the UV filtering and reinforcing effect of PABA-CNC (c). <sup>70</sup> .....	18
Figure 1.17. The schematic illustration of the preparation of Au NPs@CNC for the reduction of 4-nitrophenol (4NP). <sup>82</sup> .....	19
Figure 1.18. The schematic representations of the O/W classical emulsion and O/W Pickering emulsion <sup>85</sup> .....	21
Figure 1.19. The three-phase contact angle in Pickering emulsions <sup>88</sup> .....	21

Figure 1.20. SEM images of polymerized styrene droplets stabilized by different types of CNC. <sup>13</sup> a, d and g: CNC with small aspect ratio extracted from cotton; b, e, and h: bacterial cellulose; c, f and i: CNC with high aspect ratio extracted from Cladophora.....	23
Figure 1.21. The SEM images of typical colloidosomes. <sup>97</sup> .....	24
Figure 1.22. Different routes to prepare colloidosomes microcapsules <sup>98</sup> .....	25
Figure 1.23. (A) Degree of polymerization vs. monomer conversion for step-growth polymerization, chain-growth polymerization, and living polymerization; (B) The monomer conversion and $\ln [M_0/M_t]$ as a function of reaction time in living polymerization .....	27
Figure 1.24. The different steps of free radical polymerization, with the reaction rate of each step <sup>108</sup> .....	28
Figure 1.25. Reversible balance to transfer active species to dormant species .....	29
Figure 1.26. The mechanism of ATRP <sup>42</sup> .....	30
Figure 1.27. The $\ln [M_0/M_t]$ as a function of reaction time in ATRP <sup>42</sup> .....	31
Figure 1.28. The mechanism of reverse ATRP <sup>43,117</sup> .....	32
Figure 1.29. The mechanism of SR & NI ATRP <sup>118</sup> .....	33
Figure 1.30. The mechanism of AGET ATRP <sup>119</sup> .....	33
Figure 1.31. The mechanism of ARGET ATRP .....	34
Figure 1.32. The comparison of ARGET and ICAR mechanism <sup>43</sup> .....	35

Figure 1.33. Schematic of proposed mechanism for eATRP <sup>43</sup> .....	35
Figure 1.34. The surface initiated ATRP on the surface of particles or flat <sup>127</sup> .....	36
Figure 2.1. FTIR spectra of pristine CNC, CNC-Br, PS- <i>g</i> -CNC after 2 h reaction, and free PS. ....	44
Figure 2.2. <sup>13</sup> C CP-MAS NMR spectra of pristine CNC and CNC-Br. ....	45
Figure 2.3. TEM images showing the morphology of pristine CNC (A) and CNC-Br (B). ....	45
Figure 2.4. TGA thermograms (A) and DTG curves (B) of pristine CNC and CNC-Br.....	46
Figure 2.5 <sup>1</sup> H NMR spectra of the aliquots in CDCl <sub>3</sub> with different polymerization time .....	47
Figure 2.6. Kinetics of the ATRP polymerization of free PS: (A) Monomer conversion and ln([M <sub>0</sub> ]/[M <sub>t</sub> ]) vs. reaction time; (B) M <sub>n</sub> and dispersity of free PS vs. monomer conversion.....	48
Figure 2.7. Evolution of the hydrodynamic radius (R <sub>h</sub> ) of PS- <i>g</i> -CNC as a function of M <sub>n</sub> <sup>free PS</sup> . ....	49
Figure 2.8. (A) DSC curves of CNC-Br, free PS, and PS- <i>g</i> -CNC at different polymerization time; (B) T <sub>g</sub> of free PS and PS- <i>g</i> -CNC as a function of -1/M <sub>n</sub> <sup>free PS</sup> .....	51
Figure 2.9. TGA thermograms (A) and DTG curves (B) of free PS .....	51
Figure 2.10. TGA thermograms (A) and DTG curves (B) of PS- <i>g</i> -CNC.....	52
Figure 2.11. Evolution of the weight ratio of grafted PS relative to CNC-Br in PS- <i>g</i> -CNC (calculated by TGA) as a function of monomer conversion. ....	53
Figure 2.12. The M <sub>n</sub> <sup>grafted PS</sup> derived by TGA and the M <sub>n</sub> <sup>free PS</sup> measured by GPC .....	54
Figure 3.1. FTIR spectra of CNC-Br, PS1- <i>g</i> -CNC, and PS2- <i>g</i> -CNC. ....	65

Figure 3.2. (A) Hydrodynamic diameter distribution by intensity of CNC-Br, PS1- <i>g</i> -CNC and PS2- <i>g</i> -CNC; (B) DSC curves of free PS, PS1- <i>g</i> -CNC, and PS2- <i>g</i> -CNC.....	66
Figure 3.3. TGA thermograms (A) and DTG curves (B) of CNC-Br, PS1- <i>g</i> -CNC, and PS2- <i>g</i> -CNC.....	67
Figure 3.4. FTIR spectra of CNC-Br, P4VP1- <i>g</i> -CNC, and P4VP2- <i>g</i> -CNC.....	69
Figure 3.5. DSC curves of P4VP, P4VP1- <i>g</i> -CNC, and P4VP2- <i>g</i> -CNC.....	70
Figure 3.6. TGA thermograms (A) and DTG curves (B) of CNC-Br, P4VP1- <i>g</i> -CNC, P4VP2- <i>g</i> -CNC and free P4VP.....	70
Figure 3.7. Proposed mechanism to account for the different SIE found with SI-ATRP and SI-ARGET ATRP.....	72
Figure 4.1. FTIR spectra of CNC, CNC-Br, and P4VP- <i>g</i> -CNC.....	80
Figure 4.2. (A) Hydrodynamic diameter ( $D_h$ ) distribution by intensity of the CNC (■) and P4VP- <i>g</i> -CNC (▲) dispersed in water (pH = 2); (B) Evolution of the average $D_h$ (■) and Zeta-potential (●) of the P4VP- <i>g</i> -CNC suspension as a function of pH.....	81
Figure 4.3. The TEM images of CNC (A), CNC-Br (B), P4VP- <i>g</i> -CNC (C).....	81
Figure 4.4. UV-Vis absorbance spectra of the reaction medium during the preparation of Au NPs (A), Au@CNC (B) and Au@P4VP- <i>g</i> -CNC (C and D). .....	82

Figure 4.5. Photographs of the reaction medium during the preparation steps of the Au NPs, Au@CNC and Au@P4VP- <i>g</i> -CNC catalysts. Photographs were taken before (A), 1 min after (B) and 2 hours after (C) the addition of NaBH <sub>4</sub> .....	83
Figure 4.6. The TEM images of Au@CNC (A) and Au@P4VP- <i>g</i> -CNC (B) .....	84
Figure 4.7. Size distribution of Au NPs in Au@CNC and Au@P4VP- <i>g</i> -CNC. ....	85
Figure 4.8. Time-dependent UV-vis absorption spectra of the reaction medium during the 4NP reduction catalyzed by (A) pristine Au NPs, (B) Au@CNC, and (C) Au@P4VP- <i>g</i> -CNC and evolution of $\ln(A_t/A_0)$ with time (D).....	86
Figure 4.9. (A) Schematic illustrating of the recovery of Au@CNC and Au@P4VP- <i>g</i> -CNC; Time-dependent UV-vis absorption spectra of 4NP reduced by NaBH <sub>4</sub> catalyzed by recycled Au@CNC (B) and recycled Au@P4VP- <i>g</i> -CNC (C); (D) shows the plots of $\ln(A_t/A_0)$ against time for the reduction of 4NP with different catalysts.....	88
Figure 5.1. FTIR spectra of CNC, CNC-Br, PCEM- <i>g</i> -CNC and PCEM.....	99
Figure 5.2. Images of the water droplets deposited on the glass support, before and after spin-coating with CNC and PCEM- <i>g</i> -CNC.....	99
Figure 5.3. TGA thermograms (A) and DTG curves (B) of pristine CNC, CNC-Br, PCEM and PCEM- <i>g</i> -CNC. ....	100
Figure 5.4. The DSC curves of CNC, CNC-Br, PCEM, and CPEM- <i>g</i> -CNC.....	101

Figure 5.5. Evolution of the UV absorption of the conjugated C=C bond in PCEM (A) and PCEM-*g*-CNC (C) films irradiated at 365 nm for several hours; and evolution upon irradiation of the maximum absorbance (●) and reciprocal (▲) at 276 nm, for both PCEM (B) and PCEM-*g*-CNC (D) films. .... 103

Figure 5.6. FTIR spectra of PCEM and PCEM-*g*-CNC samples, before and after irradiation at 365 nm of their solution/dispersion (overnight irradiation accompanied by an evaporation of the solvent).... 104

Figure 5.7. DSC curves of the PCEM and PCEM-*g*-CNC samples, before and after irradiation at 365 nm of their solution/dispersion (overnight irradiation accompanied by an evaporation of the solvent). ..... 105

Figure 5.8. PVC, PVC/CNC (5 wt. %) and PVC/PCEM-*g*-CNC (5 wt. %) composite films obtained by solution casting of the corresponding DMF solutions/suspensions followed by heat annealing. .... 106

Figure 5.9. Transmittance of the PVC, PVC/CNC and PVC/PCEM-*g*-CNC films, before and after heat annealing at 80 °C..... 107

Figure 5.10. Schematic representation depicting the UV-filtering and reinforcing effect of the PCEM-*g*-CNC filler in PVC, before and after heat annealing. The transmittances given were measured at 320 nm (UV) and 555 nm (Visible)..... 107

Figure 5.11. Transmittance of the PVC, PVC/CNC and PVC/PCEM-*g*-CNC films before and after UV irradiation. .... 109

Figure 5.12. Tensile stress-strain curves obtained after analysis of the PVC, PVC/CNC and PVC/PCEM-*g*-CNC films before and after the UV irradiation. .... 110

Figure 6.1. FTIR spectra of pristine CNC and Cin-CNC.....	118
Figure 6.2. TEM images of pristine CNC and Cin-CNC.....	119
Figure 6.3. TGA thermograms (A) and DTG curves (B) of pristine CNC and Cin-CNC.....	120
Figure 6.4. Optical images of CNC and Cin-CNC dispersions in solvents of different polarity (the dielectric constants of water, DMF, and THF are 78.54, 38.25, and 7.52, respectively). ....	120
Figure 6.5. Size distribution by intensity of the CNC and Cin-CNC particles dispersed in water, DMF or THF (0.2 mg/ml) .....	121
Figure 6.6. Images of the water droplets deposited on the glass support, before and after spin-coating with the CNC and Cin-CNC material.....	121
Figure 6.7. Optical micrographs of the inverse water/toluene emulsion droplets stabilized with different concentrations of Cin-CNC (A, 0.25 mg/mL; B, 0.5 mg/mL; C, 1 mg/mL; D, 2 mg/mL; E, 2 mg/mL; and F, 4 mg/mL); and fluorescent micrograph of the water droplets stained by rhodamine B (E). The length of scale bar in the micrographs is 50 $\mu$ m.....	122
Figure 6.8. Size distribution of the emulsion droplets obtained at different concentrations of Cin-CNC(A); and number-average diameter $D(1,0)$ as a function of Cin-CNC concentration.....	123
Figure 6.9. Evolution of $1/D(3,2)$ as a function of Cin-CNC concentration. ....	124
Figure 6.10. Evolution of surface tension of the Cin-CNC toluene suspension and interfacial tension between toluene and water as a function of Cin-CNC concentration. ....	125

Figure 6.11. Evolution with time of the number-average diameter  $D(1,0)$  of the emulsion droplets in the Pickering systems containing TEOS or TBOS precursors (pH = 1 or 7; [Cin-CNC] = 2 or 5 mg/mL).  
..... 126

Figure 6.12. Evolution of the inverse water/toluene emulsion droplets with increasing amounts of ethanol: A, 0  $\mu\text{L}$ ; B, 20  $\mu\text{L}$ ; C, 40  $\mu\text{L}$ ; and D, 100  $\mu\text{L}$  (initial volume = 200  $\mu\text{L}$ ; pH = 7; ([Cin-CNC] = 2 mg/mL) The length of scale bar in the optical micrographs is 50  $\mu\text{m}$ . ..... 128

Figure 6.13. Optical micrographs of the inverse water/toluene emulsion droplets before (A, B, C) and after (D, E, F) evaporation of the toluene (for 6 days at room temperature): A&D, without TEOS; B&E, with TEOS at pH =7; C&F, with TEOS at pH =1 ([Cin-CNC] =2 mg/mL). The length of scale bar in the micrographs is 50  $\mu\text{m}$ . ..... 129

Figure 6.14. Optical micrographs of the colloidosomes cross-linked with TEOS for 2 days (A) or 6 days (B) and diluted in EtOH. ([Cin-CNC] =5 mg/mL; pH =1). The length of scale bar in the optical micrographs is 50  $\mu\text{m}$ . ..... 129

Figure 6.15. SEM images of Cin-CNC/silica colloidosomes crosslinked with TEOS for 6 days ([Cin-CNC] = 5 mg/mL). The length of the scales bars in the optical micrographs is 5  $\mu\text{m}$ . ..... 130

Figure 6.16. Fluorescent optical micrographs of the colloidosome after encapsulation of rhodamine B (A) or fluorescent DNA (B). ([Cin-CNC] =5 mg/mL; pH =1). The length of scale bar in the optical micrographs is 50  $\mu\text{m}$ . ..... 131

## List of Tables

Table 1.1. The different types of nanocellulose materials <sup>1</sup> .....	4
Table 1.2.The fundamental mechanical properties of CNC and other reinforcement materials <sup>6</sup> .....	5
Table 1.3. The summary of colloidal particles used in Pickering emulsifiers <sup>84</sup> .....	22
Table 2.1. Kinetics parameters of the ATRP polymerization of free PS.....	48
Table 2.2. $M_n^{\text{free PS}}$ and $M_n^{\text{grafted PS}}$ values of the PS- <i>g</i> -CNC samples obtained at different polymerization times. ....	53
Table 3.1. Reaction conditions and characteristics or the PS- <i>g</i> -CNC hybrid nanomaterials prepared by SI-ATRP or SI-ARGET ATRP .....	63
Table 3.2. Reaction conditions and characteristics or the P4VP- <i>g</i> -CNC hybrid nanomaterials prepared by SI-ATRP or SI-ARGET ATRP.....	68
Table 4.1. Catalytic performance of Au@CNC and Au@P4VP- <i>g</i> -CNC compared with other catalyst systems, for the reduction of 4NP. ....	89
Table 5.1. Evolution of the transmittance at 555 nm of the PVC films, before and after heat annealing or UV-irradiation. ....	108
Table 5.2. Summary of the tensile mechanical characteristics of the PVC films before and after UV-irradiation.....	111

# Chapter 1

## State-of-the-art

### 1.1 Cellulose nanocrystals (CNC)

#### 1.1.1 Introduction to CNC

##### 1.1.1.1 Cellulose

Fossil fuel is still the most important energy resource and a raw material widely used in industry. However, after the immoderate usage of fossil fuels for hundreds of years, the climate change and the environmental pollution issues have become a threat to the sustainable development of human beings. Therefore, there is an increasing demand today to replace petroleum-based synthetic materials with natural materials, which are abundant, renewable, sustainable, and inexpensive. Cellulose, in particular, has been used by mankind for thousands of years, in the form of wood or fibers (energy source, building material, furniture, clothing).<sup>1</sup> It has also been exploited as a primary raw material for more than 150 years, in paper, packaging, textile or food industry. Celluloid, for instance, is the first human-made thermoplastic polymer material, which is obtained by reacting cellulose with nitric acid.<sup>1</sup> In recent decades, the nanostructured form of cellulose has also drawn increasing attention to produce bio-based nanomaterials for advanced applications.<sup>1-6</sup>

Cellulose is the most abundant biopolymer on earth, about  $7.5 \times 10^{10}$  tons of cellulose being produced in the biosphere every year.<sup>3,7</sup> About 50% of the carbon in the biosphere exists in the form of cellulose. It is the main component of plant cell walls, in which it is produced by photosynthesis, but it can also be synthesized by bacteria or found in animals.<sup>4</sup> The structure of wood from tree to cellulose is shown in Figure 1.1.<sup>7,8</sup>

The repeat unit of cellulose is an anhydroglucose unit (AGU), which is linked by  $\beta$  (1 $\rightarrow$ 4)-glycosidic linkages. The intramolecular and intermolecular hydrogen bonds between AGU confer to cellulose a layer-by-layer structure (Figure 1.2), which is quite stable and is responsible for the high strength of the material.

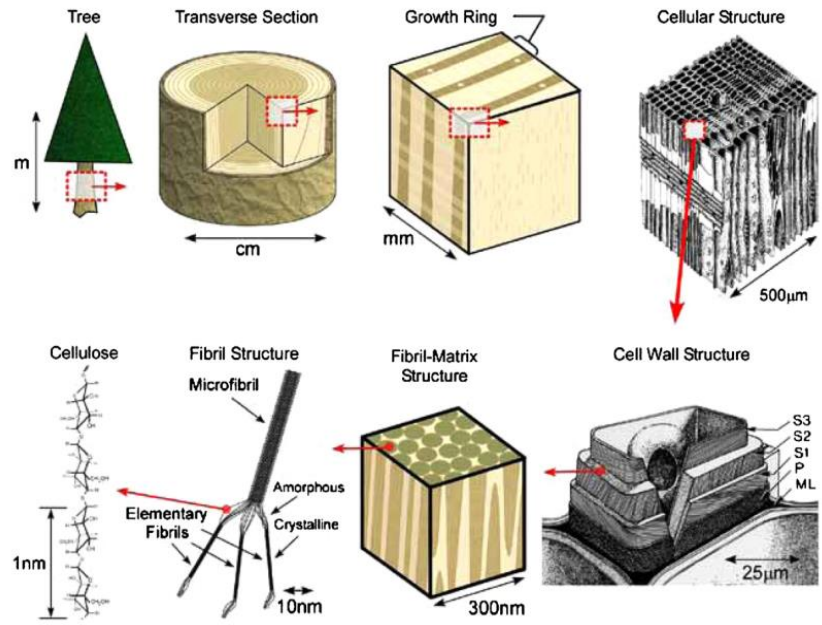


Figure 1.1. The structure of wood: from tree to cellulose<sup>8</sup>

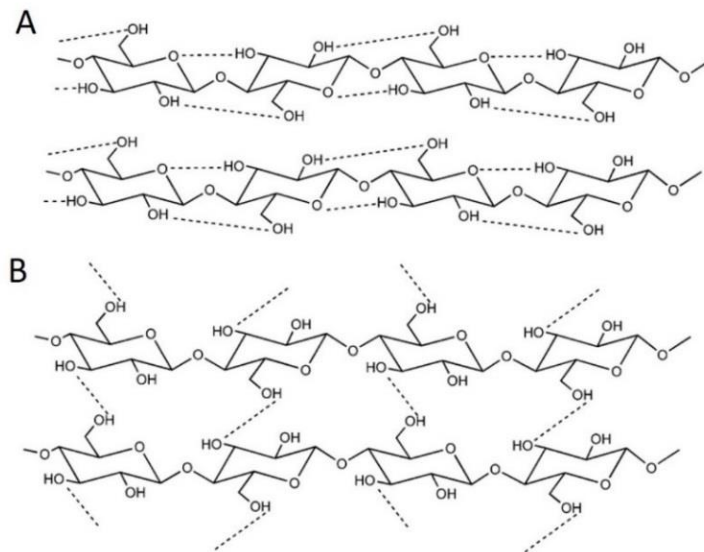
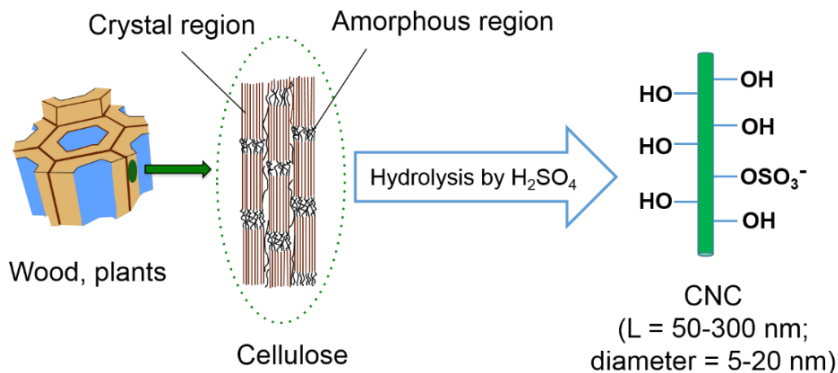


Figure 1.2. The intramolecular (A) and intermolecular (B) hydrogen bonding in the structure of cellulose<sup>9</sup>

### 1.1.1.2 The different types of nanocellulose materials

Due to the hydrogen bonds between AGUs, some cellulose chains are tightly packed together as highly ordered cellulose crystal regions, but some chains stay in an amorphous form. Therefore, two different kinds of structural domains are found in the cellulose of plants: nanometer-sized crystal regions and amorphous regions, as shown in Figure 1.3.



**Figure 1.3. Crystal and amorphous regions in the cellulose found in plant and isolation of CNC by sulfuric acid hydrolysis of the amorphous regions.**

The amorphous domains of cellulose can be removed by chemical processes, to release the nanocellulose material in the form of cellulose nanocrystals (CNC). However, cellulose nanofibers (CNF) containing both crystalline and amorphous regions can also be produced by mechanical treatment. In a third approach, nanocellulose can be biosynthesized by bacteria, and in that case, it is termed bacterial nanocellulose (BNC). So far, the terminology to refer to nanocellulose is still not consistent in the literature. Many other terms can be found like microfibrillated cellulose (MFC), nanocrystalline cellulose (NCC) or cellulose nanowhiskers (CNW). The different types of cellulose nanomaterials with their name, source, method of isolation and typical size are summarized in Table 1.1.<sup>1</sup>

CNC can be produced from some cellulosic substrates, by sulfuric acid treatment combined with sonication.<sup>2,3,10-12</sup> The treatment provokes the hydrolysis of the amorphous regions, leading to the release of nano-sized rod-like particles bearing sulfate ester groups on their surface (Figure 1.3). The

diameter of CNC is similar to that of CNF, but the length is smaller (usually between 50 and 300 nm). Since the amorphous domains have been removed, the crystallinity index of CNC is quite high (about 90% in general). CNF are the nano-fibrils of cellulose with a high aspect ratio. Generally, the diameter of CNF is in the range of 5-20 nm, and the length in the order of several micrometers.<sup>1</sup> CNF is typically produced by mechanical disintegration of pulp, cotton or microcrystalline cellulose and is composed of both crystalline and amorphous regions. Therefore, the crystallinity index of CNF is lower than that of CNC. BNC is produced by aerobic bacteria belonging to the *Gluconacetobacter* genus and is composed of interconnected fibrils.<sup>13</sup> The dimensions, physical and chemical properties of nanocellulose depend on the source and preparation process.

**Table 1.1. The different types of nanocellulose materials<sup>1</sup>**

Type of nano-cellulose	Selected references and synonyms	Typical sources	Formation and average size
microfibrillated cellulose (MFC)	microfibrillated cellulose, <sup>[1]</sup> nanofibrils and microfibrils, nanofibrillated cellulose	wood, sugar beet, potato tuber, hemp, flax	delamination of wood pulp by mechanical pressure before and/or after chemical or enzymatic treatment diameter: 5–60 nm length: several micrometers
nanocrystalline cellulose (NCC)	cellulose nanocrystals, crystallites, <sup>[2]</sup> whiskers, <sup>[3]</sup> rodlike cellulose microcrystals <sup>[4]</sup>	wood, cotton, hemp, flax, wheat straw, mulberry bark, ramie, Avicel, tunicin, cellulose from algae and bacteria	acid hydrolysis of cellulose from many sources diameter: 5–70 nm length: 100–250 nm (from plant celluloses); 100 nm to several micrometers (from celluloses of tunicates, algae, bacteria)
bacterial nano-cellulose (BNC)	bacterial cellulose, <sup>[5]</sup> microbial cellulose, <sup>[6]</sup> biocellulose <sup>[7]</sup>	low-molecular-weight sugars and alcohols	bacterial synthesis diameter: 20–100 nm; different types of nanofiber networks

### 1.1.1.3 The preparation of CNC

The first colloidal suspension of CNC was obtained by sulfuric acid degradation of cellulose fibers, following the work of Rånby in the 1950s.<sup>3,14</sup> This is the most popular method to prepare CNC.<sup>3</sup> The treatment provokes the hydrolysis of the amorphous regions, but the nanocrystals are preserved, their resistance to acid hydrolysis being higher. With sulfuric acid, a small part of the hydroxyl groups at the CNC surface is concurrently substituted by sulfate ester groups, leading to negatively charged particles (Figure 1.3). As a consequence, CNC form stable dispersions in water by electrostatic repulsion between the negative charges. When hydrochloric acid is used instead of sulfuric acid, the nanoparticles are not negatively charged and a limited dispersibility in water is obtained.

The production of CNC by sulfuric acid hydrolysis has been recently scaled-up, but many parameters can influence the quality of the final product, in particular, the temperature, the hydrolysis time and the ratio of acid to cellulose. Typically, a high concentration of sulfuric acid (about 65 wt%) is used in the hydrolysis process. The temperature ranges between 20 and 70 °C, and the reaction can be conducted for 30 min to several hours. The size, crystallinity index, mechanical properties, and amount of surface charges depend strongly on the hydrolysis condition. Generally, an increase in temperature, hydrolysis time or acid to cellulose ratio leads to a decreased length of the nano-rods obtained.<sup>15,16</sup> After the treatment, wash-centrifugation cycles and dialysis are generally required to remove the acid and other residues. The final CNC product is typically dried by freeze-drying or spray-drying.<sup>17</sup>

#### 1.1.1.4 The properties of CNC

The 20th century witnessed the emergence of nanotechnology and nanomaterials, but critical challenges related to the sustainability, stability, biocompatibility, scalability, and cost of these materials still need to be tackled. Nanocellulose materials can help addressing part of these issues.

**Table 1.2. The fundamental mechanical properties of CNC and other reinforcement materials<sup>6</sup>**

Material	$\rho/\text{g cm}^{-3}$	$\sigma_f$ (GPa)	$E_A$ (GPa)	$E_T$ (GPa)
Kevlar-49 fiber	1.4	3.5	124–130	2.5
Carbon fiber	1.8	1.5–5.5	150–500	—
Steel Wire	7.8	4.1	210	—
Clay Nanoplatelets	—	—	170	—
Carbon Nanotubes	—	11–63	270–950	0.8–30
Boron nanowhiskers	—	2–8	250–360	—
<b>Crystalline Cellulose</b>	<b>1.6</b>	<b>7.5–7.7</b>	<b>110–220</b>	<b>10–50</b>

$\rho$  = density,  $\sigma_f$  = tensile strength,  $E_A$  = elastic modulus in axial direction,  $E_T$  = elastic modulus in transverse direction.

CNC are renewable and biocompatible nano-rods, with a high specific area (400 m<sup>2</sup>/g), high aspect ratio, low density and excellent mechanical properties. As shown in Table 1.2,<sup>6</sup> the density of CNC is as low as 1.6 g/cm<sup>3</sup>, which is comparable to the density of carbon fiber and Kevlar-49 fiber and represents one-fifth of the density of steel wire. The elastic modulus of CNC in the axial direction is in the same range as that of Kevlar-49 fiber, carbon fiber, or steel wire, but the tensile strength is greater. Because of these excellent mechanical properties, CNC can be used as a reinforcement agent in polymer matrices.<sup>18</sup> In addition, CNC are transparent to visible light (due to their nano-size) and display a very low coefficient of thermal expansion (CTE), making them a promising material for flexible displays.<sup>6,19</sup>

The CTE of CNC is only 0.1 ppm/K, which is much lower than most of the common polymers (86 ppm/K for acrylic resins and 120 ppm/K for epoxy resins).

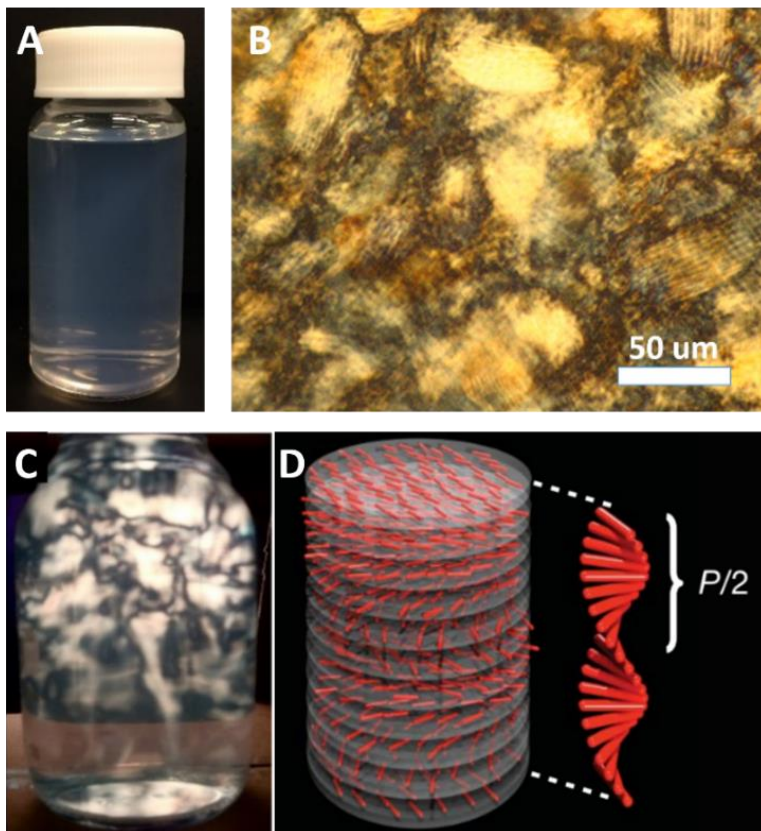


**Figure 1.4. (A) Optical image of CNC aqueous dispersion (10 mg/ml); (B) the fingerprint patterns of CNC film when observed by polarized optical microscopy; (C) optical image of flow-induced birefringence for 1.5 mg/mL CNC aqueous suspension observed between cross-polarizers;<sup>20</sup> (D) schematic representation of the chiral nematic self-assembly of CNC, along with an illustration of the half-helical pitch  $P/2$  ( $\sim 150\text{-}650$  nm).<sup>21</sup>**

As rod-like stiff particles, CNC also display liquid crystal properties in suspensions, like viruses or rod-like alumina.<sup>22,23</sup> As a consequence, CNC aqueous dispersions display flow-induced birefringence when observed between cross-polarizers under gentle stirring, provoked by the entropically driven self-assembly of the CNC (Figure 1.4).<sup>24</sup> Above a critical concentration, the CNC suspension separates into

two phases after several days: an isotropic phase on top, and a liquid crystal phase at the bottom.<sup>25</sup> The critical concentration mainly depends on the dimension of the CNC but is generally near 2 wt.%. The isotropic phase requires gentle stirring to observe the birefringence between cross-polarizers, but the crystal phase is birefringent without stirring. After the evaporation of water, an iridescent film with fingerprint patterns is obtained. When observed by polarized optical microscopy, the fingerprint patterns are characteristic of a chiral nematic phase (Figure 1.4B).<sup>3</sup> A schematic representation of the chiral nematic structure is represented in Figure 1.4D.

### **1.1.2 The chemical modification of CNC**

The application field of nanocellulose materials is a priori vast, but the engineering of innovative nanomaterials from CNC generally requires a fine control of their surface properties by chemical modification.<sup>26-28</sup> Because of their hydrophilic surface, CNC are prone to self-aggregation by hydrogen bonding and can be hardly dispersed in low polarity solvents or polymers. The dispersive, interfacial and self-assembling properties of the CNC can however be tailored by surface functionalization. The method can also be used to introduce novel functions that can impart original properties to the material.

The surface chemistry of the CNC can be modified by four different approaches: (1) Surface modification during the isolation of the CNC, (2) post-modification by adsorption of cationic molecules, (3) post-modification by covalent grafting of small molecules, and (4) post-modification by polymer grafting.

#### **1.1.2.1 Surface modification during the isolation of the CNC**

Different surface chemistry can be obtained depending on the method used to extract the CNC, as shown in Figure 1.5. The sulfuric acid treatment (the most used method) leads to the production of CNC with negative sulfate ester groups at their surface.<sup>29,30</sup> The concentration of sulfuric acid and the hydrolysis time determine the amount of surface charge. The electrostatic repulsion between the negative charges CNC is responsible for their good dispersion in water. When necessary, the sulfuric ester groups can be removed by treating the nanoparticles with a sodium hydroxide solution.<sup>31</sup>

Hydrochloric acid can also be used to remove the amorphous cellulose from the initial substrate and produce CNC, but in that case the surface is only hydroxylated. An acetylated surface can also be obtained by treating the CNC with acetic acid.<sup>32</sup>

Finally, CNC bearing carboxylic acid groups at the surface can be obtained by oxidation with 2,2,6,6-tetramethyl-piperidinyl-1-oxyl (TEMPO), coupled with a mechanical treatment.<sup>33</sup>

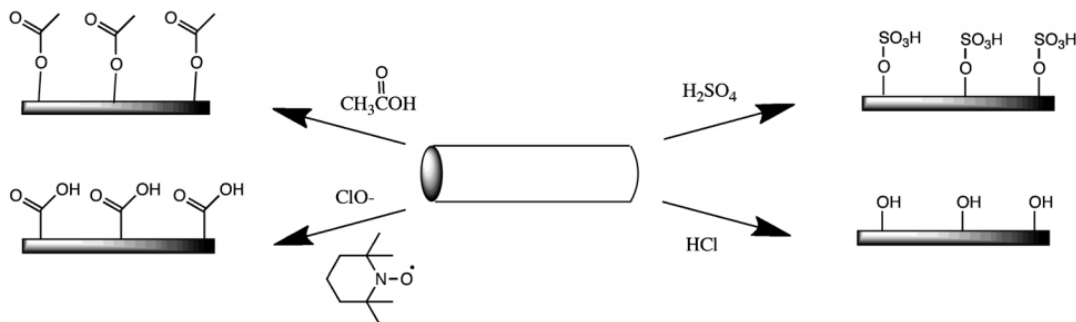


**Figure 1.5. Surface chemistry of the CNC extracted by different methods<sup>6</sup>**

#### 1.1.2.2 Post-modification by adsorption of cationic molecules

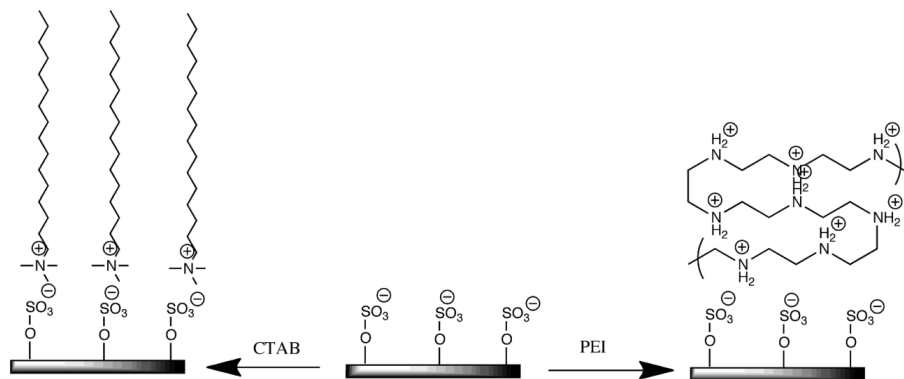


**Figure 1.6. The surface modification of CNC by adsorption.<sup>7</sup>**

Due to the negatively charged surface of the CNC produced by sulfuric acid hydrolysis, cationic molecules can be further adsorbed by electrostatic adsorption. In particular, positively charged polymers, such as cetyltrimethyl ammonium bromide (CTAB) or polyethylenimine (PEI), have been successfully adsorbed at the CNC surface as shown in Figure 1.6.<sup>24,25</sup> In the latter case, other

polyelectrolytes can be sequentially absorbed using a layer-by-layer technique, to form multilayer surfaces.

### 1.1.2.3 Post-modification by covalent grafting of small molecules

The many hydroxyl groups at the CNC surface can be used as reactive sites to graft many molecules using different chemical strategies. The CNC used in our study were produced by sulfuric acid hydrolysis of wood pulp, according to a general procedure previously described. They consist of rod-like particles with estimated dimensions of  $110.3 \pm 47.7$  nm in length and  $4.8 \pm 1.1$  nm in diameter, based on AFM topography images.<sup>28</sup> The amount of accessible hydroxyl groups at the surface of these CNC were estimated to be  $3.10 \pm 0.11$  mmol.g<sup>-1</sup>, using a method based on phosphorylation coupled with <sup>31</sup>P NMR and FT-IR analysis.<sup>28</sup> This represents 16.7 mol% of the total OH groups contained in the CNC.

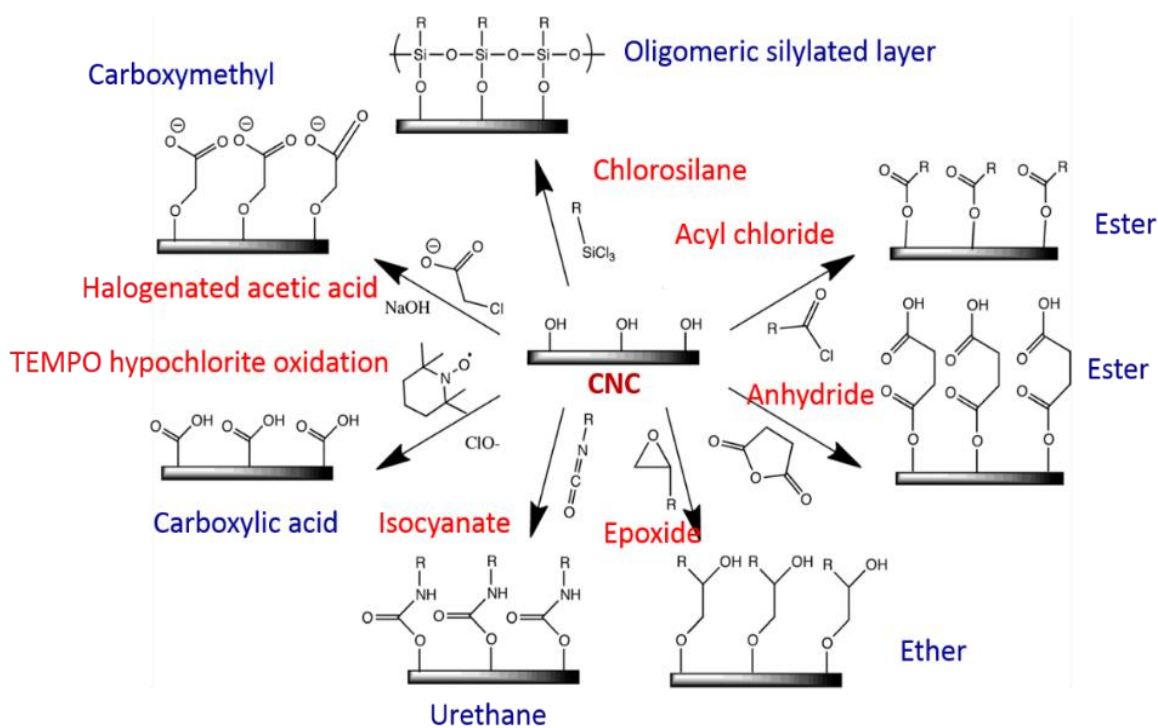


**Figure 1.7. Common modification methods used for the surface modification of CNC by small molecules.<sup>6</sup>**

Theoretically, any chemical reactive towards hydroxyl groups can be employed to modify the surface of CNC. Some common modification methods used for the surface modification of CNC by small molecules are listed as Figure 1.7.<sup>6</sup>

When CNC are modified with acyl chlorides or anhydrides, CNC bearing ester groups at their surface are formed.<sup>29,34</sup> The modification with epoxides and isocyanates leads to CNC bearing ether and urethane groups, respectively.<sup>35,36</sup> The oxidation of CNC by TEMPO converts the primary alcohol groups of CNC into carboxylic acid.<sup>37</sup> Halogenated acetic acid are used to graft carboxymethyl groups and chlorosilanes to silylate the surface.<sup>38</sup>

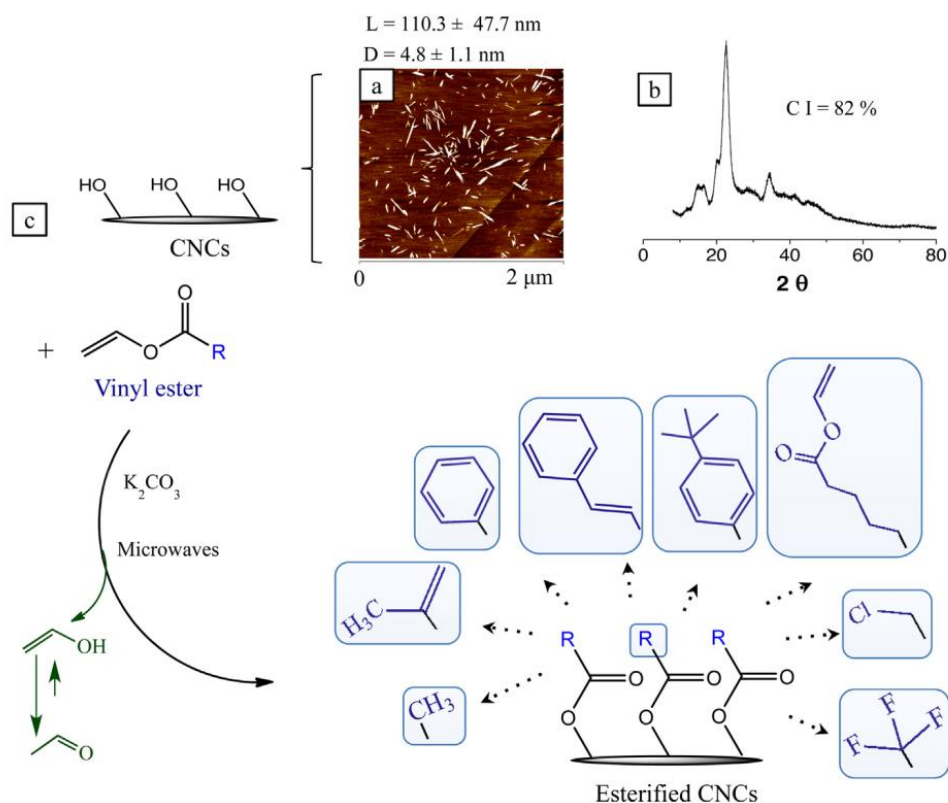


**Figure 1.8. The Surface functionalization of CNC by transesterification of vinyl esters.**<sup>20,28</sup>

In a recent work, Šeb̆e et al. reported an original method for the surface functionalization of CNC, by transesterification of vinyl esters, as shown in Figure 1.8.<sup>20</sup> The reaction proceeds in mild conditions,

with  $K_2CO_3$  as a catalyst. The leaving group is vinyl alcohol, which immediately tautomerizes to acetaldehyde thereby driving the reaction towards the formation of the expected ester.

#### 1.1.2.4 Post-modification by polymer grafting

##### 1.1.2.4.1 Principle

Another promising method to modify CNC is polymer grafting. Polymer grafting is a very popular method to functionalize nanoparticles with long chains at the surface, as shown in Figure 1.9. Numerous inorganic and organic nanoparticles have been grafted with polymer brushes for various applications:<sup>39</sup> polymer grafted silver nanoparticles for catalysis and photography, polymer grafted gold nanoparticles for electronics and biosensors, and polymer grafted  $TiO_2$  for photoelectrochemistry.<sup>39</sup> Nanoparticles are prone to aggregation due to their high specific surface area, but the steric hindrance imparted by the grafted polymers increases the stability of the nanoparticles. Moreover, many types of polymers can be grafted at the nanoparticles surface, which allows introducing a wide variety of functionalities.

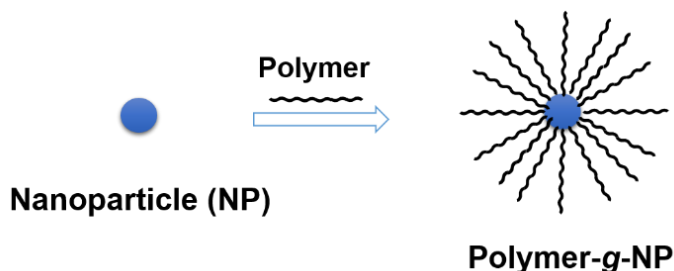


**Figure 1.9. Grafting of polymers on nanoparticles**

##### 1.1.2.4.2 Grafting methods: “grafting to” and “grafting from” approaches

There are two different strategies to graft polymer brushes on the surface of a substrate: the “grafting to” or “grafting from” approaches, as shown in Figure 1.10.

With the “grafting to” strategy, pre-synthesized polymers are anchored at the surface of nanoparticles. The molecular weight of the anchored polymers can be easily characterized by Gel Permeation Chromatography (GPC), so the chain length of the grafted polymer brushes is well controlled and

similar for all graft. However, due to the high steric hindrance of polymers, the grafting density in the “grafting to” approach is not high.

With the “grafting from” method, initiators are first anchored to the surface of the nanoparticles, then a polymerization of monomers is initiated from these sites. The method is often called “surface-initiated polymerization (SIP)”. The steric hindrance being much lower with this method, polymer brushes with high grafting density can be grafted on the nanoparticles surface. For this reason, the “Grafting from” strategy is generally more popular than the “grafting to” approach.<sup>40,41</sup> However, the molecule weight and chain length of the polymers grafted with this method is hard to characterize. The control of the chain length and the characterization of the grafted polymers are the two main challenges still needing to be addressed in the “grafting from” approach. Living radical polymerization, such as Atom transfer radical polymerization (ATRP), is a common “grafting from” technology.<sup>42,43</sup> When applied to cellulosic substrates such as CNC, Surface-Initiated ATRP (SI-ATRP) is an efficient method to graft polymers with a fine control of the chain length and a high grafting density.<sup>44-46,9</sup>

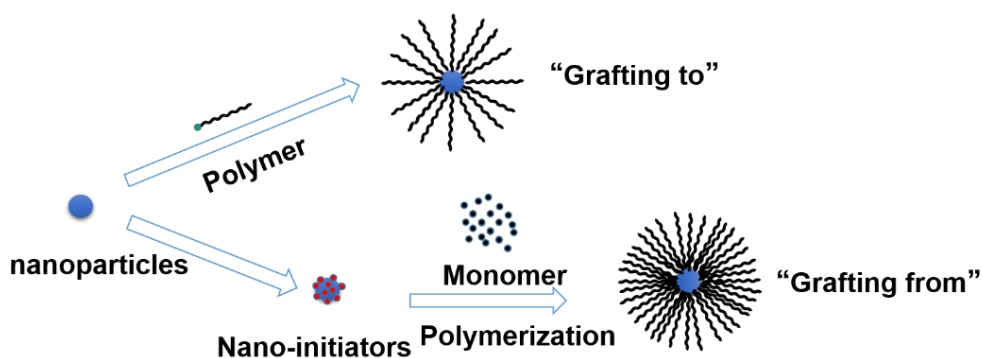


**Figure 1.10. Main strategies used to graft polymers on nanoparticles: “grafting to” or “grafting from” approaches.**

So far, a variety of polymers has been introduced at the surface of CNC by both “grafting to” and “grafting from” technologies, as shown in Figure 1.11.<sup>47,48</sup> For example, after grafting polystyrene (PS) on CNC via SI-ATRP, the material obtained exhibits enhanced absorption capacity with regards to pollutant 1,2,4-Trichlorobenzene.<sup>46</sup> The grafting of poly(ethylene oxide) (PEO) on CNC by ring opening polymerization, results in a material (presenting chiral nematic properties in water).<sup>35</sup> Poly[2-

(dimethylamino)ethyl methacrylate] (PDMAEMA) is another polymer that has been grafted on CNC to produce Pickering stabilizers with responsive properties (PDMAEMA-*g*-CNC). Since PDMAEMA displays both pH- and thermo-responsiveness, the emulsification and demulsification of Pickering emulsions stabilized by PDMAEMA-*g*-CNC can be triggered by both pH and temperature change.<sup>49</sup> The grafting of poly(4-vinyl pyridine) (P4VP) on CNC allows producing reversible flocculants with pH-responsiveness.<sup>50</sup> The SI-ATRP grafting of poly(oligo(ethylene glycol) methyl ether methacrylate) (POEGMA) – a biocompatible and temperature-responsive polymer – leads to CNC with a controlled lower critical solution temperature (LCST).<sup>51</sup> Among the other polymers that have been grafted on CNC, we can mention poly(methyl methacrylate) (PMMA),<sup>52</sup> poly-6-[4-(4-methoxyphenylazo)phenoxy]hexyl methacrylate (PMMAZO),<sup>53</sup> poly(ethylene oxide),<sup>35</sup> poly(ethylene glycol),<sup>54</sup> poly(acrylic acid) (PAA),<sup>55</sup> poly(methyl acrylate) (PMA),<sup>56</sup> and poly(*N*-isopropyl acrylamide) (PNiPAAm).<sup>44</sup>

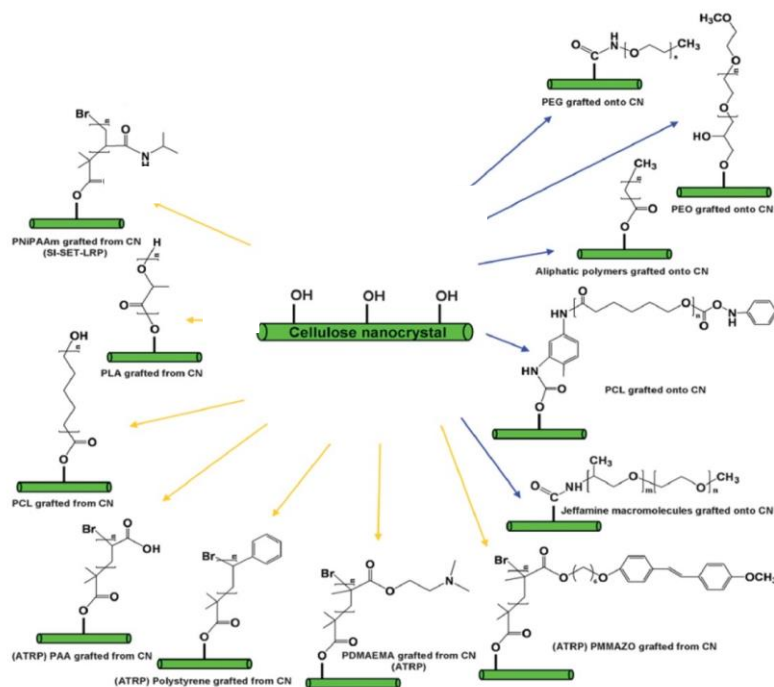


**Figure 1.11. Common modification methods used for the surface modification of CNC by polymer grafting (blue arrows = “grafting to”; yellow arrows = “grafting from”).<sup>47</sup>**

#### 1.1.2.4.3 SI-ATRP grafting of polymers on CNC

One of the first publication mentioning the SI-ATRP grafting of polymers on CNC was reported by Zhang, et al. in 2008 (Figure 1.12).<sup>57</sup> In this work, PS was successfully grafted on CNC in the presence of sacrificial initiators: the analysis of the free polymer initiated by the sacrificial initiator provides some indirect information about the structure of the polymer at the CNC surface. Initiator sites were first introduced on the surface of CNC (CNC-Br) by reacting the surface hydroxyl groups with 2-bromoisobutyrylbromide (BIBB) in DMF. The content of Br in the CNC-Br material (determined by the oxygen flask method) was ca. 0.6 wt. %. The SI-ATRP grafting of PS was then conducted on the CNC-Br particles, in the presence of ethyl  $\alpha$ -bromoisobutyrate (EBiB) as a sacrificial initiator. The number-average molar mass ( $M_n = 74,7000$  g/mol) and dispersity (1.2) of the grafted PS was determined by GPC analysis of the cleaved polymer chains (HCl treatment). The weight percentage of PS in PS-g-CNC (68%) was calculated from the weight of cleaved PS and weight of PS-g-CNC. The TGA analysis of PS-g-CNC showed that the thermal stability of CNC was significantly improved by the grafting of PS. The differential scanning calorimeter (DSC) and polarizing optical microscopy (POM) analyses suggested the PS-g-CNC particles self-assembled in both thermotropic and lyotropic states.

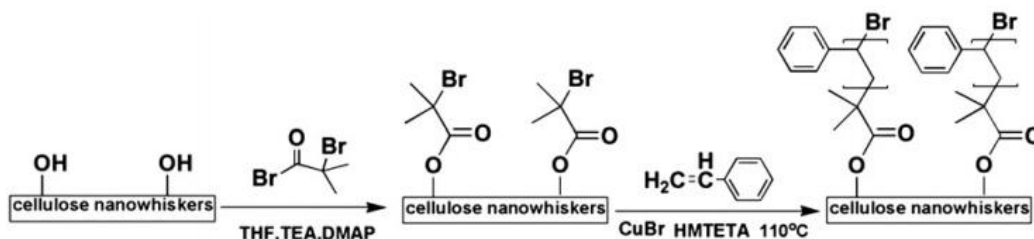


**Figure 1.12. The preparation of PS-g-CNC by SI-ATRP<sup>57</sup>**

Morandi, G., L. Heath, et al. (2009) also grafted PS by the same SI-ATRP method.<sup>46</sup> The Br content in BIBB modified CNC (CNC-Br) was characterized by elemental analysis (EA). The authors found that the Br content increased with the amount of BIBB and reaction time. Therefore, the grafting density of PS could be controlled by the reaction conditions used in the preparation of CNC-Br. When 52 mL BIBB was used to modify 1 g of CNC (at 70 °C and for 24 hours) in DMF, 70% of the surface hydroxyl groups were converted into Br initiating sites. The kinetics of the ATRP grafting was evaluated by

analyzing the free polymer produced by the sacrificial initiators added in the medium (EBiB), assuming that the kinetics of polymerization for the free and grafted PS are the same. The  $M_n$  measured increased linearly with the monomer conversion with a relatively low dispersity (1.1), indicating that the living radical polymerization process was well-controlled. The Fourier transform infrared spectroscopy (FTIR), EA and X-ray photoelectron spectroscopy (XPS) analyses also suggested that the weight percentage of grafted PS in PS-g-CNC increased with the  $M_n$  of the free PS. The contact angle measurements showed that the CNC became hydrophobic after the grafting of PS, which allowed increasing its absorption capacity towards 1,2,4-trichlorobenzene.<sup>46</sup>

To obtain CNC-Br initiators with a high Br content, Olli Ikkala's group developed a two-step method (Figure 1.13)<sup>55</sup> In a first step, chemical vapor deposition (CVD) was used to produce CNC-Br with about 5 wt% (characterized by EA). In a second step, the Br content was further increased by treating CNC-Br with BIBB in DMF. The final Br content was 15 wt. % and the density of Br initiator sites at the CNC surface was 4.6 per nm<sup>2</sup>. Poly(*tert*-butyl acrylate) (PtBA) brushes were then subsequently grafted by SI-ATRP, with a high grafting density. Starting from this material, the authors also produced hydrophilic PAA-g-CNC nanoparticles, after acid hydrolysis of PtBA-g-CNC (Figure 1.14).

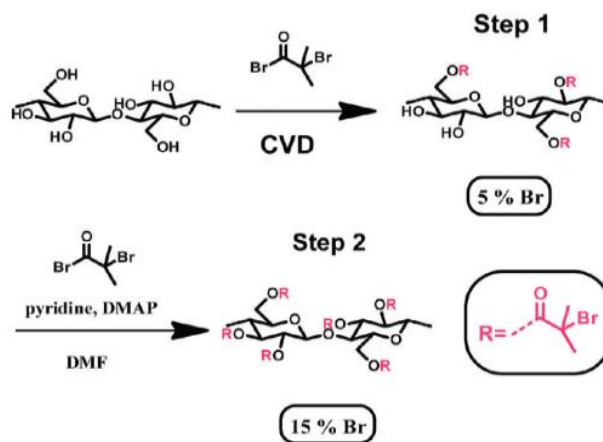


**Figure 1.13.** The preparation of CNC-Br with high Br content by the two steps method.<sup>55</sup>

A few other interesting polymers have also been grafted on CNC by SI-ATRP. Zhang's group published a paper, in which they reported the grafting of PMMAZO, a liquid crystalline polymer.<sup>53</sup> The

PMMAZO-*g*-CNC material exhibited thermotropic and lyotropic states. They later extended the reaction to PDMAEMA, a thermo-sensitive polymer exhibiting a temperature-dependent solubility and a LCST in the range 32–53 °C (Figure 1.15).<sup>58</sup> The PDMAEMA-*g*-CNC showed temperature-induced fingerprint texture, the spacing between the fingerprint lines decreasing with the increasing temperature. PDMAEMA-*g*-CNC was also quaternized with methyl iodide to produce positive charged PQDMAEMA-*g*-CNC, which had a high affinity for cowpea chlorotic mottle virus.<sup>59</sup> Poly(*N*-isopropyl acrylamide) (PNiPAAm), one of the most studied thermoresponsive polymers with a LCST of 32 °C, was also recently grafted on CNC by SI-ATRP.<sup>44</sup> In this study, the density and chain length of the grafted polymer could be tuned by controlling the density of initiator sites and SI-ATRP process, respectively.<sup>44</sup> The SI-ATRP has also been recently used to graft block copolymers on CNC.<sup>60,61</sup>

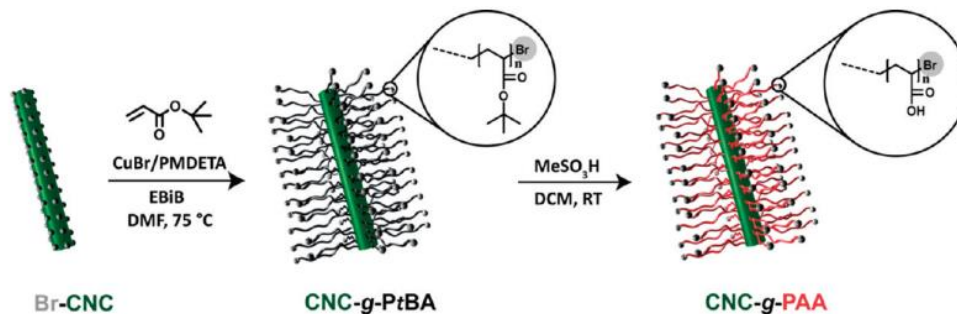


**Figure 1.14.** The preparation of PtBA-*g*-CNC and PAA-*g*-CNC by SI-ATRP.<sup>55</sup>

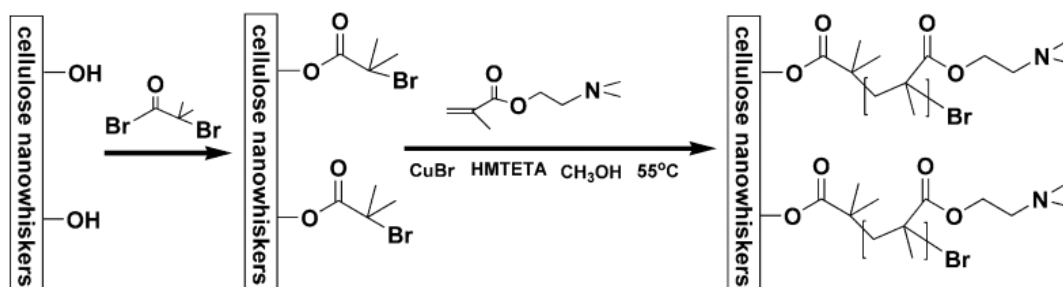


**Figure 1.15.** The preparation of PDMAEMA-*g*-CNC by SI-ATRP.<sup>58</sup>

Despite the interesting results obtained up to now, the indirect characterization of the grafted polymer through the analysis of the free polymer produced by the sacrificial initiator is still controversial, as the

kinetics of homogeneous polymerization are not the same with the kinetics of surface initiated polymerization.<sup>62-64</sup> To verify if the method is accurate, Morandi and Thielemans prepared photocleavable CNC-Br initiators.<sup>65</sup> After the SI-ATRP grafting of PS in the presence of a sacrificial initiator, the grafted chains were cleaved by UV-irradiation and analyzed by GPC. Results showed that the  $M_n$  of cleaved PS (with a dispersity of only 1.08) was consistent with the  $M_n$  of free PS, suggesting that the polymerization rates of the free and grafted polymers were the same.

### **1.1.3 The application of CNC**

#### **1.1.3.1 Reinforcing agent in polymer matrices**

Because of their outstanding mechanical properties and low density, CNC are ideal reinforcing agents for a wide variety of polymer matrices.<sup>66,67</sup> In hydrophilic polymer matrices, unmodified CNC can be used directly, as they are compatible. However, the chemical modification of the CNC surface is generally required to disperse the filler in hydrophobic polymer matrices.<sup>68</sup>

CNC have been used to reinforce poly(vinyl acetate) (PVAc) and poly(butyl methacrylate) (PBMA) matrices.<sup>69</sup> After the incorporation of 15% v/v CNC in the PVAc matrix, the tensile storage modulus below the glass transition temperature ( $T_g$ ) of the polymer was remarkably increased from 2 GPa for neat PVAc to 5.2 GPa. For the PBMA, the tensile storage modulus increased from 0.6 GPa for neat PBMA to 3.8 GPa with the same filler content. The tensile storage moduli of the pristine polymers decreased dramatically above the  $T_g$  of the polymers. CNC exhibit excellent reinforcing ability in polymer matrices above the  $T_g$  of the polymers. Above the  $T_g$ , the tensile storage modulus increased from 1.2 MPa to 690 MPa for PVAc after the incorporation of CNC and from 1 MPa to 1.1 GPa for PBMA.

Juho, et al. modified the CNC with p-aminobenzoic acid (PABA) to obtain photoactive PABA-CNC.<sup>70</sup> The resultant PABA-CNC was transparent in the visible light range but had a high UV absorption. Therefore, the PABA-CNC was employed as both a reinforcing agent and UV-filter in PVA films, as shown in Figure 1.16. The tensile strength and modulus of PVA films were found to increase with increasing amount of PABA-CNC.

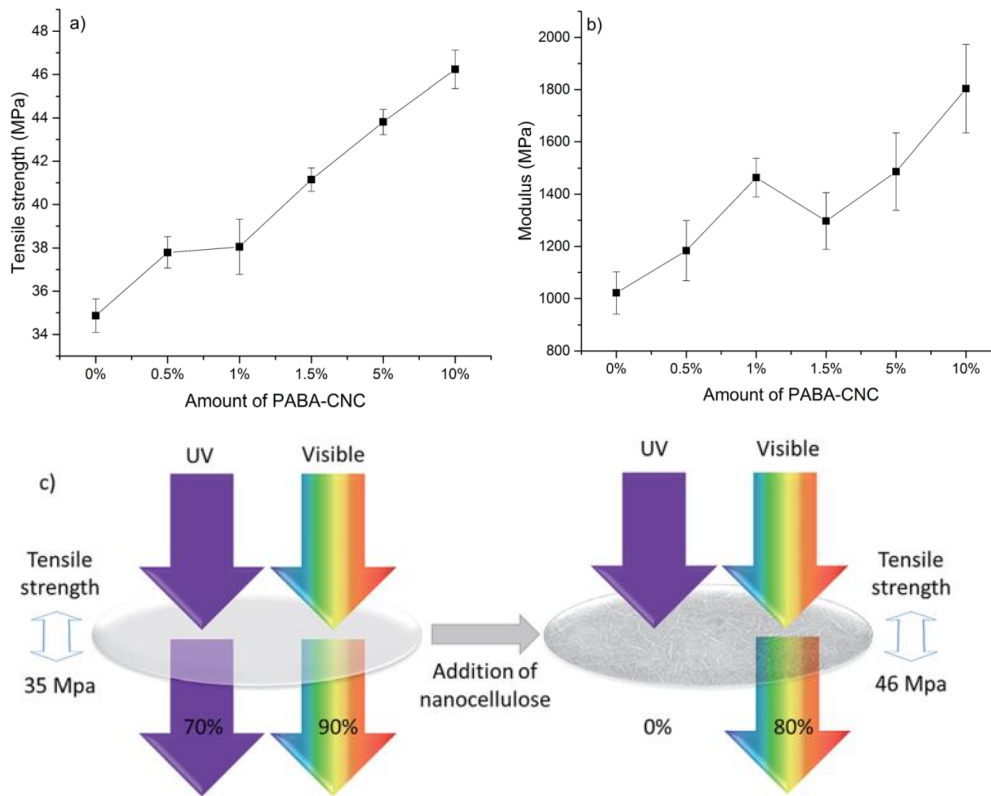


**Figure 1.16. The tensile strength (a) and modulus (b) of the PVA film reinforced with increasing amounts of PABA; and schematic representation of the UV filtering and reinforcing effect of PABA-CNC (c).<sup>70</sup>**

CNC have been also used to reinforce inorganic matrices, such as cement paste.<sup>71</sup> With the addition of 0.2 vol% of CNC in the cement paste, the flexural strength of the material could be increased by approximately 30%.<sup>71</sup>

### 1.1.3.2 Stabilizer for metal nanoparticles

Metal and metal oxide nanoparticles (NPs) have attracted significant attention due to their activities and applications as catalysts, anti-bacterial materials etc.<sup>72-76</sup> However, NPs are not stable and tend to self-aggregate – due to their high surface area – which decreases their performance.<sup>77,78</sup> To limit this problem, stabilizers are commonly required to enhance the stability of metal nanoparticles. Due to the

large specific surface area and stability in water, sustainable CNC are ideal stabilizers for metal nanoparticles.<sup>73,78,79</sup>

Pristine CNC have been used to stabilize Au-Ag alloy nanoparticles with a diameter of about 3-7 nm.<sup>80</sup> For Ag NPs, the sulfate ester groups at the surface of the CNC were found to impact significantly the size of the nanoparticles.<sup>81</sup>

Wu, et al. reported a one-step method to deposit gold nanoparticles (Au NPs) on the surface of CNC without reducing agents, and under hydrothermal condition, as shown in Figure 1.17.<sup>82</sup> The CNC were used as both reducing agents and stabilizers. The resultant Au@CNC supported NPs showed better stability and catalytic performance than the unsupported Au NPs for the reduction of 4-nitrophenol (4NP). The same method was also employed to prepare Pd@CNC supported NPs.<sup>83</sup> One of the biggest advantages of this approach is that no additional reducing agents are required for the reduction of the metal ion. However, the Au or Pd NPs deposited on CNC were bigger than 10 nm (ca. 10-40 nm in diameter).

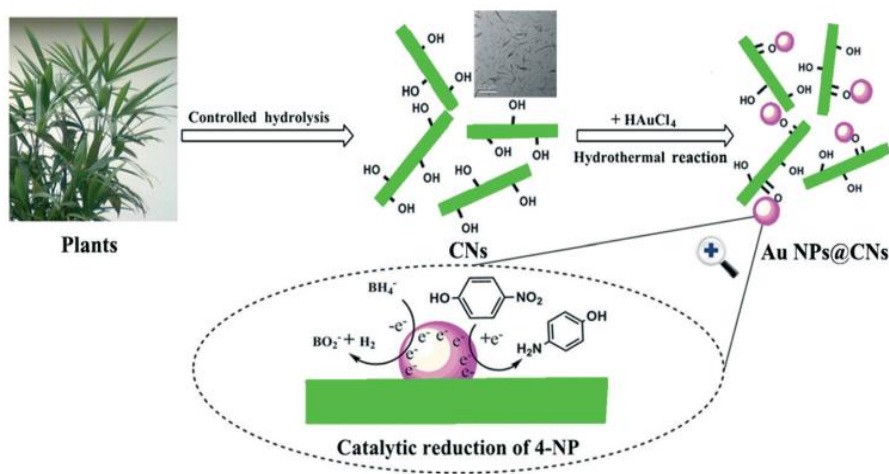


**Figure 1.17. The schematic illustration of the preparation of Au NPs@CNC for the reduction of 4-nitrophenol (4NP).<sup>82</sup>**

To improve the interaction between CNC and NPs and further enhance the stability of NPs, CNC were often modified by polymer grafting or coating. Chen, et al. grafted poly(amidoamine) (PAMAM) dendrimers onto the surface of TEMPO-CNC *via* the formation of amide bonds to enhance the

interaction between the CNC and the metal.<sup>72</sup> The PAMAM dendrimers could be used as reducing agents to reduce the metal ion. When CNC-PAMAM was employed as the reducing agent, the size of Au NPs supported by CNC-PAMAM was in the range of 10-50 nm, and the turnover frequency (TOF) was 2590 h<sup>-1</sup>. When NaBH<sub>4</sub> was employed as the reducing agent, Au NPs with a smaller size (2-4 nm) were obtained, and the catalyst systems exhibited even better catalytic activities (TOF =5400 h<sup>-1</sup>).<sup>72</sup>

### 1.1.3.3 Colloid stabilizers in Pickering emulsions

#### 1.1.3.3.1 Pickering emulsions stabilized by CNC

The traditional or classic emulsions are typically prepared with chemical surfactants. Due to the amphiphilic properties of the surfactant, the surface tension between the water and the oil phase is decreased and the emulsion is stabilized. The amphiphilic properties of surfactant can be represented by the hydrophilic-lipophilic balance (HLB). If the HLB of a surfactant is above 7, the surfactant is more hydrophilic and tend to form an oil in water (O/W) emulsion; and if the HLB of surfactant is below 7, the surfactant is more lipophilic and tend to stabilize a water in oil (W/O) emulsion.<sup>84</sup> The classical chemical surfactants are commonly considered as toxic, especially in food, pharmacy, and cosmetic fields.<sup>85</sup> Moreover, the residues of surfactant have an enormous impact on the performance of the final products and their removal is often required for some specific applications. Therefore, alternative surfactants, such as the colloid stabilizers used in Pickering emulsions, have been developed in recent decades.

The emulsions stabilized by colloidal particles, called Pickering emulsions, have been discovered more than one hundred years ago,<sup>86,87</sup> but the research on the subject was somehow neglected in the last century. But in the last two decades, Pickering emulsions have regained interest due to their excellent properties. Pickering emulsions are surfactant-free emulsions, which are more stable and less toxic than the classical emulsions stabilized by chemicals. In these systems, colloidal particles with amphiphilic properties are used. As shown in Figure 1.20, the solid particles used in Pickering emulsions show partial wettability with both the oil and the water phases and are irreversibly adsorbed at the interface between oil and water.<sup>85</sup>

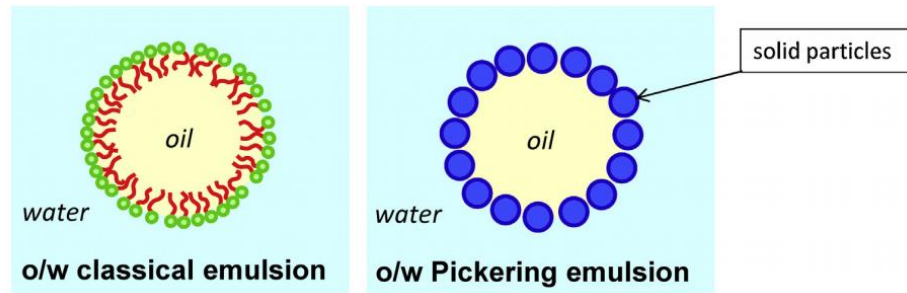


**Figure 1.18** The schematic representations of the O/W classical emulsion and O/W Pickering emulsion<sup>85</sup>

Similarly to the HLB used for surfactants, the three-phase contact angle  $\theta_{ow}$  is used to evaluate the wettability at the solid/oil/water interface (Figure 1.19).<sup>88</sup> If  $\theta_{ow}$  is lower than  $90^\circ$ , the solid particles have more affinity with the water phase (they are more hydrophilic), resulting in O/W Pickering emulsions. If  $\theta_{ow}$  is higher than  $90^\circ$ , the solid particles have more affinity with the oil phase (they are more lipophilic), leading to inverse W/O Pickering emulsions. If the solid particles are only hydrophilic or only hydrophobic, they will be dispersed in a single phase (water or oil, respectively) and no stable Pickering emulsions will be formed.<sup>84,89</sup>

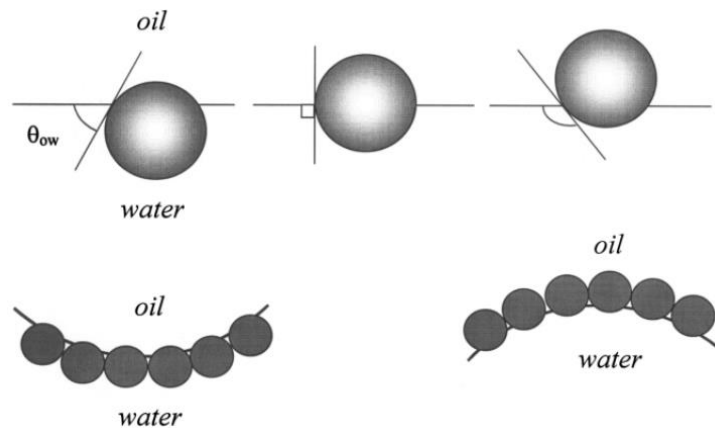


**Figure 1.19.** The three-phase contact angle in Pickering emulsions<sup>88</sup>

Compared to the emulsions stabilized by surfactant, Pickering emulsions are more stable. Once solid particles are absorbed at the interface, a high energy is required to remove the solid particles.<sup>90</sup> The required desorption energy is expressed as:

$$\Delta E = \pi r^2 \gamma (1 - |\cos \theta|)^2$$

where  $r$  is the radius of the solid particles and  $\gamma$  is the interfacial tension.<sup>91</sup>

**Table 1.3. The summary of colloidal particles used in Pickering emulsifiers<sup>84</sup>**

	Particle type	Particles	Emulsion type
Inorganic	Silica	Fumed silica	o/w or w/o
		Carbonyl iron particles	o/w
	Metal oxide	Fe <sub>3</sub> O <sub>4</sub> nanoparticles	w/o
		TiO <sub>2</sub>	o/w
		CuO	o/w
	Clay	Montmorillonite (MMT)	o/w
		LAPONITE <sup>®</sup> RD	o/w
		Layered double hydroxide (LDH)	o/w
	Carbon	Carbon nanotube (CNT)	w/o
		Graphene oxide (GO)	o/w
Carbon black (CB)		w/o	
Organic	Protein	Bovine serum albumin coupled with PNIPAM	o/w
	Polysaccharide nanocrystals	Cellulose nanocrystals	o/w
		Chitin nanocrystals	o/w
		Starch nanocrystals	o/w
	Polymeric	Poly(divinylbenzene-methacrylic acid) (P(DVB-MAA)) particles	w/o
		Polystyrene (PS) or poly(methyl methacrylate) (PMMA) nanoparticles	w/o
		Poly{(styrene- <i>alt</i> -maleic acid)- <i>co</i> -[styrene-( <i>N</i> -3,4-dihydroxyphenylethyl-maleamic acid)]} (P(SMA-dopa))	o/w
Composite/hybrid		Ag <sub>3</sub> PO <sub>4</sub> -MWNT nanohybrid	w/o
		Lightly crosslinked poly(4-vinylpyridine) (P4VP)-silica nanocomposite microgels	o/w

Both inorganic and organic colloidal particles can be used as stabilizers in Pickering emulsions, such as silica, metal oxide, carbon nanotube, proteins, and polysaccharides, as shown in Table 1.3.<sup>84</sup> Polysaccharides, as bio-based materials, are increasingly considered as an alternative to inorganic solid particles, as they are biocompatible and biodegradable. In particular, CNC have recently proven to be efficient for the stabilization of Pickering emulsions.<sup>20,49,89,92-94</sup> The pristine CNC produced by sulfuric acid treatment are not able to stabilize Pickering emulsions efficiently, due to the electrostatic repulsions imparted by the sulfate ester groups at their surface.<sup>95</sup> Therefore, salt is generally required to screen these repulsions and obtain a stabilized O/W emulsion.<sup>96</sup>

CNC extracted from different resources and with different aspect ratios were compared as stabilizers for O/W Pickering emulsions in a recent study.<sup>13</sup> The results showed that the aspect ratio of CNC had a significant influence on the coverage ratio around the oil droplets. As shown in Figure 1.20, a high surface coverage is required for short CNC to stabilize Pickering emulsions, while a lower coverage is sufficient with longer CNC.<sup>13</sup>

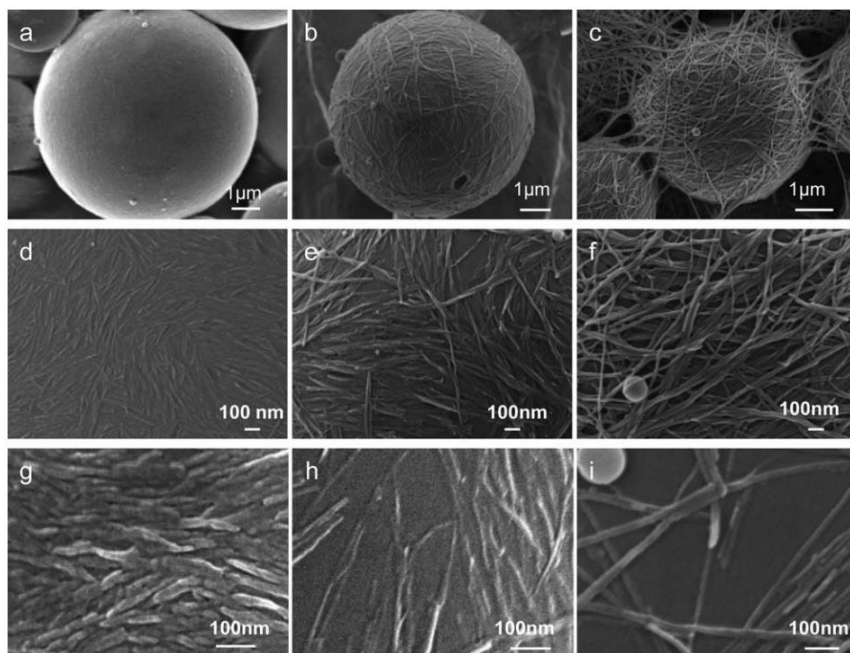


**Figure 1.20. SEM images of polymerized styrene droplets stabilized by different types of CNC.<sup>13</sup> a, d and g: CNC with small aspect ratio extracted from cotton; b, e, and h: bacterial cellulose; c, f and i: CNC with high aspect ratio extracted from Cladophora**

A limited number of O/W emulsions have been stabilized by pristine CNC so far, but chemically modified CNC can be used to extend the field of application. Indeed, the hydrophilic/hydrophobic balance at the CNC surface can be adjusted by chemical modification, which allows stabilizing novel O/W or W/O emulsions. For instance, remarkably stable O/W emulsions of ethyl acetate, toluene or cyclohexane were recently obtained with acetate- or cinnamate-grafted CNC.<sup>20</sup> Thermally responsive polymers such as PNiPPAm have also been grafted on CNC to prepare stimuli-responsive Pickering emulsions.<sup>84</sup> The PNiPPAm-g-CNC were able to stabilize O/W emulsions of heptane below the LCST

of the polymer. When the emulsions were heated above the LCST, the PNiPPAm-g-CNC particles changed to hydrophobic and the Pickering emulsions were broken.<sup>95</sup> Pickering emulsions stabilized by CNC grafted with PDMAEMA, a pH and thermal responsive polymer, were also recently prepared. The emulsions displayed both pH and thermal responsiveness.<sup>49</sup> W/O inverse Pickering emulsions can also be prepared by grafting hydrophobic moieties at the CNC surface.<sup>93</sup> Double Pickering emulsions systems have also been recently developed with lauroyl chloride modified CNC.<sup>94,96</sup>

#### 1.1.3.3.2 Application to the elaboration of colloidosomes

The concept of colloidosomes was proposed by Dinsmore, et al. in 2002 by analogy with liposomes.<sup>97</sup> Liposomes are capsules composed of phospholipid bilayers, while colloidosomes are capsules composed of colloids with selective permeability (Figure 1.21). The colloidosomes are prepared by Pickering emulsification, using colloidal particles, which are locked together at the interface and form a hollow shell structure. The permeability and mechanical performance of the colloidosomes are highly dependent on the conditions used for their preparation (colloidal particles, solvent, way to lock the colloids...).

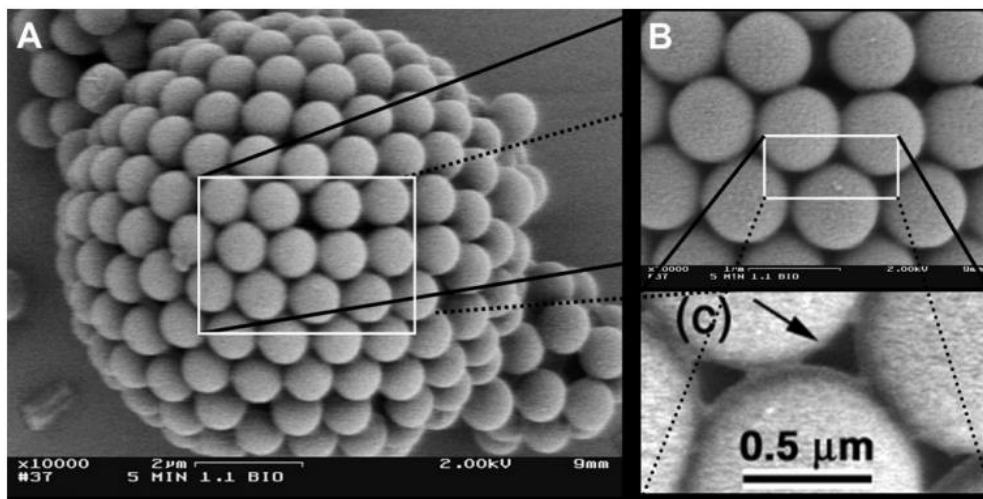


**Figure 1.21. The SEM images of typical colloidosomes.<sup>97</sup>**

Different routes have been used to prepare colloidosomes, such as thermal annealing, gel trapping, covalent cross-linking, polyelectrolyte complexation, and polymerization of droplet phase, as shown in

Figure 1.22.<sup>98</sup> However, most of these methods are time-consuming, requiring high temperature, multiple steps, or lacking enough mechanical strength, leading to some disadvantages to scale-up.<sup>98</sup>

Thermal annealing is performed above the glass transition temperature of the polymer to fuse the polymer colloidal particles together. Therefore, when PS latex particles were employed as the emulsifiers, glycerol was added in the water phase to raise its boiling point, the  $T_g$  of PS exceeding 100 °C.<sup>99</sup> The permeability of colloidosomes could be tuned by changing the sintering time. Besides the requirement of high temperatures, another significant disadvantage of thermal annealing is related to the extensive inter-colloidosomes fusion. Polyelectrolyte complexation and layer-by-layer deposition are two methods, which allow preparing colloidosomes at room temperature. However, the encapsulation efficiency is poor with polyelectrolytes, due to the porosity of microcapsule walls, and the layer-by-layer technique is time-consuming, especially for multi-layers.<sup>98,100</sup>

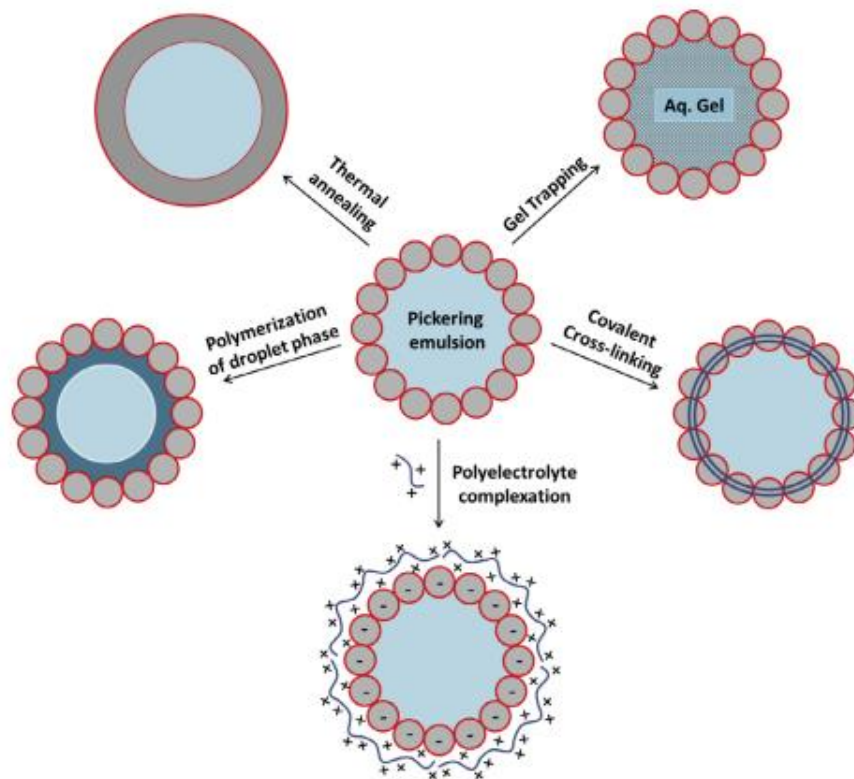


Figure 1.22. Different routes to prepare colloidosomes microcapsules<sup>98</sup>

The gel trapping technique provides another approach to prepare colloidosomes. With this technique, an aqueous gel was used as the emulsion internal phase. The Pickering emulsion was prepared at high temperature, and the colloidosomes were then formed via cooling to set the gel.<sup>101</sup>

In another method, the colloid particles can be locked together by polymerization or sol-gel process. For example, TiO<sub>2</sub> stabilized Pickering emulsions were used as templates to prepare organic-inorganic hybrid hollow spheres, via the polymerization of styrene and divinyl benzene.<sup>102,103</sup> The sol-gel reaction of silica precursor has also proven efficient as a facile method to prepare colloidosomes at room temperature.<sup>104,105</sup>

The colloidosomes prepared by all these methods normally display insufficient encapsulation performance, due to the loose linkage between colloidal particles. The ingredients encapsulated inside the colloidosomes are generally released within 1 day, which is far away from what is expected for most commercial applications.<sup>98,106,107</sup> Therefore, there is a high demand for novel technologies to form robust colloidosomes with adequate encapsulation performance.

#### 1.1.3.4 The commercialization of CNC

CNC have been commercially produced in the first pilot plant operated by CelluForce (Canada) since 2012, and other factories have emerged within the last 5 years. Nanocellulose is now commercialized in many countries, such as Canada, Japan, America, Norway, Sweden, France, Finland, Netherlands, Israel, Iran, China, India, and so on. Thanks to the development of these commercial plants, the cost of CNC has now been reduced to less than \$ 100 per kg. The large-scale production of CNC paves the way for the more commercial materials and products based on CNC.

## 1.2 Atom transfer radical polymerization (ATRP)

### 1.2.1 Living free radical polymerization

The molecular weight of polymers is an essential defining parameter for polymers, as it influences many properties of polymer materials, including processing characteristics and mechanical properties. Generally, polymers with low molecular weight have better processing performance, while polymers with high molecular weight possess better mechanical properties. Therefore, if the molecular weight of

polymers is not high enough, the polymer materials normally show poor mechanical performance and is useless as material; if the molecular weight of polymers is too high, the polymer materials may be difficult to process with classical technologies like extrusion molding. Therefore, the molecular weight of polymers should be in a particular range that keep the balance between processability and mechanical performance.

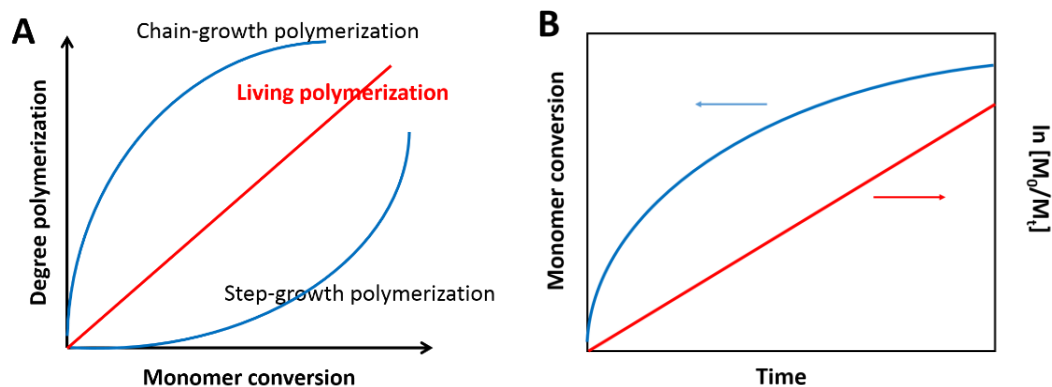


**Figure 1.23. (A) Degree of polymerization vs. monomer conversion for step-growth polymerization, chain-growth polymerization, and living polymerization; (B) The monomer conversion and  $\ln [M_0/M_t]$  as a function of reaction time in living polymerization**

Depending on their kinetics, polymerization reactions can be classified into two general processes called step-growth polymerization or chain-growth polymerization (Figure 1.23A). When in a chain-growth polymerization, chain transfer and chain termination are absent, the reaction is called living polymerization. In that particular case, the molecular weight of the polymers proportionally increases with the monomer conversion. To achieve these conditions, the rate of chain initiation must be much faster than the rate of chain propagation, in order to keep a stable concentration of kinetic-chain carriers during the polymerization process.<sup>42,43</sup> The degree of polymerization is then equal to  $[M]C/[I_0]$ , in which  $[M]$  is the mole of monomer,  $C$  is the monomer conversion, and  $[I_0]$  is the mole of initiator. One direct way to demonstrate livingness of a polymerization is to draw the curve of  $M_n$  vs. monomer conversion. In living polymerization,  $M_n$  increases linearly with the monomer conversion. At the same time, the dispersity of the polymer, defined as  $M_w/M_n$ , is quite low, below 1.2. According to the kinetics

of living polymerization, the concentration of active species  $[R^*]$  is constant in the equation of  $\ln[M_0/M_t] = k_p[R^*]t$ , where  $[M_0]$  is the initial monomer concentration,  $[M_t]$  is the monomer concentration at the time  $t$ ,  $k_p$  is the propagation rate, and  $[R^*]$  is the concentration of active species. Therefore,  $\ln [M_0/M_t]$  will linearly increase with reaction time in living polymerization, as shown in Figure 1.23. The linear increase of  $\ln [M_0/M_t]$  vs time indicates that the concentration of active species is constant, and the propagation rate is first order with active species.

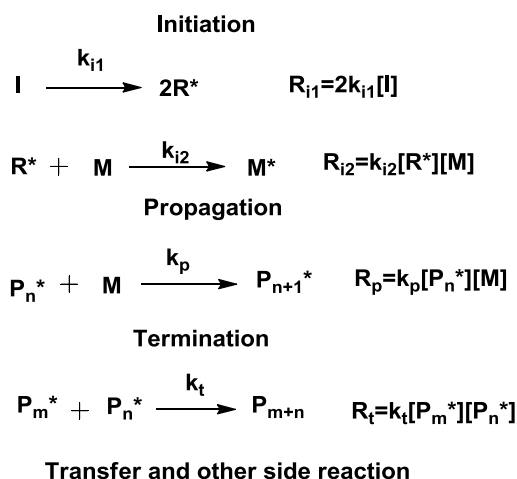


**Figure 1.24. The different steps of free radical polymerization, with the reaction rate of each step<sup>108</sup>**

Depending on the active species, chain-growth polymerization can be also classified as ionic polymerization (anionic and cationic polymerization) or free radical polymerization. Compared to ionic polymerization, free radical polymerization is tolerant to impurities and moisture, and can even be conducted in aqueous solution. A variety of monomers can be polymerized by free radical polymerization. More than 50% of the synthetic polymers are today prepared by free radical polymerization. Polymerizing monomers from free radicals in a living way (method called living free radical polymerization), is a popular topic and it has drawn increasing attention in recent decades. A typical free radical polymerization occurs in 5 steps: chain initiation, propagation, termination, transfer and other side reactions, as shown in Figure 1.24. Here, “I” represents the initiator,  $R^*$ ,  $M^*$ ,  $P_n^*$ ,  $P_{n+1}^*$ ,  $P_m^*$  are the radicals, M is the monomer, and k is the reaction rate constant for each step. In free radical

polymerization, reaction between radicals is very easy, which can lead to early termination of the polymerization. The rate of propagation is proportional to the concentration of radicals, while the rate of termination is proportional to the square of the concentration of radicals. Therefore, when the concentration of radicals is decreased, the rate of termination reduces dramatically compared to the rate of propagation. When the concentration of radicals is low enough, the termination and transfer are negligible compared to the propagation. As a result, free radical polymerization behaves like a “living” polymerization.<sup>109</sup>

Low concentration of radical species is insufficient to maintain a living free radical polymerization. As we know, there are still termination, chain transfer and other side reactions in the polymerization, so the radical species still will be consumed. Therefore, the concentration of the radical species needs not only be low, but also be kept constant. The basic strategy to obtain a living free radical polymerization is to build a reversible balance, and transfer most of the radical species into dormant species (Figure 1.25). At present, several methods have been developed to realize these conditions, including ATRP,<sup>42,43</sup> Reversible Addition-Fragmentation chain Transfer (RAFT) polymerization,<sup>110,111</sup> and nitroxide mediated polymerization (NMP).<sup>112</sup> It can be noted that, after the development of these strategies, IUPAC recommended to use the term "reversible-deactivation radical polymerization" (RDRP) instead of “living free radical polymerization”.<sup>113</sup> The  $k_{act}$  and  $k_{deact}$  are two critical parameters allowing the control of the livingness in living radical polymerization (Figure 1.25). If  $k_{act}$  is too small, the active species concentration will be too low to propagate the reaction efficiently. If  $k_{deact}$  is too small, the concentration of active species will be too high to obtain a well-controlled living free radical polymerization. In conclusion, a sufficient  $k_{act}$  is needed to propagate the polymerization, and at the same time,  $k_{deact}$  must be bigger than  $k_{act}$  to keep the concentration of active species low and constant.

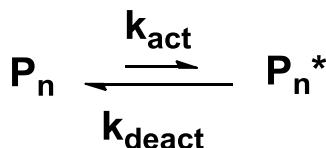


**Figure 1.25. Reversible balance to transfer active species to dormant species**

## 1.2.2 The mechanism of ATRP

ATRP has gained popularity since its development in 1995.<sup>42,114-116</sup> The mechanism of ATRP is shown in Figure 1.26, where  $P_n$  is the radical species, X and Y are the initiating sites,  $M_t$  is the transition metal, and m and m+1 are the valences of  $M_t$ .

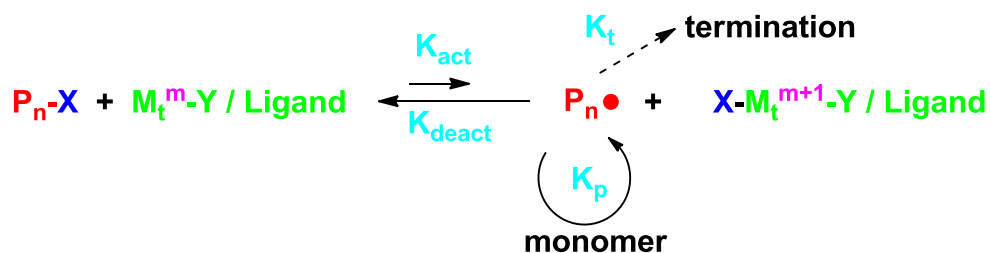


**Figure 1.26. The mechanism of ATRP**<sup>42</sup>

The radicals or the active species are generated through a reversible redox process catalysed by a transition metal complex ( $M_t^m-Y/\text{Ligand}$ ), where Y may be another ligand or the counterion which undergoes a one-electron oxidation with concomitant abstraction of a (pseudo)halogen atom, X, from a dormant species, R-X.<sup>42</sup> This process is a reversible reaction with a rate constant of activation,  $k_{act}$ , and deactivation  $k_{deact}$ . Polymer chains grow by the addition of the intermediate radicals to monomers like a conventional radical polymerization, with the rate constant of propagation  $k_p$ . Termination reactions ( $k_t$ ) also occur in ATRP, mainly through radical coupling and disproportionation. However, in a well-controlled ATRP, no more than a few percent of the polymer chains undergo a termination process. The termination can be negligible compared with propagation. Other side reactions may additionally limit the targeted molecular weights. This process generates oxidized metal complexes,  $X-M_t^{m+1}$ , as persistent radicals to reduce the stationary concentration of growing radicals and thereby minimize the possibility of termination reaction. Fast initiation and rapidly reversible deactivation are also necessary for a successful ATRP process.<sup>42</sup> A variety of monomers have been successfully polymerized using ATRP, such as styrene, (meth) acrylates, (meth) acrylamides, dienes, acrylonitrile, and other monomers containing substituents that can stabilize the propagating radicals. In a well-controlled ATRP,  $\ln[M_0/M_t]$  will linearly increase with time, which indicates a constant concentration of active species. Sometimes, the ATRP is not well controlled due to apparent termination or slow

initiation. If the termination is not suppressed enough, the concentration of the active species will decrease with time; if the initiation step is not fast enough, the concentration of the active species is low at the beginning and will increase with time, as shown in Figure 1.27.

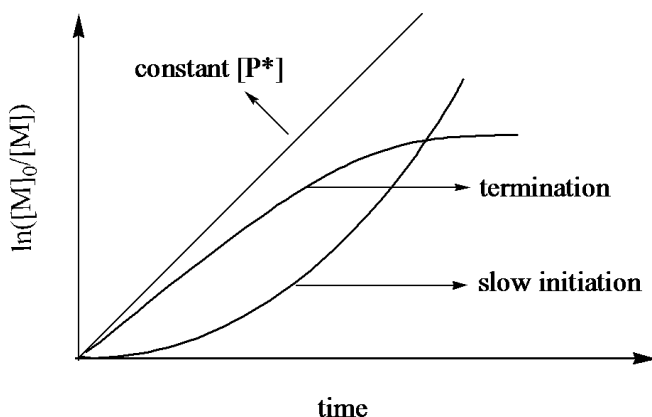


**Figure 1.27.** The  $\ln [M_0/M_t]$  as a function of reaction time in ATRP<sup>42</sup>

### 1.2.3 Development of ATRP

Despite the interesting results obtained with normal ATRP, there are some drawbacks which need to be addressed: (1) normal ATRP is very sensitive to oxygen or air, and tedious degassing procedures, such as pump-freeze-thaw cycles, need to be conducted; (2) the transition metal catalyst needs to be removed after reaction. To overcome these disadvantages, different modifications of the ATRP process have been developed, to decrease the usage of metal catalyst or the sensitiveness of the reaction to oxygen.

#### 1.2.3.1 Reverse ATRP

In a normal ATRP, a transition metal with low oxidation state is added as a catalyst. This metal can be easily oxidized, which makes normal ATRP very sensitive to air. Moreover, the catalyst needs to be handled carefully. In reverse ATRP, a transition metal with higher oxidation state is used as a catalyst, and a conventional free radical initiator is used instead of the halogenated initiator.<sup>43,117</sup> The mechanism is shown in Figure 1.28. The thermal decomposition of the conventional free radical initiator generates radicals. Then the ATRP initiator (I-X or I-P1-X) and the activator are generated *in situ* by the reduction

of the transition metal of high oxidation state into a transition metal of low oxidation state. The ATRP is then initiated by the low oxidation state of the transition metal and the initiators.

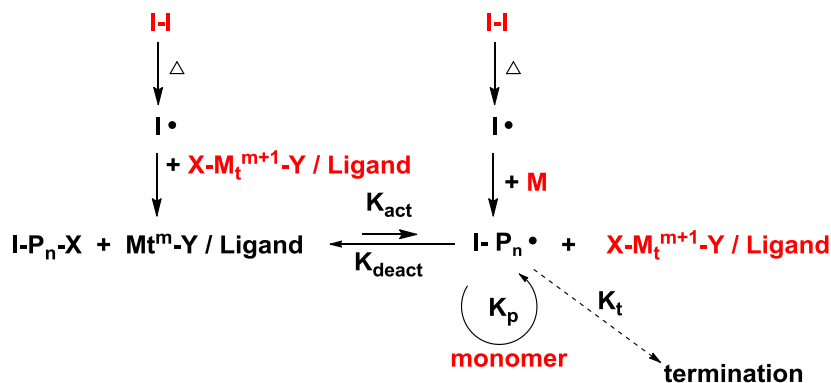


**Figure 1.28. The mechanism of reverse ATRP<sup>43,117</sup>**

One of the disadvantages of reverse ATRP is the presence of “I” radical initiator residues in the final polymer I-P<sub>n</sub>. Moreover, only the linear polymers can be polymerized by reverse ATRP. With conventional radical instead of ATRP initiators, the monomers are polymerized randomly. Therefore, reverse ATRP cannot be initiated from particle surfaces to prepare hybrid materials.

### 1.2.3.2 Simultaneous Reverse & Normal Initiation (SR&NI) ATRP

To overcome the problems of normal ATRP and reverse ATRP, SR&NI ATRP has been developed.<sup>118</sup> In SR & NI ATRP, the alkyl halide is still used as the initiator, and most of the polymers are initiated by the alkyl halide. Therefore, the polymer will be polymerized precisely on the initiating sites. At the same time, conventional radical initiator and higher oxidation state of metal are used to initiate reverse ATRP. The mechanism of SR & NI ATRP is shown in Figure 1.29. The metal catalyst of high oxidation state is reduced to low oxidation state as the catalyst by the radicals formed via the decomposition of the conventional initiator. Then the normal ATRP is initiated by the low oxidation of the catalyst. The SR & NI ATRP combines the advantage of normal ATRP and reverse ATRP. The use of the higher oxidation state of metal as catalyst decreases the sensitiveness of catalyst to air. Meanwhile, the initiation of normal ATRP allows the preparation of block and star polymers, and even composites or hybrid materials.<sup>118</sup>

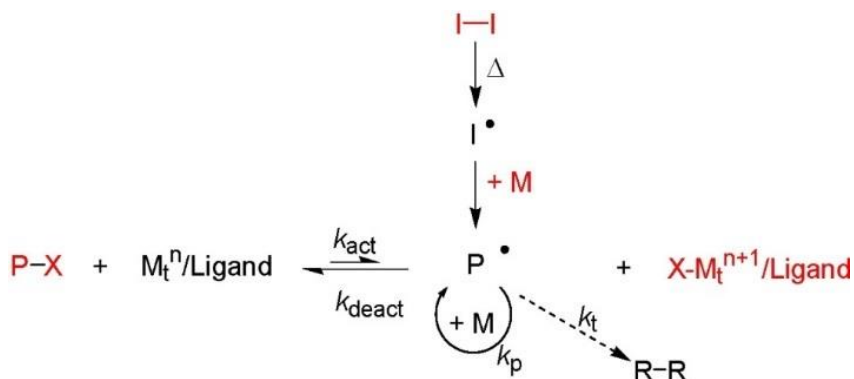


**Figure 1.29. The mechanism of SR & NI ATRP<sup>118</sup>**

### 1.2.3.3 Activator Generated by Electron Transfer (AGET) ATRP

In the AGET ATRP, alkyl halides are employed as initiators and transition metal complexes of high oxidation state are used as the catalyst precursors.<sup>119</sup> A non-radical-forming reducing agent is used to reduce metal complexes of high oxidation state to low oxidation state. Reducing agents such as tin 2-ethylhexanoate and ascorbic acid can be employed. The mechanism of AGET ATRP is shown in Figure 1.30. All the added chemicals are stable in the presence of oxygen. The AGET ATRP is even tolerant to dissolved oxygen and can be conducted with a limited amount of air. The concentration of catalyst can also be decreased to get well-controlled ATRP.<sup>119</sup>

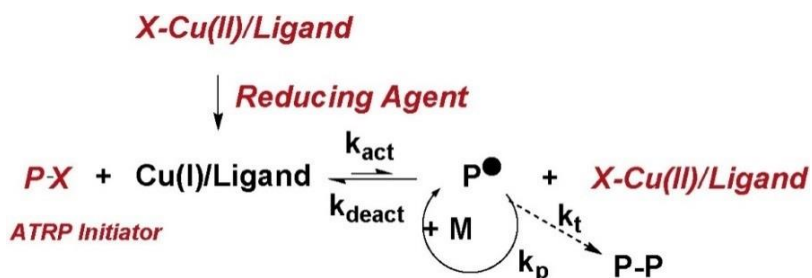


**Figure 1.30. The mechanism of AGET ATRP<sup>119</sup>**

### 1.2.3.4 Activator Re-Generated by Electron Transfer (ARGET) ATRP

In normal ATRP process, the termination is suppressed, but not eliminated. During the termination process, transition metals of high oxidation state are continuously produced. In ARGET ATRP, the

reducing agents in excess are used to constantly regenerate the ATRP activator from the transition metal of high oxidation state generated during the termination process. The mechanism of ARGET ATRP is shown in Figure 1.31. As all the chemicals added in AGET and ARGET ATRP are the same, AGET ATRP can be mistaken with ARGET ATRP. In AGET ATRP process, essentially all Cu(II) species are quickly reduced to the Cu(I) state, and then a normal ATRP starts in the presence of high concentration of catalyst. The ARGET process uses a much lower concentration of catalyst and relies on a slow steady regeneration of Cu(I) from Cu(II) species.<sup>120</sup> Compared to AGET ATRP, ARGET ATRP uses a much lower concentration of catalyst and a higher amount of reducing agent to regenerate the activator.

With the presence of reducing agent, the catalyst amount can be reduced to ppm level. Moreover, some FDA approved chemicals such as tin<sup>II</sup> 2-ethylhexanoate (Sn(EH)<sub>2</sub>), glucose, ascorbic acid, hydrazine or phenyl hydrazine, can be used as reducing agents. ARGET ATRP is also tolerant to dissolved oxygen.<sup>121</sup>

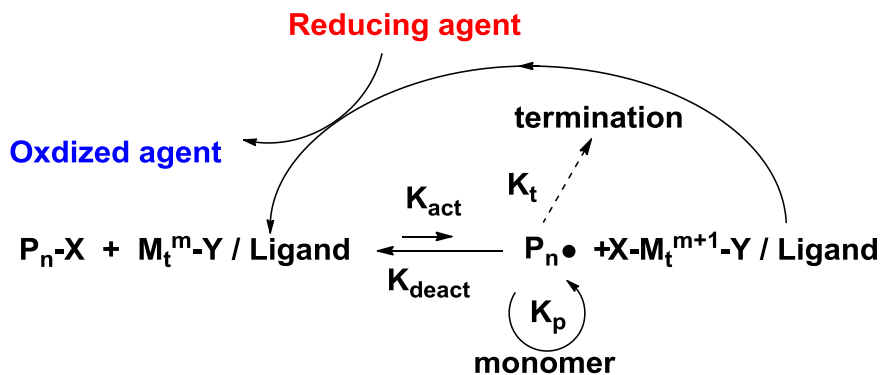


**Figure 1.31. The mechanism of ARGET ATRP**

#### 1.2.3.5 Initiators for Continuous Activator Regeneration (ICAR) ATRP

The mechanism of ICAR ATRP is somewhat similar to ARGET ATRP. The comparison of ARGET and ICAR mechanism is shown in Figure 1.32. In ARGET ATRP, the reducing agent is employed to reduce the high oxidation state transitional metal and regenerate the Cu<sup>I</sup> activator. In the ICAR ATRP,

other types of initiators are added to continuously regenerate the  $\text{Cu}^{\text{I}}$  activator. With this technique, the well-controlled ATRP of PS and PMA is performed with ppm level of catalyst.<sup>43</sup>

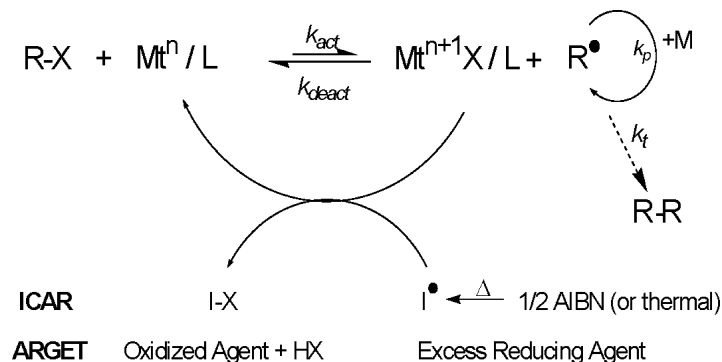


**Figure 1.32. The comparison of ARGET and ICAR mechanism<sup>43</sup>**

### 1.2.3.6 Electrochemical ATRP

ATRP also can be performed with the help of electrochemical control, which is called electrochemical ATRP (eATRP). The mechanism of eATRP is shown in Figure 1.33. In an eATRP, current is employed to reduce the high oxidation state transition metal into the activator. Electrochemical methods provide many easily tunable parameters, such as current or potential. These tunable parameters can help control the redox cycle in the ATRP process to obtain a better control of the polymerization.

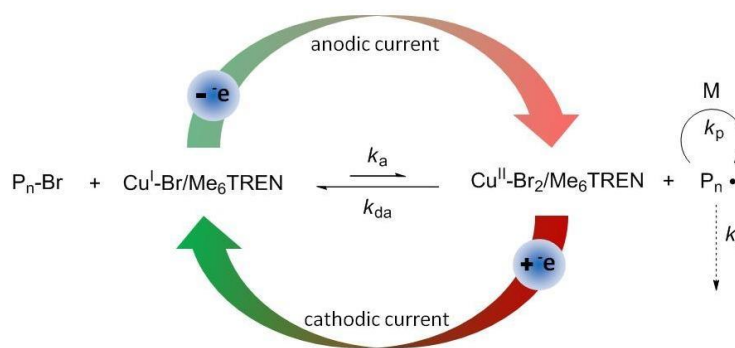
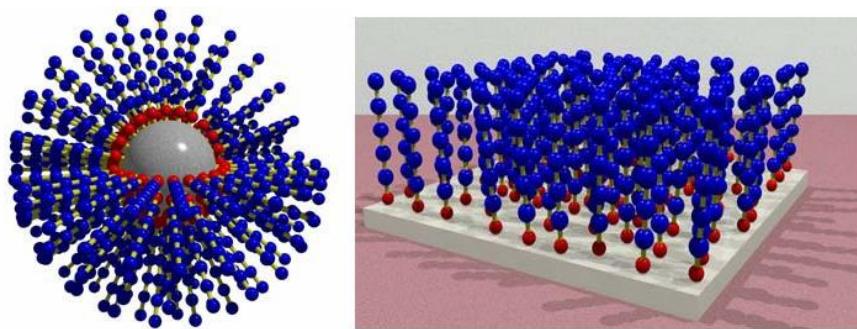


**Figure 1.33. Schematic of proposed mechanism for eATRP<sup>43</sup>**

### 1.2.3.7 Surface-initiated ATRP (SI-ATRP)

ATRP has been widely employed as a very promising tool to graft polymers from different surfaces, and it is called SI-ATRP in that case.<sup>39,121-126</sup> As a “grafting from” method, SI-ATRP can be used to graft polymer brushes on surfaces in a controlled manner, with high graft density. As shown in Figure 1.34, polymers can be grafted from the surface of particles or flat surfaces. With the application of SI-ATRP, hybrid nanomaterials or nanocomposites with well-defined polymer brush structure can be prepared precisely.



Spherical Particles

Flat Surfaces

**Figure 1.34. The surface initiated ATRP on the surface of particles or flat<sup>127</sup>**

In summary, ATRP is one of the most promising living radical polymerization methods. At present, different kinds of ATRP have been developed to overcome the disadvantages of the normal ATRP, such as reverse ATRP, SR & NI ATRP, AGET ATRP, ARGET ATRP, ICAR ATRP, eATRP and SI-ATRP.

## 1.3 Conclusions

As was highlighted in this chapter, cellulose nanocrystals (CNC) are bio-based nanoparticles, which display an array of interesting properties related to their renewability, biocompatibility, high tensile strength and elastic modulus, high aspect ratio, low density, low coefficient of thermal expansion, and crystal liquid behavior. As a result, CNC can be exploited in a wide variety of applications, which include the fields of composites, catalysts, emulsions or colloidosomes. However, the engineering of innovative nanomaterials from CNC generally requires a fine control of their surface properties by

chemical modification, to tailor their dispersive, interfacial and self-assembling properties, or to introduce novel functionalities. Among the different strategies that can be used, the chemical grafting of polymers by Surface-Initiated Atom Transfer Radical Polymerization (SI-ATRP) is particularly attractive as it allows preparing polymer-grafted nanoparticles with quite a good control, and with a high grafting density. The method requires the prior introduction of alkyl bromide initiating sites at the CNC surface, which can be easily achieved by esterification of the surface hydroxyl groups. A wide variety of polymers can then be grafted from these sites. The SI-ATRP grafting of polymers has been already reported in the literature, but the field of research is recent, and the potential benefit of many other polymers need to be explored. Moreover, the properties of the final material are highly dependent on the grafting density and chain length of grafted polymer, which need to be characterized precisely. Such characterization is not straightforward and still requires research efforts to develop convenient and accurate methods.

In this thesis, the surface functionalization of cellulose nanocrystals by esterification and ATRP reactions was envisaged, with the objective to develop novel advanced materials. The thesis is divided into six chapters. Following the current chapter, a brief overview of the SI-ATRP reaction is also given. In the second chapter, a convenient method is proposed to characterize polymers grafted by Si-ATRP on CNC. The method is based on dynamic light scattering (DLS), differential scanning calorimetry (DSC) and thermogravimetric analysis (TGA). The third chapter is a comparative study in which polystyrene and poly(4-vinylpyridine) (P4VP) were grafted on CNC, by SI-ATRP and SI-ARGET ATRP. The two methods were particularly compared. In the fourth chapter, pH-responsive P4VP-g-CNC nanohybrids was prepared by SI-ATRP and subsequently used to stabilize gold nanoparticles (AuNPs). The catalytic activity and recyclability of the material obtained was then investigated. In the fifth chapter, UV-responsive poly(cinnamoyloxy ethyl methacrylate) were grafted on CNC by SI-ATRP, to produce nanocrystals with UV absorbing properties. The nanohybrids were subsequently used as UV/thermal stabilizers and reinforcing agents for PVC films. In the sixth chapter, a facile method to prepare colloidosomes from w/o inverse Pickering emulsions stabilized by cinnamate modified CNC is proposed. In the last chapter, we summarized the general conclusions of the thesis and proposed some recommendations for the future work.

## Chapter 2

### Convenient Method for the Characterization of Polymers Grafted by SI-ATRP on Cellulose Nanocrystals, Using DLS, DSC and TGA

The cleavage of the grafted polymers is usually required to characterize the molecular weight of polymers grafted on solid substrates by surface-initiated polymerization. Here, we developed a method based on thermal analysis, which allowed the characterization to be performed without cleaving the grafted polymers. Polystyrene-grafted cellulose nanocrystals (PS-*g*-CNC) were prepared by Surface-Initiated Atom Transfer Radical Polymerization (SI-ATRP), in the presence of a sacrificial initiator. Different techniques, such as differential scanning calorimetry (DSC), dynamic light scattering (DLS) and thermogravimetric analysis (TGA), were conducted to characterize the PS-*g*-CNC. Results revealed that the number-average molecular weight ( $M_n$ ) of the PS grafted from the brominated CNC initiators (CNC-Br) was proportionally to the monomer conversion. The method also confirmed that the  $M_n$  of the grafted PS and free PS initiated by the sacrificial initiator were the same. Thermal analysis can therefore be used as a facile method for the characterization of grafted polymers without chain cleavage.

## 2.1 Introduction

The grafting of polymers on nanoparticles is a promising “bottom-up” strategy to prepare well-designed nanocomposites with controlled properties.<sup>128,129</sup> The combination of different types of nanoparticles and polymers offers many opportunities for material innovation.<sup>128,130</sup> Two methods are commonly used for the grafting. The “grafting to” method, in which pre-synthesized and characterized polymers are covalently attached on the nanoparticles, usually leads to a low grafting density due to high steric hindrance. This problem can be circumvented by applying the “grafting from” approach, also known as Surface-Initiated Polymerization (SIP), in which the polymerization of monomers is initiated from the surface of the nanoparticles. The steric hindrance being much lower in that case, this method is generally preferred.<sup>123,131,132</sup> Surface-Initiated Atom Transfer Radical Polymerization (SI-ATRP) is one of the most popular SIP methods. This living radical polymerization has been widely used to graft polymers on silica and metal nanoparticles,<sup>133-136</sup> and has been recently applied to cellulose nanocrystals (CNC), a promising biobased and biocompatible material.<sup>9,29,137</sup> CNC are innovative nanoparticles with a high potential in various areas, where they can be used as reinforcing agents,<sup>70</sup> stabilizers for metal nanoparticles,<sup>81</sup> colloid stabilizers of Pickering emulsions,<sup>49,89</sup> and so on.<sup>28,51,68,138,139</sup> However, the engineering of innovative nanomaterials from CNC generally requires a fine control of their surface properties by chemical modification. In this context, the CNC modification via SI-ATRP grafting is particularly promising, as it allows preparing hybrid nanomaterials (poly-*g*-CNC) with tailored properties. In particular, the method has been recently applied to modify the surface of CNC with polystyrene (PS),<sup>46,57,65</sup> poly(N,N-dimethyl aminoethyl methacrylate) (PDMAEMA),<sup>58,59</sup> poly(*tert*-butyl acrylate) (PtBA),<sup>55</sup> poly(N-isopropyl acrylamide) (PNiPAAm),<sup>44,95</sup> and poly(oligo (ethylene glycol) methacrylate) (POEGMA).<sup>51</sup>

The properties of the polymer-*g*-CNC obtained depend both on the chain length of the polymer and grafting density, which therefore need to be characterized precisely.<sup>51,63,132,140-142</sup> However, the characterization for the molecular weight of the grafted polymer is not easy and generally requires its cleavage and subsequent analysis by Gel Permeation Chromatography (GPC), which is tedious and time-consuming.<sup>44,52,56,58,143,144</sup> The severe conditions used for the cleavage can also degrade the cellulosic material or denature the polymer, resulting in inaccurate information.<sup>1,5,59</sup> The cleavage can

be too difficult,<sup>40,145-147</sup> sometimes requiring special modification of nanoparticles.<sup>52,65</sup> To circumvent this problem, a sacrificial initiator is generally introduced in the reaction medium to produce an ungrafted free polymer, that can be later characterized.<sup>46,55,65,148</sup> This method is based on the assumption that the molecular weights of the grafted and free polymers are similar.<sup>52,65</sup> However, the method remains controversial and is still debated.<sup>62,63</sup> Indeed, the SI-ATRP reaction is influenced by the steric hindrance of the grafted polymers, which is related to the grafting density and the morphology of the substrate.<sup>62,63</sup> The equivalency between grafted and free polymers is therefore not straightforward and needs to be verified in each particular case. Techniques to evaluate the molecular weight of the grafted polymers *via a* direct characterization of the poly-g-CNC material have not been reported so far and should be very useful for researchers working in this area.

In this chapter, we propose a convenient method allowing the direct characterization of the polymer grafted by SI-ATRP on the CNC surface, without cleaving the polymer from the nanoparticle. The SI-ATRP grafting of PS at the CNC surface was performed from brominated CNC initiators (CNC-Br), in the presence of a sacrificial initiator. PS was selected as a model polymer, as its surface grafting by ATRP has been performed on a wide variety of substrates and is well documented in the literature. With this work, we show that dynamic light scattering (DLS) is a convenient tool to monitor the polymerization process, while differential scanning calorimetry (DSC) can be used to verify if the polymerization rates of the grafted and free polymers coincide. Finally, we demonstrate that thermogravimetric analysis (TGA) can be used to directly estimate the molecular weight of the PS grafted at the surface of the CNC without cleaving the polymer from the nanoparticle.

## 2.2 Experimental

### 2.2.1 Materials

CNC were purchased from the University of Maine. Acetic acid, CuBr, CuBr<sub>2</sub>, ascorbic acid, N,N,N',N'',N'''-pentamethyldiethylenetriamine (PMDETA), tris [2-(dimethylamino)ethyl]amine (Me<sub>6</sub>TREN), calcium hydride, styrene, dimethylformamide (DMF), tetrahydrofuran (THF), diethyl ether, ethanol and other solvents were purchased from Sigma-Aldrich. Ethyl  $\alpha$ -bromoisobutyrate (EBiB) and  $\alpha$ -bromoisobutyryl bromide (BIBB) were purchased from Alfa Aesar. 4-

dimethylaminopyridine (DMAP) and triethylamine (TEA) were purchased from Fisher. CuBr was purified by acetic acid at 80 °C under N<sub>2</sub> for 24 h, and then washed with acetic acid and dried under vacuum at 50 °C. All the other chemicals were used as received.

### **2.2.2 Preparation of the brominated CNC nano-initiator: CNC-Br**

BIBB was used to modify CNC and prepare the brominated CNC nano-initiator (CNC-Br), later used to initiate the SI-ATRP reaction. Firstly, CNC (500 mg) were dispersed in DMF (50 mL) by sonication. TEA (4 mL) and DMAP (2 g) were added to the suspension. The suspension was evacuated under vacuum and backfilled with argon three times. Then BIBB (4 mL) was added dropwise to the suspension in an ice bath. After 24 h, EtOH was added, and the CNC-Br was recovered by centrifugation. CNC-Br was Soxhlet extracted with THF for 2 days, then dialyzed with deionized H<sub>2</sub>O for 6 days. Finally, CNC-Br was obtained by freeze-drying. The freeze-dried CNC-Br was re-dispersed in THF by sonication again. The supernatant was dried and analyzed by <sup>1</sup>H NMR in CDCl<sub>3</sub>. The <sup>1</sup>H NMR results showed no residues were left.

### **2.2.3 Grafting PS from CNC-Br by SI-ATRP: PS-g-CNC**

In brief, the SI-ATRP of PS from CNC-Br was conducted at 100 °C, with the molar ratio of [Styrene]: [EBiB]: [CuBr]: [PMDETA]: [DMF] = 500: 1: 1: 1: 500. In detail, CuBr (72 mg) was transferred into the Schlenk tube in the glove box. CNC-Br (50 mg) was dispersed in DMF (250 mmol) via sonication. Then styrene (250 mmol) and EBiB (0.5 mmol) were added to the suspension. After the suspension had been bubbled with argon for 20 min, the suspension was transferred to the Schlenk tube under the protection of argon. The suspension was degassed by three freeze-pump-thaw cycles. After the addition of PMDETA (0.5 mmol) under Ar, the reaction was initiated at 100 °C. At a designed interval time (2 h, 4 h, 6 h, and 7.3 h), an amount of reaction mixture was withdrawn by a degassed syringe. The monomer conversion was calculated from the <sup>1</sup>H NMR analysis of the mixture in CDCl<sub>3</sub>. The mixture was centrifuged to recover the PS-g-CNC nanoparticles. PS-g-CNC was washed with THF and EtOH three times respectively, to remove the free polymer and other unreacted chemicals. In the last washing recycle, the THF supernatant was collected and dried. The <sup>1</sup>H NMR in CDCl<sub>3</sub> showed no PS or other residues were left. The PS-g-CNC nanocomposites were obtained after drying at 50 °C under vacuum.

The green supernatant became colorless after the catalyst was removed by passing the solution through an Al<sub>2</sub>O<sub>3</sub> column. The colorless supernatant was then poured into excess MeOH, and the precipitated free PS was recovered through filtration and drying at 50 °C under vacuum.

#### **2.2.4 Characterization**

Fourier transform infrared spectroscopy (FTIR) spectra of all the samples were obtained with the potassium bromide technique, using a Thermo Nicolet Avatar 970 FTIR spectrometer, as a resolution of 8 cm<sup>-1</sup> (64 scans).

Transmission electron microscopy (TEM) was conducted on Philips CM10 at an acceleration voltage of 60 keV. The TEM samples were prepared by drop coating the dispersion onto copper grids (200 mesh coated with copper) and allowing them to dry at ambient temperature overnight. The pristine CNC dispersion for TEM samples was stained by FeCl<sub>3</sub>.

Thermogravimetric analysis (TGA) was performed on TGA-Q50 system (TA Instruments) at a heating rate of 10 °C /min under nitrogen atmosphere.

Differential scanning calorimetry (DSC) was carried out using a DSC Q100 apparatus (TA Instruments). All samples were first heated from 0 °C to 200 °C to remove the moisture, cooled down to 0 °C, and then heated to 200 °C. The T<sub>g</sub> values were determined from the second heating run of the DSC curve.

Dynamic light scattering (DLS) was performed using a particle size analyzer Vasco™ DL135 (Cordouan Technologies).

Gel Permeation Chromatography (GPC) analysis was conducted in THF with LiBr, on a PL-GPC 50 plus Integrated GPC (Polymer Laboratories-Varian). The elution of the filtered samples was monitored using a simultaneous refractive index and UV detection system. The elution times were converted to molar mass using a calibration curve based on low dispersity (M<sub>w</sub>/M<sub>n</sub>) polystyrene standards.

<sup>1</sup>H NMR spectra were recorded using a Bruker AC-400 NMR at room temperature by dissolving the samples in CDCl<sub>3</sub>.

Elemental analysis (EA) data were obtained from SGS Multilab (France). Carbon, hydrogen, and nitrogen were measured by thermal conductivity, according to protocols MO 240 LA 2008 (carbon and hydrogen) and MO 150 LA 2007 (nitrogen). Oxygen and sulfur were measured with infrared detectors, according to protocols MO 238 LA 2008 (oxygen) and MO 240 LA 2008 (sulfur). Bromide was measured by ionic chromatography, according to protocol MLE-MO-LAB-O78. All samples were dried at 105 °C before analysis.

The molecular ratio of anhydroglucose units relative to the grafted Br was evaluated based on a method reported in the literature.<sup>55</sup> The calculation is detailed below:

M (anhydroglucose) = 162 g/mol; M (initiator fragment) = 150 g/mol ; M (Br) =80 g/mol

Weight percentage of Br evaluated by EA: 11.9%;

Assuming 1 g of CNC-Br:  $n(\text{Br}) = 1 \times 11.9\% / 80 = 1.49 \times 10^{-3} \text{ mol} = n(\text{initiator fragment})$ ;

$m(\text{initiator fragment}) = 1.49 \times 10^{-3} \times 150 = 0.223 \text{ g}$ ;  $n(\text{anhydroglucose}) = (1 - 0.223) / 162 = 4.80 \times 10^{-3} \text{ mol}$ . The molar ratio of  $n(\text{anhydroglucose})$  relative to  $n(\text{initiator fragment})$  is then:  $4.80 / 1.49 = 3.2$ .

## 2.3 Results and discussion

### 2.3.1 Preparation and characterization of the CNC-Br initiator

The CNC used in this study were isolated by sulfuric acid hydrolysis of wood pulp, according to a general procedure widely described in the literature.<sup>16,149</sup> They consist of rod-like particles with estimated dimensions of  $110.3 \pm 47.7 \text{ nm}$  in length and  $4.8 \pm 1.1 \text{ nm}$  in diameter, based on a former study performed with particles taken from the same batch (estimated from AFM pictures).<sup>28</sup> The amount of accessible hydroxyl groups at their surface was estimated to be  $3.10 \pm 0.11 \text{ mmol.g}^{-1}$ , using a method based on phosphorylation coupled with <sup>31</sup>P NMR and FT-IR analysis.<sup>28</sup>

As shown in Scheme 2.1, a widely reported esterification method with BIBB as reactant was employed to anchor the Br initiating sites on the surface of the CNC.<sup>29,44,46,52,53,57,58,143,147,150</sup> The successful preparation of CNC-Br was confirmed by FTIR spectroscopy in Figure 2.1. Compared with the unmodified material, the FTIR spectrum of CNC-Br shows an additional band at  $1739 \text{ cm}^{-1}$ , which was assigned as the carbonyl stretching vibration of the grafted ester group.

**Scheme 2.1. Synthetic route used for the preparation of the PS-g-CNC**

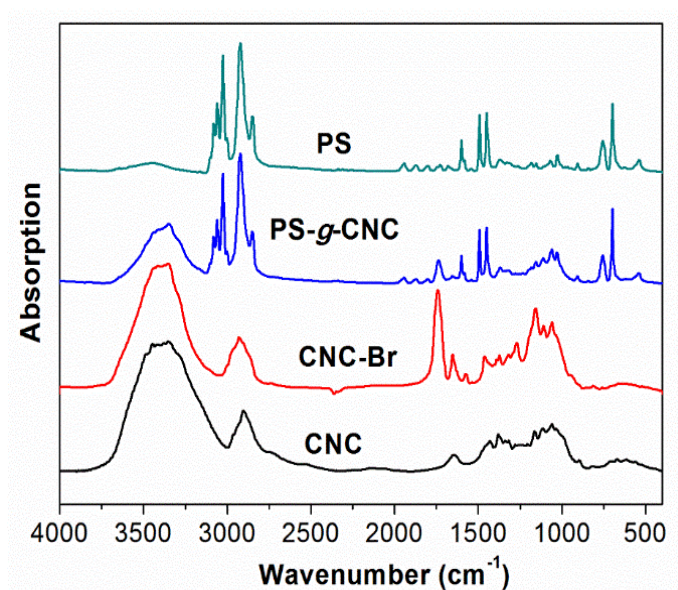
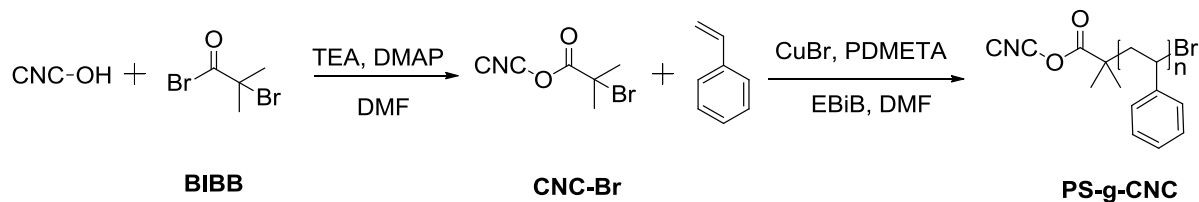


**Figure 2.1. FTIR spectra of pristine CNC, CNC-Br, PS-g-CNC after 2 h reaction, and free PS.**

The ester grafting was further confirmed by <sup>13</sup>C CP-MAS NMR spectroscopy in Figure 2.2. The pattern of cellulose is observed at 105 ppm (C<sub>1</sub>), 89 ppm (C<sub>4</sub> crystalline), 84 ppm (C<sub>4</sub> amorphous), 75-72 ppm (C<sub>2</sub>/C<sub>3</sub>/C<sub>5</sub>), 65 ppm (C<sub>6</sub> crystalline) and 63 ppm (C<sub>6</sub> amorphous).<sup>151-153</sup> After the reaction with BIBB, the spectrum of CNC-Br displays additional signals at 171, 57 and 31 ppm, corresponding to the C<sub>7</sub>, C<sub>8</sub> and C<sub>9</sub> carbons of the grafted moieties, respectively. The cellulose pattern in the CNC-Br spectrum was not affected by the treatment, and the signals of crystalline domains retained their sharpness, indicating that the ester grafting was limited to the outer surface of the CNC.

The morphologies of pristine CNC and CNC-Br were investigated by TEM. As shown in Figure 2.3, the pristine CNC consist of rod-like particles, and are slightly aggregated due to the addition of FeCl<sub>3</sub>

before analysis, to stain the particles. Therefore, their size is hard to evaluate from the TEM pictures. After modification by BIBB, the rod-like morphology of the cellulose nanocrystals is retained, and the dimensions of CNC-Br estimated from the TEM images are ca.  $189 \pm 49$  nm in length and  $8.0 \pm 2.8$  nm in diameter (aspect ratio  $\sim 19.5$ ).

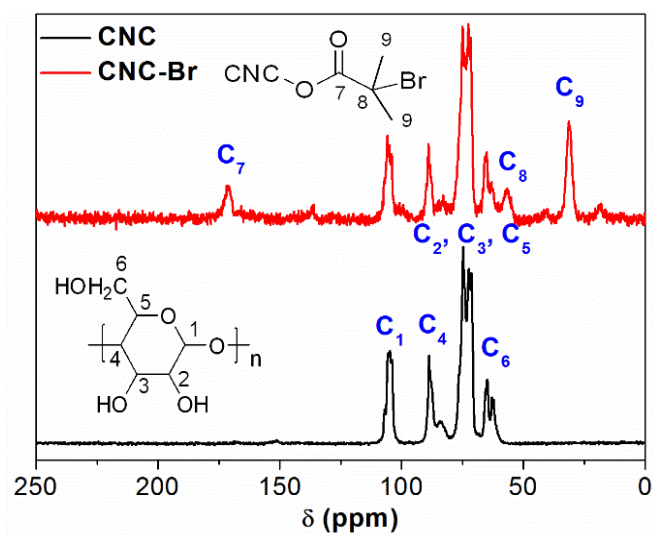


**Figure 2.2.**  $^{13}\text{C}$  CP-MAS NMR spectra of pristine CNC and CNC-Br.

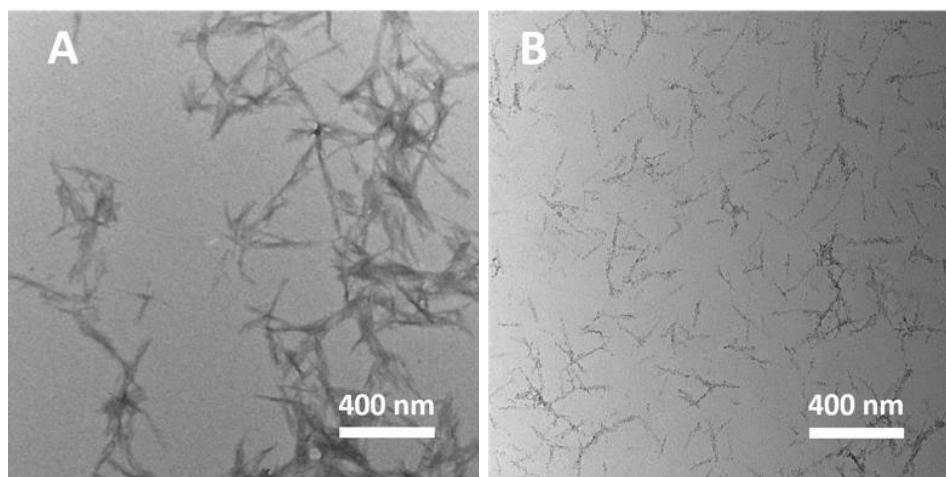


**Figure 2.3.** TEM images showing the morphology of pristine CNC (A) and CNC-Br (B).

The thermal stability of the pristine CNC and CNC-Br was investigated by TGA. The thermograms and corresponding DTG derivatives are shown in Figure 2.4. Both samples display a slight weight loss below 100 °C, due to the presence of residual adsorbed moisture. The lower weight loss noted with CNC-Br is assigned to the decreased hydrophilicity imparted by the esterification treatment. The thermogram of pristine CNC is consistent with the thermal behavior generally observed for CNC bearing sulfate ester groups.<sup>44,154</sup> Even small amounts of sulfate ester groups at the CNC surface are known to catalyze the thermal degradation of cellulose.<sup>44,154</sup> Compared with pristine CNC, CNC-Br displays a decreased thermal stability. This result should be related to the presence of the labile bromine within CNC-Br, which might accelerate the degradation of cellulose through free radical mechanisms or by forming HBr upon heating.<sup>147</sup>

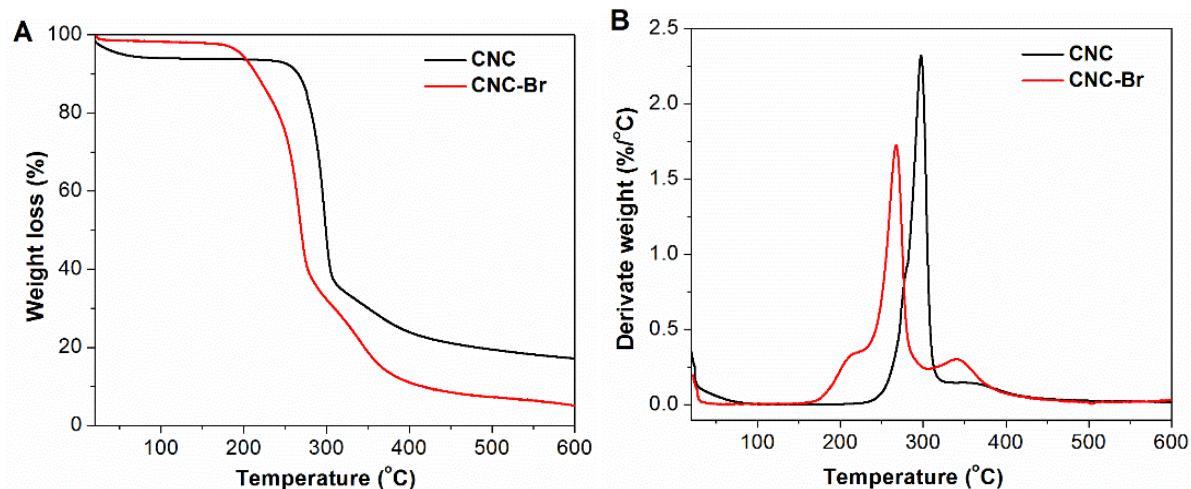


**Figure 2.4. TGA thermograms (A) and DTG curves (B) of pristine CNC and CNC-Br.**

The bromine content in CNC-Br, evaluated by elemental analysis (EA) was estimated to be 11.9 wt. % (other elements: C 42.7 wt. %, O 34.3 wt. %, H 5.2 wt. % and N 0.88 wt. %). The EA results also confirm the successful anchoring of Br initiator sites on CNC. Based on the Br content, the molecular ratio of anhydroglucose relative to the grafted Br was estimated to be 3.2, using a method reported in the literature.<sup>55</sup> The detailed calculation is given in the experimental section. Hence, the molecular composition of CNC-Br can be simplified as  $(C_6H_{10}O_5)_{3.2}(C_4H_6OBr)$ . If necessary, the amount of initiating Br sites can be finely tuned by controlling the reaction conditions with BIBB.

### 2.3.2 SI-ATRP grafting of PS from CNC-Br

The ATRP grafting of PS from CNC-Br was performed in DMF, in the presence of ethyl  $\alpha$ -bromoisobutyrate (EBiB) as sacrificial initiator (Figure 2.1).<sup>46</sup> Aliquots were taken at designed polymerization intervals and analyzed by  $^1\text{H}$  NMR, to evaluate the monomer conversion with time. The monomer conversion is calculated based on the ratio of styrene to DMF in the aliquots. The  $^1\text{H}$  NMR spectra of the aliquots in  $\text{CDCl}_3$  with different polymerization time are shown in Figure 2.5. The free PS and PS-g-CNC in the aliquots, were separated by centrifugation. The monomer conversion is given by  $([\text{M}_0]-[\text{M}_t])/[\text{M}_0]$ , where  $[\text{M}_0]$  and  $[\text{M}_t]$  are the monomer concentration at initial and time  $t$ , respectively.

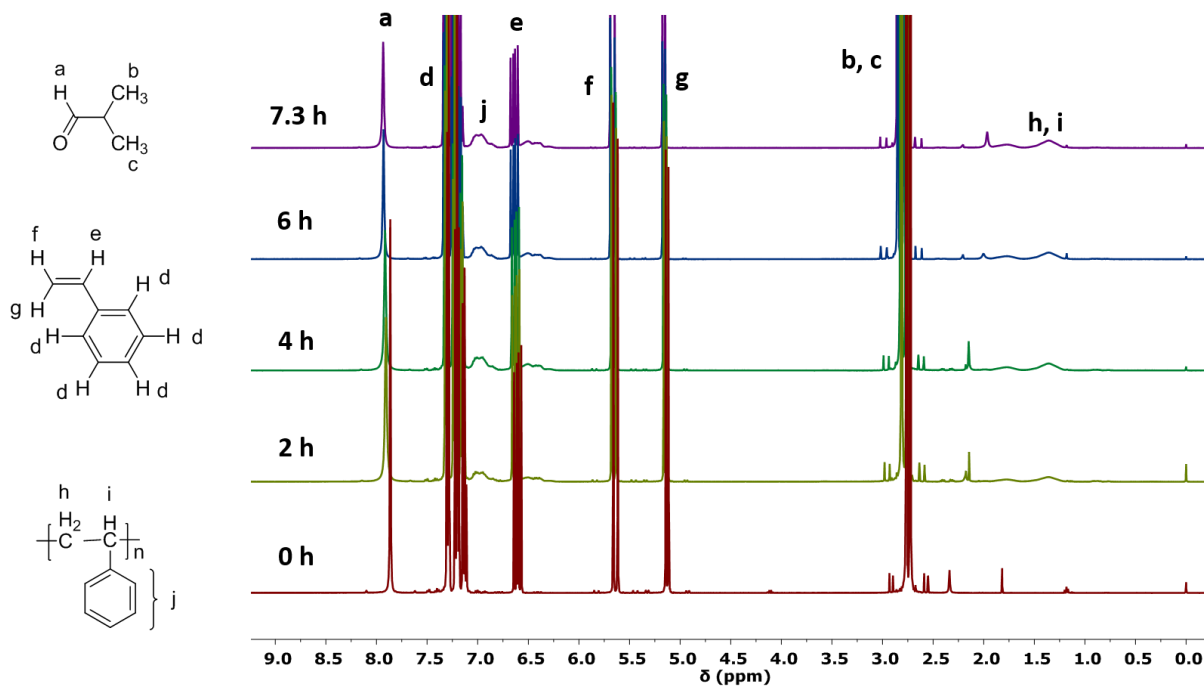


**Figure 2.5**  $^1\text{H}$  NMR spectra of the aliquots in  $\text{CDCl}_3$  with different polymerization time

#### 2.3.2.1 Kinetics of the ATRP polymerization of free PS

The monomer conversion and  $\ln([\text{M}_0]/[\text{M}_t])$  are plotted as a function of reaction time in Figure 2.6, while the kinetic parameters are summarized in Table 2.1. The monomer concentration decreases with

time, leading to a gradual decrease of the propagation rate  $R_p = K_p[M_i][P_n^*]$ . As a consequence, the increase in monomer conversion with time exhibits a convex shape. The  $\ln([M_0]/[M_t])$  increases linearly with time, suggesting first-order kinetics with a constant concentration of radicals, which is characteristic of a well-controlled ATRP.<sup>42</sup>

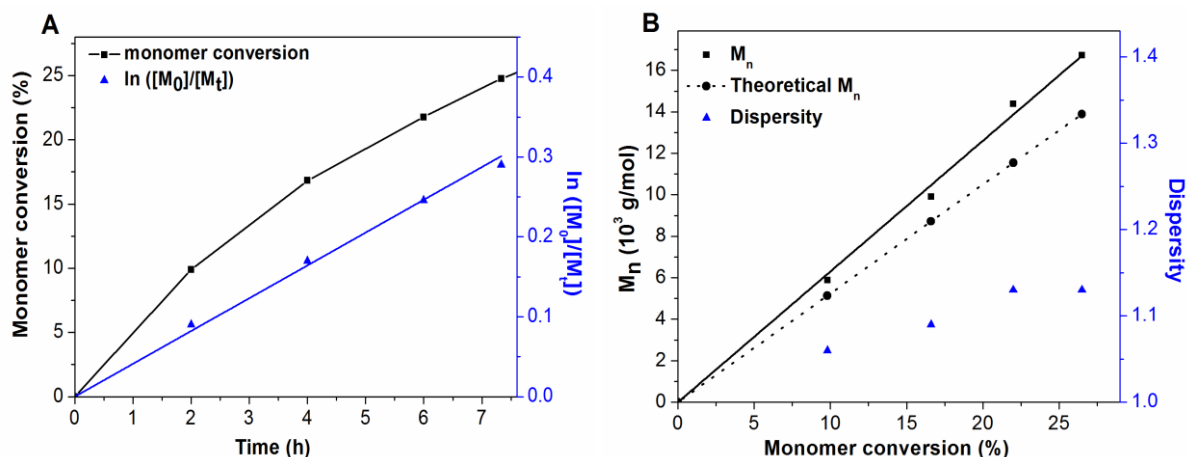


**Figure 2.6. Kinetics of the ATRP polymerization of free PS: (A) Monomer conversion and  $\ln([M_0]/[M_t])$  vs. reaction time; (B)  $M_n$  and dispersity of free PS vs. monomer conversion.**

**Table 2.1. Kinetics parameters of the ATRP polymerization of free PS.**

Samples (Polymerization time h)	Monomer conversion (%)	$\ln([M_0]/[M_t])$	Theor. $M_n^{\text{free PS}}$ (g/mol)	$M_n^{\text{free PS}}$ measured by GPC (g/mol)	Initiating efficiency
Free PS (2h)	9.77	0.09	5128	5886	87.1%
Free PS (4h)	16.60	0.17	8713	10575	82.4%
Free PS (6h)	22.00	0.24	11546	14389	80.2%
Free PS (7.3h)	26.45	0.29	13886	16732	83.0%

The number-average molecular weight ( $M_n^{\text{free PS}}$ ) and dispersity of free PS at different polymerization times, were evaluated by GPC. As shown in Figure 2.6B,  $M_n^{\text{free PS}}$  increases proportionally with respect to the monomer conversion, and the dispersity values remain below 1.15 (1.06-1.13), further confirming

that the PS polymerized according to a “living” polymerization process. As the amount of initiating sites on CNC-Br is negligible compared with the amount of sacrificial initiator, a theoretical  $M_n^{\text{free PS}}$  value can be calculated based on the monomer conversion and molar ratio of monomer to initiator. The theoretical value found is slightly smaller than the one measured by GPC (Figure 2.6 and Table 2.1), indicating that the sacrificial initiators did not all initiate a polymerization. The initiating efficiency of the EBiB, calculated as the ratio of theoretical  $M_n^{\text{free PS}}$  to the GPC measured  $M_n^{\text{free PS}}$ , is summarized in Table 2.1. Results indicate that most of the EBiB reacted in the system.

### 2.3.2.2 Characterization of PS-*g*-CNC by FTIR spectroscopy

The successful grafting of PS from CNC-Br was confirmed by the FTIR spectroscopy, as shown in Figure 2.2. Compared with CNC-Br, the PS-*g*-CNC material reacted for 2 h displays additional infrared vibrations characteristic of PS at 3059/3025  $\text{cm}^{-1}$  (aromatic C-H stretching vibrations), 1600/1494/1451  $\text{cm}^{-1}$  (C=C stretching vibrations), 756  $\text{cm}^{-1}$  (out-of-plane aromatic C-H bending vibrations), and 700  $\text{cm}^{-1}$  (deformation vibration of the C-H group of the mono-substituted benzene ring).

### 2.3.2.3 Evolution of the hydrodynamic radius of PS-*g*-CNC during polymerization

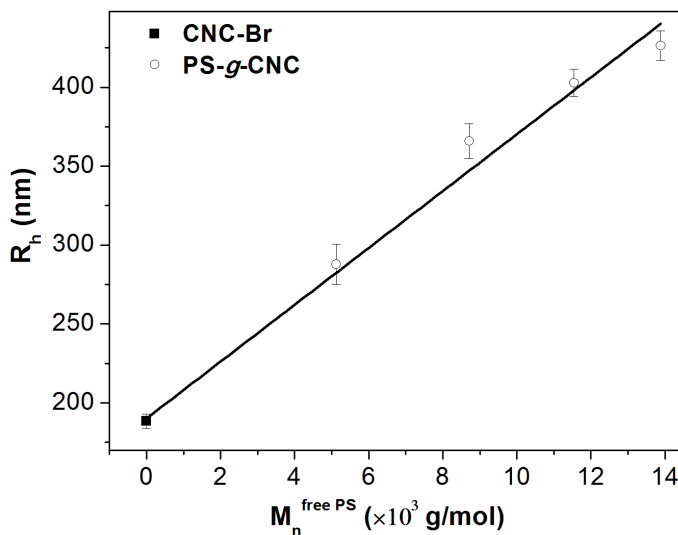


**Figure 2.7.** Evolution of the hydrodynamic radius ( $R_h$ ) of PS-*g*-CNC as a function of  $M_n^{\text{free PS}}$ .

The hydrodynamic radius ( $R_h$ ) of the polymer-grafted nanoparticles measured by DLS, can be used to follow the evolution of the ATRP process.<sup>133,155</sup> Since the cellulose nanocrystals are not spherical; the  $R_h$  only provides an indication of the apparent size of the nanoparticles.<sup>144</sup> It is indeed expected that, with the growth of the grafted PS chains, the  $R_h$  would increase correspondingly.<sup>31</sup> The  $R_h$  of the PS-*g*-CNC nanoparticles dispersed in THF was then measured by DLS and plotted as a function of the  $M_n^{\text{free PS}}$  in Figure 2.7. Results indicate that the size of the PS-*g*-CNC remains in the nanometer range. The large  $R_h$  of PS-*g*-CNC is due to the slightly aggregation in the THF suspension.<sup>31</sup> Zoppe et al. also reported a quite large  $R_h$  for polymer grafted CNC which were also prepared by SI-ATRP.<sup>31</sup> The  $R_h$  increased linearly with  $M_n^{\text{free PS}}$ , suggesting the polymer at the CNC surface grows at the same speed as the free polymer ( $M_n^{\text{grafted PS}}$  increases linearly with the  $M_n^{\text{free PS}}$ ). Since DLS is easy to perform, it can be used as a practical tool to monitor the polymerization process at the CNC surface. However, the actual  $M_n^{\text{grafted PS}}$  value cannot be obtained using this technique.

#### 2.3.2.4 Evolution of the $T_g$ of free PS and PS-*g*-CNC during polymerization

The glass transition temperatures ( $T_g$ ) of free PS ( $T_g^{\text{free PS}}$ ) and PS-*g*-CNC ( $T_g^{\text{PS-}g\text{-CNC}}$ ) were measured by DSC, for different polymerization times. As shown in Figure 2.8A, both  $T_g^{\text{free PS}}$  and  $T_g^{\text{PS-}g\text{-CNC}}$  increase as the polymerization time increase, while no  $T_g$  was observed for the CNC-Br sample. This result confirms that a PS polymer of increasing size was grafted at the CNC surface. According to the free volume theory proposed by Fox and Flory,<sup>156-158</sup> the  $T_g$  of the polymer should increase proportionally with  $1/M_n$  due to the decrease of free volume, and follow the empirical equation:

$$T_g = T_g^\infty - K_g/M_n,$$

where  $T_g^\infty$  refers to the  $T_g$  of PS with infinite  $M_n$  and  $K_g$  is an empirical constant of the polymer.<sup>159</sup>

Such linear correlation between  $T_g$  and  $-1/M_n$  was confirmed for the free polymer in Figure 2.8B. Moreover, the  $T_g^{\text{PS-}g\text{-CNC}}$  also increases linearly with  $-1/M_n^{\text{free PS}}$  (Figure 2.8B), suggesting that the  $M_n^{\text{grafted PS}}$  is proportionally correlated to the  $M_n^{\text{free PS}}$ . However, we still cannot deduce the exact  $M_n^{\text{grafted PS}}$  value from these data. The  $T_g^{\text{PS-}g\text{-CNC}}$  is higher than the corresponding  $T_g^{\text{free PS}}$ , especially in the low  $M_n$  range, which is consistent with the results obtained when PS was grafted on SiO<sub>2</sub>.<sup>142</sup> The higher  $T_g$  of PS-*g*-CNC results from the increased steric hindrance after grafting.

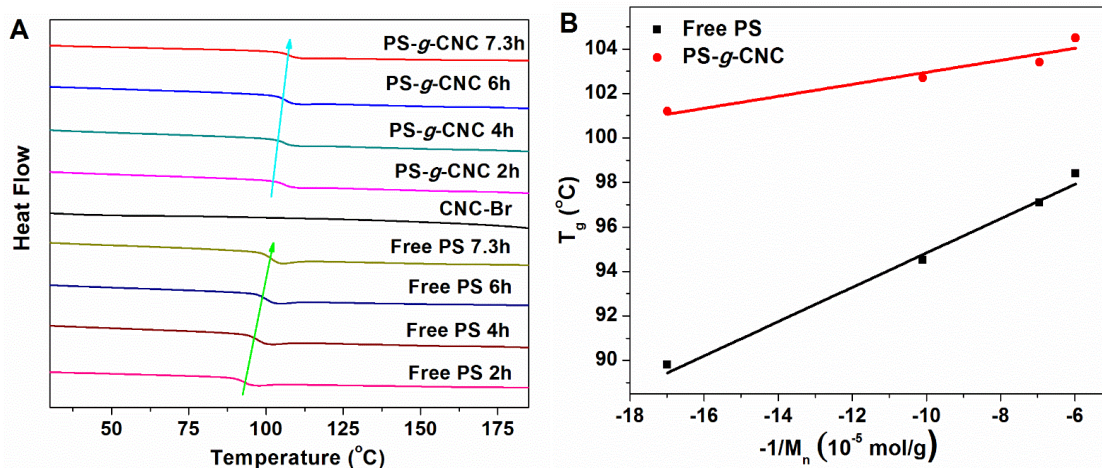


**Figure 2.8.** (A) DSC curves of CNC-Br, free PS, and PS-g-CNC at different polymerization time; (B)  $T_g$  of free PS and PS-g-CNC as a function of  $-1/M_n^{\text{free PS}}$ .

### 2.3.2.5 Evaluation of the molecular weight of the grafted PS by thermal analysis

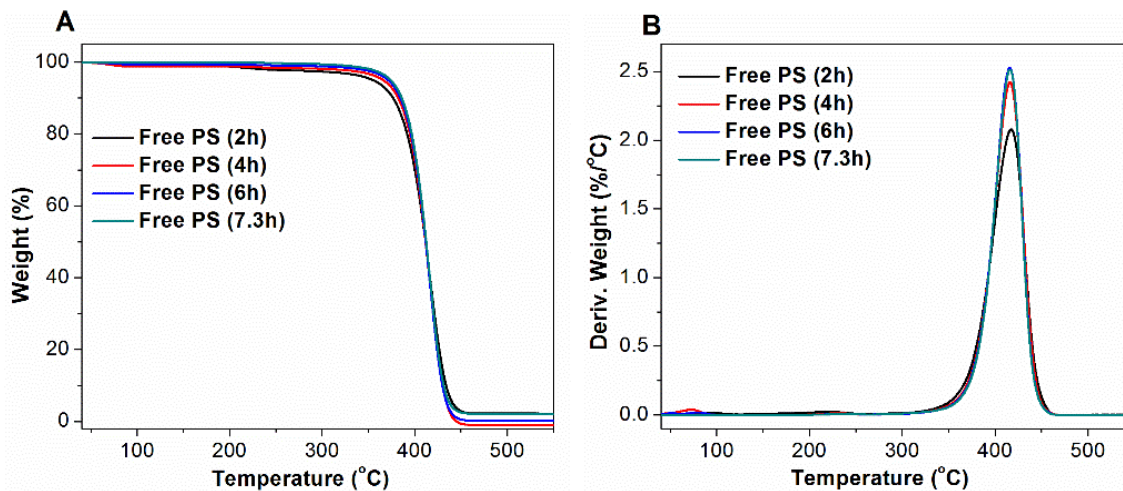


**Figure 2.9.** TGA thermograms (A) and DTG curves (B) of free PS

The thermal stability of free PS and PS-g-CNC samples was evaluated by TGA, for different polymerization times. The thermograms and corresponding DTG derivatives of the free PS are shown in Figure 2.9. The onset degradation temperature ( $T_{\text{onset}}$ ) of the free PS increases slightly with reaction

time, *i.e.* with increasing  $M_n$ . The main decomposition temperature of PS is in the range between 350 and 450 °C, which accounts for more than 95% of the PS weight loss.

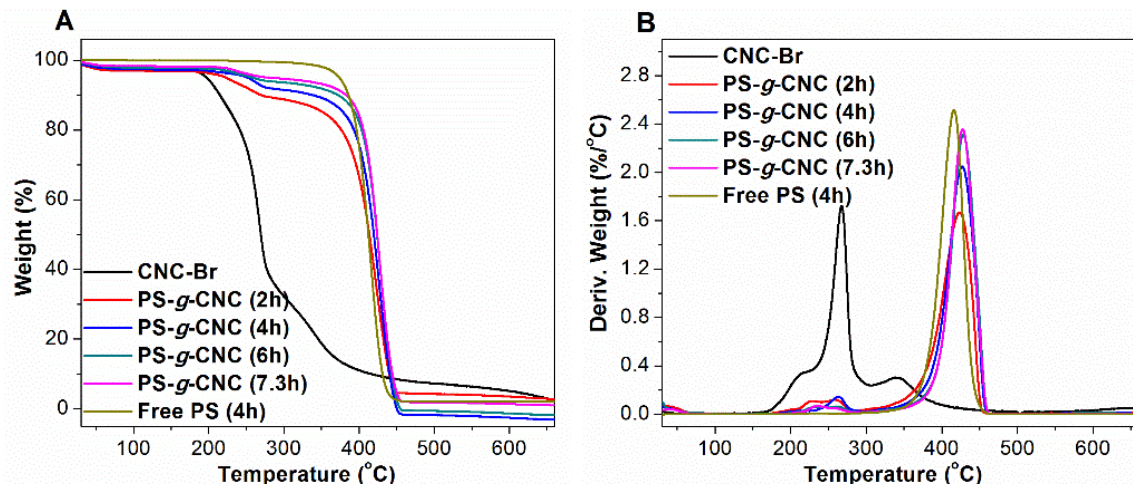


**Figure 2.10.** TGA thermograms (A) and DTG curves (B) of PS-*g*-CNC.

The TGA thermograms and DTG curves of PS-*g*-CNC are shown in Figure 2.10. The PS-*g*-CNC nanoparticles exhibit an enhanced thermal stability and display two stages of thermal loss, consistent with literature data.<sup>57</sup> The first weight loss (from 180 to 320 °C) is associated with the degradation of CNC and the second weight loss (from 350 to 450 °C) with the degradation of PS. We already showed that CNC-Br displays a decreased thermal stability compared with pristine CNC (Figure 2.5), assigned to the labile bromine, which probably accelerates cellulose degradation. The bromine atom in PS-*g*-CNC is also labile, and should therefore be cleaved at a lower temperature than PS. As far CNC-Br, the released Br probably favors cellulose degradation, as suggested by the lower temperature of maximal degradation found in the composite ( $T_{\max} = 260$  °C) compared to pristine CNC ( $T_{\max} = 297$  °C). The ratio of second weight loss relative to first weight loss should then represent an accurate estimation of the weight ratio of grafted PS relative to CNC-Br in the PS-*g*-CNC nanocomposites. This ratio was plotted as a function of the monomer conversion in Figure 2.11. The linear correlation obtain suggests that the  $M_n^{\text{grafted PS}}$  increases proportionally with respect to the monomer conversion.

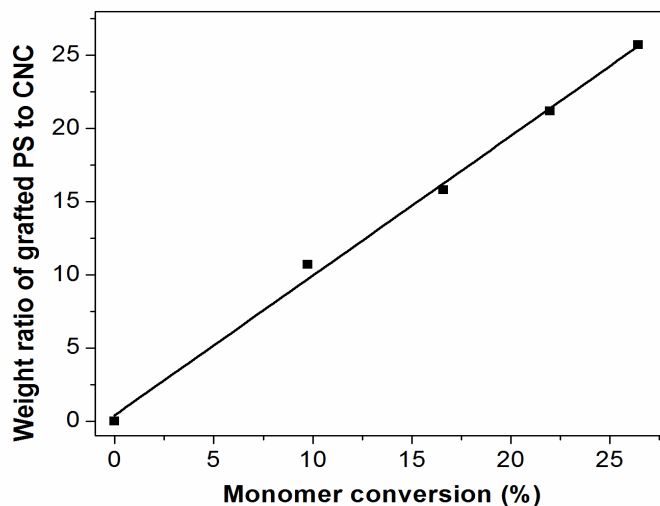


**Figure 2.11. Evolution of the weight ratio of grafted PS relative to CNC-Br in PS-g-CNC (calculated by TGA) as a function of monomer conversion.**

By comparing the weight of the grafted polymers with the number of initiating sites on CNC-Br, the exact  $M_n^{\text{grafted PS}}$  can be calculated. Assuming that all Br sites on CNC-Br have reacted, the  $M_n^{\text{grafted PS}}$  in PS-g-CNC after 2h reaction is calculated as an example.

**Table 2.2.  $M_n^{\text{free PS}}$  and  $M_n^{\text{grafted PS}}$  values of the PS-g-CNC samples obtained at different polymerization times.**

Samples (polymerization time)	$M_n^{\text{free PS}}$ measured by GPC (g/mol)	Weight ratio of grafted PS relative to CNC measured by TGA	$M_n^{\text{grafted PS}}$ (g/mol)
PS-g-CNC (2h)	5886	10.69	7140
PS-g-CNC (4h)	10575	15.80	10554
PS-g-CNC (6h)	14389	21.18	14148
PS-g-CNC (7.3h)	16732	25.72	17181

According to the EA results of CNC-Br, the molecular composition of CNC-Br can be simplified as  $(C_6H_{10}O_5)_{3.2}(C_4H_6OBr)$ ; the composition of PS-g-CNC can be simplified as

$(C_6H_{10}O_5)_{3.2}(C_4H_6OBr)(PS)_n$ ; the monomer conversion after 2h is 9.77%, determined by  $^1H$  NMR; the weight ratio of grafted PS relative to CNC-Br calculated by TGA is 10.7;  $M [(C_6H_{10}O_5)_{3.2}(C_4H_6OBr)] = 668$  g/mol;  $M$  (styrene) = 104 g/mol. The number  $n$  of styrene units in the grafted polymer can then be deduced from the following equation:  $104n/668 = 10.7$ . We find an  $n$  value of about 69, corresponding to a  $M_n^{grafted\ PS}$  value of ca. 7140 g/mol. The calculated  $M_n^{grafted\ PS}$  values of the PS-g-CNC samples obtained at different polymerization times are compared with the  $M_n$  values of the free polymers in Table 2.2.

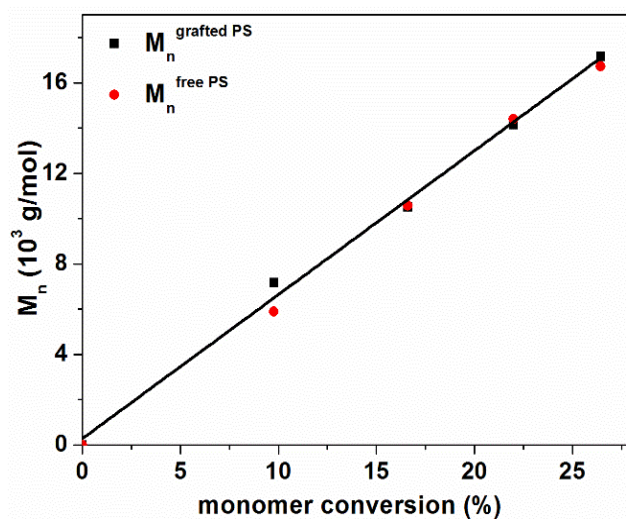


**Figure 2.12.** The  $M_n^{grafted\ PS}$  derived by TGA and the  $M_n^{free\ PS}$  measured by GPC

The  $M_n^{grafted\ PS}$  derived from the thermal analysis agree quite well with the  $M_n^{free\ PS}$  measured by GPC. Both parameters increased linearly with the monomer conversion (Figure 2.12), confirming that the polymerization rates of the grafted and free polymers are the same. Therefore, the characterization of the free polymer is a convenient way to estimate the molecular weight of the polymer grafted on CNC-Br by SI-ATRP. Moreover, the agreement between  $M_n^{free\ PS}$  and  $M_n^{grafted\ PS}$  suggests that most of the initiation sites on CNC-Br have reacted. The thermal analysis of polymer-grafted particles is therefore a convenient method to estimate the molecular weight of the grafted polymer as long as the particles and grafted polymers are totally decomposed and display two separate weight losses in the TGA thermograms.

## 2.4 Conclusions

In this chapter, we developed a convenient method based on DLS, DSC and TGA to characterize directly the PS grafted on the CNC surface by SI-ATRP, without cleaving the polymer from the nanoparticle. Br initiating sites were first introduced at the surface of the CNC by esterification with BIBB (CNC-Br), and subsequently reacted with styrene for various times, to produce CNC nanohybrids grafted with PS chains of various lengths (PS-*g*-CNC). The addition of a sacrificial initiator in the reaction medium allowed verifying the good controlling of the living radical polymerization, through the analysis of the free polymer produced. DLS proved to be a convenient tool to monitor the polymerization process through the measure of the hydrodynamic radius of the PS-*g*-CNC nanoparticles, which was found to increase linearly with the molecular weight of the free polymer. The DSC curves of the PS-*g*-CNC particles revealed a linear relationship between the glass transition temperature of PS-*g*-CNC and the  $-1/M_n$  value of the free polymer. This relation allowed confirming that the molecular weight of the grafted PS was correlated with the molecular weight of the free PS. Finally, we developed an original method based on TGA, to directly estimate the molecular weight of the PS grafted at the surface of the CNC without cleaving the polymer from the nanoparticle, by comparing the weight losses imparted to the cellulosic material and grafted PS. We found that the  $M_n$  of grafted and free PS coincided quite well, confirming that the free polymer produced by the sacrificial initiator can be used to indirectly characterize the PS grafted at the CNC surface.

## **Chapter 3**

### **A comparative study on the Surface grafting of Polystyrene and Poly(4-vinylpyridine) on Cellulose Nanocrystals by SI-ATRP and SI-ARGET ATRP**

Both Surface-Initiated Atom Transfer Radical Polymerization (SI-ATRP) and Surface-Initiated Activator Re-Generated by Electron Transfer ATRP (SI-ARGET ATRP) were conducted to graft polystyrene (PS) and poly(4-vinylpyridine) (P4VP) on the surface of CNC. The SI-ATRP and SI-ARGET ATRP approaches were systematically compared to evaluate the potential benefit of each method. The surface initiating efficiencies (SIE) of the CNC-Br macroinitiators with regard to styrene or 4-vinylpyridine were evaluated by TGA and EA, respectively. The combination of analytical methods such as FT-IR, DLS, DSC, TGA, and EA allowed demonstrating that the SI-ARGET ATRP reaction favored the grafting of longer polymer chains with lower grafting densities compared with the classical SI-ATRP method. The impact of catalyst concentration and propagation rate on the differences noted were particularly discussed.

### 3.1 Introduction

Replacing petroleum-based synthetic materials by sustainable materials has attracted much attention in recent decades due to the global warming and worldwide pollution.<sup>117,160</sup> The valorization of bio-sourced materials such as cellulose has become a hot topic because of its biocompatibility, biodegradability, renewability, environment-friendliness, and low cost.<sup>36,47,137,160,161</sup> In this context, cellulose nanocrystals (CNC) offer an array of properties, which can be exploited in the field of cosmetics, emulsions, electronics, liquid crystals, enforcing nano-fillers, foods, and catalysts fields.<sup>1,3-5,21,162,163</sup> In particular, these nanoparticles are renewable, biocompatible, display a high tensile strength and elastic modulus, have a low density and low coefficient of thermal expansion, and tend to self-assemble in the form of nematic phases.<sup>1,3-5,21,162,163</sup> CNC are typically produced from microcrystalline cellulose, paper or pulp, by submitting the cellulose substrate to concentrate sulfuric acid combined with sonication.<sup>1,3,4</sup> The treatment provokes the hydrolysis of the amorphous regions of the initial semi-crystalline material, leading to the release of nano-sized rod-like cellulose crystallites bearing sulfate ester groups at their surface.

However, the hydrophilic nature of the CNC surface tends to limit its field of application, especially for the hydrophobic matrix. Indeed, the engineering of innovative functional materials from CNC generally requires a fine tuning of their surface properties, which can be achieved by chemical functionalization.<sup>26,28,164</sup> In the area of nanocomposites, for instance, the grafting of hydrophobic moieties or polymer chains at the CNC surface can help improve their miscibility with hydrophobic matrices.<sup>9</sup> Surface functionalization can also be used as a tool to impart the material with novel functionalities. The CNC modification via polymer grafting is particularly promising, as it allows preparing hybrid nanomaterials that can be used for a wide range of advanced applications.<sup>1,3-5,29,47,162</sup> As a “grafting from” strategy, Surface-Initiated Atom Transfer Radical Polymerization (SI-ATRP) has been widely used to graft different polymer brushes on CNC, such as polystyrene (PS),<sup>46,57</sup> poly(6-(4-(4-methoxyphenylazo) phenoxy) hexyl methacrylate) (PMMAZO),<sup>53</sup> poly(2-(dimethyl amino)ethyl methacrylate) (PDMAEMA),<sup>58</sup> poly(methyl acrylate) (PMA),<sup>56</sup> poly(N-isopropyl acrylamide) (PNiPAAm),<sup>44</sup> and poly(oligo (ethylene glycol) methyl ether methacrylate) (POEGMA).<sup>51</sup>

However, one of the major drawbacks of ATRP is that the method requires the utilization of high amounts of transition metal complexes as a catalyst, which are generally toxic.<sup>165</sup> In particular, the Cu(II) species generated after reaction with the classical CuBr catalyst, generally needs to be removed from the final products in sensitive applications, like in electronics or medicine.<sup>117</sup> Several methods have been developed to remove the metal catalyst, but these processes are highly energy consuming, which limits the development of ATRP in industry. Moreover, the classical ATRP process is very sensitive to oxygen (the Cu(I) species can be easily oxidized), and tedious air-removing steps are needed to obtain a well-controlled polymerization process (such as freeze-thaw cycles). To reduce the impact of catalyst and sensitivity to oxygen, alternative methods such as Activator Re-Generated by Electron Transfer (ARGET) ATRP have been developed. With this method, a reducing agent is added in excess, to steadily regenerate the Cu(I) species from the Cu(II) continuously formed during the radical termination reactions.<sup>120,166</sup> The ARGET ATRP can reduce the amount of catalyst used in the process to ppm amount and can be conducted in the presence of limited air.<sup>165</sup> Moreover, some FDA approved chemicals such as tin<sup>II</sup> 2-ethylhexanoate (Sn(EH)<sub>2</sub>), glucose, ascorbic acid, hydrazine or phenyl hydrazine, can be used as reducing agents.<sup>120,121,143,166-169</sup> Compared with traditional ATRP, ARGET ATRP is a relatively “green” method to obtain a well-controlled polymerization. The method has been employed to graft different polymers on the surface of various substrates,<sup>121,166,170</sup> but not on CNC. Moreover, the comparative studies between the SI-ATRP and SI-ARGET ATRP are rare.

Herein, the efficiencies of the SI-ATRP and SI-ARGET ATRP methods to initiate the grafting of polymer chains at the CNC surface were compared. The experiments were performed with two different polymers with different chemical structures and polarities. PS was selected as a model hydrophobic polymer, as its surface grafting by ATRP has been performed on a wide variety of substrates and is well documented in the literature. P4VP was selected as a hydrophilic polymer which can be easily characterized *via* elemental analysis of the nitrogen atom. This polymer is also pH-responsive and displays various interesting properties related to its catalytic activity,<sup>171</sup> gas permselectivity,<sup>172</sup> electrical conductivity, and ability to serve as a ligand for metal coordination.<sup>173</sup> The PS grafted CNC (PS-*g*-CNC) and P4VP grafted CNC (P4VP-*g*-CNC) were characterized by Fourier transform infrared spectroscopy (FTIR), differential scanning calorimetry (DSC), thermogravimetric analysis (TGA), and

element analysis (EA), and the grafting densities obtained by SI-ATRP and SI-ARGET ATRP were compared.

## **3.2 Experimental**

### **3.2.1 Materials**

CNC were purchased from The University of Maine. Acetic acid, CuBr, N,N,N',N'',N'''-pentamethyldiethylenetriamine (PMDETA), calcium hydride, polystyrene (PS,  $M_n$  250000) and all the solvents were purchased from Sigma-Aldrich. Ethyl  $\alpha$ -bromoisobutyrate (EBiB),  $\alpha$ -bromoisobutyryl bromide (BIBB), tris [2-(dimethylamino)ethyl]amine ( $Me_6$ TREN), 4-vinylpyridine (4VP) were purchased from Alfa Aesar. 4-Dimethylaminopyridine (DMAP) and triethylamine (TEA) were purchased from Fisher. CuBr was purified with acetic acid at 80 °C under the protection of N<sub>2</sub> for 24 h and washed with acetic acid and then dried under vacuum at 50 °C. Purified CuBr was stored in the glove box. 4VP was purified by distillation from calcium hydride under reduced pressure and was stored at -20 °C. The other chemicals were used as received.

### **3.2.2 Preparation of the brominated CNC nano-initiator: CNC-Br**

BIBB was used to modify CNC and prepare the brominated CNC nano-initiator (CNC-Br), later used to initiate the SI-ATRP reaction. Firstly, CNC (500 mg) were dispersed in DMF (50 mL) by sonication. TEA (4 mL) and DMAP (2 g) were added to the suspension. The suspension was evacuated under vacuum and backfilled with argon three times. Then BIBB (4 mL) was added dropwise to the suspension in an ice bath. After 24 h, EtOH was added, and the CNC-Br was recovered by centrifugation. CNC-Br was Soxhlet extracted with THF, then dialyzed with deionized H<sub>2</sub>O. Finally, CNC-Br was obtained by freeze-drying.

### **3.2.3 Grafting PS from CNC-Br using SI-ATRP: PS1-g-CNC**

In brief, the SI-ATRP of PS from CNC-Br was conducted at 100 °C, with the molar ratio [Styrene]: [EBiB]: [CuBr]: [PMDETA]: [DMF] = 500: 1: 1: 1: 500. In detail, CuBr (72 mg) was transferred into the Schlenk flask in the glove box. CNC-Br (50 mg) was dispersed in DMF (250 mmol) via sonication. Then styrene (250 mmol) and EBiB (0.5 mmol) were added to the suspension. After the suspension had

been bubbled with argon for 20 min, the suspension was transferred to the Schlenk flask under the protection of argon. The suspension was degassed by three freeze-pump-thaw cycles. After the addition of PMDETA (0.5 mmol) under argon, the reaction was initiated at 100 °C. The monomer conversion was calculated from the  $^1\text{H}$  NMR of the mixture in  $\text{CDCl}_3$ . The mixture was centrifuged to recover the PS-*g*-CNC nanoparticles. PS-*g*-CNC was washed with THF and EtOH three times respectively to remove free polymer and other unreacted chemicals. After drying at 50 °C under vacuum, the PS-*g*-CNC nanocomposites were obtained. The green supernatant became colorless after the catalyst was removed by passing it through the  $\text{Al}_2\text{O}_3$  column. The colorless supernatant was poured into excess MeOH, and the free PS precipitate was recovered through filtration followed drying at 50 °C under vacuum. The free polymer and hybrid material obtained are named free PS1 and PS1-*g*-CNC, respectively. After polymerization for 4h, the monomer conversion is about 16.6%, so the theoretical  $M_n$  of the free PS1 is about 8714 g/mol. The  $M_n$  of the free PS1 measured by GPC is about 9903 g/mol (dispersity =1.09).

### **3.2.4 Grafting PS from CNC-Br using SI-ARGET ATRP: PS2-*g*-CNC**

The catalyst solution for ARGET ATRP was first prepared by solubilizing  $\text{CuBr}_2$  (0.1 mmol) and  $\text{Me}_6\text{TREN}$  (1 mmol) in DMF (5 mL). CNC-Br (100 mg) was dispersed in DMF (7.7 mL). Then EBiB (0.1 mmol), styrene (50 mmol), ascorbic acid (0.1 mmol) and catalyst solution (125  $\mu\text{L}$  (including  $2.5 \times 10^{-3}$  mmol  $\text{CuBr}_2$  and  $2.5 \times 10^{-2}$  mmol  $\text{Me}_6\text{TREN}$ )) were added to the suspension. The mixture was degassed by three freeze-pump-thaw cycles. The polymerization was conducted at 100 °C. The molar ratio of each component is [Styrene]: [EBiB]: [Ascorbic acid]: [ $\text{CuBr}_2$ ]: [ $\text{Me}_6\text{TREN}$ ] =500: 1: 1:  $1.25 \times 10^{-2}$ :  $1.25 \times 10^{-1}$ . After 1h, the polymerization was terminated by exposing to air. The free PS and PS-*g*-CNC obtained using SI-ARGET ATRP are denoted as free PS2 and PS2-*g*-CNC. Free PS2 and PS2-*g*-CNC were recovered and purified by the same procedure as free PS1 and PS1-*g*-CNC. The monomer conversion calculated by  $^1\text{H}$  NMR is 25.0%, and the theoretical  $M_n$  of the free PS is about 13,019 g/mol. The  $M_n$  of the free PS measured by GPC is about 13,126 g/mol (dispersity =1.19).

### 3.2.5 Grafting P4VP from CNC-Br using SI-ATRP: P4VP1-g-CNC

The SI-ATRP of P4VP from CNC-Br was conducted at 40 °C with the molar ratio [4VP]: [EBiB]: [CuBr]: [Me<sub>6</sub>TREN] =500: 1: 1: 2, and the other procedures were similar as the SI-ATRP of PS. The free P4VP and P4VP-g-CNC obtained using SI-ATRP are denoted as free P4VP1 and P4VP1-g-CNC, respectively. After reaction for 4h, the monomer conversion is 13.2%, so the theoretical degree of polymerization (DP) of the free P4VP1 is about 66. As 4VP and P4VP have strong coordination with the Cu catalyst, a much stronger ligand Me<sub>6</sub>TREN is used in the SI-ATRP process of P4VP. Even so, it is still difficult to remove all the Cu catalyst residue from the free P4VP1. The free P4VP1 still display slight green color after passing through an Al<sub>2</sub>O<sub>3</sub> chromatography column. Therefore, the experimental M<sub>n</sub> of the free polymer could not be accurately determined by GPC (unreliable values were found). The resultant P4VP1-g-CNC was washed with ethanol three times to remove the free polymers and then was dialyzed against EDTA-Na<sub>2</sub> aqueous solution and deionized water for 6 days to remove the Cu catalyst residues. The final P4VP1-g-CNC was obtained by freeze-drying.

### 3.2.6 Grafting P4VP from CNC-Br using SI-ARGET ATRP: P4VP2-g-CNC

The P4VP grafting procedure from CNC-Br using SI-ARGET ATRP was similar to the procedure used with PS. The polymerization was conducted at 40 °C and the molar ratio of each component is [4VP]: [EBiB]: [Ascorbic acid]: [CuBr<sub>2</sub>]: [Me<sub>6</sub>TREN] =500: 1: 1: 1.25×10<sup>-2</sup>: 1.25×10<sup>-1</sup>. After 1 h, the polymerization was terminated by exposing to air. The free polymer and hybrid material obtained are named free P4VP2 and P4VP2-g-CNC, respectively. The monomer conversion calculated by <sup>1</sup>H NMR is 15.6%, and the theoretical DP of the free P4VP2 is about 78.

### 3.2.7 Characterization

The Fourier transform infrared (FTIR) spectra of all samples were obtained with the potassium bromide technique, using a Thermo Nicolet Avatar 970 FTIR spectrometer, at a resolution of 8 cm<sup>-1</sup> (64 scans).

Thermogravimetric analysis (TGA) was performed on the TGA-Q50 system from TA instruments at a heating rate of 10 °C /min under nitrogen atmosphere.

Differential scanning calorimetry (DSC) was carried out using a DSC Q100 apparatus from TA Instruments. All samples were first heated from 0 °C to 200 °C to remove the moisture, then were cooled

down to 0 °C, and then were heated to 200 °C again. The  $T_g$  values were calculated from the second heating run.

Gel permeation chromatography (GPC) analysis was performed in THF with LiBr on a PL-GPC 50 plus Integrated GPC from Polymer Laboratories-Varian. The elution of the filtered samples was monitored using the simultaneous refractive index and UV detection. The elution times were converted to molar mass using a calibration curve based on low dispersity ( $M_w/M_n$ ) polystyrene standards.  $^1\text{H}$  NMR spectra were recorded using a Bruker AC-400 NMR at room temperature by dissolving the samples in  $\text{CDCl}_3$ .

Elemental analysis data were obtained from SGS Multilab (France). Carbon, hydrogen, and nitrogen were measured by thermal conductivity, according to protocols MO 240 LA 2008 (carbon and hydrogen) and MO 150 LA 2007 (nitrogen). Oxygen and sulfur were measured with infrared detectors, according to protocols MO 238 LA 2008 (oxygen) and MO 240 LA 2008 (sulfur). Bromide was measured by ionic chromatography, according to protocol MLE-MO-LAB-O78. All samples were dried at 105 °C before analysis.

### **3.3 Results and discussion**

#### **3.3.1 Preparation of the CNC-Br initiator**

Br initiating sites were first introduced at the surface of the CNC by esterification with BIBB (CNC-Br), as was described in Chapter 2 (the same CNC-Br material was used for these experiments). The successful preparation of CNC-Br has been demonstrated by FTIR,  $^{13}\text{C}$  NMR, XPS and EA in the previous chapter. According to the EA results, the molar ratio of anhydroglucose to Br is about 3.2, and the molecular component of CNC-Br can be simplified as  $(\text{C}_6\text{H}_{10}\text{O}_5)_{3.2}(\text{C}_4\text{H}_6\text{OBr})$ . The brominated CNC were then subsequently reacted with styrene or P4VP, using both SI-ATRP and SI-ARGET ATRP, and the results obtained by the two methods were compared.

### 3.3.2 SI-ATRP and SI-ARGET ATRP grafting of PS on CNC

#### 3.3.2.1 Characterization of the free PS produced by the sacrificial initiator

**Table 3.1. Reaction conditions and characteristics of the PS-g-CNC hybrid nanomaterials prepared by SI-ATRP or SI-ARGET ATRP**

Method	SI-ATRP*	SI-ARGET ATRP**
Sample	PS1-g-CNC	PS2-g-CNC
Catalyst (amount)	CuBr (2000 ppm)	CuBr <sub>2</sub> (25 ppm)
Reducing agent	/	Ascorbic acid
Polymerization time	4 h	1 h
Monomer conversion	16.6%	25.0%
M <sub>n</sub> of free PS measured by GPC (g/mol)	10575 (dispersity =1.09)	13126 (dispersity =1.19)
Theoretical M <sub>n</sub> of free PS (g/mol)	8714	13019
Initiating efficiency (IE) of EBiB	82.4 %	99.2%
D <sub>h</sub> of PS-g-CNC in THF measured by DLS	747 nm	880 nm
T <sub>g</sub> of PS-g-CNC (°C) measured by DSC	106.0	102.0
Weight ratio of grafted PS to CNC (R <sub>w</sub> ) measured by TGA	15.8	1.23
Surface initiating efficiency (SIE) of CNC-Br	99.8%	6.3%

\*SI-ATRP of PS from CNC-Br with the molar ratio of [Styrene]: [EBiB]: [CuBr]: [PMDETA] =500: 1: 1: 1 at 100 °C for 4 hours.

\*\*SI-ARGET ATRP of PS from CNC-Br with the molar ratio of [Styrene]: [EBiB]: [Ascorbic acid]: [CuBr<sub>2</sub>]: [Me<sub>6</sub>TREN] =500: 1: 1: 1.25×10<sup>-2</sup>: 1.25×10<sup>-1</sup> at 100 °C for 1 hour.

Both SI-ATRP and SI-ARGET ATRP reaction were performed in the presence of ethyl  $\alpha$ -bromoisobutyrate (EBiB) as a sacrificial initiator. The addition of sacrificial initiator can facilitate the control of the grafted polymer chain length by tuning the monomer and sacrificial initiator molar ratio.<sup>46,55</sup> As we demonstrated in Chapter 2, the free polymer produced by the sacrificial initiator can

be used to indirectly characterize the PS grafted at the CNC surface by SI-ATRP with a quite good accuracy. Indeed, we previously showed by TGA, that the grafted and free polymers have the same number-average molecular weight  $M_n$ . Since SI-ARGET ATRP is based on the same reaction process, the free polymer should be representative of the grafted polymer also in that case. Indeed, some researchers demonstrated by the cleaving method, that the  $M_n$  of free and grafted polymers were consistent with each other.<sup>52</sup>

Compared with the classical ATRP reaction thoroughly described in Chapter 2, the SI-ARGET ATRP is performed in the presence of an excess ascorbic acid as a reducing agent, to ensure steady regeneration of Cu(I) from Cu(II). Moreover, the amount of Cu catalyst is quite low (ppm level) in the SI-ARGET ATRP process. The molar ratio of Cu catalyst to monomer styrene for the SI-ATRP is  $2 \times 10^{-3}$  (2000 ppm), while the molar ratio for the SI-ARGET ATRP is as low as  $2.5 \times 10^{-5}$  (25 ppm). In our experiments, the SI-ATRP reaction was performed for 4 h at 100 °C, while the SI-ARGET ATRP was performed for only 1 h to obtain similar grafting polymer chain length.

The  $M_n$  of free PS obtained after the SI-ATRP and SI-ARGET ATRP treatments (PS1 and PS2, respectively) were measured by GPC and summarized in Table 3.1. The higher value obtained with PS2 indicates that longer PS chains are grafted on CNC with the SI-ARGET ATRP process. Both free PS1 and PS2 display a low dispersity, suggesting that the living radical polymerization was well controlled. Moreover, the polymerization time of ARGET ATRP is much shorter than that of ATRP. Hence, its propagation rate ( $R_p$ ) is much faster. The amount of initiating sites on the surface of CNC-Br being negligible compared to the amount of sacrificial initiator, the theoretical  $M_n$  of the free PS1 and PS2 can be calculated from the monomer conversion and molar ratio of monomer to sacrificial initiator (see Chapter 2). The theoretical  $M_n$  of free PS1 and PS2 are listed in Table 3.1. The agreement between the theoretical values and  $M_n$  measured by GPC indicates that almost all the EBiB introduced reacted by ATRP or ARGET ATRP. The initiating efficiency (IE) of EBiB – calculated as the ratio of theoretical  $M_n$  relative to the  $M_n$  measured by GPC – is 82.4% for ATRP and 99.2% for ARGET ATRP (Table 3.1).

### 3.3.2.2 Characterization of the PS-*g*-CNC hybrids

The successful grafting of PS at the CNC surface was confirmed by FTIR spectroscopy, for both SI-ATRP and SI-ARGET ATRP reactions (Figure 3.1). Compared with CNC-Br, both PS1-*g*-CNC and PS2-*g*-CNC samples display additional infrared vibrations characteristics of the grafted PS in their FTIR spectra: the aromatic C-H stretchings at 3059 cm<sup>-1</sup> and 3025 cm<sup>-1</sup>; the aromatic C=C stretchings at 1600 cm<sup>-1</sup>, 1494 cm<sup>-1</sup> and 1451 cm<sup>-1</sup>; and the out-of-plane aromatic C-H bending at 756 cm<sup>-1</sup> and 700 cm<sup>-1</sup>. To compare the grafting levels between samples, the C-H bending of grafted PS at 700 cm<sup>-1</sup> was normalized to the C-O stretching of cellulose backbone at 1060 cm<sup>-1</sup> (used as an internal standard), through the calculation of the  $I_{700}/I_{1060}$  peak heights ratio.<sup>151</sup> The  $I_{700}/I_{1060}$  ratio of the PS1-*g*-CNC sample is ca. 2.16, while that of PS2-*g*-CNC is about 0.68. The lower value obtained with PS2-*g*-CNC indicates that a lower amount of PS is grafted at the CNC surface with the SI-ARGET ATRP method. Therefore, the surface initiating efficiency (SIE) of CNC-Br is probably lower in that case.

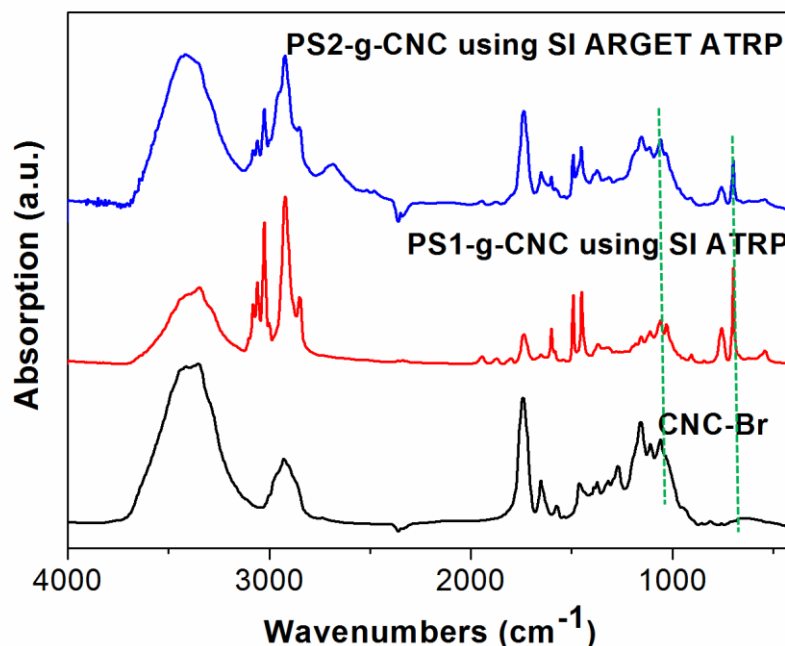


**Figure 3.1.** FTIR spectra of CNC-Br, PS1-*g*-CNC, and PS2-*g*-CNC.

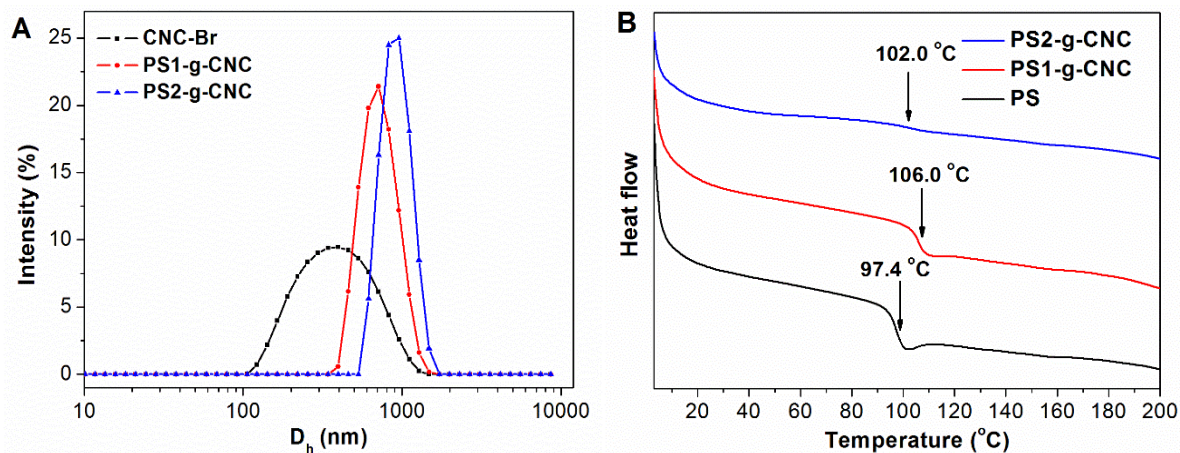


**Figure 3.2. (A) Hydrodynamic diameter distribution by intensity of CNC-Br, PS1-g-CNC and PS2-g-CNC; (B) DSC curves of free PS, PS1-g-CNC, and PS2-g-CNC.**

DLS and DSC were also performed to characterize further the PS1-g-CNC and PS2-g-CNC samples. Figure 3.2A shows the hydrodynamic diameter ( $D_h$ ) distribution by intensity of CNC-Br, PS1-g-CNC, and PS2-g-CNC suspension in THF. The average  $D_h$  of CNC-Br is 377 nm, while that of PS1-g-CNC and PS2-g-CNC are 747 nm and 880 nm, respectively (Table 3.1). As expected, the grafting of PS brushes at the CNC surface leads to an increase in particles size but the dimensions remain in the nanometer range. The higher  $D_h$  obtained with PS2-g-CNC suggests that longer PS chains are grafted when SI-ARGET ATRP is used, which is consistent with the higher  $M_n$  found for free PS in that case. The DSC curves of free PS, PS1-g-CNC, and PS2-g-CNC are shown in Figure 3.2B. Both PS1-g-CNC and PS2-g-CNC show an enhanced glass transition temperature ( $T_g$ ) compared with free PS, due to the anchoring of one end of the grafted polymer. However, this increase is lower with PS2-g-CNC, despite the higher molecular weight of the grafted polymer. According to our previous report (Chapter 2), the  $T_g$  of PS-g-CNC is expected to increase with  $M_n$  for a given grafting density. Therefore, the lower  $T_g$  of PS2-g-CNC can be only explained by the lower grafting density of the samples grafted by SI-ARGET ATRP. Hence, the DSC results further confirm that the SIE of CNC-Br is lower with this method.

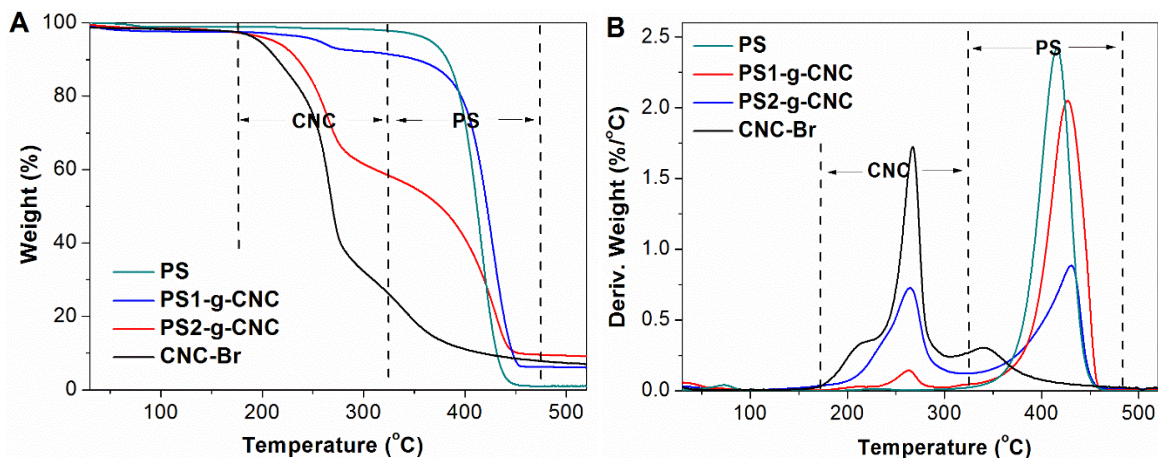


**Figure 3.3.** TGA thermograms (A) and DTG curves (B) of CNC-Br, PS1-g-CNC, and PS2-g-CNC.

The thermal stability of the PS1-g-CNC and PS2-g-CNC samples was evaluated by TGA and compared with the stability of PS and CNC-Br. The thermograms and corresponding DTG derivatives are shown in Figure 3.3. Both PS1-g-CNC and PS2-g-CNC nanomaterials decomposed in two steps. The first weight loss is associated with the decomposition of CNC (from 180 to 320 °C), while the second one is attributed to the decomposition of grafted PS (from 350 to 450 °C). In Chapter 2, we showed that the ratio of the second weight loss relative to the first weight loss represents an accurate estimation of the weight ratio of grafted PS relative to CNC-Br ( $R_w$ ) in the grafted nanocomposites. Compared with the  $R_w$  of PS1-g-CNC (15.8), the  $R_w$  of PS2-g-CNC is only 1.23 (Table 3.1). Since the molecular weight of PS2 is *a priori* higher than that of PS1, this result confirms that the grafting density at the surface of PS2-g-CNC is lower than that of PS1-g-CNC. Assuming that the  $M_n$  of grafted and free PS are similar, the surface initiating efficiency (SIE) of CNC-Br could be calculated from the  $R_w$  of the PS-grafted nanoparticles and  $M_n$  of free PS according to the formula:

$$SIE = R_w \times (M [(C_6H_{10}O_5)_{3.2}(C_4H_6OBr)]) / (M_n \text{ of free PS}),$$

where the molecular composition of CNC-Br is simplified by  $(C_6H_{10}O_5)_{3.2}(C_4H_6OBr)$ ;  $M [(C_6H_{10}O_5)_{3.2}(C_4H_6OBr)] = 668$  g/mol; and  $M_n$  of grafted PS =  $M_n$  of free PS.

After calculation, we find that almost all the initiation Br sites on CNC-Br have reacted with styrene by SI-ATRP (99.8%), while only 6.3% of the sites have reacted by SI-ARGET ATRP (Table 3.1).

### 3.3.3 SI-ATRP and SI-ARGET ATRP grafting of P4VP on CNC

**Table 3.2. Reaction conditions and characteristics of the P4VP-g-CNC hybrid nanomaterials prepared by SI-ATRP or SI-ARGET ATRP.**

Method	SI-ATRP*	SI-ARGET ATRP**
Sample	P4VP1-g-CNC	P4VP2-g-CNC
Catalyst (amount)	CuBr (2000 ppm)	CuBr <sub>2</sub> (25 ppm)
Reducing agent	/	Ascorbic acid
Polymerization time	4 h	1 h
Monomer conversion	13.2%	15.6%
Theoretical M <sub>n</sub> of free P4VP	6930	8190
T <sub>g</sub> of P4VP-g-CNC measured by DSC (°C)	157.5	155.9
N content measured by EA (wt. %)	11.97	6.21
SIE of CNC-Br determined by EA	84.7%	7.1%

\*SI-ATRP of P4VP from CNC-Br with the molar ratio of [4VP]: [EBiB]: [CuBr]: [Me6TREN] =500: 1: 1: 2 at 40 °C for 4 hours

\*\*SI-ARGET ATRP of P4VP from CNC-Br with the molar ratio of [4VP]: [EBiB]: [Ascorbic acid]: [CuBr<sub>2</sub>]: [Me6TREN] =500: 1: 1: 1.25 ×10<sup>-2</sup>: 1.25 ×10<sup>-1</sup> at 40 °C for 1 hour.

To further demonstrate the low SIE of CNC-Br in SI-ARGET ATRP and the accuracy of the thermal analysis method, P4VP was grafted from CNC-Br using both SI-ATRP and SI-ARGET ATRP. P4VP and 4VP are strong coordinating ligands for the Cu catalyst, so it is generally a challenge to achieve a well-controlled polymerization of P4VP by ATRP.<sup>174-178</sup> For these experiments, we also performed the polymerization in the presence of a sacrificial initiator, but the free polymer obtained could not be analyzed by GPC as we could not remove the Cu chelated by the pyridine moieties. The M<sub>n</sub> of the free P4VP was thus estimated from its theoretical value, calculated according to the monomer conversion

measured by  $^1\text{H}$  NMR. On the other hand, the amount of grafted P4VP could be precisely calculated by elemental analysis (EA) owing to the presence of the nitrogen element in P4VP.

The reaction conditions and characteristics of the PS-g-CNC hybrid nanomaterials prepared by SI-ATRP or SI-ARGET ATRP are summarized in Table 3.2. Here again, the SI-ARGET ATRP polymerization is faster than the classical SI-ATRP and leads to the grafting of longer P4VP chains.

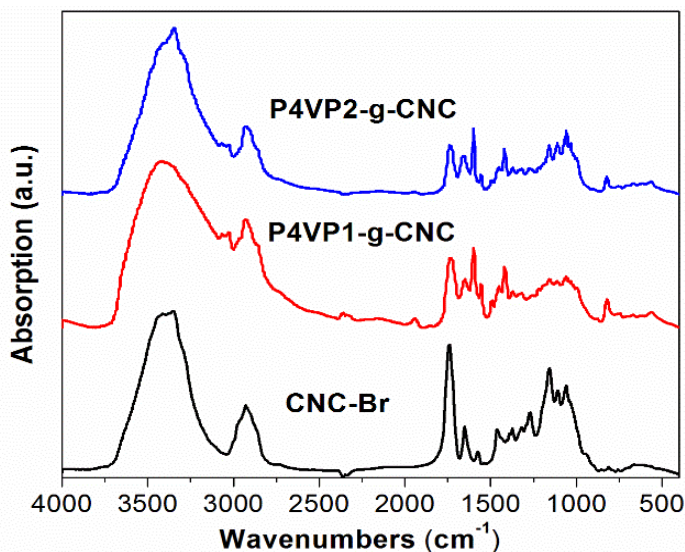


**Figure 3.4.** FTIR spectra of CNC-Br, P4VP1-g-CNC, and P4VP2-g-CNC.

The successful grafting of P4VP was confirmed by FTIR spectroscopy, for both SI-ATRP and SI-ARGET ATRP (Figure 3.4). The FTIR spectra of both P4VP1-g-CNC and P4VP2-g-CNC show additional infrared vibration characteristics of P4VP: the aromatic C=C stretching band at  $1600\text{ cm}^{-1}$ ; and the C=N stretching of the pyridine rings at  $1419\text{ cm}^{-1}$ .<sup>171</sup> The peak height ratio of C=N stretching at  $1419\text{ cm}^{-1}$  normalized to the C-O stretching of cellulose at  $1060\text{ cm}^{-1}$  ( $I_{1419}/I_{1060}$ ) is about 1.18 for P4VP1-g-CNC and 0.72 for P4VP2-g-CNC. Here again, a lower amount of PS is grafted at the CNC surface with the SI-ARGET ATRP method.

Both P4VP1-g-CNC ( $T_g = 157.5\text{ }^\circ\text{C}$ ) and P4VP2-g-CNC ( $T_g = 155.9\text{ }^\circ\text{C}$ ) show an enhanced glass transition temperature compared with free PV4P ( $T_g = 151.6\text{ }^\circ\text{C}$ ), due to the bulking effect imparted by

the grafting (Figure 3.5). The lower  $T_g$  of P4VP2-*g*-CNC compared with P4VP1-*g*-CNC can be once again assigned to the lower grafting density obtained with the SI-ARGET ATRP method.

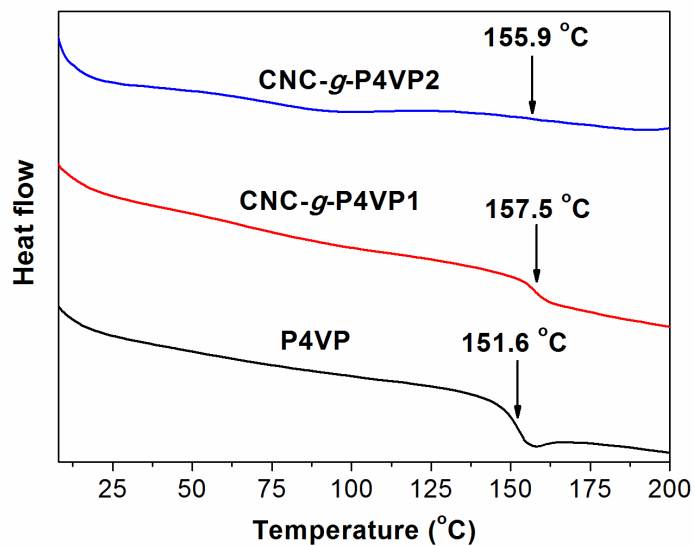


Figure 3.5. DSC curves of P4VP, P4VP1-*g*-CNC, and P4VP2-*g*-CNC.

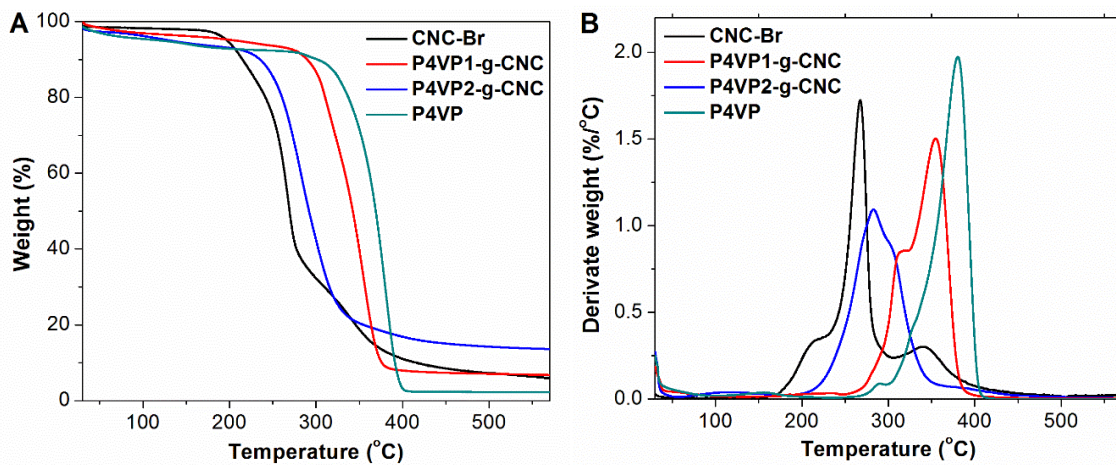


Figure 3.6. TGA thermograms (A) and DTG curves (B) of CNC-Br, P4VP1-*g*-CNC, P4VP2-*g*-CNC and free P4VP.

The TGA results under a nitrogen atmosphere indicate that P4VP decomposes at the temperature range between 300 °C and 400 °C (Figure 3.6). After the grafting, both P4VP1-g-CNC and P4VP2-g-CNC samples display an increased thermal stability compared with that of CNC-Br. The greater increase was obtained with P4VP1-g-CNC, suggesting more P4VP brushes were grafted with the classical ATRP method, in agreement with the FTIR and DSC results. Unlike the PS-grafted CNC, the P4VP-grafted hybrids do not exhibit a two-steps decomposition profile in the TGA thermograms, most probably because the cellulosic material is somehow protected by the surrounding polymer. This may be due to the better interaction expected between P4VP and the hydrophilic CNC. Therefore, the TGA is not a suitable tool to evaluate the surface initiating efficiency of CNC-Br anymore in the P4VP-g-CNC.

Nevertheless, the SIE can still be evaluated from the elemental analysis (EA) of the nitrogen element contained in the P4VP-grafted samples. The N content in P4VP1-g-CNC and P4VP2-g-CNC was found to be ca. 11.97% and 6.21%, respectively (Table 3.2), confirming again that more polymeric material was grafted with the classical ATRP method. The SIE of CNC-Br initiators can be calculated from the EA results based on the formula:

$$14 \times (\text{DP}) \times \text{SIE} / (668 + M_n \times \text{SIE}) = \text{N content by EA (wt. \%)},$$

where 14 is the molecular weight of N;  $M [(C_6H_{10}O_5)_{3.2}(C_4H_6OBr)] = 668$  g/mol, and  $M_n$  is the theoretical molecular weight of grafted P4VP.

After calculation, we find that 84.7% of the initiation Br sites on CNC-Br have reacted with 4VP by SI-ATRP, while only 7.1% of the sites have reacted by SI-ARGET ATRP (Table 3.1). This result is consistent with previous results obtained with PS.

### 3.3.4 Proposed mechanism to account for the different SIE found with SI-ATRP and SI-ARGET ATRP

In SI-ATRP reactions, the surface initiating efficiency may be affected by many factors, such as the surface curvature of the particle, chemical structure and density of the macroinitiators, solvent, propagation rate ( $R_p$ ), catalyst concentration and catalyst-to-deactivator ratio.<sup>63,64,133,179-181</sup> When classical Si-ATRP was performed from CNC-Br, the catalyst concentration was quite high, and the  $R_p$  was relatively low, which favored the initiation of most Br initiating sites at the CNC surface, leading

to a high grafting density and brush-like regime (Figure 3.7).<sup>182</sup> In the SI-ARGET ATRP experiments, excess ascorbic acid was added as a reducing agent, to continually reduce Cu(II) to Cu(I) during the process. Therefore, the catalyst-to-deactivator ratio (Cu(I)/Cu(II)) was much higher in SI-ARGET ATRP than in SI-ATRP, which resulted in a much higher  $R_p$ .<sup>121,165</sup> In addition, the catalyst concentration in SI-ARGET ATRP (25 ppm) was much lower than in SI-ATRP (2000 ppm). As a consequence, the monomer concentration per activation cycles was higher with SI-ARGET ATRP,<sup>64,180</sup> leading to a fast propagation of the first initiated radicals. It is then expected that these grafted chains would shield the neighboring initiating sites,<sup>180</sup> resulting in a low SIE, low grafting density and mushroom-like regime (Figure 3.7).<sup>182</sup>

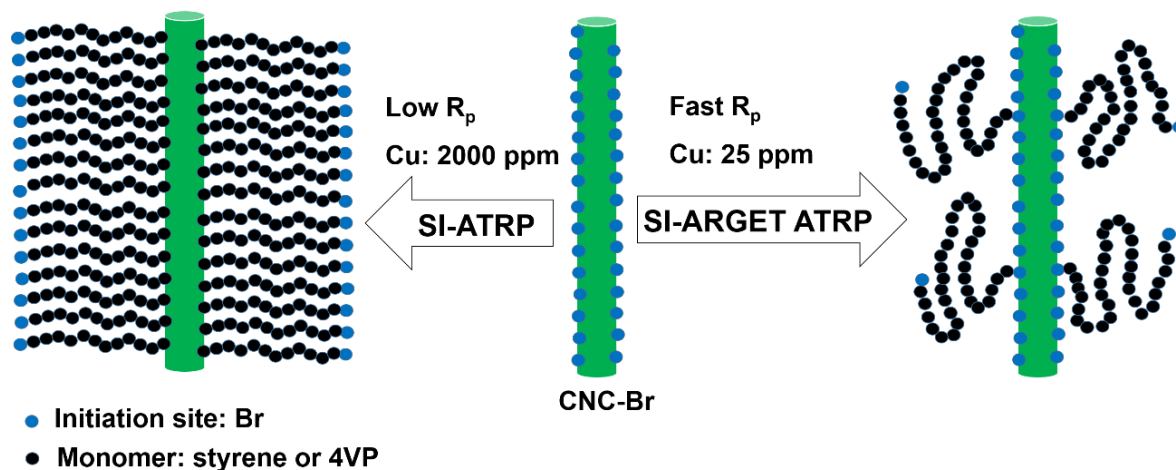


**Figure 3.7. Proposed mechanism to account for the different SIE found with SI-ATRP and SI-ARGET ATRP.**

### 3.4 Conclusions

In this chapter, the efficiencies of the SI-ATRP and SI-ARGET ATRP methods to initiate the grafting of polymer chains at the CNC surface were compared. Br initiating sites were first introduced at the surface of the CNC by esterification with BIBB (CNC-Br) and subsequently reacted with styrene (St) or 4-vinylpyridine (4VP) in the presence of a sacrificial initiator. The surface initiating efficiencies (SIE) of the CNC-Br macroinitiators with regards to St or 4VP were evaluated by TGA and EA, respectively. The combination of analytical methods such as FT-IR, DLS, DSC, TGA, and EA

demonstrated that the SI-ARGET ATRP reaction favored the grafting of longer polymer chains with lower grafting densities compared with the classical SI-ATRP method. While almost all initiating sites on CNC-Br reacted by SI-ATRP, only 6-7% of the sites reacted by SI-ARGET ATRP, with both St and 4VP. This result was assigned to the low catalyst concentration at stake in the SI-ARGET ATRP process and the high  $R_p$  of the reaction, which presumably resulted in a mushroom-like regime at the surface of the CNC. Distinctively, a brush-like regime was favored with classical SI-ATRP due to the higher catalyst concentration and lower  $R_p$ .

## **Chapter 4**

# **Recyclable Gold Nanoparticles Stabilized by Poly(4-vinylpyridine) Grafted Cellulose Nanocrystals for the Efficient Catalysis of 4-Nitrophenol Reduction**

pH-responsive poly(4-vinylpyridine) (P4VP) grafted cellulose nanocrystals (CNC) nanohybrids (P4VP-*g*-CNC) were prepared by Surface-Initiated Atom Transfer Radical Polymerization (SI-ATRP) and subsequently used to stabilize gold nanoparticles (Au NPs) and produce recyclable catalysts. The presence of P4VP brushes at the CNC surface led to the growing of Au NPs of lower averaged diameter compared with the diameter of the Au NPs deposited on pristine CNC. The catalytic performance of pristine Au NPs, Au@CNC and Au@P4VP-*g*-CNC was then compared, through the measurement of the turnover frequency (TOF) obtained after catalytic reduction of 4-nitrophenol (4NP), used as a model reaction. Compared with pristine Au NPs, the catalytic activity of Au@CNC and Au@P4VP-*g*-CNC were about 10 and 24 times better, respectively. Moreover, the Au@P4VP-*g*-CNC material could be conveniently recovered by flocculation at pH > 5, and the recycled catalyst remained highly active.

## 4.1 Introduction

Metal and metal oxide nanoparticles (NPs) have attracted increasing attention in recent decades due to their outstanding properties and extensive applications in the field of biosensors, catalysis, antimicrobials, and optoelectronics.<sup>72,79,123,183-187</sup> Among various metal and metal oxide NPs, Au NPs are one of the most interesting NPs owing to their high catalytic activity in a variety of chemical reactions.<sup>188</sup> However, Au NPs are prone to aggregation due to their huge specific surface area.<sup>187</sup> The catalytic activity of Au NPs is size-dependent and tends to decrease with increasing agglomeration. Therefore, stabilizers are commonly required to enhance the stability of the NPs. Among various inorganic and organic stabilizers,<sup>76,183,189,190</sup> nature derived materials, especially polysaccharides, are attractive due to the increasing concerns about environmental impacts and sustainable development.<sup>74,190,191</sup>

Cellulose nanocrystals (CNC) are bio-based nanoparticles produced by sulfuric acid hydrolysis of cellulosic substrates such as microcrystalline cellulose, paper or pulp.<sup>2,3,10</sup> These rod-shaped nanoparticles are renewable, biocompatible, display a high tensile strength and elastic modulus, have a low density and low coefficient of thermal expansion, and tend to self-assemble in the form of nematic phases.<sup>4,9,26,28,192-194</sup> As a result, CNC offer an array of properties, which can be exploited in the field of cosmetics, emulsions, electronics, liquid crystals, reinforcing nano-fillers, foods, and catalysts.<sup>7,67,68,70,72,164,195-198</sup> In particular, CNC have demonstrated their efficiency as stabilizers for many metal NPs, such as Pd,<sup>83</sup> Ag,<sup>79,81,82,184</sup> CuO,<sup>73</sup> Au,<sup>72,82</sup> and Ag-Au alloy.<sup>80</sup> Although the large specific surface area and stability of the CNC in water can help improve the stability of metal NPs, there are no specific metal ligands on CNC. The introduction of metal binding groups on the surface of CNC is therefore necessary to further increase the stability of Au NPs.

Poly(4-vinylpyridine) (P4VP) displays several interesting properties, including a good affinity for metals and a pH-responsive solubility in water.<sup>171-174,199</sup> Therefore, P4VP-grafted CNC (P4VP-*g*-CNC) can coordinate with Au NPs and act as stabilizers for these nanoparticles (Au@P4VP-*g*-CNC). Moreover, the pH-responsive solubility of P4VP can facilitate the recovery of Au@P4VP-*g*-CNC under mild condition. Since the  $pK_a$  of P4VP is about 5, the polymer is protonated and water-soluble at  $pH < 5$ , while deprotonated and hydrophobic at  $pH > 5$ .<sup>171,200-202</sup> Surface-Initiated Atom Transfer Radical

Polymerization (SI-ATRP) is a “grafting from” method, which allows the preparation of polymer-grafted nanoparticles with quite a good control.<sup>39,46,123,126,133,203</sup> The method has been recently applied to modify the surface of CNC with polystyrene (PS),<sup>46</sup> poly(*tert*-butyl acrylate) (PtBA),<sup>55</sup> poly(*N*-isopropyl acrylamide) (PNiPAAm),<sup>44</sup> and poly(oligo(ethylene glycol) methacrylate) (POEGMA).<sup>51</sup> It could therefore be used as an efficient tool to graft P4VP polymers at the CNC surface.

In this context, P4VP-*g*-CNC nanohybrids were prepared by SI-ATRP and subsequently used to stabilize gold nanoparticles (AuNPs). The catalytic activity and recyclability of the material obtained (Au@P4VP-*g*-CNC) was then investigated and compared with that of AuNPs stabilized by pristine CNC (Au@CNC). The catalytic performance of pristine Au NPs, Au@CNC and Au@P4VP-*g*-CNC was then compared, through the measurement of the turnover frequency (TOF) obtained in the catalytic reduction of 4-nitrophenol (4NP), used as a model reaction. The possibility of recycling the Au@CNC and Au@P4VP-*g*-CNC catalysts was finally discussed.

## 4.2 Experimental

### 4.2.1 Material and instrumentation

CNC were purchased from the University of Maine. Acetic acid, HAuCl<sub>4</sub>, NaBH<sub>4</sub>, 4-nitrophenol (4NP), CuBr, tris [2-(dimethylamino)ethyl]amine (Me<sub>6</sub>TREN), disodium ethylenediaminetetraacetate dihydrate, ethylenediaminetetraacetic disodium salt (EDTA-Na<sub>2</sub>) and calcium hydride were purchased from Sigma-Aldrich. Ethyl  $\alpha$ -bromoisobutyrate (EBiB),  $\alpha$ -bromoisobutyryl bromide (BIBB) and 4-vinylpyridine (4VP) were purchased from Alfa Aesar. 4-Dimethylaminopyridine (DMAP) and triethylamine (TEA) were purchased from Fisher. CuBr was purified by acetic acid at 80 °C under N<sub>2</sub> for 24 h, and washed with acetic acid and dried under vacuum at 50 °C. 4VP was purified by distillation in calcium hydride under reduced pressure and stored at -20 °C. All the other chemicals were used as received.

Fourier transform infrared spectroscopy (FTIR) was performed using the Thermo Nicolet Avatar 970 FTIR spectrometer at a resolution of 8 cm<sup>-1</sup> (64 scans).

Ultraviolet–visible (UV-vis) spectra were obtained on an Agilent Model 8453 UV-vis spectroscopy system.

$^1\text{H}$  NMR ( $\text{CDCl}_3$ ) spectra were recorded using a Bruker AC- 400 NMR at room temperature.

TEM was conducted using a Philips CM10 at an acceleration voltage of 60 keV. The TEM samples were prepared by placing a drop of the sample on the copper grid (200 mesh coated with copper) and allowed to dry overnight at ambient temperature. The CNC aqueous dispersion for TEM analysis was stained using  $\text{FeCl}_3$ . The TEM sample of CNC-Br was prepared from DMF dispersion, and the TEM samples of P4VP-*g*-CNC and Au@P4VP-*g*-CNC were prepared from aqueous dispersion at pH = 2.

#### **4.2.2 Preparation of the brominated CNC nano-initiator: CNC-Br**

CNC-Br was prepared by modifying the surface of CNC with BIBB. CNC (1.2 g) was dispersed in DMF (100 mL) by sonication. Then TEA (3.1 mL, 22.2 mmol) and DMAP (1.36 g, 11.1 mmol) were added. The solution of BIBB (1.36 mL, 11.1 mmol) in DMF (20 mL) was added dropwise to the dispersion of CNC kept in an ice bath. After 24 h,  $\text{H}_2\text{O}$  was added, and the resultant CNC-Br was recovered by centrifugation and subsequently washed with THF for 24 h using a Soxhlet extractor. The product was further dialyzed against deionized  $\text{H}_2\text{O}$  for 5 days. Finally, the purified CNC-Br was obtained via freeze-drying.

#### **4.2.3 Preparation of P4VP-*g*-CNC by SI-ATRP**

First, CuBr (72 mg, 0.5 mmol) was added into a Schlenk flask in the glove box. CNC-Br (1 g) was dispersed in DMF (43.9 g, 600 mmol) via sonication. Then  $\text{Me}_6\text{TREN}$  (0.54 mL, 2 mmol), 4VP (5.26 g, 50 mmol), and EBiB (74  $\mu\text{L}$ , 0.5 mmol) were added to the suspension and purged with argon for 20 mins. The suspension was subsequently transferred to the Schlenk flask under the argon environment. After three freeze-pump-thaw cycles, the polymerization was initiated at 40  $^\circ\text{C}$ . The polymerization was terminated after 2 h by exposing the polymerization mixture to air. The monomer conversion was calculated according to the  $^1\text{H}$  NMR in  $\text{CDCl}_3$  and was ca. 23.1%. As the sacrificial initiating sites on CNC-Br are negligible when compared to the sacrificial initiators, the theoretical degree of polymerization of the P4VP can be calculated from the monomer conversion and is about 23. P4VP-*g*-CNC was collected via the centrifugation of the polymerization mixture and washed with ethanol three times to remove the free polymers. The catalyst residues were removed via dialysis in EDTA- $\text{Na}_2$  water

solution for 6 days and then in deionized water for 6 days. The final product was obtained by freeze-drying.

#### **4.2.4 Preparation of the catalysts dispersions: pristine Au NPs, Au@CNC, and Au@P4VP-g-CNC**

The Au@CNC and Au@P4VP-g-CNC catalysts dispersions were prepared using the same procedure. A water solution of HAuCl<sub>4</sub> (1 mL, 1 mM) was added to 5 mL aqueous dispersion (pH = 2, adjusted using HNO<sub>3</sub>) of CNC (1 mg/mL) or P4VP-g-CNC (1 mg/mL), respectively. The resultant dispersions were stirred for 12 h, and excess NaBH<sub>4</sub> (1 mL, 10 mM) was added during stirring. Both dispersions turned red immediately, and the dispersions were kept under stirring for another 2 h. Pristine Au NPs dispersion was prepared using the same procedure without any stabilizer. After the addition of NaBH<sub>4</sub>, the solution turned black in 1 min, and after stirring for 30 min, the mixture became colorless due to the aggregation of Au NPs.

#### **4.2.5 Evaluation of the catalytic performance of pristine Au NPs, Au@CNC, and Au@P4VP-g-CNC**

The reduction of 4NP by NaBH<sub>4</sub> was used as a model reaction to compare the catalytic performance of pristine Au NPs, Au@CNC, and Au@P4VP-g-CNC, the reaction requiring the utilization of a catalyst like gold NPs. The molar ratio of [Au]: [4NP]: [NaBH<sub>4</sub>] was fixed at 1:100:10000 for all reactions.

NaBH<sub>4</sub> (5.7 mg, 0.15 mmol, 100 equivalents per 4NP) was added to a 4NP water solution (3 mL, 0.5 mM), and then was transferred to a quartz cell. The catalyst suspension (105 μL, corresponding to 100 equivalents 4NP per gold atom) was then added, and the mixture was vortexed for 10 s. The UV-vis absorption of the mixture was then recorded to monitor the reaction process.

For the recyclability tests, the Au@CNC or Au@P4VP-g-CNC catalyst dispersion (0.5 mL) was employed to catalyze the reduction of 5 mL 4NP water solution (0.5 mM). After 3 h, the catalyst was recovered via centrifugation. The recovered catalyst was again dispersed in H<sub>2</sub>O (0.5 mL, pH = 2) and the catalytic properties of the recovered Au@CNC or Au@P4VP-g-CNC nanoparticles were evaluated again using the same procedure.

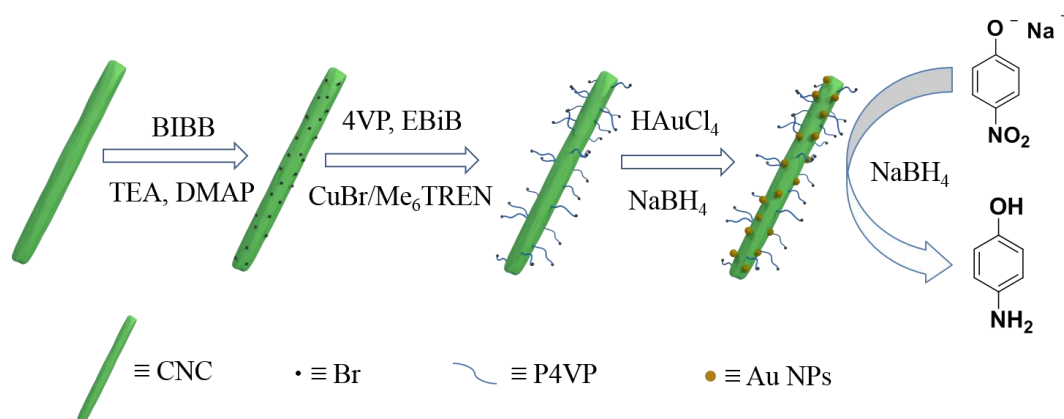
## 4.3 Results and discussion

### 4.3.1 Preparation and characterization of P4VP-g-CNC

The schematic illustrating of preparation of the Au@P4VP-g-CNC as catalysts for the reduction of 4NP is presented in Scheme 4.1.

The CNC used in this study were isolated by sulfuric acid hydrolysis of wood pulp, according to a general procedure described in the literature.<sup>16,149</sup> They consist of rod-like particles with estimated dimensions of  $110.3 \pm 47.7$  nm in length and  $4.8 \pm 1.1$  nm in diameter, based on a former study performed with particles taken from the same batch (estimated from AFM pictures).<sup>28</sup> The amount of accessible hydroxyl groups at their surface was estimated to be  $3.10 \pm 0.11$  mmol.g<sup>-1</sup>, using a method based on phosphorylation coupled with <sup>31</sup>P NMR and FT-IR analysis.<sup>28</sup> The CNC are also negatively charged (zeta-potential in water = -48 mV) due to the presence of sulfate ester groups at the surface, imparted by the sulphuric acid treatment.

**Scheme 4.1. Schematic illustrating of preparation of the Au@P4VP-g-CNC as catalysts for the reduction of 4NP**



Br initiating sites were first introduced at the surface of the CNC by esterification with BIBB, as shown in Scheme 4.1. The resultant CNC-Br material was characterized by FTIR. As shown in Figure 4.1, CNC-Br displays the expected carbonyl stretching vibration of the grafted ester moieties at  $1739$  cm<sup>-1</sup>, confirming the successful modification of the CNC.<sup>31,51,59</sup> The SI-ATRP grafting of P4VP from CNC-

Br was conducted at 40 °C, in the presence of ethyl  $\alpha$ -bromoisobutyrate (EBiB) as sacrificial initiator, as shown in Scheme 4.1. The successful grafting of P4VP on CNC was also confirmed by the FTIR spectra (Figure 4.1). Compared to CNC-Br, the P4VP-g-CNC hybrid displays additional infrared vibrations characteristic of the pyridine ring at 1600  $\text{cm}^{-1}$  (C=C stretchings), 1419  $\text{cm}^{-1}$  (C=N stretching) and 817  $\text{cm}^{-1}$  (out-of-plane C-H bendings).<sup>148,171</sup>

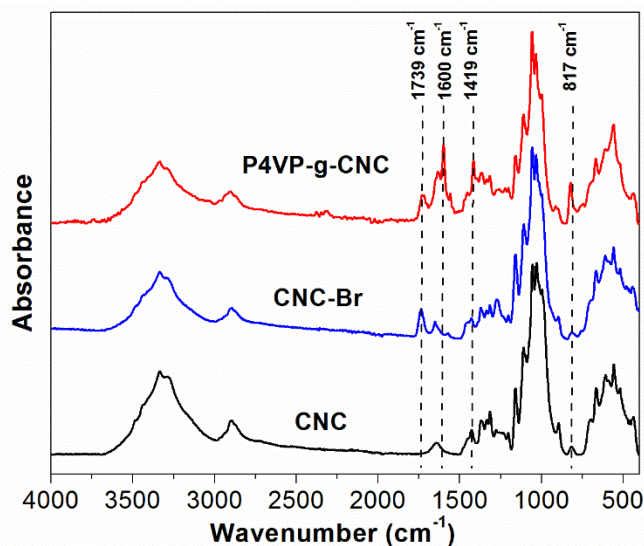


**Figure 4.1. FTIR spectra of CNC, CNC-Br, and P4VP-g-CNC.**

The hydrodynamic diameter ( $D_h$ ) of the CNC and P4VP-g-CNC nanoparticles in water at pH = 2, was evaluated using DLS. The  $D_h$  distributions by intensity are shown in Figure 4.2A. The average  $D_h$  of pristine CNC is about 99 nm, while that of P4VP-g-CNC is about 405 nm. As expected, the grafting of P4VP at the CNC surface leads to an increase in particles size, but the dimensions remain in the nanometer range. Part of this increase could also arise from the partial flocculation of the modified particles in water.<sup>31</sup> The evolution of the average  $D_h$  and Zeta-potential of the P4VP-g-CNC suspension is reported as a function of pH in Figure 4.2B. We observe a significant decrease in Zeta-potential with a concurrent increase in average  $D_h$  (from 410 nm to 2300 nm) when the pH is incremented from 4 to 6. At low pH, the P4VP grafted at the CNC surface is in its protonated form, and the positively charged hybrids form stable dispersions in water, by electrostatic repulsion. When the pH augments, the particles are progressively deprotonated, which leads to their increasing flocculation and increasing  $D_h$ .

This result confirms the successful grafting of P4VP at the CNC surface and the pH-responsiveness of the P4VP-g-CNC nanoparticles. The negative potential zeta measured at pH 10 is assigned to the remaining sulfate ester groups decorating the P4VP-g-CNC surface.

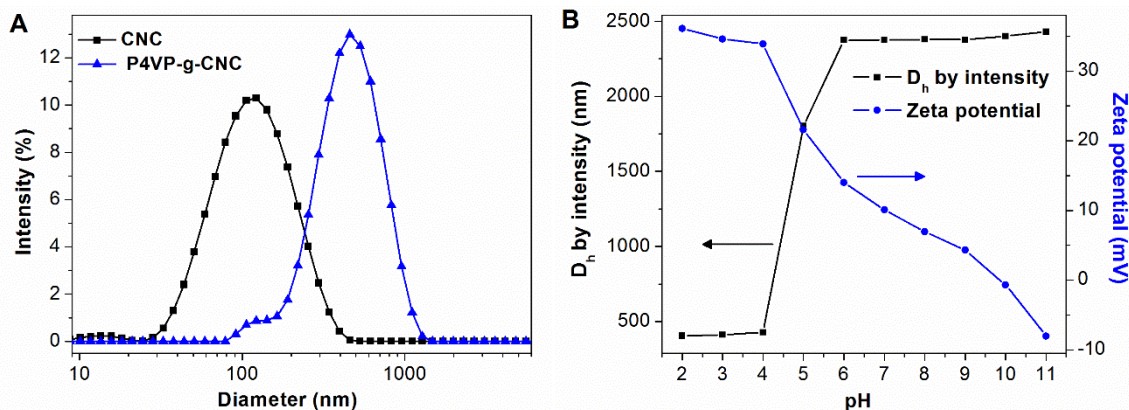


**Figure 4.2.** (A) Hydrodynamic diameter ( $D_h$ ) distribution by intensity of the CNC (■) and P4VP-g-CNC (▲) dispersed in water (pH = 2); (B) Evolution of the average  $D_h$  (■) and Zeta potential (●) of the P4VP-g-CNC suspension as a function of pH.

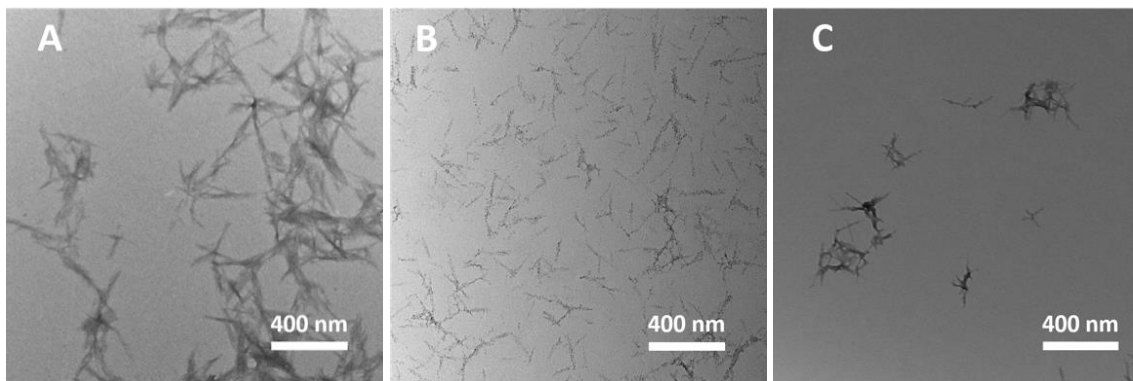


**Figure 4.3.** The TEM images of CNC (A), CNC-Br (B), P4VP-g-CNC (C)

The morphologies of pristine CNC, CNC-Br and P4VP-g-CNC were compared by TEM in Figure 4.3. The pristine CNC consist in rod-like particles, which are slightly aggregated due to the addition of  $\text{FeCl}_3$  before analysis, to stain the particles. Therefore, it is difficult to have an accurate evaluation of their size from the TEM pictures. As CNC-Br could not be dispersed in water, the TEM pictures were

taken from suspensions in DMF, the particles being highly dispersible in this solvent. After modification by BIBB, the rod-like morphology of the cellulose nanocrystals is retained and the dimensions of CNC-Br estimated from the TEM images are ca.  $189 \pm 49$  nm in length and  $8.0 \pm 2.8$  nm in diameter (aspect ratio  $\sim 19.5$ ). The TEM pictures of P4VP-*g*-CNC were taken from water suspensions at pH = 2. Like the CNC, CNC-Br are slightly aggregated and it is difficult to evaluate the size of CNC-Br, but their nano-dimensions and rod-shape are preserved.

### 4.3.2 The preparation and characterization of the Au@ P4VP-*g*-CNC catalyst

#### 4.3.2.1 Synthesis of the Au NPs reference catalyst

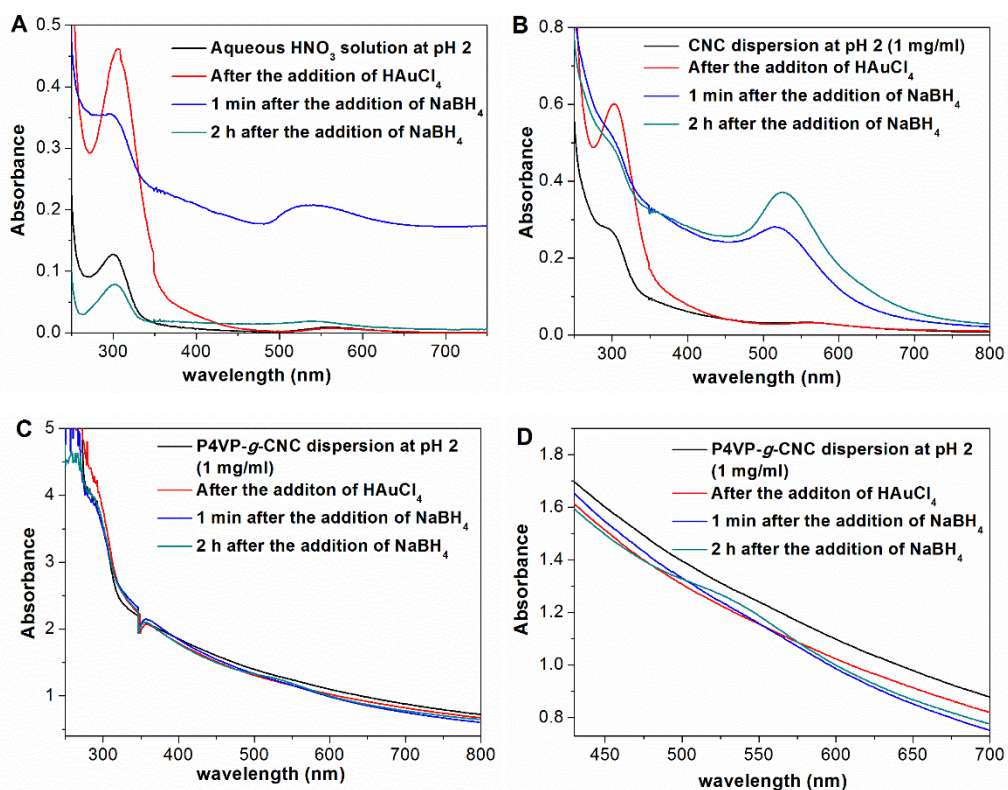


**Figure 4.4. UV-Vis absorbance spectra of the reaction medium during the preparation of Au NPs (A), Au@CNC (B) and Au@P4VP-*g*-CNC (C and D).**

Pristine Au NPs were first synthesized without any stabilizer and used as reference catalyst.  $\text{HAuCl}_4$  was reduced by sodium borohydride ( $\text{NaBH}_4$ ) in acidic water ( $\text{pH} = 2$ , tuned by  $\text{HNO}_3$ ), and the reaction was monitored by UV-Vis spectroscopy. As shown in Figure 4.4A, the initial aqueous  $\text{HNO}_3$  solution displays an absorbance band at 300 nm assigned to the UV absorption of the  $\text{NO}_3^-$  ions. After addition of the  $\text{HAuCl}_4$  solution, the spectrum exhibits a more intense absorption at 305 nm, corresponding to the ligand to metal charge transfer (LMCT) bands of  $\text{HAuCl}_4$ .<sup>204,205</sup> When  $\text{NaBH}_4$  was subsequently added in excess, the colorless solution turned immediately black (Figure 4.5B). In the UV-Vis spectrum recorded 1 min after the addition of  $\text{NaBH}_4$ , the intensity of the LMCT band decreased, while a new band – attributed to the surface plasmon resonance (SPR) of Au NPs – emerged at 534 nm, confirming the reduction of  $\text{HAuCl}_4$  to Au NPs.<sup>39,186,204,206</sup> Two hours later, the black dispersion became colorless again due to the sedimentation of large Au agglomerates (Figure 4.5C), and both the LMCT and SPR bands disappeared (Figure 4.4A). Therefore, all the  $\text{HAuCl}_4$  was reduced to Au NPs after 2h, but the synthesized nanoparticles also quickly aggregated and sedimented in the absence of a stabilizer.

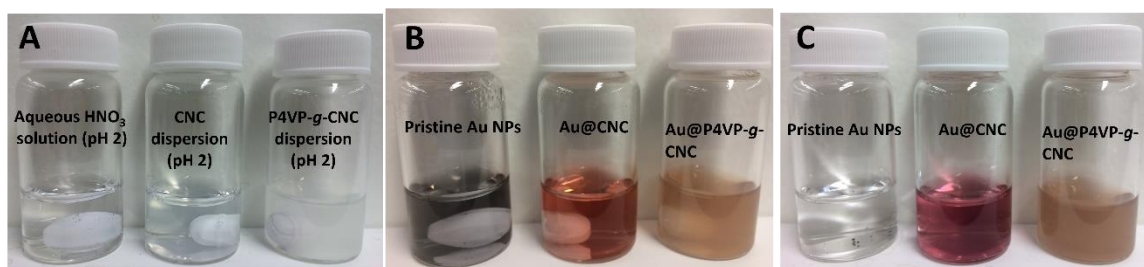


**Figure 4.5. Photographs of the reaction medium during the preparation steps of the Au NPs, Au@CNC and Au@P4VP-g-CNC catalysts. Photographs were taken before (A), 1 min after (B) and 2 hours after (C) the addition of  $\text{NaBH}_4$ .**

#### 4.3.2.2 Synthesis of the Au@CNC and Au@P4VP-g-CNC catalysts

Both CNC and P4VP-g-CNC nano-rods were subsequently tested as stabilizers for Au NPs. The CNC dispersion (1 mg/mL;  $\text{pH} = 2$ ) is colorless (Figure 4.5A) and its UV-Vis spectrum displays the absorbance band of  $\text{NO}_3^-$  at 300 nm (Figure 4.4B). After the addition of  $\text{HAuCl}_4$ , the LMCT absorption is again observed at 305 nm. The mixture was stirred for 12 h. When  $\text{NaBH}_4$  was added at this point, the dispersion became red within few seconds (Figure 4.5B). The intensity of the LMCT band in the

UV-Vis spectrum recorded after 1 min decreased, while the SPR band of Au NPs emerged at 516 nm, confirming the reduction of  $\text{HAuCl}_4$  to Au NPs. After continuous stirring for 2 h, the LMCT absorbance further decreased, while the SPR signal increased, indicating that more Au NPs were formed. In the meantime, the SPR peak of Au NPs was red-shifted from 516 to 525 nm, suggesting that the size of Au NPs concurrently increased.<sup>72,82,207</sup>

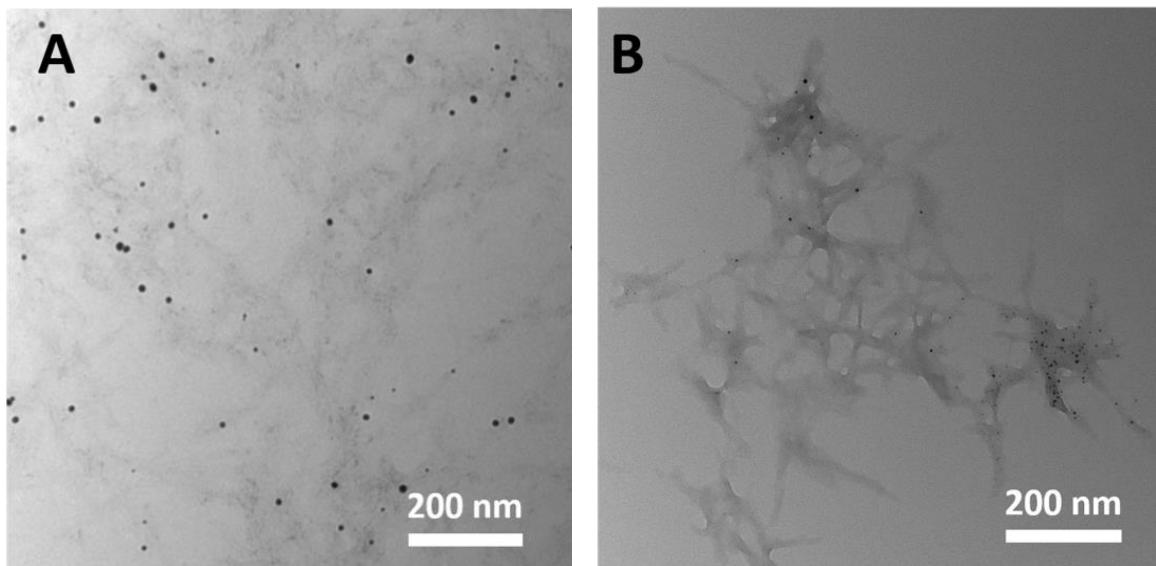


**Figure 4.6. The TEM images of Au@CNC (A) and Au@P4VP-g-CNC (B)**

The P4VP-g-CNC dispersion (1 mg/mL; pH = 2) is opalescent (Figure 4.5A) and displays a relative strong absorbance in the UV-visible region (Figure 4.4C), which complicates the interpretation of the spectra. After the addition of  $\text{HAuCl}_4$ , the absorbance increased slightly in the UV range corresponding to the LMCT, but it decreased slightly in the range of visible light due to the dilution of the P4VP-g-CNC suspension. When  $\text{NaBH}_4$  was added, the dispersion became light brown within a few seconds (Figure 4.5B). The intensity of the LMCT band in the UV-Vis spectra decreased, but the SPR band started to be visible only after 2h, in the form of a weak signal in the range of 480 to 580 nm (Figure 4.4D). The SPR band of Au@P4VP-g-CNC was at about 509 nm, which was determined by the peak of the first derivative curve of the UV-Vis spectra. Compared with the SPR band of Au@CNC at 525

nm, the SPR signal of Au@P4VP-*g*-CNC is blue-shifted to 509 nm, suggesting that the gold nanoparticles stabilized by P4VP-*g*-CNC are smaller than the one stabilized by CNC.<sup>82,207</sup>

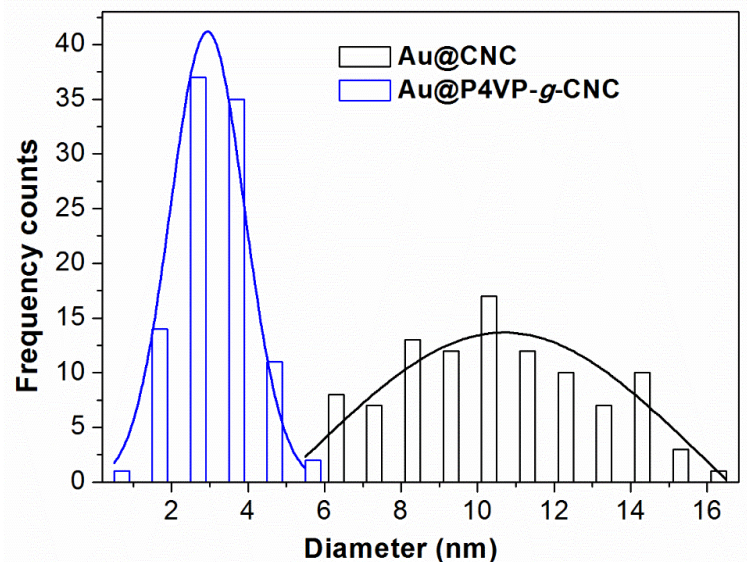


**Figure 4.7. Size distribution of Au NPs in Au@CNC and Au@P4VP-*g*-CNC.**

The successful deposition of Au nanoparticles on the CNC and P4VP-*g*-CNC substrates was evidenced by TEM, in the form of black dots (Figure 4.6). The size distribution of these particles was then estimated from the TEM pictures (Figure 4.7). The Au NPs in Au@P4VP-*g*-CNC are much smaller than those in Au@CNC. The average diameter of the gold nanoparticles is 10.6 nm in Au@CNC and only 2.9 nm in Au@P4VP-*g*-CNC. Both CNC and P4VP-*g*-CNC nano-rods are therefore efficient in stabilizing Au NPs, but aggregation is prevented more efficiently with P4VP-*g*-CNC.

#### **4.3.3 Catalytic performance and recyclability of Au@ P4VP-*g*-CNC**

The reduction of 4-nitrophenol (4NP) is considered as an ideal model reaction to evaluate the catalytic activity of various metallic nanoparticle systems.<sup>72,183,184,208,209</sup> Moreover, this reaction is important in industry because 4NP is a common pollutant found in industrial wastewater or agricultural runoff, and the reduced product (4-aminophenol, 4AP) can be used as an antipyretic drug.<sup>74,76,184</sup> Here, the reduction of 4NP by NaBH<sub>4</sub> was used as a model reaction to compare the catalytic performance of pristine Au NPs, Au@CNC and Au@P4VP-*g*-CNC. The molar ratio of [Au NPs]: [4NP]: [NaBH<sub>4</sub>] was fixed at

1:100:10000 for all reactions and the kinetics were monitored by UV-vis absorption. The 4NP/NaBH<sub>4</sub> solution displays a strong absorption peak at 403 nm, attributed to the formation of 4-nitrophenolate ions after reaction with NaBH<sub>4</sub>, which was used to test the kinetics of the catalysis.<sup>82,184</sup>

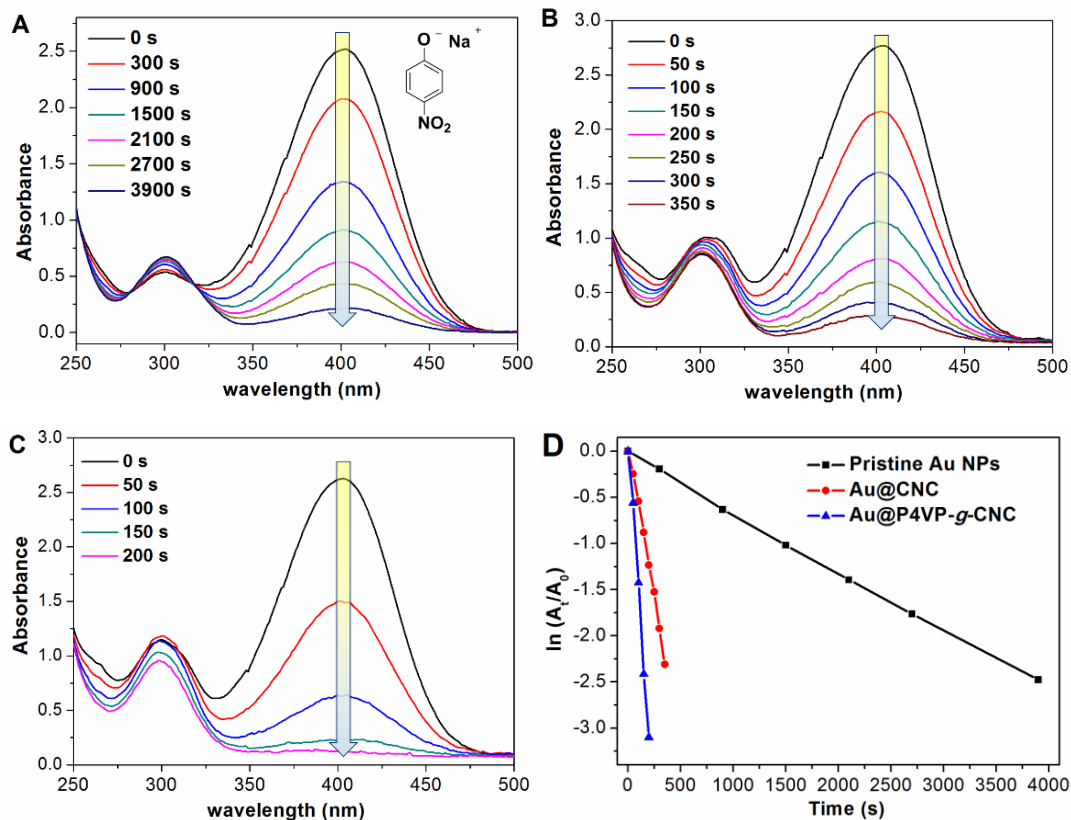


**Figure 4.8.** Time-dependent UV-vis absorption spectra of the reaction medium during the 4NP reduction catalyzed by (A) pristine Au NPs, (B) Au@CNC, and (C) Au@P4VP-g-CNC and evolution of  $\ln(A_t/A_0)$  with time (D).

The time-dependent UV-vis absorption spectra of the reaction medium during the 4NP reduction catalyzed by Au NPs, Au@CNC or Au@P4VP-g-CNC are shown in Figure 4.8. Regardless of the catalyst, we observe a decrease in the 403 nm absorption with time, confirming the gradual reduction of 4NP into 4AP. As the reaction medium was already vortexed for 10 s before performing the UV-Vis, the reaction medium exhibited an absorption peak at 301 nm even at  $t = 0$  s, corresponding to the

absorption band of 4AP. Since the reduction proceeds with an excess of  $\text{NaBH}_4$  (100 equivalents per 4NP), a first-order Langmuir-Hinshelwood kinetics is expected for this reaction.<sup>184</sup> To verify this point,  $\ln(A_t/A_0)$  was plotted as a function of reaction time, where  $A_0$  and  $A_t$  represent the absorbances at  $t = 0$  and  $t$ , for the 403 nm wavelength (Figure 4.8D). The excellent linear relationship obtained with all catalysts indicates that the Langmuir-Hinshelwood apparent first-order is appropriate to describe the kinetics. The apparent rate constant,  $k_{\text{app}}$ , was calculated as the inverse of the slope of the linear plot of  $\ln(A_t/A_0)$  versus time. The turnover frequency (TOF, defined as the number of moles of 4NP reduced per mole of catalyst per hour) could then be evaluated from  $k_{\text{app}}$ , to compare the catalytic performance of the three catalysts.<sup>72,184</sup> The TOF of pristine Au NPs is  $233.5 \text{ h}^{-1}$ , while those of Au@CNC and Au@P4VP-*g*-CNC are  $2275.2 \text{ h}^{-1}$  and  $5533.2 \text{ h}^{-1}$ , respectively. Compared with pristine Au NPs, the catalytic activity of Au@CNC and Au@P4VP-*g*-CNC are about 10 times and 24 times better, respectively. The significant improvement in the catalytic efficiency obtained with Au@P4VP-*g*-CNC was assigned to the much smaller size of gold nanoparticles stabilized by the P4VP-*g*-CNC nano-rods.

Recycling the Au NPs is an important concern in industrial applications when considering the cost of such nanoparticles. The pH-responsive solubility of P4VP can facilitate the recovery of Au@P4VP-*g*-CNC under mild condition. Figure 4.9A shows the schematic illustrating the recovery of Au@CNC and Au@P4VP-*g*-CNC. The excess use of  $\text{NaBH}_4$  leads to a basic condition of the reaction medium ( $\text{pH} = 9.6$ ). Due to the pH dependent solubility of P4VP in water, the Au@P4VP-*g*-CNC material is expected to flocculate when  $\text{pH} > 6$ . However, the reduction of 4NP catalyzed by Au@P4VP-*g*-CNC still followed the Langmuir-Hinshelwood apparent first-order, suggesting that almost no Au@P4VP-*g*-CNC was flocculated during the short catalysis process (200 s). We did not observe any flocculation of Au@P4VP-*g*-CNC even after half an hour. After 3 hours, the Au@P4VP-*g*-CNC had precipitated spontaneously from the reaction medium. On the other hand, a high-speed centrifugation step (8000 rpm) of 10 mins was required to recover the Au@CNC catalyst.

The catalytic performance of the recovered Au@CNC and Au@P4VP-*g*-CNC materials was then evaluated again, using the same reduction procedure. The time-dependent UV-vis absorption spectra of the reaction medium during the 4NP reduction catalyzed by recycled Au@CNC and Au@P4VP-*g*-CNC are shown in Figure 4.9B and Figure 4.9C, respectively. Here again we observe a decrease in the

403 nm absorption with time, confirming the gradual reduction of 4NP into 4AP. The TOF of recycled Au@CNC and Au@P4VP-*g*-CNC catalysts, determined from the  $\ln(A_t/A_0)$  vs. time curves ( Figure 4.9D), was ca. 849.6 h<sup>-1</sup> and ca. 3124.8 h<sup>-1</sup>, respectively. The catalytic efficiency was therefore reduced with both catalyst but still remained high in the case of Au@P4VP-*g*-CNC, confirming the interest of our approach.

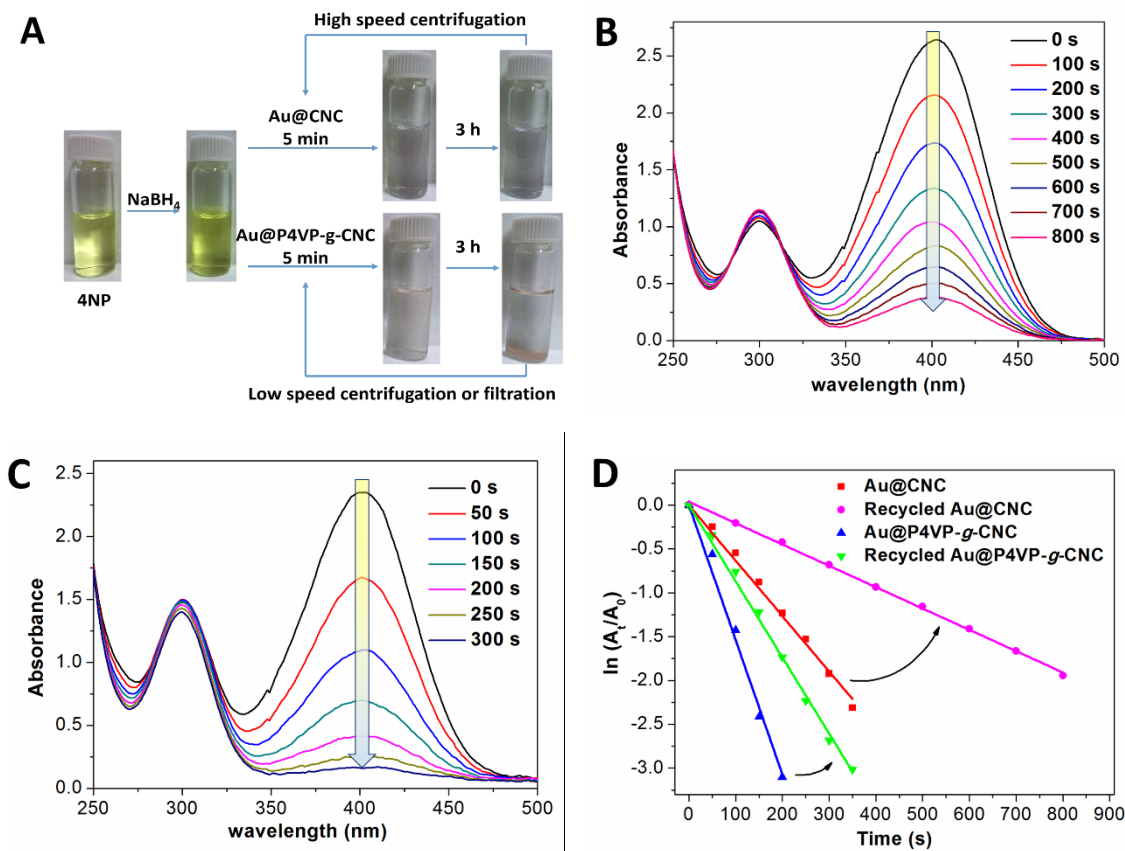


**Figure 4.9.** (A) Schematic illustrating the recovery of Au@CNC and Au@P4VP-*g*-CNC; Time-dependent UV-vis absorption spectra of 4NP reduced by NaBH<sub>4</sub> catalyzed by recycled Au@CNC (B) and recycled Au@P4VP-*g*-CNC (C); (D) shows the plots of  $\ln(A_t/A_0)$  against time for the reduction of 4NP with different catalysts.

The catalytic performance of Au@CNC and Au@P4VP-*g*-CNC for the reduction of 4NP was compared with those of other catalytic systems in Table 4.1. The Au@P4VP-*g*-CNC system exhibits excellent

catalytic activity compared with the metal NPs stabilized by other stabilizers. Moreover, the recyclability of Au@P4VP-*g*-CNC makes this catalyst attractive for industrial applications.

**Table 4.1. Catalytic performance of Au@CNC and Au@P4VP-*g*-CNC compared with other catalyst systems, for the reduction of 4NP.**

Catalyst stabilizers	Catalyst	TOF (h <sup>-1</sup> )	Reference
Fe <sub>3</sub> O <sub>4</sub>	Au	269.5	<sup>76</sup>
SiO <sub>2</sub>	Au	240	<sup>210</sup>
CNC	Au	109	<sup>82</sup>
CNC	CuO or Cu	1108.8 or 885.7	<sup>73</sup>
CNC	Pd	879.5	<sup>83</sup>
Polydopamine coated CNC	Ag	1077.3	<sup>184</sup>
CNC	Au	2275.2	This work
P4VP- <i>g</i> -CNC	Au	5533.2	This work
CNC	Recycled Au	849.6	This work
P4VP- <i>g</i> -CNC	Recycled Au	3124.8	This work

#### 4.4 Conclusions

In this chapter, P4VP-*g*-CNC nanohybrids were prepared by SI-ATRP and subsequently used to stabilize gold nanoparticles (Au NPs). The catalytic activity and recyclability of the material obtained (Au@P4VP-*g*-CNC) was investigated and compared with that of AuNPs stabilized by pristine CNC. The grafting of P4VP at the CNC surface was confirmed by FT-IR spectroscopy and the pH-responsive solubility in water of the P4VP-*g*-CNC hybrids was demonstrated by DLS and Zeta-potential measurements. Gold nanoparticles were subsequently deposited at the surface of P4VP-*g*-CNC by reducing HAuCl<sub>4</sub> with sodium borohydride (NaBH<sub>4</sub>) in the presence of the nanocellulosic material. The presence of P4VP brushes at the CNC surface led to the growing of Au NPs of lower averaged diameter (2.9 nm) compared with the diameter of the Au NPs deposited on pristine CNC (10.6 nm). The catalytic performance of pristine Au NPs, Au@CNC and Au@P4VP-*g*-CNC were then compared, through the measurement of the turnover frequency (TOF) obtained after catalytic reduction of 4-nitrophenol

(4NP), used as a model reaction. Compared with pristine Au NPs, the catalytic activity of Au@CNC and Au@P4VP were about 10 and 24 times better, respectively (TOF = 2275.2 h<sup>-1</sup> and 5533.2 h<sup>-1</sup>, respectively). In contrast to Au@CNC, the Au@P4VP-*g*-CNC material could be conveniently recovered by flocculation at pH > 5, and the recycled catalyst still displayed a relatively high activity for the reduction of 4NP (TOF = 3124.8 h<sup>-1</sup>).

## Chapter 5

### **Enhanced Thermal Stability and UV Resistance of Poly(vinyl chloride) Reinforced by UV-absorbing Poly(Cinnamoyloxy Ethyl Methacrylate) Grafted Cellulose Nanocrystals**

Ultraviolet (UV)-responsive poly(cinnamoyloxy ethyl methacrylate) (PCEM) was grafted on cellulose nanocrystals (CNC) using Surface-Initiated Atom Transfer Radical Polymerization (SI-ATRP). The resultant PCEM-grafted CNC (PCEM-*g*-CNC) exhibits high UV absorption properties and undergoes crosslinking under UV irradiation. When the PCEM-*g*-CNC nanohybrids were incorporated in poly(vinyl chloride), transparent composite films with UV-blocking properties were obtained. The comparison of the optical and mechanical properties of the films before and after UV-irradiation allowed demonstrating that the PCEM-*g*-CNC nanoparticles also acted as thermal and UV-stabilizers for PVC. Meanwhile, the tensile mechanical properties of the PVC film were significantly improved, and further increased after UV-irradiation.

## 5.1 Introduction

Poly (vinyl chloride) (PVC) is the third-most widely used synthetic plastic around the world, just after polyethylene and polypropylene.<sup>211</sup> Due to its outstanding mechanical properties, excellent chemical resistance, long durability, non-flammability, formulating versatility and low price, PVC has been widely used for pipes, window frames, packings, wires, coatings and plastic cards.<sup>212-215</sup> However, PVC exhibits very low thermal stability and starts to degrade at the glass transition temperature ( $T_g$ ) of the polymer, which increases the difficulties during manufacturing.<sup>216-219</sup> Moreover, its gradual degradation by weathering, when exposed to heat and ultraviolet (UV) light, remarkably decreases the lifetime of PVC-based products. The degradation of PVC results in discoloration, embrittlement and microcracking, leading to a change in appearance and a decrease in mechanical performance.<sup>212</sup> Therefore, thermal and UV stabilizers are often required in PVC matrices. However, many stabilizers contain toxic heavy metals, such as lead, which may leach out in drinking water and lead to safety and environmental issues.<sup>217</sup> Titanium dioxide ( $TiO_2$ ) is an essential additive in PVC matrices due to its outstanding UV absorption ability.<sup>212,220</sup> However,  $TiO_2$  also behaves as a photo-catalyst and accelerates the weathering degradation of PVC surfaces.<sup>212,221-224</sup> Therefore, there is a high demand for the development of environment-friendly and efficient thermal and UV stabilizers for PVC.

Due to increasing concern about the climate change and environmental pollution, it is highly demanded to develop sustainable materials with good performance. Cellulose nanocrystals (CNC) are bio-based nanoparticles produced by sulfuric acid hydrolysis of cellulosic substrates such as microcrystalline cellulose, paper or pulp.<sup>1,3,4,6</sup> These rod-shaped nanoparticles are renewable, biocompatible, display a high tensile strength and elastic modulus, have a low density and low coefficient of thermal expansion, and tend to self-assemble in the form of nematic phases.<sup>21,225</sup> As a result, CNC offer an array of properties, which can be exploited in the field of cosmetics, emulsions, electronics, liquid crystals, composites, foods, and catalysts.<sup>1,3-5,21,162,163</sup> In particular, the excellent mechanical properties of CNC make them ideal candidates to be used as reinforcing agents in polymer matrices.<sup>1,70</sup> However, the hydrophilic surface of CNC limits their compatibility with hydrophobic matrices, the hydroxylated nanoparticles being prone to self-aggregation through hydrogen bonding. The surface modification of CNC is therefore generally required to improve the filler/matrix interfacial adhesion; it can also be used

to introduce novel functionalities for advanced applications.<sup>29,55,226</sup> To date, only few studies have reported on the utilization of CNC as reinforcing agents in PVC matrices.<sup>227</sup>

Photo-responsive molecules containing cinnamate functions have demonstrated interesting properties in the field of light-induced shape memory materials,<sup>228-231</sup> [ENREF 228](#) polymers with crack healing properties,<sup>232</sup> or hydrogels.<sup>233-238</sup> Indeed, the cinnamate moiety exhibits a strong absorption in the UV region and can undergo  $[2\pi+2\pi]$  photodimerization and trans-cis photoisomerization upon UV irradiation (wavelength  $\lambda > 280$  nm).<sup>239,240</sup> Compared with the trans-cis photoisomerization, the photodimerization is the predominant process during UV irradiation.<sup>234,241</sup> When pendent cinnamate groups are attached to polymers, the mechanical properties of the material can be greatly enhanced by crosslinking, via the photodimerization process.<sup>242-244</sup> Meanwhile, cinnamate esters are considered non-toxic and biocompatible and are widely used in the flavor, perfume and pharmaceutical industries.<sup>228,233</sup> The grafting of photo-responsive cinnamate moieties at the CNC surface could then impart additional UV-absorbing and photo-crosslinking properties to the nanoparticle, which could have a positive impact on the mechanical and photo-stability of PVC matrices reinforced with this filler.

Different methods can be used to functionalize the CNC reinforcing particles, but the surface grafting of polymers chains is particularly attractive, as it provides a way of strengthening the interfacial adhesion by i) adjusting properly the surface wettability of the CNC and ii) promoting chain entanglements at the filler/matrix interface.<sup>60,61</sup> In particular, Surface-Initiated Atom Transfer Radical Polymerization (SI-ATRP) is a “grafting from” method, which allows preparing polymer-grafted CNC with quite a good control.<sup>2,29,46,51,55,161</sup> It could therefore serve as an efficient tool to graft polymers bearing cinnamate moieties at the CNC surface.

Herein, poly(cinnamoyloxy ethyl methacrylate)-grafted CNC nanohybrids (PCEM-g-CNC) were prepared by SI-ATRP and then employed as a UV/thermal stabilizer and reinforcing agent in PVC films. The grafted nanoparticles were characterized by Fourier transform infrared spectroscopy (FTIR), differential scanning calorimetry (DSC), thermogravimetric analysis (TGA) and water contact angle (WCA) measurements. The photoactivity of the grafted cinnamate moieties was demonstrated by UV spectroscopy, FTIR, TGA, and DSC, through the analysis of the grafted material before and after UV-irradiation. The PCEM-g-CNC nanohybrids were then incorporated in a PVC matrix to produce

transparent PVC films. The optical and mechanical properties of the films before and after UV-irradiation were subsequently investigated and compared with the properties of PVC and PVC/CNC reference materials.

## 5.2 Experimental

### 5.2.1 Materials

2-Hydroxyethyl methacrylate (HEMA), cinnamoyl chloride,  $\alpha$ -bromoisobutyryl bromide (BIBB), 4-(dimethylamino) pyridine (DMAP), ethyl  $\alpha$ -bromoisobutyrate (EBiB), triethylamine (TEA), N,N,N',N'',N'''-pentamethyldiethylenetriamine (PMDETA), CuBr, CuBr<sub>2</sub>, poly(vinyl chloride) carboxylated (PVC) ( $M_w = 220,000$  g/mol) and all solvents were purchased from Sigma. CuBr was purified with acetic acid at 80 °C under N<sub>2</sub> for 24 h, and washed with acetic acid and dried under vacuum at 50 °C. HEMA was purified by distillation from calcium hydride under reduced pressure, and all the other chemicals were used as received.

### 5.2.2 Synthesis of monomer: cinnamoyloxy ethyl methacrylate (CEM)

TEA (18.4 mL, 0.12 mol) was added to a dichloromethane (DCM, 100 mL) solution of HEMA (13 g, 0.1 mol) under argon. The mixture was cooled in an ice bath. DCM solution (80 mL) of cinnamoyl chloride (16.7 g, 0.1 mol) was added dropwise within 1 hour in the ice bath. After stirring overnight, the triethylamine hydrochloride salt byproduct was removed by filtration. The filtrate was concentrated by rotary evaporator under reduced pressure. The CEM was purified by running silica gel chromatography with a 10:1 (v/v) petroleum ether: ethyl acetate mixture as eluent. After drying at 50°C under reduced pressure overnight, 19.5 g viscous liquid was obtained as the final CEM with a yield of 68.0%.

<sup>1</sup>H NMR (400 MHz, CDCl<sub>3</sub>):  $\delta$  1.89 (3H, t, CH<sub>3</sub>); 4.37 (4H, m, -O-CH<sub>2</sub>-CH<sub>2</sub>-); 5.53 (1H, quin, =CH), 6.08(1H, quin, =CH), 6.39 (1H, d, =CH-Ar), 7.64 (1H, d, =CH-CO-), 7.3~7.5 (5H, m, ArH).

<sup>13</sup>C NMR (400 MHz, CDCl<sub>3</sub>):  $\delta$  18.30 (-CH<sub>3</sub>); 62.21, 62.52 (-O-CH<sub>2</sub>-CH<sub>2</sub>-O-); 117.54, 145.42, (-HC=CH-Ar); 126.10 (=CH<sub>2</sub>); 128.16 (2C<sub>Ar</sub>); 128.92 (2C<sub>Ar</sub>); 130.45, 134.20 (2C<sub>Ar</sub>); 135.96 (=C-); 166.69, 167.18 (2C=O).

### 5.2.3 Preparation of the brominated CNC nano-initiator: CNC-Br

CNC-Br was prepared by modifying the surface of CNC with BIBB. CNC (1.2 g) was dispersed in DMF (100 mL) by sonication. Then TEA (3.1 mL, 22.2 mmol) and DMAP (1.36 g, 11.1 mmol) were added. The solution of BIBB (1.36 mL, 11.1 mmol) in DMF (20 mL) was added dropwise to the dispersion of CNC kept in an ice bath. After 24 h, H<sub>2</sub>O was added and the resultant CNC-Br was recovered by centrifugation and subsequently washed with THF for 24 h using a Soxhlet extractor. The product was further dialyzed against deionized H<sub>2</sub>O for 5 days. Finally, the purified CNC-Br was obtained via freeze-drying.

### 5.2.4 Preparation of PCEM-*g*-CNC and PCEM

PCEM brushes were grafted from CNC-Br using SI-ATRP. In detail, CNC-Br (700 mg) was dispersed in DMF (70 mL) by sonication. CuBr<sub>2</sub> (22 mg, 0.1 mmol) and CEM (1.3 g, 5 mmol) were added. The mixture was purged with argon for 20 mins to remove oxygen. Then CuBr (58 mg, 0.4 mmol) and PMDETA (0.21 mL, 1 mmol) were added under the protection of argon. Three freeze-pump-thaw cycles were conducted to remove the oxygen in the mixture. The polymerization was conducted at 40°C. After 12 hours, the reaction was terminated by exposing the mixture to air. PCEM-*g*-CNC was then collected by centrifugation, washed with EtOH (sonication and centrifugation cycle) three times, and dialyzed against water for 6 days (molecular weight cut off is about 14,000 g/mol). Finally, the PCEM-*g*-CNC material was freeze-dried. According to the <sup>1</sup>H NMR spectrum, the monomer conversion of the SI-ATRP reaction is ca. 35%. Therefore, the weight ratio of PCEM in PCEM-*g*-CNC is ca.  $1.3 \times 35\% / (1.3 \times 35\% + 0.7) = 39\%$ .

PCEM was synthesized separately with EBiB as an initiator, using a similar ATRP procedure. The molar ratio of [CEM]: [CuBr]: [CuBr<sub>2</sub>]: [PMDETA]: [EBiB] was 88: 1: 1: 4: 2. After polymerization at 40 °C for 2 hours, the monomer conversion is 42.8% (determined by <sup>1</sup>H NMR). The average number molecular weight (*M<sub>n</sub>*) of PCEM determined by GPC is 6404, with a dispersity of ca. 1.3.

### 5.2.5 Preparation of the PVC films

The PVC films reinforced with CNC (PVC/CNC) or PCEM-*g*-CNC (PVC/PCEM-*g*-CNC) were prepared by solution casting. CNC or PCEM-*g*-CNC (25 mg) were dispersed in DMF (5 mL) by

sonication. After the addition of PVC (500 mg; weight percentage of CNC or PCEM-g-CNC relative to PVC = 5%), the mixture was stirred for 24 hours, to solubilize the PVC. The mixture was then sonicated in an ice bath for 2 mins with the output power of 16 W to finish the dissolution. The mixture was degassed for 10 mins under vacuum. The degassed mixture was then poured onto round silica mold with a fixed diameter of 65 mm. The homogeneous films were obtained after removing the solvent in the oven at 60 °C for 12 hours, followed by annealing at 80 °C for 10 hours. A neat PVC film was also prepared by the same procedure as a reference. The thickness of the films was ca. 90 μm, evaluated from the cross section analyzed by optical microscopy. The samples were for the tensile test measurements; the films were cut into samples with rectangular dimensions of 1 cm × 4 cm.

### 5.2.6 UV irradiation experiments

The impact of UV irradiation on the FTIR spectra and DSC curves of PCEM and PCEM-g-CNC samples was investigated from their THF solution (10 mg/mL) or dispersion (10 mg/mL), respectively. The solution or dispersion was irradiated at 365 nm for 12 hours, using a UV-F400 system (with a power of 450 W), leading to a concurrent evaporation of the solvent. The recovered dry material was then analyzed by FTIR and TGA.

The impact of UV irradiation on the cross-linking of PCEM and PCEM-g-CNC samples was investigated from films prepared by spin-coating THF solution/dispersion of PCEM/PCEM-g-CNC on quartz. The films deposited on the quartz support were then irradiated at 365 nm, using a handheld UV lamp (UVP) with a power of 6 W. The absorbance of the films was then measured at different time intervals with a UV-vis spectrometer in order to follow the evolution upon irradiation of the conjugated C=C absorption at 276 nm.

The PVC films were irradiated at the 365 nm wavelength for 24 hours, using a UV lamp with a power of 100 W. To protect the films from the heat produced by the UV lamp, the distance between the UV lamp and the PVC films was set to 20 cm.

### 5.2.7 Characterization

<sup>1</sup>H NMR and <sup>13</sup>C NMR spectra were recorded using a Bruker AC- 400 NMR at room temperature by dissolving the samples in CDCl<sub>3</sub>.

TGA was performed on a TGA-Q50 system (TA Instruments) at a heating rate of 10°C/min under nitrogen atmosphere. Derivative Thermogravimetric Analysis (DTG) curves were obtained from the derivation of the TGA curve.

Differential scanning calorimetry (DSC) was measured using a DSC Q100 apparatus (TA Instruments). All samples were first heated to 150 °C to remove the moisture and then cooled down to 0 °C and heated to 200 °C. The glass transition temperature ( $T_g$ ) values were determined from the second heating run of DSC.

Gel Permeation Chromatography (GPC) analysis was performed in THF with LiBr on a PL-GPC 50 plus Integrated GPC (Polymer Laboratories-Varian). The elution of the filtered samples was monitored using a simultaneous refractive index and UV detection systems. The elution times were converted to molar mass using a calibration curve based on low dispersity polystyrene standards.

Fourier transform infrared spectra (FTIR) of all the samples were taken after they were pressed into KBr pellets using the Thermo Nicolet Avatar 970 FTIR spectrometer with a resolution of 8 cm<sup>-1</sup> (64 scans).

The samples for water contact angle (WCA) measurements were prepared by spin coating the CNC aqueous dispersion or PCEM-*g*-CNC THF dispersion on glass. The static WCA was measured by analyzing the images of 3 water droplets using MATLAB.

Ultraviolet–visible (UV-vis) spectra were obtained on an Agilent Model 8453 UV-vis spectrometer.

The tensile testing of the PVC films was performed using a computer-controlled TA materials testing instrument at room temperature. The effective length for the tensile testing was 2 cm. A constant crosshead speed of 20 mm/min was maintained for all samples.

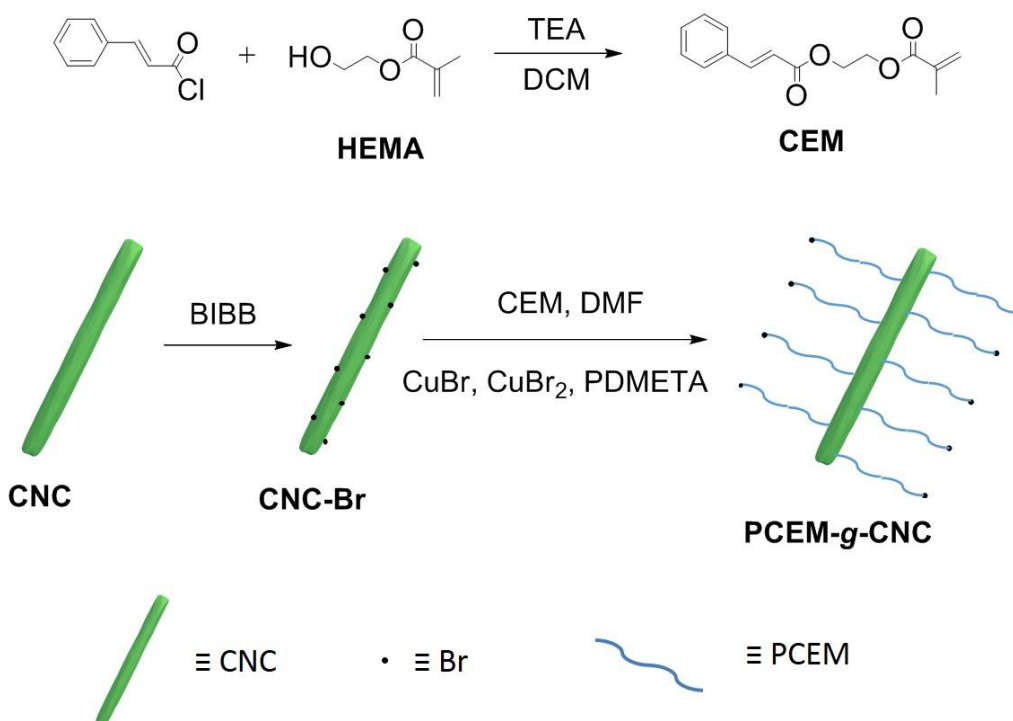
## **5.3 Results and discussion**

### **5.3.1 Preparation and characterizations of the PCEM-*g*-CNC nanohybrids**

The CNC used in this study were isolated by sulfuric acid hydrolysis of wood pulp, according to a general procedure described in the literature.<sup>16,149</sup> They consist of rod-like particles with estimated dimensions of 110.3 ± 47.7 nm in length and 4.8 ± 1.1 nm in diameter, based on a former study

performed with particles taken from the same batch (estimated from AFM pictures).<sup>28</sup> The amount of accessible hydroxyl groups at their surface was estimated to be  $3.10 \pm 0.11 \text{ mmol.g}^{-1}$ , using a method based on phosphorylation coupled with  $^{31}\text{P}$  NMR and FTIR analysis.<sup>28</sup> The CNC are also negatively charged (zeta-potential in water = -48 mV) due to the presence of sulfate ester groups at the surface, imparted by the sulphuric acid treatment.

**Scheme 5.1. Chemical route used to of prepare the PCEM-g-CNC hybrid nanoparticles.**



The chemical route used to prepare the PCEM-g-CNC nanohybrids is summarized in Scheme 5.1. The CEM monomer was synthesized by acylating HEMA with cinnamoyl chloride. The successful synthesis of CEM was confirmed by the  $^1\text{H}$  NMR and  $^{13}\text{C}$  NMR (see experimental section). To graft the polymer by SI-ATRP, Br initiating sites were first introduced at the surface of the CNC by esterification with BIBB (CNC-Br). The success of the reaction was confirmed by FTIR, through the observation of the carbonyl stretching vibration of the grafted bromoisobutyrate moiety at  $1739 \text{ cm}^{-1}$  (Figure 5.1). The SI-ATRP grafting of PCEM from CNC-Br was performed in the absence of sacrificial initiator. Therefore, there is no free PCEM produced in the SI-ATRP process, and only PCEM brushes

are initiated from the surface of CNC-Br. A reference PCEM polymer was nevertheless synthesized separately, using the same ATRP process, with ethyl  $\alpha$ -bromoisobutyrate (EBiB) as an initiator. The FTIR spectra of PCEM-*g*-CNC and PCEM are shown in Figure 5.1. Compared with CNC-Br, the FTIR spectrum of PCEM-*g*-CNC display additional vibration bands characteristic of the PCEM polymer at  $1716\text{ cm}^{-1}$  (C=O stretching of the two carbonyl groups),  $1635\text{ cm}^{-1}$  (C=C stretching) and  $768\text{ cm}^{-1}$  (out-of-plane C-H bending of the aromatic ring), suggesting that the grafting was successful.<sup>236</sup>

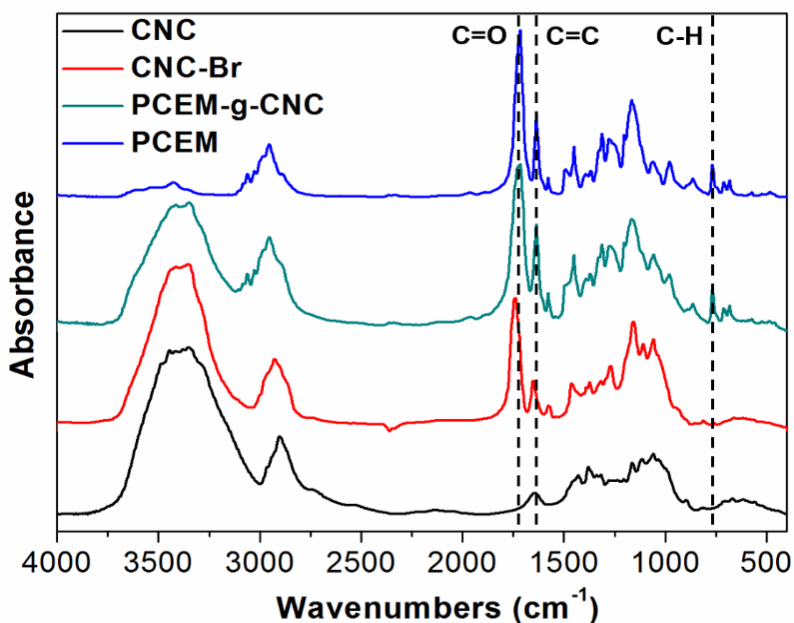


Figure 5.1. FTIR spectra of CNC, CNC-Br, PCEM-*g*-CNC and PCEM.

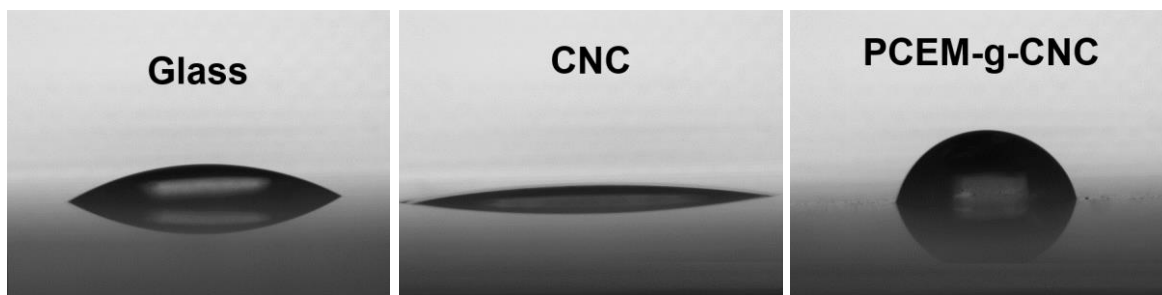
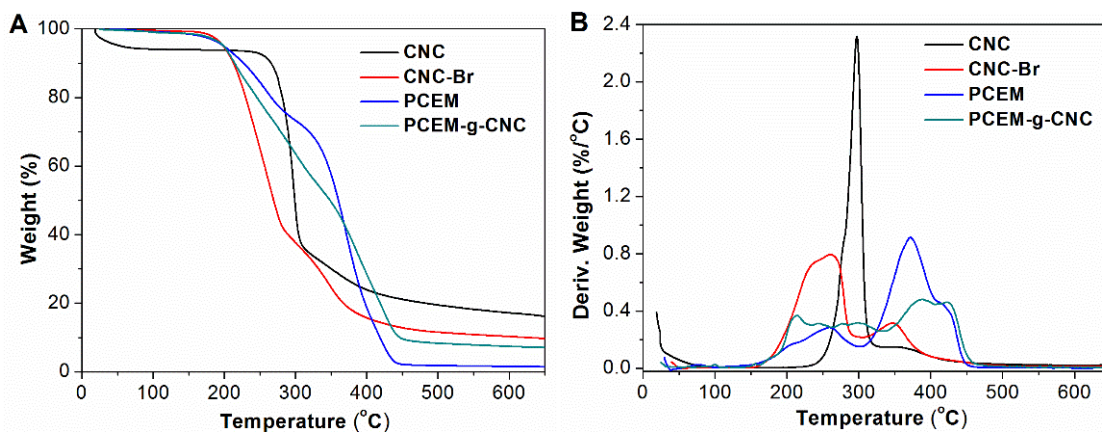


Figure 5.2. Images of the water droplets deposited on the glass support, before and after spin-coating with CNC and PCEM-*g*-CNC.

The surface wettability of CNC and PCEM-g-CNC was evaluated by WCA measurements performed at the surface of films prepared by spin-coating a water or THF dispersion (respectively) of the nanoparticles on glass. The water droplet images on the different surfaces are shown in Figure 5.2. The WCA on the pristine glass support is ca. 28.6°. The average WCA on CNC-coated glass is only ca. 14.0°, confirming the hydrophilic nature of the unmodified CNC. On the other hand, the WCA of PCEM-g-CNC coated glass is about 66.6°, indicating that the polymers grafted at the CNC surface imparted some hydrophobic properties to the material.



**Figure 5.3. TGA thermograms (A) and DTG curves (B) of pristine CNC, CNC-Br, PCEM and PCEM-g-CNC.**

The thermal stability of PCEM-g-CNC was investigated by TGA and compared with that of CNC, CNC-Br, and PCEM. The thermograms and corresponding DTG derivatives are shown in Figure 5.3. The thermogram of pristine CNC is consistent with the thermal behavior generally observed for CNC bearing sulfate ester groups.<sup>68</sup> The CNC-Br material displays a decreased thermal stability associated with the labile bromine, which may form HBr upon heating and can catalyze cellulose degradation.<sup>51,147</sup> The unmodified CNC exhibit a 6% weight loss below 100 °C, associated to the absorbed moisture. This weight loss is absent or small in the thermograms of PCEM, CNC-Br, and PCEM-g-CNC, due to the more hydrophobic character of these samples. The PCEM degradation occurs in two step, consistent with literature data.<sup>245</sup> The first weight loss of low decomposition rate (from 190 to 300 °C) is associated with the cleavage of the cinnamate moieties, while the second weight loss of higher decomposition rate

(from 300 to 450 °C) corresponds to the decomposition of the main polymer chains. Compared with the CNC-Br nano-initiators, the PCEM-g-CNC nanoparticles exhibit a much better thermal stability, with a decomposition process approaching that of the free polymer.

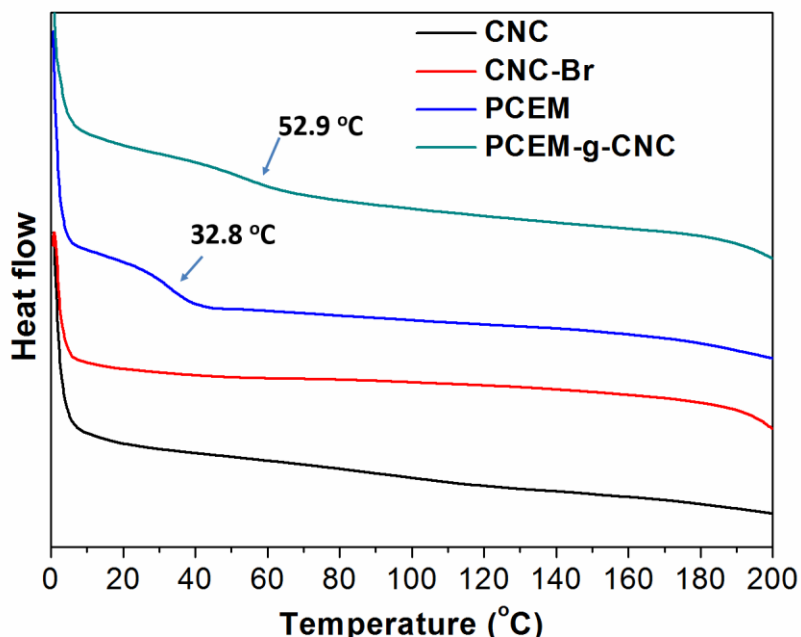


**Figure 5.4. The DSC curves of CNC, CNC-Br, PCEM, and PCEM-g-CNC**

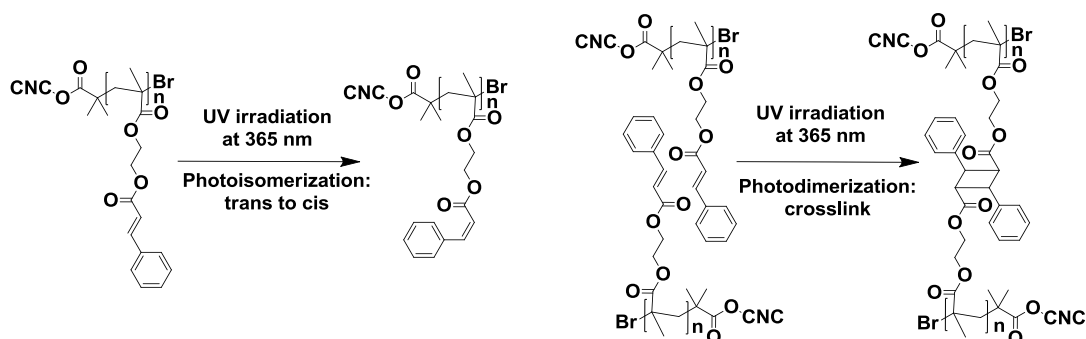
The glass transition temperature ( $T_g$ ) of PCEM and PCEM-g-CNC were measured by DSC, from the second heating scan (Figure 5.4). As expected, the crystalline CNC and CNC-Br materials do not display any glass transition. PCEM-g-CNC shows an enhanced apparent  $T_g$  of 52.9 °C compared with free PCEM ( $T_g = 32.8$  °C), which was attributed to the restriction of the chains movement after the grafting at the CNC surface.

### 5.3.2 Impact of UV irradiation on PCEM-g-CNC

PCEM is known to undergo photoisomerization and photodimerization when irradiated by UV light (wavelength  $\lambda > 280$  nm). Upon irradiation at 365 nm, the cinnamate moiety can indeed isomerize from the trans to cis form and/or dimerize by  $[2\pi+2\pi]$  photocyclization (Scheme 5.2). The photodimerization process is believed to be the predominant process during UV irradiation.

Since the conjugated C=C bond in the cinnamate moiety displays a UV absorption band at 276 nm, due to the  $\pi\text{-}\pi^*$  electronic transition, the photodimerization process can be monitored by UV spectroscopy. Hence, PCEM and PCEM-g-CNC films – prepared by spin-coating THF solutions or dispersions of the polymer or nanohybrids – were irradiated at 365 nm for several hours. The evolution of their absorbance was then recorded with time, with a UV-Vis spectrometer (Figure 5.5A and Figure 5.5C). As expected, the UV absorbance of the conjugated C=C bond of both the free and grafted polymer is observed between 240 and 320 nm, but its intensity tends to decrease with increasing irradiation time at 365 nm. This decrease was assigned to the  $[2\pi+2\pi]$  photocyclization of neighboring cinnamate moieties within the free or grafted polymers. The evolution of the maximum UV absorbance ( $A_t$ ) and reciprocal ( $1/A_t$ ) at 276 nm, were then plotted as a function of irradiation time for both PCEM and PCEM-g-CNC films (Figure 5.5B and Figure 5.5D).  $1/A_t$  increases proportionally with time, indicating that the photodimerization occurred in bulk, and followed second-order kinetics. The slope of the fitting line of  $1/A_t$  vs. time is much smaller for the PCEM-g-CNC than for PCEM, suggesting that the photodimerization of PCEM-g-CNC occurred at a much slower rate.

**Scheme 5.2. Photoisomerization and photodimerization of PCEM-g-CNC under UV irradiation at 365 nm.**



The impact of UV irradiation on the FTIR spectra and DSC curves of PCEM and PCEM-g-CNC samples was investigated from their THF solution or dispersion, respectively. The solution or dispersion was irradiated at 365 nm for 12 hours, leading to a concurrent evaporation of the solvent. The recovered dry material was then analyzed by FTIR and DSC.

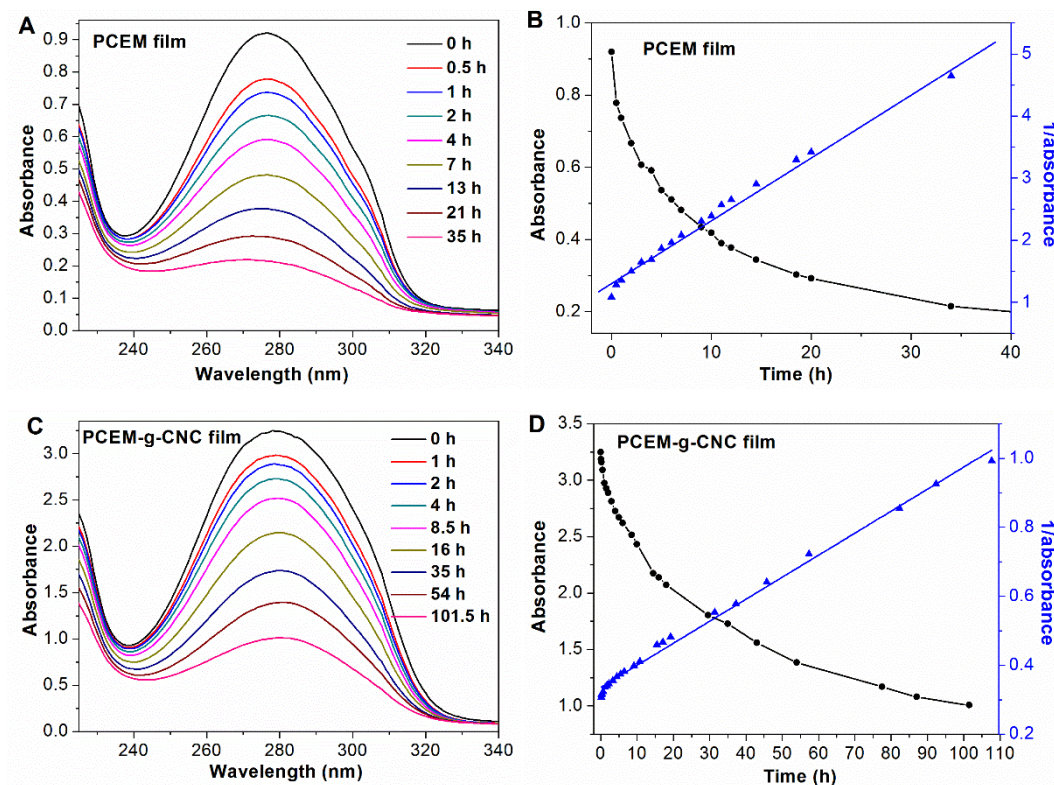


**Figure 5.5. Evolution of the UV absorption of the conjugated C=C bond in PCEM (A) and PCEM-g-CNC (C) films irradiated at 365 nm for several hours; and evolution upon irradiation of the maximum absorbance (●) and reciprocal (▲) at 276 nm, for both PCEM (B) and PCEM-g-CNC (D) films.**

The FTIR spectra of the PCEM and PCEM-g-CNC samples, before and after irradiation at 365 nm are presented in Figure 5.6. In both cases, the intensity of the stretching vibration of the conjugated C=C at  $1635\text{ cm}^{-1}$  decreases after UV irradiation, consistent with the photodimerization expected. Meanwhile, the conjugated C=O at  $1716\text{ cm}^{-1}$  is up-shifted to  $1731\text{ cm}^{-1}$ , which is consistent with the loss of conjugation expected after the cycloaddition.<sup>246</sup> The decrease in the intensity of the trans-vinylene C-H deformation at  $980\text{ cm}^{-1}$  after irradiation, could be related to both the dimerization and trans-cis isomerization processes.<sup>241</sup> This band completely disappears from the spectrum of PCEM-g-CNC after irradiation, while a weak C=C signal is still observed, suggesting that partial photoisomerization may also have occurred in that case. However, since no distinguishable cis-vinylene

C-H band could be detected in the spectra of both irradiated samples, photodimerization should be the main process. With PCEM-g-CNC nanohybrids, the photo-crosslinking should be highly favored between neighboring chains grafted at the surface of the single nanoparticles. With the PCEM solutions, the inter-chain contact should be more difficult, which may explain why a significant amount of cinnamate moieties remains uncross-linked after UV-radiation (the intensity of the C=C band remains quite high).

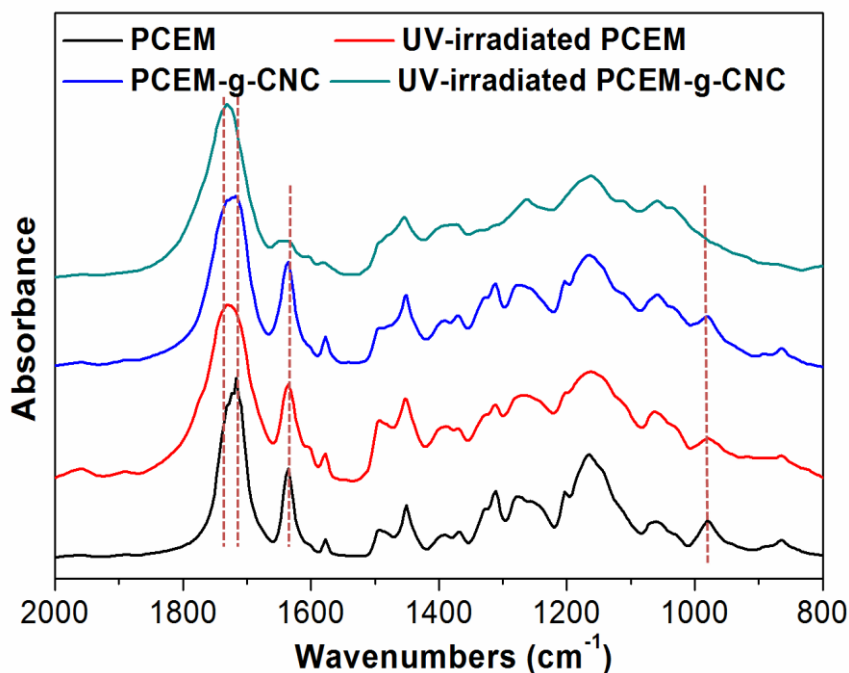


**Figure 5.6. FTIR spectra of PCEM and PCEM-g-CNC samples, before and after irradiation at 365 nm of their solution/dispersion (overnight irradiation accompanied by an evaporation of the solvent).**

The DSC curves of the PCEM and PCEM-g-CNC samples before and after irradiation at 365 nm are shown in Figure 5.7. The  $T_g$  of both samples disappears after UV irradiation in the temperature range investigated. The movement of the polymer chains being restrained by the crosslinking, the  $T_g$  is indeed expected to shift to a higher temperature or to completely disappear, depending on the degree of crosslinking.

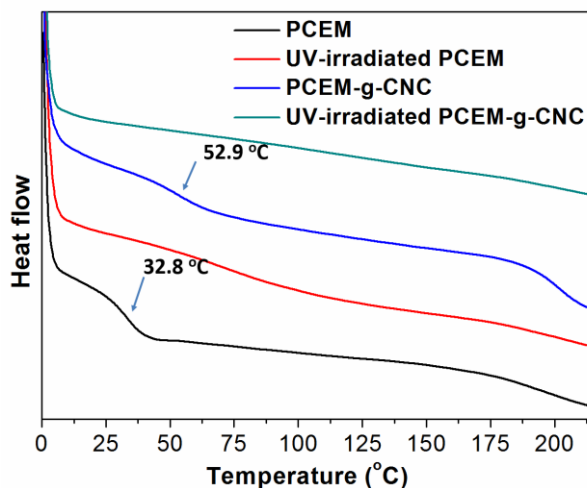


**Figure 5.7.** DSC curves of the PCEM and PCEM-g-CNC samples, before and after irradiation at 365 nm of their solution/dispersion (overnight irradiation accompanied by an evaporation of the solvent).

### 5.3.3 Preparation and properties of composite PVC films filled with PCEM-g-CNC nanohybrids

Composite PVC films were prepared via the solution casting method. DMF was chosen as the co-solvent to favor the miscibility between the cellulosic nanoparticles and PVC. The PVC solution in DMF is transparent and colorless, while the PVC/CNC dispersion is opaque, and the PVC/PCEM-g-CNC dispersion is slightly translucent. As shown in Figure 5.8, homogeneous and highly transparent PVC films were obtained after evaporation of the DMF and subsequent heat annealing at 80 °C. The thickness of the films was ca. 90  $\mu\text{m}$ , evaluated from the cross section analyzed by optical microscopy.

The effect of weathering on PVC has been widely studied and is influenced by many parameters, such as temperature, sunlight intensity, moisture, oxygen, additives and so on.<sup>214,247</sup> Generally, two main degradation reactions occur during the weathering of PVC: (1) through the action of heat, hydrogen chloride is eliminated while conjugated polyenes are formed, leading to the discoloration of the material,<sup>248-251</sup> (2) through the action of light, the photo-induced free radicals in the polyenes are rapidly

quenched by oxygen or crosslinked, leading to a bleaching of the material.<sup>247,252-254</sup> A small exposure to heat or light can result in a significant color change of the PVC material. Therefore, the color change of the PVC induced by heat or light could be employed to represent the degradation of PVC.



**Figure 5.8. PVC, PVC/CNC (5 wt. %) and PVC/PCEM-g-CNC (5 wt. %) composite films obtained by solution casting of the corresponding DMF solutions/suspensions followed by heat annealing.**

The optical properties of the PVC films before heat annealing were investigated by UV-vis spectroscopy. As shown in Figure 5.9, all unheated films exhibit a quite high transmittance in the visible light range. The addition of CNC and PCEM-g-CNC in the PVC matrix further enhanced the transmittance in this range, the best transparency being obtained with the PCEM-g-CNC filler. Unlike the other materials, the transmittance of the PVC/PCEM-g-CNC film is significantly reduced in the UVA range (320 - 400 nm) and all UVB and UVC (below 320 nm) are blocked. Therefore, the PCEM-g-CNC filler act as a UV-blocking agent within the PVC film before annealing, as schematized in Figure 5.10. It could find applications where both high visible light transparency and UV-blocking properties are required, such as film for the glass of car.

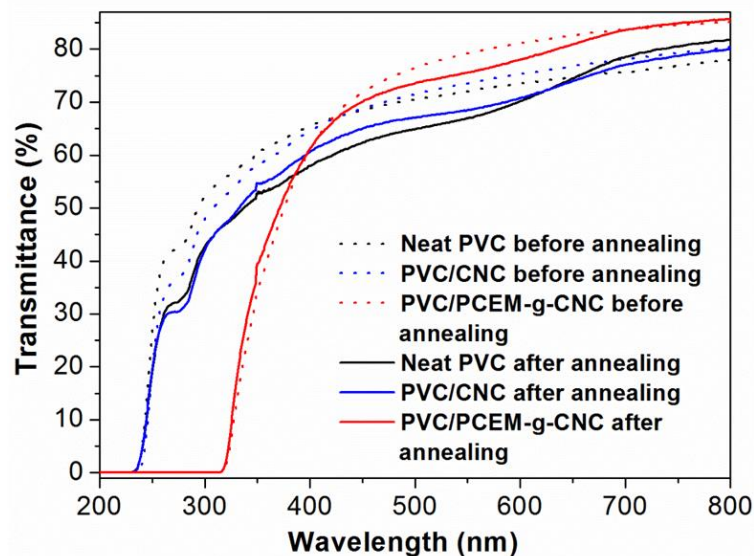


Figure 5.9. Transmittance of the PVC, PVC/CNC and PVC/PCEM-g-CNC films, before and after heat annealing at 80 °C.

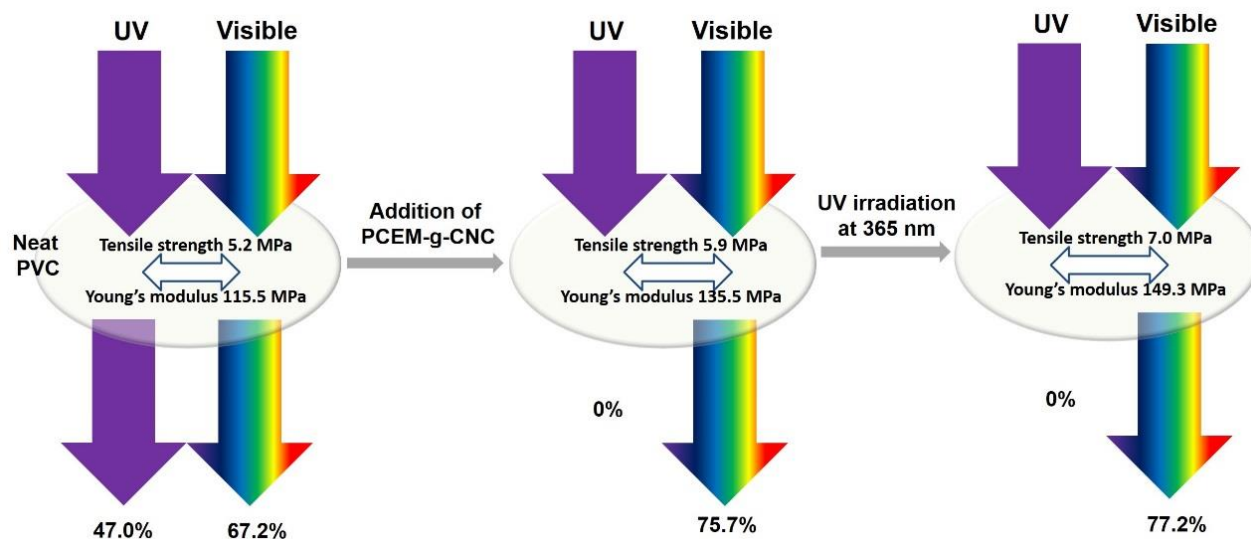


Figure 5.10. Schematic representation depicting the UV-filtering and reinforcing effect of the PCEM-g-CNC filler in PVC, before and after heat annealing. The transmittances given were measured at 320 nm (UV) and 555 nm (Visible).

After heat annealing, the transmittance of all PVC films decreases, but the PVC/PCEM-g-CNC film remains highly transparent in the visible region and still display UV-blocking properties (Figure 5.9). The decrease in transmittance is assigned to the formation of conjugated polyenes after dehydrochlorination, when the temperature reaches 70-80 °C.<sup>216-219</sup> Since 555 nm is the most sensitive wavelength for human beings, it was used as a reference to follow the evolution of the optical properties of the PVC films in the visible range, before and after heat annealing (Table 5.1). The PVC/PCEM-g-CNC film exhibits the lowest transmittance change after heat annealing, indicating that the PCEM-g-CNC filler also acted as a thermal stabilizer of PVC.

**Table 5.1. Evolution of the transmittance at 555 nm of the PVC films, before and after heat annealing or UV-irradiation.**

Samples	Before annealing (%)	After annealing (%)	Transmittance variation during annealing (%)	After UV irradiation (%)	Transmittance variation during UV irradiation (%)
Neat PVC film	72.2	67.2	-7.0	75.8	12.9
PVC/CNC film	73.8	68.8	-6.8	71.5	4.2
PVC/PCEM-g-CNC film	79.4	75.7	-4.7	77.2	2.0

The optical properties of the annealed PVC films before and after 24h UV irradiation at 365 nm were also compared. As shown in Figure 5.11, all the PVC films display a higher transmittance in the UV-visible region after UV irradiation. This increase was assigned to the degradation of PVC due to the bleaching effect associated with the photo-induced oxidation and crosslinking of the conjugated polyenes.<sup>247,252,253</sup> The evolution of the transmittance at 555 nm of the PVC films before and after UV-irradiation, is summarized in Table 5.1. The PVC/CNC and PVC/PCEM-g-CNC samples exhibit a lower transmittance change after UV-irradiation compared with pure PVC, indicating that both cellulosic fillers photo-stabilized the PVC to some extent. The best results were obtained with PCEM-g-CNC, most probably because the grafted cinnamate moieties acted as UV-absorbers within the PVC matrix. Moreover, PVC/PCEM-g-CNC films exhibited increased transmittance in the 320-420 nm

region after the UV irradiation, which was associated with consumption of the conjugated C=C in PCEM-g-CNC. This was attributed to the crosslinking among the cinnamate groups or between the cinnamate groups and the PVC chains. The photoinduced radicals in the PVC matrices could be trapped and crosslinked with the cinnamate moieties of PCEM-g-CNC under UV irradiation.

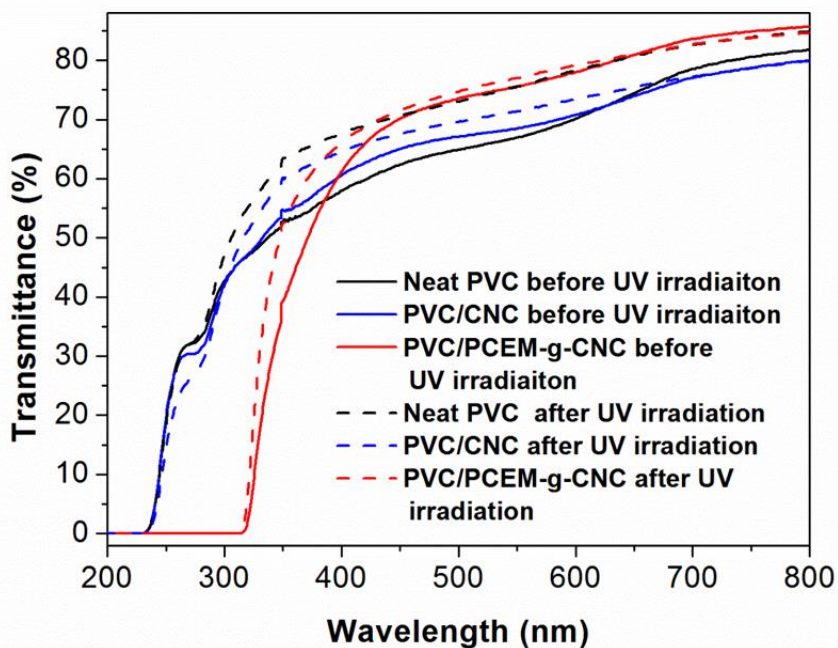


**Figure 5.11. Transmittance of the PVC, PVC/CNC and PVC/PCEM-g-CNC films before and after UV irradiation.**

The mechanical performance of the PVC films were evaluated by tensile tests measurements. The tensile stress-strain curves obtained before and after 24h UV irradiation of the films at 365 nm are shown in Figure 5.12, while the mechanical characteristics – including yield strength ( $\sigma_y$ ), Young's modulus ( $E_Y$ ), and elongation at break ( $\epsilon_b$ ) – are summarized in Table 5.2. The neat PVC film displays a typical ductile tensile curve with a prominent plastic deformation.<sup>2, 55-57</sup> After the addition of CNC or PCEM-g-CNC, both PVC/CNC and PVC/PCEM-g-CNC composite films exhibit higher  $\sigma_y$ ,  $E_Y$  and  $\epsilon_b$  values, indicating that both cellulosic fillers acted as reinforcing agents in the PVC matrix. PVC/PCEM-g-CNC film shows much better  $\epsilon_b$  than PVC/CNC, which is due to the better miscibility between PVC and PCEM-g-CNC than that between PVC and CNC.<sup>227,255</sup>

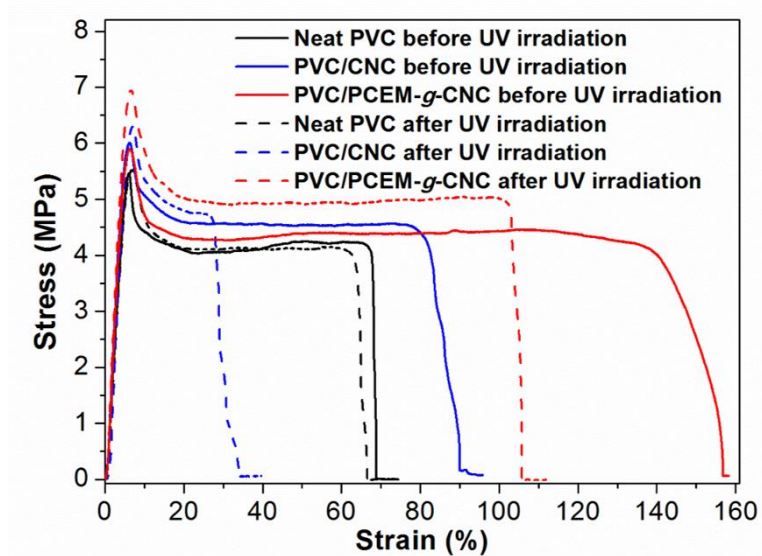


**Figure 5.12. Tensile stress-strain curves obtained after analysis of the PVC, PVC/CNC and PVC/PCEM-*g*-CNC films before and after the UV irradiation.**

After the UV irradiation, both neat PVC and PVC/CNC films displayed a slight increase in  $\sigma_y$  (ca. 5-6%) and  $E_Y$  (ca. 2-3%), which was associated with the UV-induced crosslinking among the PVC chains.<sup>256</sup> Moreover, compared with the neat PVC, the  $\epsilon_b$  of the PVC/CNC was significantly decreased after the UV irradiation, which could be attributed to the phase separation between CNC and PVC during the UV irradiation.<sup>214</sup> On the other hand, the PVC/PCEM-*g*-CNC exhibited remarkably increase in  $\sigma_y$  (ca. 18.6%) and  $E_Y$  (ca. 15.3%), which was mostly due to the UV-induced crosslinking among the cinnamate moieties of PCEM-*g*-CNC and the PVC chains. The radicals induced by the UV irradiation in the PVC matrices are trapped by the cinnamate moieties of PCEM-*g*-CNC, leading to crosslinking between the PCEM-*g*-CNC and PVC under UV irradiation. Moreover, the PVC/PCEM-*g*-CNC still exhibited a relatively high  $\epsilon_b$  after the UV irradiation, suggesting a good miscibility between PCEM-*g*-CNC and PVC even after the UV irradiation. Therefore, the mechanical performance of PVC/PCEM-*g*-CNC were further improved due to the UV-induced crosslinking.

**Table 5.2. Summary of the tensile mechanical characteristics of the PVC films before and after UV-irradiation.**

Samples	Neat PVC		PVC/CNC		PVC/PCEM-g-CNC	
	Before UV irradiation	After UV irradiation	Before UV irradiation	After UV irradiation	Before UV irradiation	After UV irradiation
$\sigma_y$ (MPa)	5.2	5.5	6.0	6.3	5.9	7.0
$E_Y$ (MPa)	114.9	118.0	14.9	147.6	135.6	156.3
$\varepsilon_b$ (%)	68.8	66.5	90.0	33.9	156.8	105.9

## 5.4 Conclusion

In this chapter, poly(cinnamoyloxy ethyl methacrylate)-grafted CNC nanohybrids (PCEM-g-CNC) were prepared by SI-ATRP and then employed as a UV/thermal stabilizers and reinforcing agents in PVC films. WCA measurements indicated that the grafting of PCEM on CNC – confirmed by FTIR, TGA and DSC – led to a more hydrophobic surface. The photoactivity of the grafted cinnamate moieties was demonstrated by analyzing PCEM-g-CNC film before and after irradiation at 365 nm. The  $[2\pi+2\pi]$  photocyclization of neighboring cinnamate moieties was evidenced by observing the decrease in the intensities of the C=C absorbance (UV spectroscopy) and C=C stretching vibration (FTIR) upon irradiation; the  $T_g$  of the grafted polymer also disappeared; confirming further the cross-linking of the material. When the PCEM-g-CNC nanohybrids were incorporated in PVC, transparent composite films were obtained. The comparison of the optical and mechanical properties of the films before and after UV-irradiation at 365 nm allowed demonstrating that the PCEM-g-CNC nanoparticles acted as thermal and UV-stabilizers for PVC. The material also displayed UV-blocking properties, while the high transparency in the visible range was preserved. Meanwhile, the tensile mechanical properties of the PVC film were significantly improved after incorporation of the PCEM-g-CNC filler. A further increase in the mechanical performance of the composite film was even noted after UV-irradiation, which could result from a radical coupling between the grafted PCEM chains and the PVC matrix.

## **Chapter 6**

### **Inverse Pickering Emulsions Stabilized by Cinnamate Modified Cellulose Nanocrystals (Cin-CNC) as Templates to Prepare Cin-CNC/Silica Colloidosomes**

A facile method to prepare colloidosomes at room temperature is proposed from w/o inverse Pickering emulsions containing silica precursors and stabilized by cinnamate modified cellulose nanocrystals (Cin-CNC). Cin-CNC Pickering emulsifiers were prepared by acylation with an excess of cinnamoyl chloride. The Cin-CNC surface displayed partial wettability with both toluene and water, which allowed stabilization of w/o inverse Pickering emulsions. The Cin-CNC particles around the droplets were subsequently locked by cross-linking TEOS or TBOS silica precursors at the water/toluene interface, leading to an intricate network of polysiloxane within the Cin-CNC shell. In optimized conditions, the Cin-CNC/silica colloidosomes obtained displayed a robust shell and slow releasing capacity with regards to encapsulated molecules such as rhodamine B or fluorescent deoxyribonucleic acid (DNA).

## 6.1 Introduction

Colloidosomes are hollow microcapsules templated from Pickering emulsions, whose shell consists of coagulated or fused colloid particles.<sup>97,105,257,258</sup> They possess a great potential for the microencapsulation of active ingredients such as drugs, pesticides, flavors, proteins, and even deoxyribonucleic acid (DNA), enabling promising applications in the field of food, pharmacy, personal care and cosmetics.<sup>98</sup> Colloidosomes are prepared from emulsions stabilized by colloidal particles instead of surfactants, called Pickering emulsions.<sup>84,91,105,257,259-261</sup> In these systems, the particles display partial wettability with both the oil and the water phase and are irreversibly absorbed at the oil/water interface. Both inorganic and organic colloidal particles can be used as solid surfactants, including silica, metal oxides, polymers, carbon nanotubes and polysaccharides.<sup>85,91</sup> In colloidosomes, the Pickering particles at the interface of the emulsion droplets are locked together to form a solid shell. The properties of the colloidosomes obtained – i.e. the size, permeability, biocompatibility and mechanical properties – are then controlled by varying the conditions of preparation (type of colloidal particles, solvent, method used to lock the colloidal particles...<sup>97</sup>).

Many methods can be used to convert the Pickering emulsion templates into robust colloidosomes, such as thermal annealing, gel trapping, polymerization of the droplet phase, polyelectrolyte complexation and covalent cross-linking.<sup>98,99,101,106,107,262-267</sup> However, most of these methods are multi-steps, time-consuming, require high temperatures, or lead to shells with poor mechanical strength.<sup>98</sup> Moreover, the colloidosomes generally display insufficient encapsulation performance, due to the loose linkage between colloidal particles. The encapsulated ingredients inside the colloidosomes are often released within one day, which is still too fast for most commercial applications.<sup>98,106,107</sup> Recently, an alternative method based on the sol-gel reaction of silica precursors at room temperature has been proposed.<sup>104,105,257,261</sup> In this sol-gel method, hydrophobically modified silica nanoparticles were employed as Pickering emulsifiers, while hyperbranched polyethoxysiloxane (PEOS) was used as sol-gel precursor to lock the nanoparticles. The method resulted in outstanding encapsulation performance owing to the robust and dense silica shell obtained after the condensation of PEOS. Although the method is promising, the inorganic nature of the cross-linked shell leads to a brittle structure, and the tedious synthesis of PEOS increases the preparation steps of the colloidosomes.<sup>268</sup> It is believed that

the utilization of organic nanoparticles and simple sol-gel precursors – such as tetraethyl orthosilicate (TEOS) – could improve the process.

Very recently, it has been shown that cellulose nanocrystals (CNC) – a sustainable bio-sourced material – could serve as a valuable colloidal stabilizer in Pickering emulsions.<sup>13,269-271</sup> CNC are nanoparticles produced by sulfuric acid hydrolysis of cellulosic substrates such as microcrystalline cellulose, paper or pulp.<sup>3,4</sup> The treatment provokes the hydrolysis of the amorphous regions, leading to the release of nanorods bearing sulfate ester groups at their surface. They are renewable, biocompatible and display a high tensile strength and elastic modulus,<sup>1,4</sup> which could be an asset to improve the mechanical strength of the colloidosome shell. Moreover, they can be easily crosslinked with polysiloxane matrices via the sol-gel method, due to the abundant hydroxyl groups present at their surface.<sup>21,38,192,272,273</sup>

Pristine CNC have demonstrated good performance in stabilizing various oil-in-water (o/w) emulsions systems, but they generally require the utilization of salt to screen the repulsion between the negatively charged particles.<sup>13,269-271</sup> Another method consists in adjusting the hydrophilic/hydrophobic balance at the CNC surface by chemical modification.<sup>24,25,27,28</sup> In particular, remarkably stable o/w emulsions of ethyl acetate, toluene or cyclohexane were recently obtained with acetylated CNC or cinnamate-grafted CNC.<sup>24</sup> Inverse w/o emulsions can also be obtained if the nanocellulose surface is sufficiently hydrophobic, but studies are rare.<sup>96,274</sup>

Herein, cinnamate-grafted cellulose nanocrystals (Cin-CNC) were prepared by acylation with cinnamoyl chloride and used to prepare colloidosomes from w/o inverse Pickering emulsions containing silica precursors. The grafted nanoparticles were characterized by Fourier transform infrared spectroscopy (FTIR), transmission electron microscopy (TEM), thermogravimetric analysis (TGA), dynamic Light Scattering (DLS) and water contact angle (WCA) measurements. The Cin-CNC nanoparticles were subsequently used as Pickering emulsifiers to stabilize inverse water/toluene Pickering emulsions. The impact of Cin-CNC concentration on the stability and size of the emulsion droplets was then investigated by optical microscopy. These emulsions were further cross-linked in the presence tetraethyl orthosilicate (TEOS) or tetrabutyl orthosilicate (TBOS) precursors to produce CNC/Silica colloidosomes. The mechanical integrity and encapsulating properties of the microcapsules obtained were particularly discussed.

## **6.2 Experimental**

### **6.2.1 Materials**

The CNC were purchased from the University of Maine (containing 1.05% wt. % of sulfur). Dimethylaminopyridine (DMAP), triethylamine (TEA), cinnamoyl chloride, tetraethyl orthosilicate (TEOS), and tetrabutyl orthosilicate (TBOS) were purchased from Sigma-Aldrich. Fluorescent DNA used here is 6-carboxyfluorescein (FAM) labeled A<sub>15</sub> DNA (FAM-A<sub>15</sub>), which was kindly donated by Zhicheng Huang from Dr. Juewen Liu's lab. And the sequence of fluorescent DNA is FAM-AAAAAAAAAAAAAAAAA.<sup>275</sup>

### **6.2.2 Preparation of the Cin-CNC Pickering emulsifiers**

CNC (1 g) were dispersed in DMF (80 mL) by sonication. After the addition of TEA (2.58 mL, 18.5 mmol) and DMAP (1.133 g, 9.3 mmol), the dispersion was cooled down by an ice bath. Then a solution of cinnamoyl chloride (3.33 g, 20 mmol) in DMF (20 mL) was added dropwise in an ice bath. The reaction was conducted at room temperature. After 24 hours, water (50 mL) was added to terminate the reaction. The resultant products were purified by Soxhlet extraction with THF for 24 hours and then dialyzed in deionized water for 7 days. The final Cin-CNC were obtained by freeze-drying.

### **6.2.3 Preparation of the inverse Pickering emulsions stabilized by Cin-CNC**

A Cin-CNC stock dispersion (10 mg/mL) was prepared by dispersing Cin-CNC (200 mg) in toluene (20 mL). Cin-CNC dispersions with lower concentrations were then prepared by dilution. Deionized water or a rhodamine B aqueous solution (3 mL) was then added in the Cin-CNC dispersion (7 mL). The volume ratio of oil phase to water phase was fixed at 7:3. The inverse Pickering emulsion was prepared by sonicating the mixture for 30 s at the output power of 16 watts. The distribution of the diameter of the emulsion droplets was estimated from the measure of 500 emulsion droplets in the optical micrograph images.

### **6.2.4 Preparation of the Cin-CNC/silica colloidosomes**

TEOS (3.5 mL) was added to toluene dispersions of Cin-CNC (3.5 mL) with concentrations of 4 mg/mL or 10 mg/mL, and vortexed for 1 min. The corresponding Cin-CNC concentration in the oil phase was

2 mg/mL or 5 mg/mL. After the addition of water (3 mL), the mixture was sonicated for 30 s at the output power of 16 W to prepare the inverse Pickering emulsion. The emulsion was kept still at room temperature for 6 or 10 days to allow the cross-linking of the TEOS or TBOS precursors, respectively. The emulsion was then washed with ethanol or acetone three times. After dialysis against deionized water for 5 days, the final Cin-CNC/silica colloidosomes were obtained by freeze-drying. The encapsulation of fluorescent molecules was performed using the same procedure, but with rhodamine B or fluorescent DNA aqueous solution (0.05 mg/mL) as the water phase.

### 6.2.5 Characterization

Fourier transform infrared spectra (FTIR) of all the samples were acquired KBr using the Thermo Nicolet Avatar 970 FTIR spectrometer, with a resolution of  $8\text{ cm}^{-1}$  (64 scans). Transmission electron microscopy (TEM) was conducted on Philips CM10 at an acceleration voltage of 60 keV. The TEM samples were prepared by drop coating water dispersions of CNC or THF dispersions of Cin-CNC onto copper grids (200 mesh coated with copper), then drying the samples overnight at ambient temperature. The pristine CNC dispersion for TEM samples was stained by  $\text{FeCl}_3$ .

Thermogravimetric analysis (TGA) was performed on TGA-Q50 system (TA Instruments) at a heating rate of  $10\text{ }^\circ\text{C}/\text{min}$  under nitrogen atmosphere.

Dynamic light scattering (DLS) and  $\zeta$ -potential experiments were performed using a Malvern Instrument Zetasizer Nanoseries.

The samples for water contact angle (WCA) measurements were prepared by spin coating the CNC aqueous dispersion or Cin-CNC dispersion in THF on the glass. The static water contact angle (WCA) was measured by analyzing the images of 3 water droplets using MATLAB. The optical images were captured using an inverted optical microscope (Nikon Elipse Ti-S) equipped with a CCD camera (QImaging ReTIGA 2000R).

The surface tension of the Cin-CNC toluene suspension and the interfacial tension between toluene and water were measured on a Data Physics DCAT 21 tensiometer.

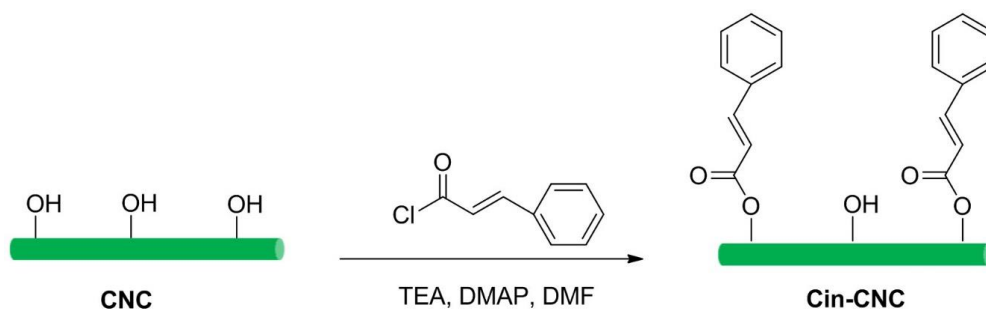
Scanning electron microscopy (SEM) measurements were performed on a Hitachi S4800 scanning electron microscope with an accelerating voltage of 2 kV.

## 6.3 Results and discussions

### 6.3.1 Preparation and characterization of the Cin-CNC Pickering emulsifier

The type of Pickering emulsions obtained with solid particles is determined by the particle wettability, expressed in terms of the three-phase contact angle  $\theta_w$  that particles make at the oil-water interface.<sup>84,91,96</sup> If  $\theta_w$  is lower than  $90^\circ$ , the solid particles have more affinity for the water phase (there are more hydrophilic), resulting in o/w Pickering emulsions. If  $\theta_w$  is higher than  $90^\circ$ , the solid particles have more affinity for the oil phase (they are more lipophilic), leading to inverse w/o Pickering emulsions.<sup>84</sup> Pristine CNC have demonstrated good performance in stabilizing various o/w emulsions systems, but they generally require the utilization of salt to screen the repulsion between the negatively charged particles.<sup>13,269-271</sup> Another method consists in adjusting the hydrophilic/lipophilic balance (HLB) at the CNC surface by chemical modification.<sup>49,89,92,95</sup> In particular, hydrophobic moieties can be grafted at the nanocellulose surface, to impart the surface with the right wettability ( $\theta_w > 90^\circ$ ) and stabilize w/o inverse Pickering emulsion.<sup>94,96</sup> In our study, this surface hydrophobization was performed by grafting hydrophobic cinnamate moieties at the CNC surface, through an acylation reaction with an excess of cinnamoyl chloride.

**Scheme 6.1. Synthetic route used to prepare the Cin-CNC Pickering emulsifier from cinnamoyl chloride.**



The CNC used were isolated by sulfuric acid hydrolysis of wood pulp, according to a general procedure described in the literature.<sup>16,149</sup> They consist of rod-like particles with estimated dimensions of  $110.3 \pm 47.7$  nm in length and  $4.8 \pm 1.1$  nm in diameter, based on a previous study performed with particles taken from the same batch (estimated from AFM pictures).<sup>28</sup> The amount of accessible hydroxyl groups

at their surface was estimated to be  $3.10 \pm 0.11 \text{ mmol.g}^{-1}$ , using a method based on phosphorylation coupled with  $^{31}\text{P}$  NMR and FT-IR analysis.<sup>28</sup> The CNC are also negatively charged (zeta-potential in water = -48 mV) due to the presence of sulfate ester groups at the surface, imparted by the sulphuric acid treatment. They form stable dispersions in water by ionic repulsion.

The surface modification of CNC was conducted by reaction with an excess cinnamoyl chloride in DMF for 24h at room temperature (Scheme 6.1). The successful grafting was confirmed by the FTIR spectroscopy (Figure 6.1). The Cin-CNC material displays additional signals characteristic of the grafted cinnamate moieties at  $1718 \text{ cm}^{-1}$  (C=O stretching),  $1635 \text{ cm}^{-1}$  (exocyclic C=C stretching) and  $765 \text{ cm}^{-1}$  (out-of-plane aromatic C-H bending).<sup>20</sup>

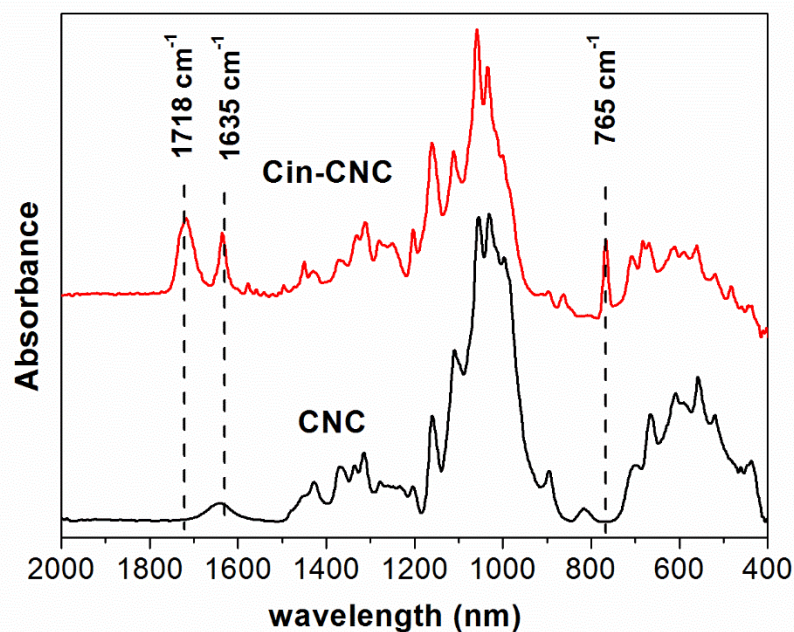


**Figure 6.1. FTIR spectra of pristine CNC and Cin-CNC.**

The morphologies of pristine CNC and Cin-CNC were compared by TEM image in Figure 6.2. The pristine CNC consist in rod-like particles, which are slightly aggregated due to the addition of  $\text{FeCl}_3$  before analysis, to stain the particles. After the esterification, the rod-like morphology of the cellulose nanocrystals is retained, and the dimensions of Cin-CNC estimated from the TEM images are  $\text{ca. } 138.9 \pm 35.4 \text{ nm}$  in length and  $8.1 \pm 3.2 \text{ nm}$  in diameter.

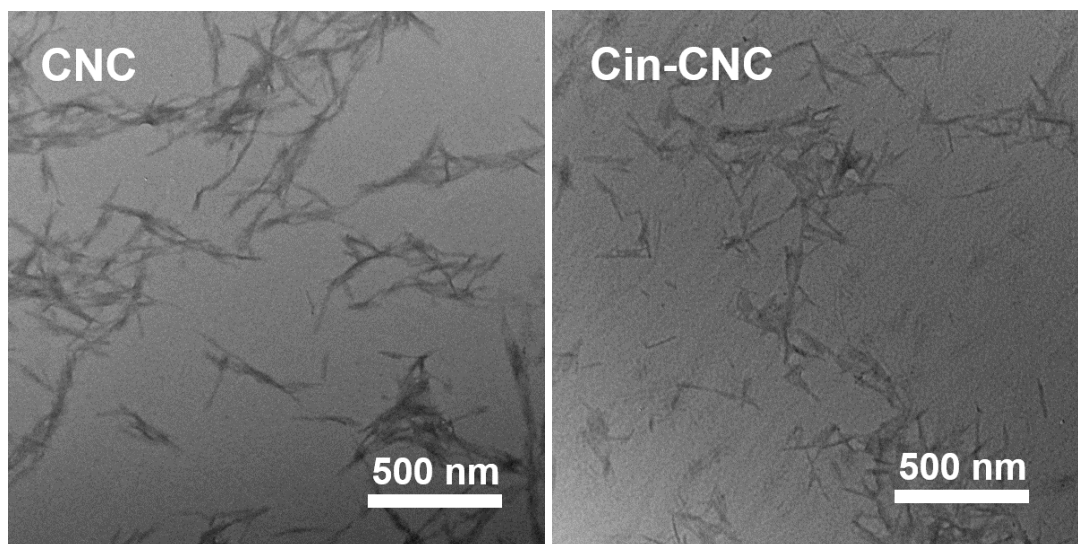


**Figure 6.2. TEM images of pristine CNC and Cin-CNC.**

The thermal stability of CNC and Cin-CNC was characterized by TGA. The thermograms and corresponding DTG derivatives are shown in Figure 6.3. The thermogram of pristine CNC is consistent with the thermal behavior generally observed for CNC bearing sulfate ester groups.<sup>68</sup> It exhibits a 6% weight loss below 100 °C, associated with the absorbed moisture. This weight loss is absent in the thermogram of Cin-CNC, due to the more hydrophobic character of this sample. The main decomposition temperature range of CNC is between 250 and 320 °C, with an onset degradation temperature ( $T_{\text{onset}}$ ) of 281 °C and maximum degradation temperature ( $T_{\text{max}}$ ) of 297 °C. After the modification, the Cin-CNC material displays a decreased thermal stability ( $T_{\text{onset}} = 263$  °C and  $T_{\text{max}} = 277$  °C), which was assigned to the thermal sensitivity of the cinnamate moieties since cinnamate derivatives can undergo radical *trans-cis* isomerization under thermal activation.<sup>234</sup> The cinnamate groups probably accelerated the degradation of cellulose, by promoting chain scissions through free-radical mechanisms.

After the functionalization, the Cin-CNC nanocrystals did not form stable dispersions in water, the turbid suspension flocculating progressively within hours (Figure 6.4). The dispersibility of the CNC and Cin-CNC particles in solvents of different polarities was investigated by DLS, through the measurement of the apparent hydrodynamic diameter ( $D_h$ ).

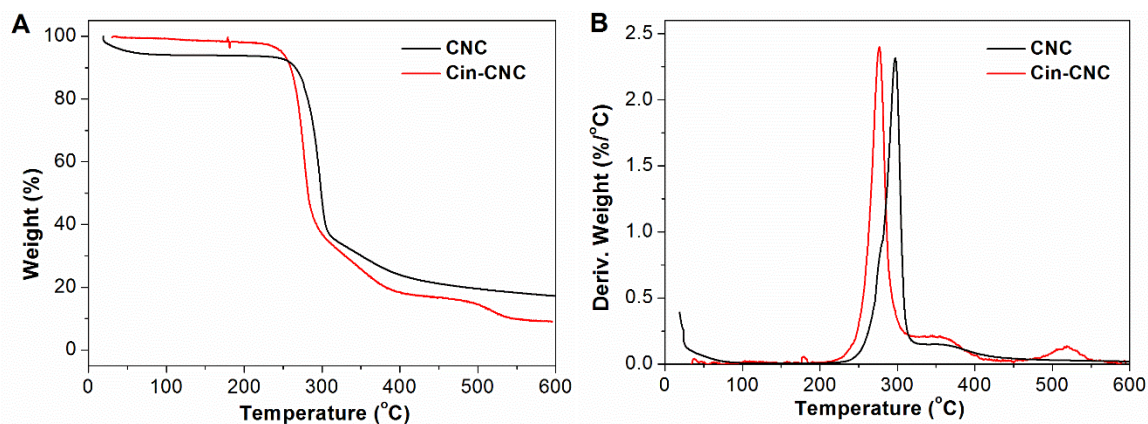


**Figure 6.3. TGA thermograms (A) and DTG curves (B) of pristine CNC and Cin-CNC.**

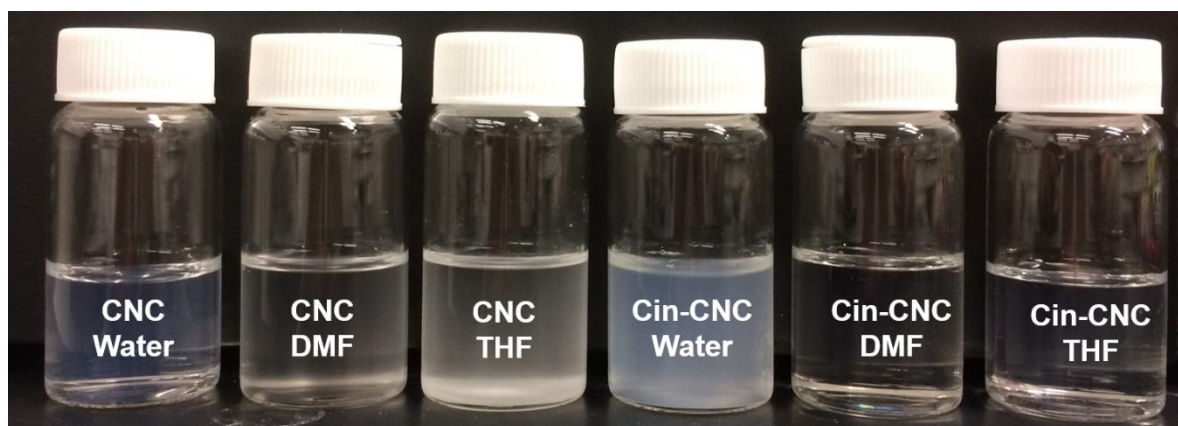


**Figure 6.4. Optical images of CNC and Cin-CNC dispersions in solvents of different polarity (the dielectric constants of water, DMF, and THF are 78.54, 38.25, and 7.52, respectively).**

The size distributions by intensity of CNC and Cin-CNC in water, DMF and THF are shown in Figure 6.5. The dispersibility of the unmodified CNC in water is quite good, the  $D_h$  measured by DLS (93 nm) being consistent with the length of the nano-rods estimated by AFM.<sup>28</sup> In DMF, the size distribution by intensity displays two peaks ( $D_{h1} = 189$  nm and  $D_{h2} = 645$  in Figure 6.5). This result suggests that the CNC tend to flocculate in DMF, although a clear suspension was obtained (Figure 6.5). The quality of the dispersion is still better than in the low polarity THF solvent, in which the CNC could not be

dispersed at all, even after strong sonication (Figure 6.4). After esterification, the Cin-CNC nanoparticles tend to flocculate in water ( $D_{h1} = 469$  nm and  $D_{h2} = 4708$  nm), while their dispersibility in DMF ( $D_h = 93$  nm) and THF ( $D_h = 189$  nm) is highly improved. This result is further confirmed by the turbidity observed in water and transparency obtained in DMF and THF (Figure 6.4).

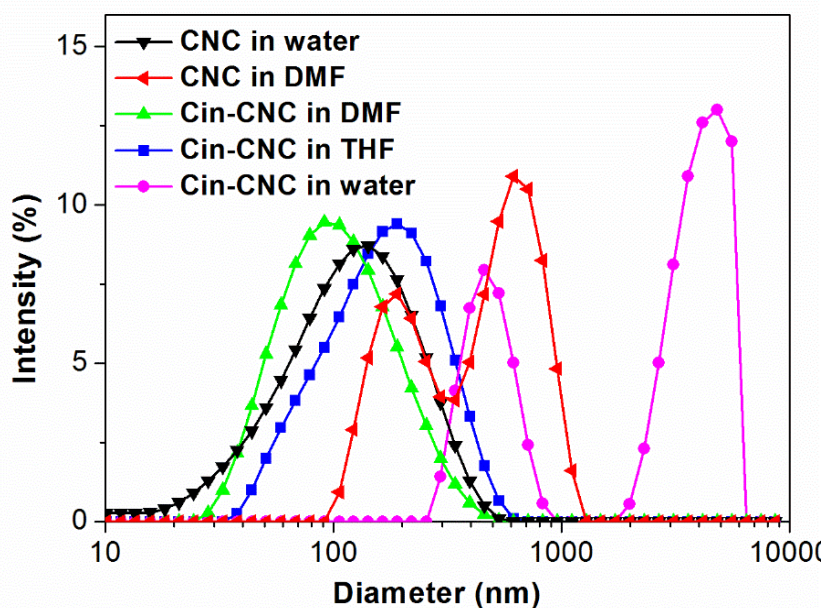


**Figure 6.5. Size distribution by intensity of the CNC and Cin-CNC particles dispersed in water, DMF or THF (0.2 mg/ml)**

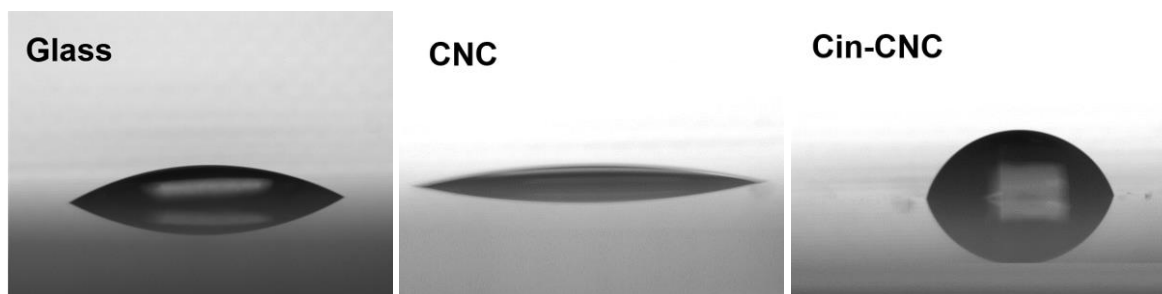


**Figure 6.6. Images of the water droplets deposited on the glass support, before and after spin-coating with the CNC and Cin-CNC material.**

The surface wettability of CNC and Cin-CNC was evaluated by WCA measurements performed at the surface of films prepared by spin-coating a water or THF dispersion (respectively) of the nanoparticles on glass supports. The water droplet images on the different surfaces are shown in Figure 6.6. The WCA on the pristine glass support is ca. 28.6°. The average WCA on CNC-coated glass is only ca. 14.0°, confirming the hydrophilic nature of the unmodified CNC. On the other hand, the WCA of Cin-CNC coated glass is about 75.9°, indicating that the grafted cinnamate moieties imparted some hydrophobic properties to the material.

### 6.3.2 Preparation and properties of the inverse Pickering emulsions stabilized by Cin-CNC

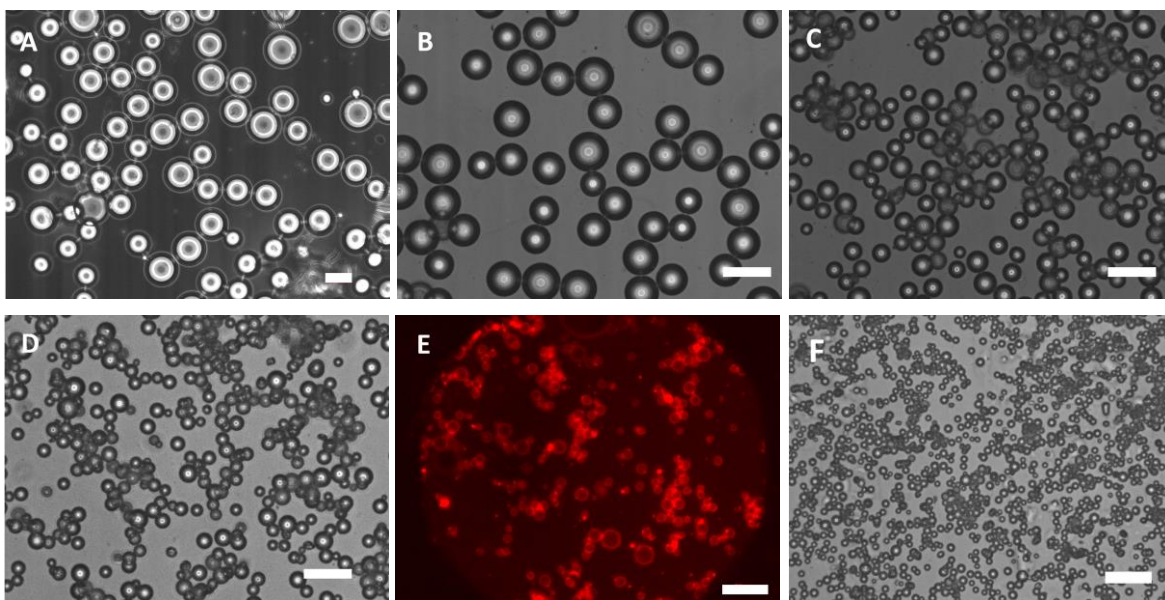


**Figure 6.7.** Optical micrographs of the inverse water/toluene emulsion droplets stabilized with different concentrations of Cin-CNC (A, 0.25 mg/mL; B, 0.5 mg/mL; C, 1 mg/mL; D, 2 mg/mL; E, 2 mg/mL; and F, 4 mg/mL); and fluorescent micrograph of the water droplets stained by rhodamine B (E). The length of scale bar in the micrographs is 50 μm.

In the current study, we were able to prepare stable w/o inverse emulsions using the Cin-CNC particles as Pickering emulsifiers. Water/toluene emulsions were prepared by sonicating a mixture of toluene, water and Cin-CNC for 30 s (final w/o ratio = 30/70 v/v). The emulsion type was inferred by observing

what happened when a drop of the emulsion was added to a volume of pure toluene. In addition, the production of w/o inverse emulsions was confirmed by preparing emulsions with water stained with rhodamine B and analyzing the droplets with a fluorescent microscope (Figure 6.7E). The suspensions were characterized 24 hours after emulsification, to allow time for the system to stabilize through the so-called limited coalescence process.<sup>276</sup>

The optical micrographs of the emulsion droplets obtained with various concentrations of Cin-CNC are shown in Figure 6.7. The size distribution of the emulsion droplets is presented in Figure 6.8. The emulsion diameter distribution fits the Gaussian distribution quite well. The dispersity of the emulsion droplets, defined as the ratio of volume-average diameter ( $D(4,3)$ ) relative to the number-average diameter ( $D(1,0)$ ),<sup>277</sup> is quite narrow (between 1.08 and 1.14). Stable inverse Pickering emulsions were obtained even when a low concentration of Cin-CNC was used (0.25 mg/mL), but the diameter of the droplets was higher in that case ( $D(1,0) = 62.0 \mu\text{m}$ ). As shown in Figure 6.8B, the  $D(1,0)$  of the emulsion droplets decreases with increasing Cin-CNC concentration, which is expected since more stabilizers can stabilize a larger interface. Our inverse water/toluene Pickering emulsions were stable for at least 6 months.

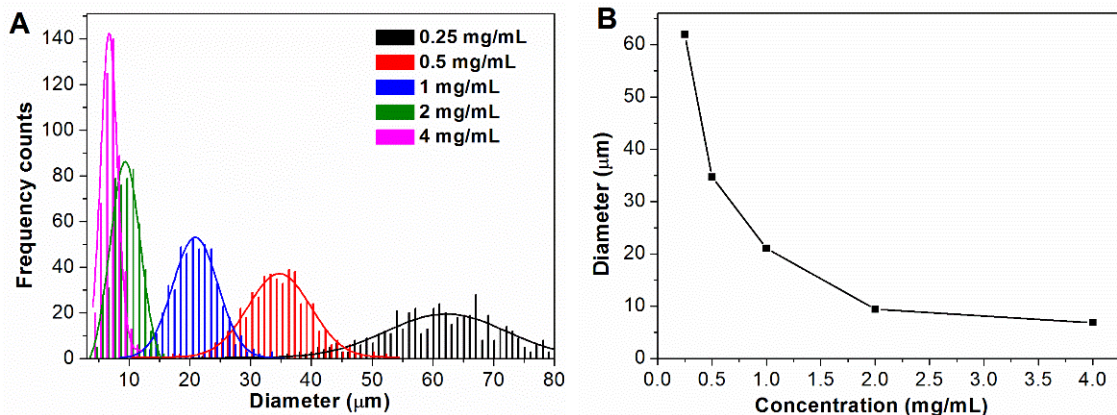


**Figure 6.8. Size distribution of the emulsion droplets obtained at different concentrations of Cin-CNC(A); and number-average diameter  $D(1,0)$  as a function of Cin-CNC concentration.**

The evolution of the inverse diameter  $1/D(3,2)$  as a function of Cin-CNC concentration is shown in Figure 6.9, where  $D(3,2)$  is the surface-average diameter. In agreement with the limited coalescence

mechanism, the  $1/D(3,2)$  increases linearly with Cin-CNC concentration when the Cin-CNC concentration is between 0.25 and 2 mg/mL ( $R^2 = 0.996$ ), indicating that the surface coverage is constant in this range of concentration.<sup>49</sup> This “minimum” surface coverage can be calculated using the equation below:<sup>85,270,278</sup>

$$1/D(3,2) = [\text{Cin-CNC}]V_{\text{oil}}/(6h\rho V_{\text{water}}C)$$

where [Cin-CNC] is the concentration of Cin-CNC in the oil phase, C is the surface coverage, h is the thickness of the Cin-CNC (equal to the diameter of Cin-CNC nanoparticles, about 8 nm from the TEM images of Cin-CNC),  $\rho$  is the density of Cin-CNC (assume that the density of Cin-CNC is equal to the density of CNC, about 1.6 g/cm<sup>3</sup>),  $V_{\text{oil}}$  is the volume of the oil phase (7 mL), and  $V_{\text{water}}$  is the volume of the water phase (3 mL).

According to this calculation, a minimum surface coverage of ca. 62% is sufficient to stabilize our water/toluene inverse emulsion system, which is in agreement with the values found in the literature for other systems stabilized by CNC Pickering surfactants.<sup>13,49,89,270</sup> When the Cin-CNC concentration is increased to 4 mg/mL, the  $1/D(3,2)$  value is far below the fitting line, indicating that the surface coverage is higher than the minimum surface coverage (this coverage reaches 90% according to our calculations).

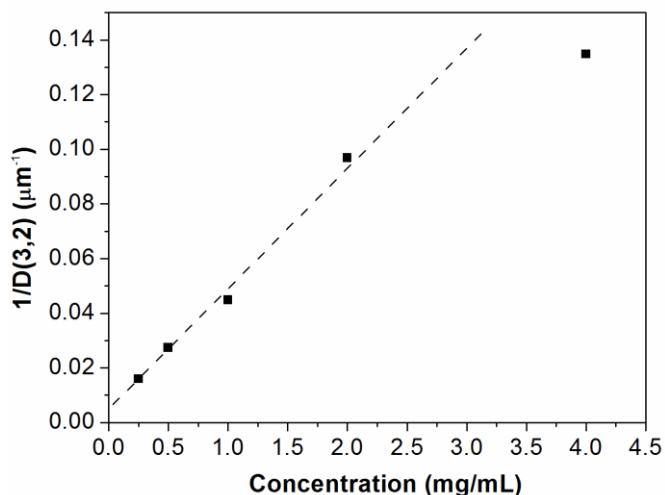


**Figure 6.9. Evolution of  $1/D(3,2)$  as a function of Cin-CNC concentration.**

In traditional emulsions with amphiphilic surfactants, the emulsions are stabilized because the interfacial tension between oil and water is reduced. In Pickering emulsions, solid particles are irreversibly adsorbed at the interphase of water and oil, and the reduction of interfacial tension is not compulsory.<sup>90,279</sup> To verify the point, the surface tension of Cin-CNC toluene suspension and interfacial tension between toluene and water was measured as a function of Cin-CNC concentration in Figure 6.10. The surface tension did not vary with Cin-CNC concentration; the interfacial tension slightly decreased but remained constant for a wide range of Cin-CNC concentrations (up to 10 mg/mL). Therefore, the mechanism of stabilization is based on the partial wetting of the Cin-CNC particles with both the oil and water phases, as expected.

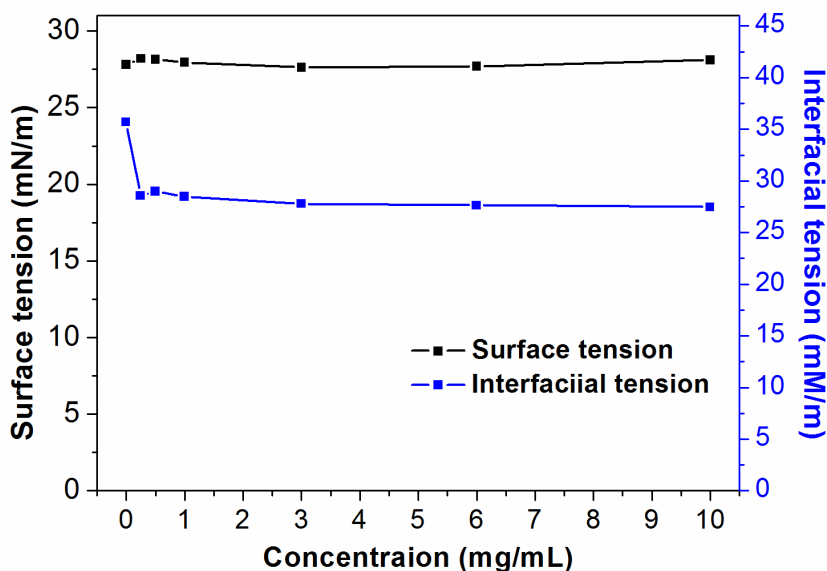


**Figure 6.10. Evolution of surface tension of the Cin-CNC toluene suspension and interfacial tension between toluene and water as a function of Cin-CNC concentration.**

### 6.3.3 Preparation and characterization of Cin-CNC/Silica colloidosomes

To obtain colloidosomes from our water/toluene inverse Pickering emulsions, we envisaged using tetraethyl orthosilicate (TEOS) or tetrabutyl orthosilicate (TBOS) as sol-gel precursors to lock the Cin-CNC nanoparticles surrounding the droplets, as shown in Scheme 6.2.

**Scheme 6.2. Schematic representation of the method used to prepare the Cin-CNC/Silica colloidosomes.**

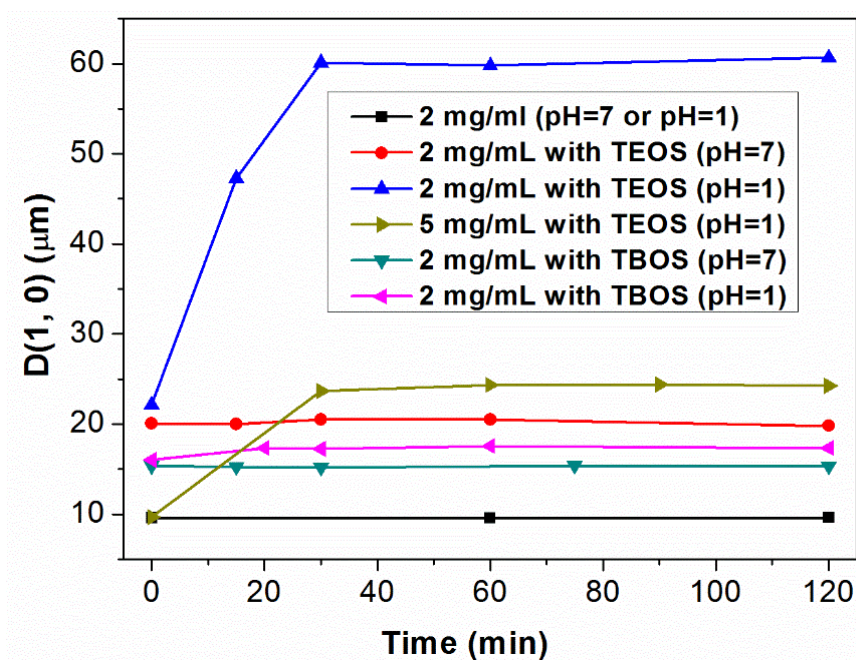
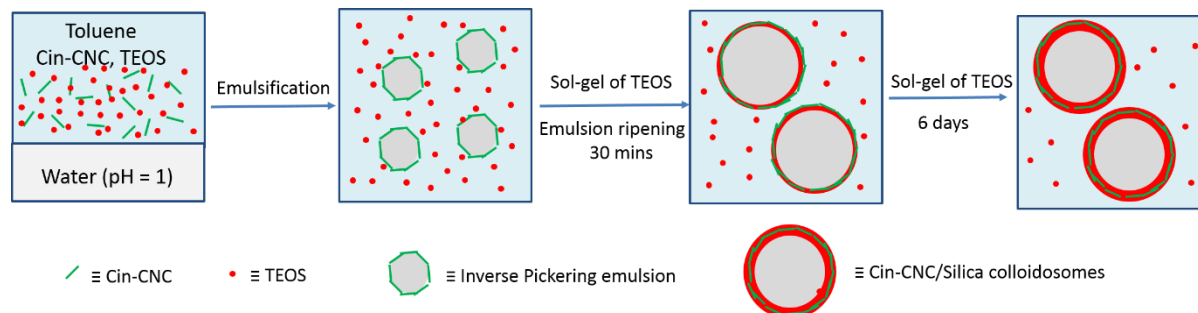


**Figure 6.11. Evolution with time of the number-average diameter  $D(1,0)$  of the emulsion droplets in the Pickering systems containing TEOS or TBOS precursors (pH = 1 or 7; [Cin-CNC] = 2 or 5 mg/mL).**

Water/toluene inverse Pickering emulsions were prepared at pH 1 or 7 in the presence of TEOS or TBOS precursors, and the evolution with time of the droplets diameter  $D(1,0)$  was measured (Figure

6.11). Without silica precursors ( $[\text{Cin-CNC}] = 2 \text{ mg/mL}$ ), the droplet diameter is stable with time (at about  $9.6 \text{ }\mu\text{m}$ ) and does not vary with pH. When TEOS is added at  $\text{pH} = 7$ , the droplets diameter is also stable with time, but the droplets size is increased to  $20.3 \text{ }\mu\text{m}$ . When TEOS is added at  $\text{pH} = 1$ , the droplets diameter increases significantly from  $22.1$  to  $60.1 \text{ }\mu\text{m}$  during the initial 30 mins, due to the reactivity of TEOS at this pH. TEOS is not soluble in water, but is expected to hydrolyze and condense at the water/toluene interface at  $\text{pH} = 1$ , to form an intricate network of polysiloxane within the Cin-CNC shell.<sup>104,105,268</sup> The increase in droplets size observed can then be explained by the ethanol released in the course of the reaction, which is soluble in water and increases the droplet volume. This increase stops when the cellulosic shell is sufficiently rigidified by the crosslinked silica layer (after 30 min). When the Cin-CNC concentration is increased to  $5 \text{ mg/mL}$ , the increase in droplet size during the first 30 min is still observed, but the final size is a smaller size ( $24.2 \text{ }\mu\text{m}$ ), which is consistent with the better coverage expected at this concentration. To further confirm that ethanol is responsible for the variations in droplet size, water/toluene droplets were observed by optical microscopy while ethanol was progressively added in the emulsion system (Figure 6.12). An increase in droplet size was indeed observed when more ethanol was added, in coherence with the so-called Ostwald ripening process.<sup>91,96,260,280</sup>

When TEOS was replaced by TBOS at  $\text{pH} 7$  ( $[\text{Cin-CNC}] = 2 \text{ mg/mL}$ ), the droplets diameter decreased to  $15.3 \text{ }\mu\text{m}$  (instead of  $20.3 \text{ }\mu\text{m}$ ), supposedly because TBOS has more affinity with the Cin-CNC particles. At  $\text{pH} = 1$ , the emulsion size increased only slightly during the first 30 min (from  $16.0$  to  $17.4 \text{ }\mu\text{m}$ ), which was explained by the limited miscibility of the butanol released in water.

The morphology of the different inverse Pickering emulsions, before and after the evaporation of the toluene, was characterized by optical microscope (Figure 6.13). When no silica precursor is added, the inverse Pickering emulsion is broken as soon as the toluene is evaporated (Figure 6.13D). With TEOS, the emulsion is also quickly broken at  $\text{pH} = 7$  (Figure 6.13E), but the droplets retain their spherical shape at  $\text{pH} = 1$  (Figure 6.13F), suggesting that the Cin-CNC shell at the droplets surface was locked by the silica layer formed after hydrolysis and condensation of TEOS at this pH (the particles displayed a crumpled surface).

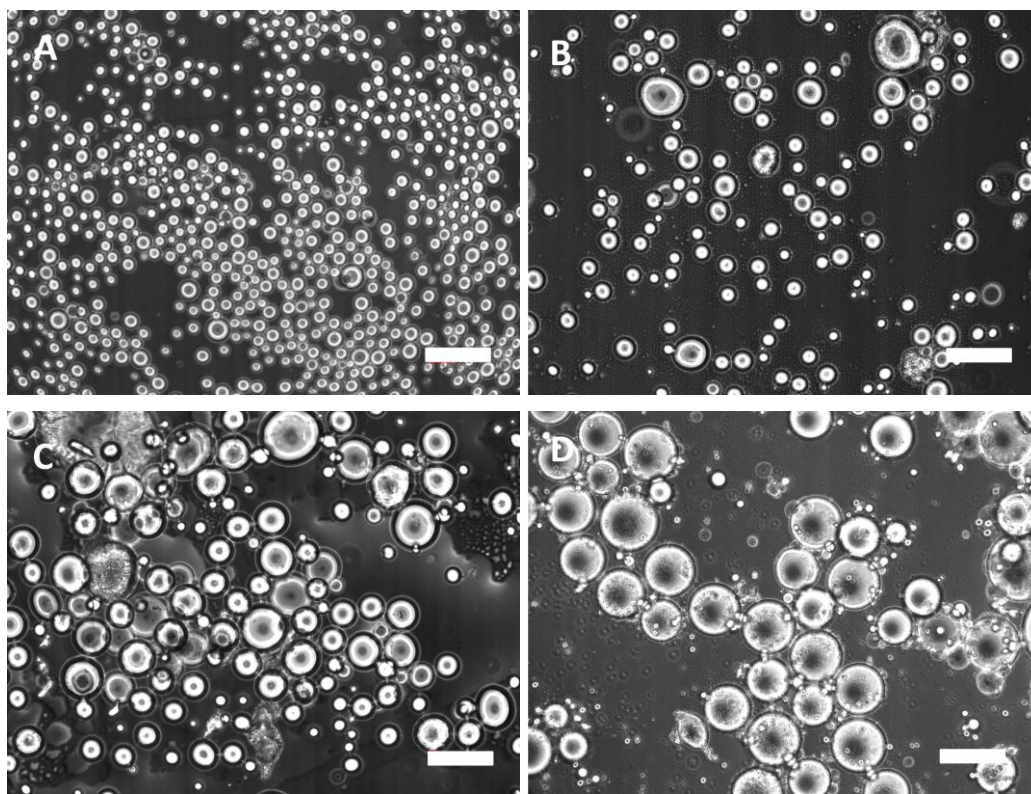


**Figure 6.12. Evolution of the inverse water/toluene emulsion droplets with increasing amounts of ethanol: A, 0  $\mu\text{L}$ ; B, 20  $\mu\text{L}$ ; C, 40  $\mu\text{L}$ ; and D, 100  $\mu\text{L}$  (initial volume = 200  $\mu\text{L}$ ; pH = 7; ([Cin-CNC] = 2 mg/mL) The length of scale bar in the optical micrographs is 100  $\mu\text{m}$ .**

The sol-gel reaction at the water/toluene interface is initially fast at pH = 1, but is expected to slow down while the silica layer is progressively formed.<sup>105</sup> An incomplete reaction should have a negative impact on the mechanical strength of the colloidosome shell. Therefore, the impact of cross-linking time was investigated by cross-linking colloidosomes with TEOS for 2 or 6 days at room temperature. The capsules obtained were then diluted in ethanol and observed by optical microscopy (Figure 6.14). After two days, the Cin-CNC/silica colloidosomes were not strong enough and quickly broke in contact with ethanol (Figure 6.14A). On the other hand, the colloidosomes cross-linked for 6 days retained their integrity in ethanol, and supported mild sonication or freeze-drying. A cross-linking time of at least 6 days was required to form a robust silica layer with TEOS as a precursor, but 10 days were necessary with TBOS.

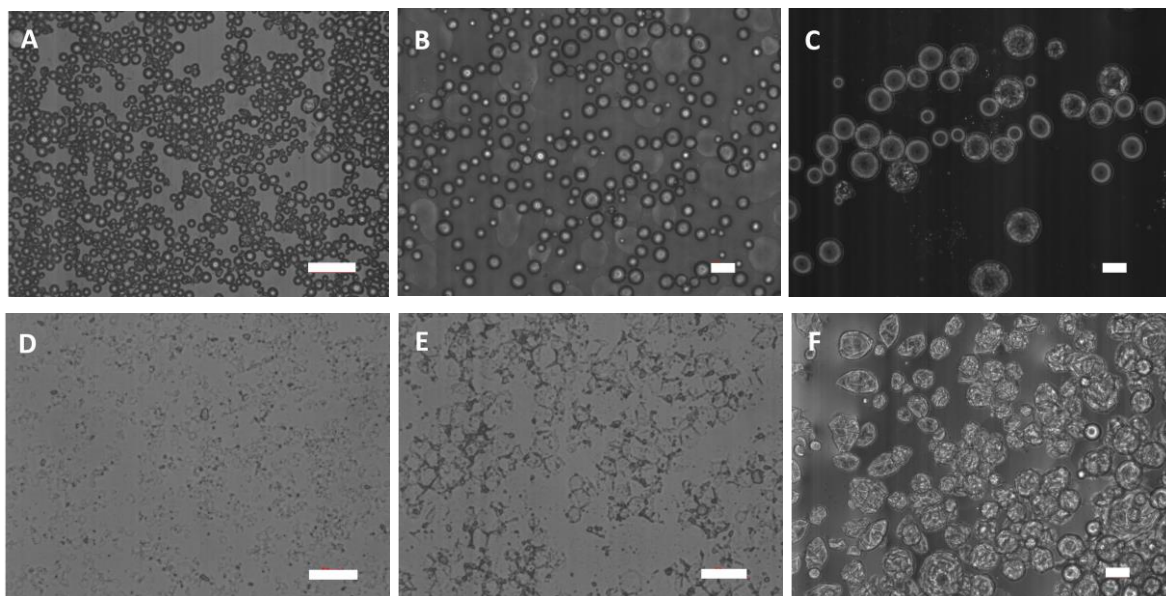


**Figure 6.13.** Optical micrographs of the inverse water/toluene emulsion droplets before (A, B, C) and after (D, E, F) evaporation of the toluene (for 6 days at room temperature): A&D, without TEOS; B&E, with TEOS at pH =7; C&F, with TEOS at pH =1 ([Cin-CNC] =2 mg/mL). The length of scale bar in the micrographs is 50  $\mu\text{m}$ .

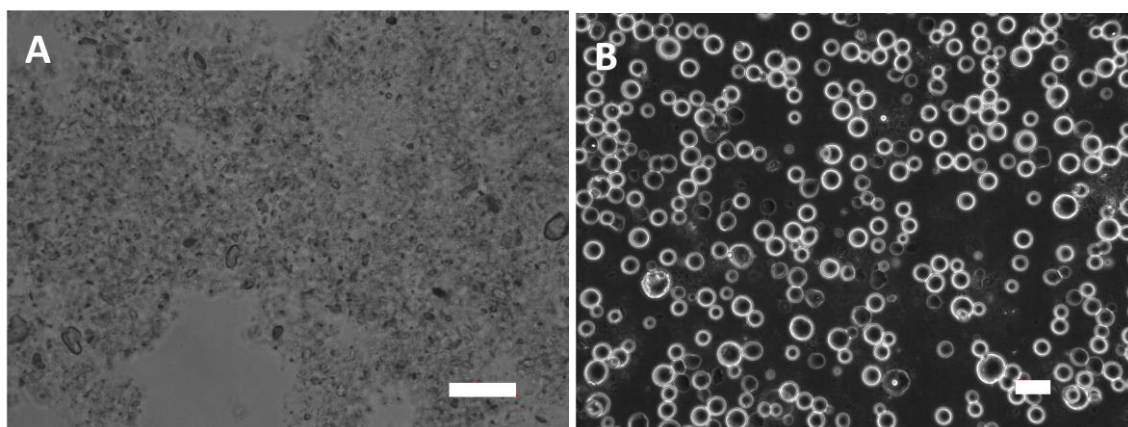


**Figure 6.14.** Optical micrographs of the colloidosomes cross-linked with TEOS for 2 days (A) or 6 days (B) and diluted in EtOH. ([Cin-CNC] =5 mg/mL; pH =1). The length of scale bar in the optical micrographs is 50  $\mu\text{m}$ .

The morphology of the Cin-CNC/silica colloidosomes was also characterized by SEM (Figure 6.15). The colloidosomes are spherical (Figure 6.16.A), with a shell thickness of about 1.2  $\mu\text{m}$ , estimated from the picture of a broken colloidosome (Figure 6.16.B).

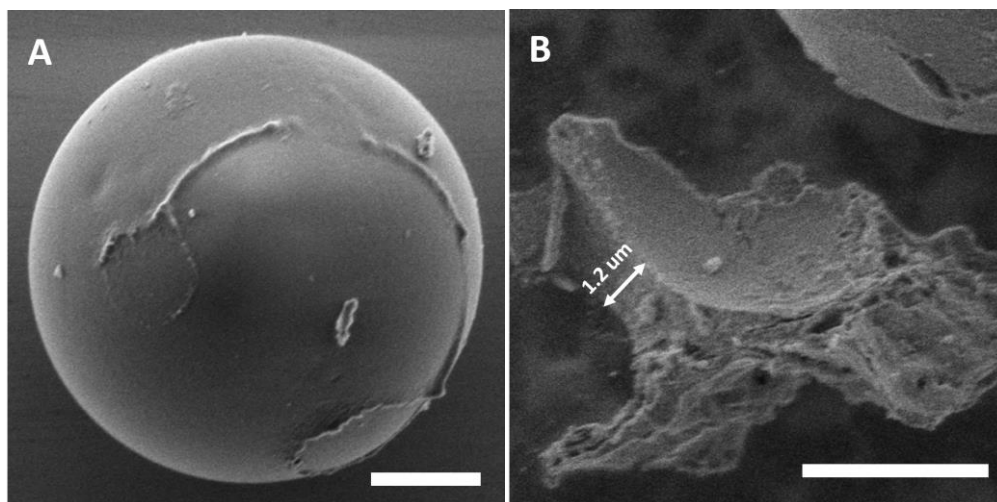


**Figure 6.15. SEM images of Cin-CNC/silica colloidosomes crosslinked with TEOS for 6 days ([Cin-CNC] = 5 mg/mL). The length of the scales bars in the optical micrographs is 5  $\mu\text{m}$ .**

The encapsulating properties of the Cin-CNC/silica colloidosomes were investigated by preparing samples with water solutions of rhodamine B or fluorescent DNA (FAM-A<sub>15</sub>). The colloidosomes obtained were observed by fluorescent optical microscopy, which confirmed the encapsulation of the molecules (Figure 6.16). When the colloidosomes containing rhodamine B were isolated and placed in water, no rhodamine B was released even after three months. Therefore, the compact Cin-CNC/Silica shell structure displays a low permeability to rhodamine B, as in the case of the silica colloidosomes prepared in the literature.<sup>104,105</sup> With fluorescent DNA, no encapsulated molecules were released after two months, confirming further the slow releasing capacity of this material.

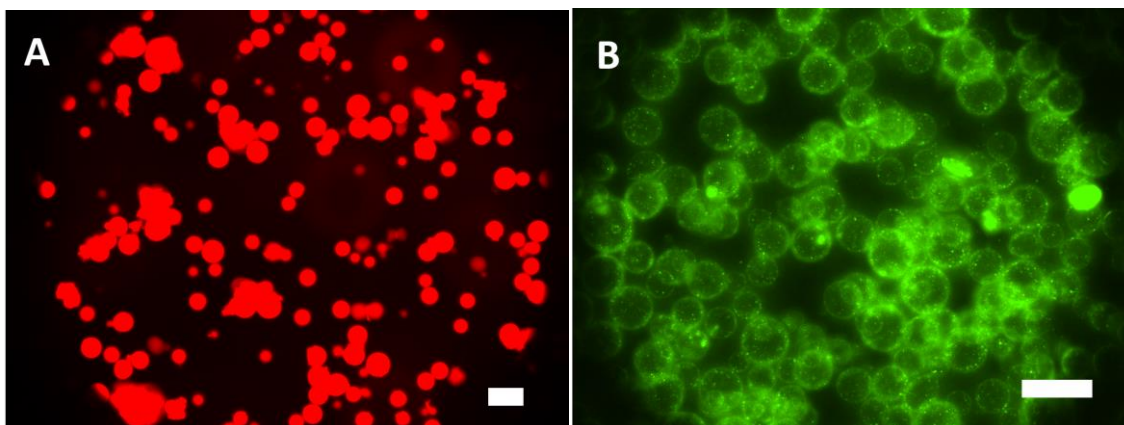


**Figure 6.16. Fluorescent optical micrographs of the colloidosome after encapsulation of rhodamine B (A) or fluorescent DNA (B). ([Cin-CNC] =5 mg/mL; pH =1). The length of scale bar in the optical micrographs is 50  $\mu\text{m}$ .**

## 6.4 Conclusions

In this study, we developed a facile method to prepare colloidosomes from w/o inverse Pickering emulsions containing silica precursors and stabilized by chemically modified cellulose nanocrystals. Cin-CNC Pickering surfactants were prepared by acylation with an excess of cinnamoyl chloride. The grafting of cinnamate moieties at the CNC surface imparted the material with hydrophobic properties, which improved its dispersibility in hydrophobic solvents such as THF. In addition, the Cin-CNC surface displayed partial wettability with both toluene and water, which was utilized to stabilize w/o inverse Pickering emulsions. The size of the water emulsion droplets was found to decrease with increasing Cin-CNC concentration, in agreement with the limited coalescence process. A minimum surface coverage of ca. 62% was sufficient to stabilize the emulsion system. To obtain colloidosomes from these dispersions, the Cin-CNC particles around the droplets were locked by cross-linking TEOS or TBOS silica precursors at the water/toluene interface, leading to the formation of an intricate network of polysiloxane within the Cin-CNC shell. In optimized conditions, the Cin-CNC/silica colloidosomes obtained displayed a robust shell and slow releasing capacity with regards to encapsulated molecules such as rhodamine B or fluorescent DNA.

## Chapter 7

### General Conclusions

In this thesis, the surface functionalization of cellulose nanocrystals by esterification and ATRP reactions was envisaged, with the objective to develop novel advanced materials.

We first developed a convenient method to characterize directly the polymer grafted on the CNC surface by SI-ATRP, without cleaving the polymer from the nanoparticle. PS was selected as a model polymer, as its surface grafting by ATRP has been performed on a wide variety of substrates and is well documented in the literature. DLS proved to be a convenient tool to monitor the polymerization process through the measure of the hydrodynamic radius of the PS-g-CNC nanoparticles, which was found to increase linearly with the molecular weight of the free polymer. The DSC curves of the PS-g-CNC particles confirmed that the molecular weight of the grafted PS was correlated with the molecular weight of the free PS. We also developed an original method based on TGA, to directly estimate the molecular weight of the PS grafted at the surface of the CNC without cleaving the polymer from the nanoparticle, by comparing the weight losses imparted to the cellulosic material and grafted PS.

After this work, the efficiencies of the SI-ATRP and SI-ARGET ATRP methods to initiate the grafting of polymer chains at the CNC surface were compared. Br initiating sites were first introduced at the surface of the CNC by esterification with BIBB (CNC-Br) and subsequently reacted with styrene (St) or 4-vinylpyridine (4VP) in the presence of a sacrificial initiator. The combination of analytical methods such as FT-IR, DLS, DSC, TGA, and EA allowed demonstrating that the SI-ARGET ATRP reaction favored the grafting of longer polymer chains with lower grafting densities compared with the classical SI-ATRP method. While almost all initiating sites on CNC-Br reacted by SI-ATRP, only 6-7% of the sites reacted by SI-ARGET ATRP, with both St and 4VP. This result was assigned to the low catalyst concentration at stake in the SI-ARGET ATRP process and the high  $R_p$  of the reaction, which presumably resulted in a mushroom-like regime at the surface of the CNC. Distinctively, a brush-like regime was favored with classical SI-ATRP due to the higher catalyst concentration and lower  $R_p$ . The pH-responsive P4VP-g-CNC nanohybrids prepared by SI-ATRP were subsequently utilized to stabilize gold nanoparticles (Au NPs), in view of producing recyclable catalysts. The pH-responsive

solubility in water of the P4VP-*g*-CNC hybrids was demonstrated by DLS and Zeta-potential measurements. Gold nanoparticles were subsequently deposited at the surface of P4VP-*g*-CNC by reducing H<sub>2</sub>AuCl<sub>4</sub> with sodium borohydride (NaBH<sub>4</sub>) in the presence of the nanocellulosic material. The presence of P4VP brushes at the CNC surface led to the growing of Au NPs of lower averaged diameter (2.9 nm) compared with the diameter of the Au NPs deposited on pristine CNC (10.6 nm). The catalytic performance of pristine Au NPs, Au@CNC and Au@P4VP-*g*-CNC were then compared, through the measurement of the turnover frequency (TOF) obtained after catalytic reduction of 4-nitrophenol (4NP), used as a model reaction. Compared with pristine Au NPs, the catalytic activity of Au@CNC and Au@P4VP were about 10 and 24 times better, respectively (TOF = 2275.2 h<sup>-1</sup> and 5533.2 h<sup>-1</sup>, respectively). Distinctively from Au@CNC, the Au@P4VP-*g*-CNC material could be conveniently recovered by flocculation at basic pH (pH > 6), and the recycled catalyst still displayed a relatively high activity for the reduction of 4NP (TOF = 3124.8 h<sup>-1</sup>).

The SI-ATRP method was further extended to the grafting of poly(cinnamoyloxy ethyl methacrylate chains (PCEM-*g*-CNC) to impart UV-absorbing properties to the material. The PCEM-*g*-CNC nanohybrids were then employed as UV/thermal stabilizers and reinforcing agents in PVC films. The photoactivity of the grafted cinnamate moieties was demonstrated by analyzing PCEM-*g*-CNC films before and after irradiation at 365 nm. When the PCEM-*g*-CNC nanohybrids were incorporated in PVC, transparent composite films were obtained. The comparison of the optical and mechanical properties of the films before and after UV-irradiation at 365 nm allowed demonstrating that the PCEM-*g*-CNC nanoparticles acted as thermal and UV-stabilizers for PVC. The material also displayed UV-blocking properties, while the high transparency in the visible range was preserved. Meanwhile, the tensile mechanical properties of the PVC film were significantly improved after incorporation of the PCEM-*g*-CNC filler. A further increase in the mechanical performance of the composite film was even noted after UV-irradiation, which could result from a radical coupling between the grafted PCEM chains and the PVC matrix.

Finally, we developed a facile method to prepare colloidosomes from w/o inverse Pickering emulsions containing silica precursors and stabilized by chemically modified cellulose nanocrystals. Cin-CNC Pickering surfactants were prepared by acylation with an excess of cinnamoyl chloride. The grafting of

cinnamate moieties at the CNC surface imparted the material with partial wettability with both toluene and water, allowing the stabilization of w/o inverse Pickering emulsions. A minimum surface coverage of ca. 62% was sufficient to stabilize the emulsion system. To obtain colloidosomes from these dispersions, the Cin-CNC particles around the droplets were locked by cross-linking TEOS or TBOS silica precursors at the water/toluene interface, leading to the formation of an intricate network of polysiloxane within the Cin-CNC shell. In optimized conditions, the Cin-CNC/silica colloidosomes obtained displayed a robust shell and slow releasing capacity with regards to encapsulated molecules such as rhodamine B or fluorescent DNA.

The engineering of innovative nanomaterials from CNC generally requires a fine control of their surface properties by chemical modification, to tailor their dispersive, interfacial and self-assembling properties, or to introduce novel functionalities. In this thesis, the surface functionalization of cellulose nanocrystals by esterification and ATRP reactions was successfully performed, and the benefit of the modifications performed for a selection of advanced applications was demonstrated. Based on the research and results in this project, the following recommendations are proposed for the future studies of CNC.

- (1) The SI-ATRP is a promising method to graft polymers on the surface of CNC with high grafting density and controlled  $M_n$ . A variety of functional polymers can be grafted on CNC via SI-ATRP. The polymer-g-CNC can be exploited in broad applications, such as hydrogel, aerogel, Pickering emulsion, antibacterial, et al.
- (2) A variety of metal or metal NPs can be stabilized by P4VP-g-CNC, and the NPs stabilized by P4VP-g-CNC can be used as catalysts in many fields.
- (3) PCEM-g-CNC can be exploited in many UV-blocking applications, such as UV-blocking PMMA, UV-blocking glasses and so on. PCEM-g-CNC also can be used to reinforce many polymer matrices. PCEM-g-CNC has potential application for self-healing materials due to the UV-induced crosslinking.
- (4) Many o/w or inverse w/o Pickering emulsions systems can be obtained through the control of the surface properties of the CNC by esterification or ATRP reactions. These systems can be used as the

templates to conduct interfacial reactions at the surface of emulsion droplets, which can find application in food and drug delivery.

## Bibliography

- (1) Klemm, D.; Kramer, F.; Moritz, S.; Lindström, T.; Ankerfors, M.; Gray, D.; Dorris, A. *Angewandte Chemie International Edition* **2011**, *50*, 5438.
- (2) Peng, B. L.; Dhar, N.; Liu, H. L.; Tam, K. C. *The Canadian Journal of Chemical Engineering* **2011**, *89*, 1191.
- (3) Habibi, Y.; Lucia, L. A.; Rojas, O. J. *Chemical Reviews* **2010**, *110*, 3479.
- (4) Eichhorn, S. J. *Soft Matter* **2011**, *7*, 303.
- (5) Qiu, X.; Hu, S. *Materials* **2013**, *6*, 738.
- (6) Moon, R. J.; Martini, A.; Nairn, J.; Simonsen, J.; Youngblood, J. *Chemical Society Reviews* **2011**, *40*, 3941.
- (7) Zhu, H.; Luo, W.; Ciesielski, P. N.; Fang, Z.; Zhu, J. Y.; Henriksson, G.; Himmel, M. E.; Hu, L. *Chem Rev* **2016**, *116*, 9305.
- (8) Postek, M. T.; Vladár, A.; Dagata, J.; Farkas, N.; Ming, B.; Wagner, R.; Raman, A.; Moon, R. J.; Sabo, R.; Wegner, T. H.; Beecher, J. *Measurement Science and Technology* **2011**, *22*, 024005.
- (9) Roy, D.; Semsarilar, M.; Guthrie, J. T.; Perrier, S. *Chemical Society Reviews* **2009**, *38*, 2046.
- (10) Siqueira, G.; Bras, J.; Dufresne, A. *Polymers* **2010**, *2*, 728.
- (11) Siqueira, G.; Kokkinis, D.; Libanori, R.; Hausmann, M. K.; Gladman, A. S.; Neels, A.; Tingaut, P.; Zimmermann, T.; Lewis, J. A.; Studart, A. R. *Advanced Functional Materials* **2017**, *27*, 1604619.
- (12) Reid, M. S.; Villalobos, M.; Cranston, E. D. *Langmuir* **2017**, *33*, 1583.
- (13) Kalashnikova, I.; Bizot, H.; Bertoncini, P.; Cathala, B.; Capron, I. *Soft Matter* **2013**, *9*, 952.
- (14) Rånby, B. G. *Acta Chemica Scandinavica* **1949**, *3*, 649.
- (15) Elazzouzi-Hafraoui, S.; Nishiyama, Y.; Putaux, J.-L.; Heux, L.; Dubreuil, F.; Rochas, C. *Biomacromolecules* **2008**, *9*, 57.
- (16) DONG, X. M.; REVOL, J.-F.; GRAY, D. G. *Cellulose* **1998**, *5*, 19.
- (17) Peng, Y.; Gardner, D. J.; Han, Y.; Kiziltas, A.; Cai, Z.; Tshabalala, M. A. *Cellulose* **2013**, *20*, 2379.
- (18) Li, W. D.; Ding, E. Y. *Journal of Applied Polymer Science* **2007**, *105*, 373.
- (19) Okahisa, Y.; Yoshida, A.; Miyaguchi, S.; Yano, H. *Composites Science and Technology* **2009**, *69*, 1958.
- (20) Sèbe, G.; Ham-Pichavant, F.; Pecastaings, G. *Biomacromolecules* **2013**, *14*, 2937.
- (21) Shopsowitz, K. E.; Qi, H.; Hamad, W. Y.; MacLachlan, M. J. *Nature* **2010**, *468*, 422.
- (22) Liu, Q.; Campbell, M. G.; Evans, J. S.; Smalyukh, I. I. *Advanced Materials* **2014**, *26*, 7178.
- (23) Chen, Q.; Liu, P.; Sheng, C.; Zhou, L.; Duan, Y.; Zhang, J. *RSC Advances* **2014**, *4*, 39301.
- (24) Tingaut, P.; Zimmermann, T.; Sebe, G. *Journal of Materials Chemistry* **2012**, *22*, 20105.

- (25) Orts, W. J.; Godbout, L.; Marchessault, R. H.; Revol, J. F. *Macromolecules* **1998**, *31*, 5717.
- (26) Tang, J.; Sisler, J.; Grishkewich, N.; Tam, K. C. *J Colloid Interface Sci* **2017**, *494*, 397.
- (27) Chen, J.; Wu, D.; Tam, K. C.; Pan, K.; Zheng, Z. *Carbohydr Polym* **2017**, *157*, 1821.
- (28) Brand, J.; Pecastaings, G.; Sèbe, G. *Carbohydrate Polymers* **2017**, *169*, 189.
- (29) Eyley, S.; Thielemans, W. *Nanoscale* **2014**, *6*, 7764.
- (30) Zhang, P. P.; Tong, D. S.; Lin, C. X.; Yang, H. M.; Zhong, Z. K.; Yu, W. H.; Wang, H.; Zhou, C. H. *Asia-Pacific Journal of Chemical Engineering* **2014**, *9*, 686.
- (31) Zoppe, J. O.; Xu, X.; Kanel, C.; Orsolini, P.; Siqueira, G.; Tingaut, P.; Zimmermann, T.; Klok, H. A. *Biomacromolecules* **2016**, *17*, 1404.
- (32) Braun, B.; Dorgan, J. R. *Biomacromolecules* **2009**, *10*, 334.
- (33) Saito, T.; Nishiyama, Y.; Putaux, J.-L.; Vignon, M.; Isogai, A. *Biomacromolecules* **2006**, *7*, 1687.
- (34) Li, W. Y.; Jin, A. X.; Liu, C. F.; Sun, R. C.; Zhang, A. P.; Kennedy, J. F. *Carbohydrate Polymers* **2009**, *78*, 389.
- (35) Kloser, E.; Gray, D. G. *Langmuir* **2010**, *26*, 13450.
- (36) Habibi, Y.; Dufresne, A. *Biomacromolecules* **2008**, *9*, 1974.
- (37) Chen, L.; Lai, C.; Marchewka, R.; Berry, R. M.; Tam, K. C. *Nanoscale* **2016**, *8*, 13288.
- (38) Zhang, Z.; Sèbe, G.; Rentsch, D.; Zimmermann, T.; Tingaut, P. *Chemistry of Materials* **2014**, *26*, 2659.
- (39) Wu, L.; Glebe, U.; Boker, A. *Polymer Chemistry* **2015**, *6*, 5143.
- (40) Carlmark, A.; Malmström, E. E. *Biomacromolecules* **2003**, *4*, 1740.
- (41) Lindqvist, J.; Malmström, E. *Journal of Applied Polymer Science* **2006**, *100*, 4155.
- (42) Matyjaszewski, K.; Xia, J. *Chemical Reviews* **2001**, *101*, 2921.
- (43) Matyjaszewski, K. *Macromolecules* **2012**, *45*, 4015.
- (44) Zoppe, J. O.; Habibi, Y.; Rojas, O. J.; Venditti, R. A.; Johansson, L.-S.; Efimenko, K.; Österberg, M.; Laine, J. *Biomacromolecules* **2010**, *11*, 2683.
- (45) Roy, D.; Guthrie, J. T.; Perrier, S. *Macromolecules* **2005**, *38*, 10363.
- (46) Morandi, G.; Heath, L.; Thielemans, W. *Langmuir* **2009**, *25*, 8280.
- (47) Lin, N.; Huang, J.; Dufresne, A. *Nanoscale* **2012**, *4*, 3274.
- (48) de Castro, D. O.; Bras, J.; Gandini, A.; Belgacem, N. *Carbohydr Polym* **2016**, *137*, 1.
- (49) Tang, J.; Lee, M. F. X.; Zhang, W.; Zhao, B.; Berry, R. M.; Tam, K. C. *Biomacromolecules* **2014**, *15*, 3052.
- (50) Kan, K. H. M.; Li, J.; Wijesekera, K.; Cranston, E. D. *Biomacromolecules* **2013**, *14*, 3130.
- (51) Grishkewich, N.; Akhlaghi, S. P.; Zhaoling, Y.; Berry, R.; Tam, K. C. *Carbohydrate Polymers* **2016**, *144*, 215.
- (52) Hansson, S.; Antoni, P.; Bergenudd, H.; Malmstrom, E. *Polymer Chemistry* **2011**, *2*, 556.
- (53) Xu, Q.; Yi, J.; Zhang, X.; Zhang, H. *European Polymer Journal* **2008**, *44*, 2830.
- (54) Araki, J.; Wada, M.; Kuga, S. *Langmuir* **2000**, *17*, 21.
- (55) Majoinen, J.; Walther, A.; McKee, J. R.; Kontturi, E.; Aseyev, V.; Malho, J. M.; Ruokolainen, J.; Ikkala, O. *Biomacromolecules* **2011**, *12*, 2997.

- (56) Wang, H.-D.; Roeder, R. D.; Whitney, R. A.; Champagne, P.; Cunningham, M. F. *Journal of Polymer Science Part A: Polymer Chemistry* **2015**, n/a.
- (57) Yi, J.; Xu, Q.; Zhang, X.; Zhang, H. *Polymer* **2008**, *49*, 4406.
- (58) Yi, J.; Xu, Q.; Zhang, X.; Zhang, H. *Cellulose* **2009**, *16*, 989.
- (59) Rosilo, H.; McKee, J. R.; Kontturi, E.; Koho, T.; Hytonen, V. P.; Ikkala, O.; Kostiainen, M. A. *Nanoscale* **2014**, *6*, 11871.
- (60) McKee, J. R.; Huokuna, J.; Martikainen, L.; Karesoja, M.; Nykänen, A.; Kontturi, E.; Tenhu, H.; Ruokolainen, J.; Ikkala, O. *Angewandte Chemie International Edition* **2014**, *53*, 5049.
- (61) McKee, J. R.; Appel, E. A.; Seitsonen, J.; Kontturi, E.; Scherman, O. A.; Ikkala, O. *Advanced Functional Materials* **2014**, *24*, 2706.
- (62) Gorman, C. B.; Petrie, R. J.; Genzer, J. *Macromolecules* **2008**, *41*, 4856.
- (63) Xue, Y.-H.; Zhu, Y.-L.; Quan, W.; Qu, F.-H.; Han, C.; Fan, J.-T.; Liu, H. *Physical Chemistry Chemical Physics* **2013**, *15*, 15356.
- (64) Behling, R. E.; Williams, B. A.; Staade, B. L.; Wolf, L. M.; Cochran, E. W. *Macromolecules* **2009**, *42*, 1867.
- (65) Morandi, G.; Thielemans, W. *Polymer Chemistry* **2012**, *3*, 1402.
- (66) Wei, H.; Rodriguez, K.; Renneckar, S.; Vikesland, P. J. *Environmental Science: Nano* **2014**, *1*, 302.
- (67) Sullivan, E.; Moon, R.; Kalaitzidou, K. *Materials* **2015**, *8*, 8106.
- (68) Planes, M.; Brand, J.; Lewandowski, S.; Remaury, S.; Sole, S.; Le Coz, C.; Carlotti, S.; Sebe, G. *ACS Appl Mater Interfaces* **2016**.
- (69) Shanmuganathan, K.; Capadona, J. R.; Rowan, S. J.; Weder, C. *ACS Applied Materials & Interfaces* **2009**, *2*, 165.
- (70) Sirviö, J. A.; Visanko, M.; Heiskanen, J. P.; Liimatainen, H. *J. Mater. Chem. A* **2016**, *4*, 6368.
- (71) Cao, Y.; Zavaterra, P.; Youngblood, J.; Moon, R.; Weiss, J. *Cement and Concrete Composites* **2015**, *56*, 73.
- (72) Chen, L.; Cao, W.; Quinlan, P. J.; Berry, R. M.; Tam, K. C. *ACS Sustainable Chemistry & Engineering* **2015**, *3*, 978.
- (73) Zhou, Z.; Lu, C.; Wu, X.; Zhang, X. *RSC Advances* **2013**, *3*, 26066.
- (74) Tagad, C. K.; Rajdeo, K. S.; Kulkarni, A.; More, P.; Aiyer, R. C.; Sabharwal, S. *RSC Advances* **2014**, *4*, 24014.
- (75) Liu, C.; Xu, J.; Chen, H. *Journal of Inorganic and Organometallic Polymers and Materials* **2014**, *25*, 153.
- (76) Chang, Y.-C.; Chen, D.-H. *Journal of Hazardous Materials* **2009**, *165*, 664.
- (77) Chen, X.; Zhao, D.; An, Y.; Zhang, Y.; Cheng, J.; Wang, B.; Shi, L. *Journal of Colloid and Interface Science* **2008**, *322*, 414.
- (78) Uddin, K. M. A.; Lokanathan, A. R.; Liljeström, A.; Chen, X.; Rojas, O. J.; Laine, J. *Green Materials* **2014**, *2*, 183.
- (79) Shi, Z.; Tang, J.; Chen, L.; Yan, C.; Tanvir, S.; Anderson, W. A.; Berry, R. M.; Tam, K. C. *J. Mater. Chem. B* **2015**, *3*, 603.
- (80) Shin, Y.; Bae, I.-T.; Arey, B. W.; Exarhos, G. J. *The Journal of Physical Chemistry C* **2008**, *112*, 4844.

- (81) Lokanathan, A. R.; Uddin, K. M. A.; Rojas, O. J.; Laine, J. *Biomacromolecules* **2014**, *15*, 373.
- (82) Wu, X.; Lu, C.; Zhou, Z.; Yuan, G.; Xiong, R.; Zhang, X. *Environmental Science: Nano* **2014**, *1*, 71.
- (83) Wu, X.; Lu, C.; Zhang, W.; Yuan, G.; Xiong, R.; Zhang, X. *Journal of Materials Chemistry A* **2013**, *1*, 8645.
- (84) Tang, J.; Quinlan, P. J.; Tam, K. C. *Soft Matter* **2015**, *11*, 3512.
- (85) Chevalier, Y.; Bolzinger, M.-A. *Colloids and Surfaces A: Physicochemical and Engineering Aspects* **2013**, *439*, 23.
- (86) Ramsden, W. *Proceedings of the royal Society of London* **1903**, *72*, 156.
- (87) Pickering, S. U. *Journal of the Chemical Society, Transactions* **1907**, *91*, 2001.
- (88) Aveyard, R.; Binks, B. P.; Clint, J. H. *Advances in Colloid and Interface Science* **2003**, *100-102*, 503.
- (89) Tang, J.; Berry, R. M.; Tam, K. C. *Biomacromolecules* **2016**.
- (90) Vignati, E.; Piazza, R.; Lockhart, T. P. *Langmuir* **2003**, *19*, 6650.
- (91) Marto, J.; Ascenso, A.; Simoes, S.; Almeida, A. J.; Ribeiro, H. M. *Expert opinion on drug delivery* **2016**, *13*, 1093.
- (92) Lam, S.; Velikov, K. P.; Velev, O. D. *Current Opinion in Colloid & Interface Science* **2014**, *19*, 490.
- (93) Saidane, D.; Perrin, E.; Cherhal, F.; Guellec, F.; Capron, I. *Philosophical Transactions of the Royal Society of London A: Mathematical, Physical and Engineering Sciences* **2016**, *374*.
- (94) Nikfarjam, N.; Taheri Qazvini, N.; Deng, Y. *European Polymer Journal* **2015**, *64*, 179.
- (95) Zoppe, J. O.; Venditti, R. A.; Rojas, O. J. *Journal of Colloid and Interface Science* **2012**, *369*, 202.
- (96) Cunha, A. G.; Mougél, J.-B.; Cathala, B.; Berglund, L. A.; Capron, I. *Langmuir* **2014**, *30*, 9327.
- (97) Dinsmore, A. D.; Hsu, M. F.; Nikolaidis, M. G.; Marquez, M.; Bausch, A. R.; Weitz, D. A. *Science* **2002**, *298*, 1006.
- (98) Thompson, K. L.; Williams, M.; Armes, S. P. *J Colloid Interface Sci* **2015**, *447*, 217.
- (99) Hsu, M. F.; Nikolaidis, M. G.; Dinsmore, A. D.; Bausch, A. R.; Gordon, V. D.; Chen, X.; Hutchinson, J. W.; Weitz, D. A.; Marquez, M. *Langmuir* **2005**, *21*, 2963.
- (100) Li, J.; Stöver, H. D. H. *Langmuir* **2010**, *26*, 15554.
- (101) Noble, P. F.; Cayre, O. J.; Alargova, R. G.; Velev, O. D.; Paunov, V. N. *Journal of the American Chemical Society* **2004**, *126*, 8092.
- (102) Chen, T.; Colver, P. J.; Bon, S. A. F. *Advanced Materials* **2007**, *19*, 2286.
- (103) Hu, W.; Gu, H.; Wang, J.; Li, Y.; Wang, Z. *Colloid and Polymer Science* **2013**, *291*, 2697.
- (104) Zhang, C.; Hu, C.; Zhao, Y.; Moller, M.; Yan, K.; Zhu, X. *Langmuir* **2013**, *29*, 15457.
- (105) Wang, H.; Zhu, X.; Tsarkova, L.; Pich, A.; Möller, M. *ACS Nano* **2011**, *5*, 3937.
- (106) Yow, H. N.; Routh, A. F. *Langmuir* **2009**, *25*, 159.
- (107) Thompson, K. L.; Armes, S. P.; Howse, J. R.; Ebbens, S.; Ahmad, I.; Zaidi, J. H.; York, D. W.; Burdis, J. A. *Macromolecules* **2010**, *43*, 10466.
- (108) Banerjee, S.; Paira, T. K.; Mandal, T. K. *Polymer Chemistry* **2014**, *5*, 4153.

- (109) Matyjaszewski, K.; Gaynor, S.; Wang, J.-S. *Macromolecules* **1995**, *28*, 2093.
- (110) Moad, G.; Chiefari, J.; Chong, Y. K.; Krstina, J.; Mayadunne, R. T. A.; Postma, A.; Rizzardo, E.; Thang, S. H. *Polymer International* **2000**, *49*, 993.
- (111) Chiefari, J.; Chong, Y. K.; Ercole, F.; Krstina, J.; Jeffery, J.; Le, T. P. T.; Mayadunne, R. T. A.; Meijs, G. F.; Moad, C. L.; Moad, G.; Rizzardo, E.; Thang, S. H. *Macromolecules* **1998**, *31*, 5559.
- (112) Nicolas, J.; Guillaneuf, Y.; Lefay, C.; Bertin, D.; Gimes, D.; Charleux, B. *Progress in Polymer Science* **2013**, *38*, 63.
- (113) Jenkins, A. D.; Jones, R. G.; Moad, G. *Pure and Applied Chemistry* **2009**, *82*, 483.
- (114) Wang, J.-S.; Matyjaszewski, K. *Journal of the American Chemical Society* **1995**, *117*, 5614.
- (115) Fantin, M.; Isse, A. A.; Venzo, A.; Gennaro, A.; Matyjaszewski, K. *J Am Chem Soc* **2016**, *138*, 7216.
- (116) Rademacher, J. T.; Baum, M.; Pallack, M. E.; Brittain, W. J.; Simonsick, W. J. *Macromolecules* **1999**, *33*, 284.
- (117) Tsarevsky, N. V.; Matyjaszewski, K. *Chemical Reviews* **2007**, *107*, 2270.
- (118) Gromada, J.; Matyjaszewski, K. *Macromolecules* **2001**, *34*, 7664.
- (119) Jakubowski, W.; Matyjaszewski, K. *Macromolecules* **2005**, *38*, 4139.
- (120) Min, K.; Gao, H.; Matyjaszewski, K. *Macromolecules* **2007**, *40*, 1789.
- (121) Matyjaszewski, K.; Dong, H.; Jakubowski, W.; Pietrasik, J.; Kusumo, A. *Langmuir* **2007**, *23*, 4528.
- (122) Marutani, E.; Yamamoto, S.; Ninjbadgar, T.; Tsujii, Y.; Fukuda, T.; Takano, M. *Polymer* **2004**, *45*, 2231.
- (123) Huang, C.-F. *Polymer Journal* **2016**, *48*, 341.
- (124) Hosseiny, S.; van Rijn, P. *Polymers* **2013**, *5*, 1229.
- (125) Siegwart, D. J.; Oh, J. K.; Matyjaszewski, K. *Progress in Polymer Science* **2012**, *37*, 18.
- (126) Fristrup, C. J.; Jankova, K.; Hvilsted, S. *Soft Matter* **2009**, *5*, 4623.
- (127) Khabibullin, A.; Mastan, E.; Matyjaszewski, K.; Zhu, S. In *Controlled Radical Polymerization at and from Solid Surfaces*; Springer: 2015, p 29.
- (128) Nicole, L.; Laberty-Robert, C.; Rozes, L.; Sanchez, C. *Nanoscale* **2014**, *6*, 6267.
- (129) Tsai, Y.; Wang, W.-C. *Journal of Applied Polymer Science* **2006**, *101*, 1953.
- (130) Sanchez, C.; Belleville, P.; Popall, M.; Nicole, L. *Chemical Society Reviews* **2011**, *40*, 696.
- (131) Hansson, S.; Trouillet, V.; Tischer, T.; Goldmann, A. S.; Carlmark, A.; Barner-Kowollik, C.; Malmstrom, E. *Biomacromolecules* **2013**, *14*, 64.
- (132) Hui, C. M.; Pietrasik, J.; Schmitt, M.; Mahoney, C.; Choi, J.; Bockstaller, M. R.; Matyjaszewski, K. *Chemistry of Materials* **2014**, *26*, 745.
- (133) Yan, J.; Pan, X.; Schmitt, M.; Wang, Z.; Bockstaller, M. R.; Matyjaszewski, K. *ACS Macro Letters* **2016**, *5*, 661.
- (134) Fan, X.; Lin, L.; Messersmith, P. B. *Composites Science and Technology* **2006**, *66*, 1198.

- (135) Feng, W.; Brash, J.; Zhu, S. *Journal of Polymer Science Part A: Polymer Chemistry* **2004**, *42*, 2931.
- (136) Tugulu, S.; Barbey, R.; Harms, M.; Fricke, M.; Volkmer, D.; Rossi, A.; Klok, H.-A. *Macromolecules* **2007**, *40*, 168.
- (137) Wei, L.; McDonald, A. *Materials* **2016**, *9*, 303.
- (138) Zubik, K.; Singhsa, P.; Wang, Y.; Manuspiya, H.; Narain, R. *Polymers* **2017**, *9*, 119.
- (139) Wu, X.; Shi, Z.; Tjandra, R.; Cousins, A. J.; Sy, S.; Yu, A.; Berry, R. M.; Tam, K. C. *Journal of Materials Chemistry A* **2015**, *3*, 23768.
- (140) Yamamoto, S.; Tsujii, Y.; Fukuda, T. *Macromolecules* **2002**, *35*, 6077.
- (141) Yim, H.; Kent, M. S.; Mendez, S.; Lopez, G. P.; Satija, S.; Seo, Y. *Macromolecules* **2006**, *39*, 3420.
- (142) Dang, A.; Hui, C. M.; Ferebee, R.; Kubiak, J.; Li, T.; Matyjaszewski, K.; Bockstaller, M. R. *Macromolecular Symposia* **2013**, *331-332*, 9.
- (143) Fu, Y.; Li, G.; Yu, H.; Liu, Y. *Applied Surface Science* **2012**, *258*, 2529.
- (144) Wang, H.-D.; Roeder, R. D.; Whitney, R. A.; Champagne, P.; Cunningham, M. F. *Journal of Polymer Science Part A: Polymer Chemistry* **2015**, *53*, 2800.
- (145) Ma, L.; Liu, R.; Tan, J.; Wang, D.; Jin, X.; Kang, H.; Wu, M.; Huang, Y. *Langmuir : the ACS journal of surfaces and colloids* **2010**, *26*, 8697.
- (146) Östmark, E.; Harrison, S.; Wooley, K. L.; Malmström, E. E. *Biomacromolecules* **2007**, *8*, 1138.
- (147) Sui, X.; Yuan, J.; Zhou, M.; Zhang, J.; Yang, H.; Yuan, W.; Wei, Y.; Pan, C. *Biomacromolecules* **2008**, *9*, 2615.
- (148) Rutnakornpituk, B.; Wichai, U.; Vilaivan, T.; Rutnakornpituk, M. *J Nanopart Res* **2011**, *13*, 6847.
- (149) Beck-Candanedo, S.; Roman, M.; Gray, D. G. *Biomacromolecules* **2005**, *6*, 1048.
- (150) Meng, T.; Gao, X.; Zhang, J.; Yuan, J.; Zhang, Y.; He, J. *Polymer* **2009**, *50*, 447.
- (151) Çetin, N. S.; Tingaut, P.; Özmen, N.; Henry, N.; Harper, D.; Dadmun, M.; Sèbe, G. *Macromolecular Bioscience* **2009**, *9*, 997.
- (152) Yang, H.; Tejado, A.; Alam, N.; Antal, M.; van de Ven, T. G. M. *Langmuir* **2012**, *28*, 7834.
- (153) Earl, W. L.; VanderHart, D. L. *Journal of the American Chemical Society* **1980**, *102*, 3251.
- (154) Roman, M.; Winter, W. T. *Biomacromolecules* **2004**, *5*, 1671.
- (155) van Ravensteijn, B. G. P.; Kegel, W. K. *Polym. Chem.* **2016**, *7*, 2858.
- (156) Fox, T. G.; Flory, P. J. *Journal of Applied Physics* **1950**, *21*, 581.
- (157) Rudnick, J.; Taylor, P.; Litt, M.; Hopfinger, A. *Journal of Polymer Science: Polymer Physics Edition* **1979**, *17*, 311.
- (158) Montserrat, S.; Colomer, P. *Polymer Bulletin* **1984**, *12*, 173.
- (159) Fragneaud, B.; Masenelli-Varlot, K.; Gonzalez-Montiel, A.; Terrones, M.; Cavallé, J. Y. *Composites Science and Technology* **2008**, *68*, 3265.
- (160) Baldwin, A. D.; Kiick, K. L. *Peptide Science* **2010**, *94*, 128.
- (161) Tizzotti, M.; Charlot, A.; Fleury, E.; Stenzel, M.; Bernard, J. *Macromolecular Rapid Communications* **2010**, *31*, 1751.

- (162) Eichhorn, S. J.; Dufresne, A.; Aranguren, M.; Marcovich, N. E.; Capadona, J. R.; Rowan, S. J.; Weder, C.; Thielemans, W.; Roman, M.; Renneckar, S.; Gindl, W.; Veigel, S.; Keckes, J.; Yano, H.; Abe, K.; Nogi, M.; Nakagaito, A. N.; Mangalam, A.; Simonsen, J.; Benight, A. S.; Bismarck, A.; Berglund, L. A.; Peijs, T. *J Mater Sci* **2010**, *45*, 1.
- (163) de Souza Lima, M. M.; Borsali, R. *Macromolecular Rapid Communications* **2004**, *25*, 771.
- (164) Dong, L.; Zhang, X.; Ren, S.; Lei, T.; Sun, X.; Qi, Y.; Wu, Q. *RSC Adv.* **2016**, *6*, 6436.
- (165) Jakubowski, W.; Min, K.; Matyjaszewski, K. *Macromolecules* **2005**, *39*, 39.
- (166) Hansson, S.; Östmark, E.; Carlmark, A.; Malmström, E. *ACS Applied Materials & Interfaces* **2009**, *1*, 2651.
- (167) Hansson, S.; Carlmark, A.; Malmström, E.; Fogelström, L. *Journal of Applied Polymer Science* **2015**, *132*, n/a.
- (168) Ates, Z.; Audouin, F.; Harrington, A.; O'Connor, B.; Heise, A. *Macromol Biosci* **2014**, *14*, 1600.
- (169) Paterson, S. M.; Brown, D. H.; Chirila, T. V.; Keen, I.; Whittaker, A. K.; Baker, M. V. *Journal of Polymer Science Part A: Polymer Chemistry* **2010**, *48*, 4084.
- (170) Ma, W.; Otsuka, H.; Takahara, A. *Chem Commun (Camb)* **2011**, *47*, 5813.
- (171) Borah, K. J.; Dutta, P.; Borah, R. *ChemInform* **2011**, *42*, no.
- (172) Shieh, J.-J.; Chung, T. S. *Journal of Polymer Science Part B: Polymer Physics* **1999**, *37*, 2851.
- (173) Jiang, J.; Zhang, Y.; Cao, D.; Jiang, P. *Chemical Engineering Journal* **2013**, *215–216*, 222.
- (174) Kavitha, T.; Kang, I.-K.; Park, S.-Y. *Polymer International* **2015**, *64*, 1660.
- (175) Hofman, A. H.; Alberda van Ekenstein, G. O. R.; Woortman, A. J. J.; ten Brinke, G.; Loos, K. *Polym. Chem.* **2015**, *6*, 7015.
- (176) Pietrasik, J.; Tsarevsky, N. V. *European Polymer Journal* **2010**, *46*, 2333.
- (177) Yang, R.; Wang, Y.; Wang, X.; He, W.; Pan, C. *European Polymer Journal* **2003**, *39*, 2029.
- (178) Xia, J.; Zhang, X.; Matyjaszewski, K. *Macromolecules* **1999**, *32*, 3531.
- (179) Liu, Y.; Klep, V.; Zdyrko, B.; Luzinov, I. *Langmuir* **2004**, *20*, 6710.
- (180) Mastan, E.; Xi, L.; Zhu, S. *Macromolecular Theory and Simulations* **2016**, *25*, 220.
- (181) Sumerlin, B. S.; Neugebauer, D.; Matyjaszewski, K. *Macromolecules* **2005**, *38*, 702.
- (182) Chen, J.-K.; Hsieh, C.-Y.; Huang, C.-F.; Li, P. M.; Kuo, S.-W.; Chang, F.-C. *Macromolecules* **2008**, *41*, 8729.
- (183) Zhang, L.; Gu, J.; Song, L.; Chen, L.; Huang, Y.; Zhang, J.; Chen, T. *J. Mater. Chem. A* **2016**, *4*, 10810.
- (184) Tang, J.; Shi, Z.; Berry, R. M.; Tam, K. C. *Industrial & Engineering Chemistry Research* **2015**, *54*, 3299.
- (185) Rezayat, M.; Blundell, R. K.; Camp, J. E.; Walsh, D. A.; Thielemans, W. *ACS Sustainable Chemistry & Engineering* **2014**, *2*, 1241.
- (186) Schlesinger, M.; Giese, M.; Blusch, L. K.; Hamad, W. Y.; MacLachlan, M. J. *Chemical Communications* **2015**, *51*, 530.

- (187) Wu, X.; Shi, Z.; Fu, S.; Chen, J.; Berry, R. M.; Tam, K. C. *ACS Sustainable Chemistry & Engineering* **2016**, *4*, 5929.
- (188) Li, J.; Huang, Z.; Yang, M.; Tan, L.; Zhang, X.; Gao, H.; Tang, Y.; Ma, Q.; Wang, G. *New J. Chem.* **2015**, *39*, 2949.
- (189) Fang, Z.; Yang, D.; Gao, Y.; Li, H. *RSC Adv.* **2014**, *4*, 49866.
- (190) Shan, C.; Yang, H.; Han, D.; Zhang, Q.; Ivaska, A.; Niu, L. *Biosensors & bioelectronics* **2010**, *25*, 1070.
- (191) Pandey, S.; Goswami, G. K.; Nanda, K. K. *Carbohydr Polym* **2013**, *94*, 229.
- (192) Zhang, Z.; Tingaut, P.; Rentsch, D.; Zimmermann, T.; Sèbe, G. *ChemSusChem* **2015**, *8*, 2681.
- (193) Picard, G.; Simon, D.; Kadiri, Y.; LeBreux, J. D.; Ghozayel, F. *Langmuir* **2012**, *28*, 14799.
- (194) Lagerwall, J. P. F.; Schutz, C.; Salajkova, M.; Noh, J.; Hyun Park, J.; Scalia, G.; Bergstrom, L. *NPG Asia Mater* **2014**, *6*, e80.
- (195) Mohammed, N.; Grishkewich, N.; Berry, R. M.; Tam, K. C. *Cellulose* **2015**, *22*, 3725.
- (196) Mohammed, N.; Baidya, A.; Murugesan, V.; Kumar, A. A.; Ganayee, M. A.; Mohanty, J. S.; Tam, K. C.; Pradeep, T. *ACS Sustainable Chemistry & Engineering* **2016**, *4*, 6167.
- (197) Yang, X.; Shi, K.; Zhitomirsky, I.; Cranston, E. D. *Advanced Materials* **2015**, *27*, 6104.
- (198) Xiong, R.; Hu, K.; Grant, A. M.; Ma, R.; Xu, W.; Lu, C.; Zhang, X.; Tsukruk, V. V. *Advanced Materials* **2015**, 1501.
- (199) Zander, N. E. *Thermal and FTIR characterization of poly (4-vinylpyridine) crosslinked with metal salts*; Army Research Laboratory: Aberdeen Proving Ground, MD, 2010.
- (200) Gupta, K. C.; Sahoo, S. *Cellulose* **2001**, *8*, 233.
- (201) Lindqvist, J.; Nyström, D.; Östmark, E.; Antoni, P.; Carlmark, A.; Johansson, M.; Hult, A.; Malmström, E. *Biomacromolecules* **2008**, *9*, 2139.
- (202) Chen, J.-K.; Chang, C.-J. *Materials* **2014**, *7*, 805.
- (203) Ejaz, M.; Rai, S. C.; Wang, K.; Zhang, K.; Zhou, W.; Grayson, S. M. *Journal of Materials Chemistry C* **2014**, *2*, 4073.
- (204) Harada, M.; Kizaki, S. *Crystal Growth & Design* **2016**, *16*, 1200.
- (205) Liang, X.; Wang, Z. J.; Liu, C. J. *Nanoscale Res Lett* **2009**, *5*, 124.
- (206) Wei, H.; Rodriguez, K.; Rennecker, S.; Leng, W.; Vikesland, P. *Analyst* **2015**.
- (207) Yin, Q.; Han, X.; Ponsinet, V.; Liu, H. *Journal of colloid and interface science* **2014**, *431*, 97.
- (208) Zhao, X.; Li, Z.; Deng, Y.; Zhao, Z.; Li, X.; Xia, Y. *Materials* **2017**, *10*, 557.
- (209) Fu, S.; Ren, G.; Li, S.; Chai, F.; Wang, C.; Qu, F. *New J. Chem.* **2017**, *41*, 1509.
- (210) Liu, B.; Yu, S.; Wang, Q.; Hu, W.; Jing, P.; Liu, Y.; Jia, W.; Liu, Y.; Liu, L.; Zhang, J. *Chemical Communications* **2013**, *49*, 3757.
- (211) Yu, J.; Sun, L.; Ma, C.; Qiao, Y.; Yao, H. *Waste management* **2016**, *48*, 300.
- (212) Yang, T.-C.; Noguchi, T.; Isshiki, M.; Wu, J.-H. *Polymer Composites* **2016**, *37*, 3391.
- (213) Mallakpour, S.; Abdolmaleki, A.; Tabebordbar, H. *European Polymer Journal* **2016**, *78*, 141.
- (214) Guermazi, N.; Haddar, N.; Elleuch, K.; Ayedi, H. F. *Polymer Composites* **2016**, *37*, 2171.

- (215) Klapiszewski, L.; Pawlak, F.; Tomaszewska, J.; Jesionowski, T. *Polymers* **2015**, *7*, 1767.
- (216) Klarić, I.; Roje, U.; Bravar, M. *Journal of Applied Polymer Science* **1996**, *61*, 1123.
- (217) Folarin, O.; Sadiku, E. *International Journal of Physical Sciences* **2011**, *6*, 4323.
- (218) Saeedi, M.; Ghasemi, I.; Karrabi, M. *Iran Polym J* **2011**, *20*, 423.
- (219) Karayildirim, T.; Yanik, J.; Yuksel, M.; Saglam, M.; Vasile, C.; Bockhorn, H. *Journal of Analytical and Applied Pyrolysis* **2006**, *75*, 112.
- (220) Yang, T.-C.; Noguchi, T.; Isshiki, M.; Wu, J.-H. *Polymer Degradation and Stability* **2014**, *104*, 33.
- (221) Cho, S.; Choi, W. *Journal of Photochemistry and Photobiology A: Chemistry* **2001**, *143*, 221.
- (222) Kim, S. H.; Kwak, S.-Y.; Suzuki, T. *Polymer* **2006**, *47*, 3005.
- (223) Sokhandani, P.; Babaluo, A. A.; Rezaei, M.; Shahrezaei, M.; Hasanzadeh, A.; Mehmandoust, S. G.; Mehdizadeh, R. *Journal of Applied Polymer Science* **2013**, *129*, 3265.
- (224) Yang, C.; Gong, C.; Peng, T.; Deng, K.; Zan, L. *J Hazard Mater* **2010**, *178*, 152.
- (225) Cranston, E. D.; Gray, D. G. *Colloids and Surfaces A: Physicochemical and Engineering Aspects* **2008**, *325*, 44.
- (226) Habibi, Y. *Chemical Society Reviews* **2014**, *43*, 1519.
- (227) Sheltami, R. M.; Kargarzadeh, H.; Abdullah, I. *Sains Malaysiana* **2015**, *44*, 801.
- (228) Wu, L.; Jin, C.; Sun, X. *Biomacromolecules* **2011**, *12*, 235.
- (229) Lendlein, A.; Jiang, H.; Junger, O.; Langer, R. *Nature* **2005**, *434*, 879.
- (230) Wang, L.; Yang, X.; Chen, H.; Gong, T.; Li, W.; Yang, G.; Zhou, S. *ACS Appl Mater Interfaces* **2013**, *5*, 10520.
- (231) Garle, A.; Kong, S.; Ojha, U.; Budhlall, B. M. *ACS Appl Mater Interfaces* **2012**, *4*, 645.
- (232) Chung, C.-M.; Roh, Y.-S.; Cho, S.-Y.; Kim, J.-G. *Chemistry of Materials* **2004**, *16*, 3982.
- (233) Nakayama, Y.; Matsuda, T. *Journal of Polymer Science Part A: Polymer Chemistry* **1992**, *30*, 2451.
- (234) Abrakhi, S.; Peralta, S.; Cantin, S.; Fichet, O.; Teyssié, D. *Colloid and Polymer Science* **2011**, *290*, 423.
- (235) Li, X.; Cui, J.; Zhang, W.; Huang, J.; Li, W.; Lin, C.; Jiang, Y.; Zhang, Y.; Li, G. *Journal of Materials Chemistry* **2011**, *21*, 17953.
- (236) Petruczok, C. D.; Armagan, E.; Ince, G. O.; Gleason, K. K. *Macromolecular Rapid Communications* **2014**, *35*, 1345.
- (237) Ma, Y.; Ma, H.; Yang, Z.; Ma, J.; Su, Y.; Li, W.; Lei, Z. *Langmuir* **2015**, *31*, 4916.
- (238) Wang, G.; Henselwood, F.; Liu, G. *Langmuir* **1998**, *14*, 1554.
- (239) Kim, S.-H.; Chung, I.-D.; Ha, C.-S.; Kim, K.-J.; Cho, W.-J. *Journal of Applied Polymer Science* **1999**, *73*, 2349.
- (240) Tunc, D.; Le Coz, C.; Alexandre, M.; Desbois, P.; Lecomte, P.; Carlotti, S. *Macromolecules* **2014**, *47*, 8247.
- (241) Gupta, P.; Trenor, S. R.; Long, T. E.; Wilkes, G. L. *Macromolecules* **2004**, *37*, 9211.
- (242) Dong, C. M.; Wu, X.; Caves, J.; Rele, S. S.; Thomas, B. S.; Chaikof, E. L. *Biomaterials* **2005**, *26*, 4041.

- (243) Dong, W.; Ren, J.; Lin, L.; Shi, D.; Ni, Z.; Chen, M. *Polymer Degradation and Stability* **2012**, *97*, 578.
- (244) Williams, S. R.; Barta, Z.; Ramirez, S. M.; Long, T. E. *Macromolecular Chemistry and Physics* **2009**, *210*, 555.
- (245) Kim, H.-T.; Park, J.-K. *Polymer Bulletin* **1998**, *41*, 325.
- (246) Ni, Y.; Zheng, S. *Chemistry of Materials* **2004**, *16*, 5141.
- (247) Edge, M.; Liauw, C. M.; Allen, N. S.; Herrero, R. *Polymer Degradation and Stability* **2010**, *95*, 2022.
- (248) Geddes, W. *European Polymer Journal* **1967**, *3*, 267.
- (249) Zheng, X.-G.; Tang, L.-H.; Zhang, N.; Gao, Q.-H.; Zhang, C.-F.; Zhu, Z.-B. *Energy & Fuels* **2003**, *17*, 896.
- (250) Martinez, G.; Mijangos, C.; Millan, J.-L.; Gerrard, D. L.; Maddams, W. F. *Die Makromolekulare Chemie* **1984**, *185*, 1277.
- (251) Abbàs, K. B.; Laurence, R. L. *Journal of Polymer Science: Polymer Chemistry Edition* **1975**, *13*, 1889.
- (252) Decker, C.; Balandier, M. *Journal of Photochemistry* **1981**, *15*, 221.
- (253) Bersch, C. F.; Harvey, M. R.; Achhammer, B. G. *Journal of Research of the National Bureau of Standards* **1958**, *60*, 481.
- (254) Martin, K. G. *British Polymer Journal* **1973**, *5*, 443.
- (255) Pan, Y.-T.; Wang, D.-Y. *RSC Adv.* **2015**, *5*, 27837.
- (256) Saad, N. A.; Al-Maamory, M. H.; Mohammed, M. R.; Hashim, A. A. *Materials Sciences and Applications* **2012**, *03*, 784.
- (257) Zhao, Y.; Li, Y.; Demco, D. E.; Zhu, X.; Moller, M. *Langmuir* **2014**, *30*, 4253.
- (258) Fielding, L. A.; Armes, S. P. *Journal of Materials Chemistry* **2012**, *22*, 11235.
- (259) Thompson, K. L.; Mable, C. J.; Lane, J. A.; Derry, M. J.; Fielding, L. A.; Armes, S. P. *Langmuir* **2015**, *31*, 4137.
- (260) Berton-Carabin, C. C.; Schroën, K. *Annual Review of Food Science and Technology* **2015**, *6*, 263.
- (261) van Wijk, J.; Heunis, T.; Harmzen, E.; Dicks, L. M.; Meuldijk, J.; Klumperman, B. *Chem Commun (Camb)* **2014**, *50*, 15427.
- (262) Gordon, V. D.; Chen, X.; Hutchinson, J. W.; Bausch, A. R.; Marquez, M.; Weitz, D. A. *Journal of the American Chemical Society* **2004**, *126*, 14117.
- (263) Laïb, S.; Routh, A. F. *Journal of Colloid and Interface Science* **2008**, *317*, 121.
- (264) Lawrence, D. B.; Cai, T.; Hu, Z.; Marquez, M.; Dinsmore, A. D. *Langmuir* **2007**, *23*, 395.
- (265) Caruso, F.; Caruso, R. A.; Möhwald, H. *Science* **1998**, *282*, 1111.
- (266) Croll, L. M.; Stöver, H. D. H. *Langmuir* **2003**, *19*, 5918.
- (267) Chen, Y.; Wang, C.; Chen, J.; Liu, X.; Tong, Z. *Journal of Polymer Science Part A: Polymer Chemistry* **2009**, *47*, 1354.
- (268) Zhu, X.; Jaumann, M.; Peter, K.; Möller, M.; Melian, C.; Adams-Buda, A.; Demco, D. E.; Blümich, B. *Macromolecules* **2006**, *39*, 1701.
- (269) Kalashnikova, I.; Bizot, H.; Cathala, B.; Capron, I. *Biomacromolecules* **2012**, *13*, 267.
- (270) Kalashnikova, I.; Bizot, H.; Cathala, B.; Capron, I. *Langmuir* **2011**, *27*, 7471.

- (271) Cherhal, F.; Cousin, F.; Capron, I. *Biomacromolecules* **2016**, *17*, 496.
- (272) Buskens, P.; Mourad, M.; Meulendijks, N.; van Ee, R.; Burghoorn, M.; Verheijen, M.; van Veldhoven, E. *Colloids and Surfaces A: Physicochemical and Engineering Aspects* **2015**, *487*, 1.
- (273) Pang, Q.; Tang, J.; Huang, H.; Liang, X.; Hart, C.; Tam, K. C.; Nazar, L. F. *Adv Mater* **2015**, *27*, 6021.
- (274) Lee, K. Y.; Blaker, J. J.; Murakami, R.; Heng, J. Y.; Bismarck, A. *Langmuir* **2014**, *30*, 452.
- (275) Zhang, X.; Liu, B.; Dave, N.; Servos, M. R.; Liu, J. *Langmuir* **2012**, *28*, 17053.
- (276) Arditty, S.; Whitby, C. P.; Binks, B. P.; Schmitt, V.; Leal-Calderon, F. *The European physical journal. E, Soft matter* **2003**, *11*, 273.
- (277) van Wijk, J.; Salari, J. W. O.; Zaquen, N.; Meuldijk, J.; Klumperman, B. *Journal of Materials Chemistry B* **2013**, *1*, 2394.
- (278) Gautier, F.; Destribats, M.; Perrier-Cornet, R.; Dechezelles, J.-F.; Giermanska, J.; Heroguez, V.; Ravaine, S.; Leal-Calderon, F.; Schmitt, V. *Physical Chemistry Chemical Physics* **2007**, *9*, 6455.
- (279) Ougiya, H.; Watanabe, K.; Morinaga, Y.; Yoshinaga, F. *Bioscience, biotechnology, and biochemistry* **1997**, *61*, 1541.
- (280) Whitby, C.; Wanless, E. *Materials* **2016**, *9*, 626.